An Investigation of C_{60}/Semiconductor and C_{60}/Ferromagnetic Interfaces Using a Metastable Helium Beam

Jason Chentian Zhang

Doctor of Philosophy

University of York

Physics

September 2018

Abstract

This thesis describes the further development of an existing facility for performing electron spectroscopy, and its application to the study of organic/semiconductor and organic/oxide interfaces. A monochromated x-ray source has been installed on the system to allow x-ray photoelectron spectroscopy (XPS) to be performed in addition to ultraviolet photoelectron spectroscopy (UPS) and the uncommon technique of metastable de-excitation spectroscopy (MDS). The resulting instrument is the first of its kind in the world, allowing XPS, UPS, and MDS to all be performed on the same surface, revealing detailed and complementary information on the electronic, magnetic, and chemical properties of the sample.

To test the instrument and gain experience in XPS, a detailed study of the carbon chemistry of graphene oxide prepared under different conditions was conducted. Additional experience in the application of spin-polarised MDS, obtained during a three-month visit to the National Institute for Materials Science (NIMS) in Tsukuba, Japan, is described culminating in a study of Fe/Fe_3O_4 interfaces. It is shown that the two layers in this system are ferromagnetically coupled which leads to potential applications as a synthetic antiferromagnet in a spintronics device. The ability to grow high-quality Fe_3O_4 thin films on the York system is also demonstrated.

The final chapters of the thesis describe the study of interfaces formed from C_{60} deposited on a Si(111) substrate and a $La_{0.66}Sr_{0.33}MnO_3$ (LSMO) substrate. The former study was conducted to gain experience in the preparation of organic interfaces but revealed important details on the nature of this technologically-relevant interface. It also demonstrates the power of MDS in revealing intramolecular electronic structure that is not observable using UPS. Similarly, the study of C_{60}/LSMO interfaces is relevant to the development of organic spintronics devices. However, it is shown that C_{60} adsorbs on LSMO in clusters at low coverage with a flat film only forming at coverages of 25 monolayers and above. These findings will help in the effort to incorporate these materials in future organic devices.

Contents

List of Figures

Acknowledgements

I would firstly like to thank my supervisor Dr. Andrew Pratt for giving me the opportunity to work on this project and for having unending patience with my shenanigans.

I would like to thank the members of the surface physics group, for their support and advice.

I would also like to thank all the support staff in the department for their support. Without you this project would not be possible.

I was fortunate enough to work at the National Institute for Materials Science (NIMS) in Tsukuba, Japan during my first year and I would like to thank Yamauchi-san, Kurahashi-san and Sun-san for the guidance I received while I was there.

I would like to thank my wife Yali, without whom I probably would have finished a year earlier.

Finally, I would like to thank Phil 'Phillykins' Bentley for being a literally constant companion and a bottomless source of memes.

Declaration

I declare that the work presented in this thesis, except contributions acknowledged explicitly in the text or by reference, is based on my own research. No part of this work has previously been submitted for any award or qualification.

The following publications, either in print or soon to be submitted, have arisen from this work:

[1] K.-G. Zhou, K. S. Vasu, C. T. Cherian, M. Neek-Amal, **J. C. Zhang**, H. Ghorbanfekr-Kalashami, K. Huang, O. P. Marshall, V.G. Kravets, J. Abraham, Y. Su, A. N. Grigorenko, A. Pratt, A. K. Geim, F. M. Peeters, K. S. Novoselov, and R. R. Nair, *Electrically controlled water permeation through graphene oxide membranes*, Nature **559**, 236 (2018)

[2] Q. Yang, Y. Su, C. Chi, C. T. Cherian, K. Huang, V. G. Kravets, F. C. Wang, **J. C. Zhang**, A. Pratt, A. N. Grigorenko, F. Guinea, A. K. Geim, and R. R. Nair, *Ultrathin graphene-based membrane with precise molecular sieving and ultrafast solvent permeation*, Nature Mater. **16**, 1198 (2017)

[3] **J. C. Zhang**, P. Bentley, X. Sun, M. Kurahashi, Y. Yamauchi and A. Pratt, *Origin of antiferromagnetic exchange coupling at Fe/Fe_3O_4 interfaces*, in preparation

[4] **J. C. Zhang**, S. Mann, P. Bentley, and A. Pratt, *Observation of conformationally degenerate energy states in C_{60} molecules using a metastable helium beam*, in preparation

[5] **J. C. Zhang**, P. Graziosi, V. A. Dediu, A. Pratt, and I. Bergenti, *High-coverage flattening of clustered C_{60} molecules on LSMO*, in preparation

Chapter 1

Introduction

No longer constrained to the laboratories of academic research, organic electronics is now a multi-billion dollar industry that is still continuing to grow [1]. Organic devices have been incorporated into everyday technology such as smartphones and TVs, where the use of organic light emitting diodes (OLEDs) [2] dominates as the basis for their displays. These developments are the most impactful outcome of the field of organic semiconductor (OSC) research with associated devices presenting a number of advantages over their traditional inorganic counterparts in cheaper production costs, increased versatility, compatibility with flexible substrates, transparency etc. [3, 4, 5]. These advantages allow the application of OSCs to a wide variety of fields beyond consumer goods, such as energy (generation/storage) and biomedical [6, 7]. Although OLEDs may be ahead of other OSCs in commercialisation, with its clear and very much realised applications, many other OSCs have also been the focus of intense research, such as organic field effect transistors (OFETs) [8, 9] and organic photovoltaics [10, 11]. These have all exhibited their own unique properties, such as low spin-orbit coupling, that can give them an edge over conventional electronics devices.

Further opportunities for the application (such as organic spin-valves and organic magnetic tunnel junctions) of OSCs lie in the newfield of organic spintronics [12, 13, 14, 15]. This aims to use the intrinsic spin of electrons as a carrier of information instead of, or in addition, to the use of electric charge. The transport of a spin signal has a distinct advantage over a movement of charge in that no net electrical current is necessary, which is much more power efficient, as no heat is generated. The

potential of organic materials in spintronics devices has been acknowledged since the early experiments of spin-polarised electron injection [16] and the observation of organic magnetoresistance [17]. For these applications, many of the advantages of OSCs also apply and in addition to this, organic materials also generally exhibit low spin-orbit coupling as a result of often being made of lighter elements (such as carbon, the key building block for organic molecules). This extends the spin relaxation times in the material, although low electron mobility when compared to better conducting materials limits the spin diffusion length [13, 15]. Over the last one and half decade, an increasing amount of research has been directed into organic spintronics, and there has been considerable success in making spin-based devices, such as magnetic tunnel junctions [18, 19] and spin valves [17, 20, 21].

Despite their various attractive properties, there are limitations to OSCs that stand in the way of even further industrial use. A property common to many OSCs is that they generally have lower electron mobility through the material when compared to conventional inorganic semiconductors [22]. This reduces the efficiency in electronics applications and the transport length in spintronics devices. Due to this, even though many devices have been made in research environments that function, there is a struggle to make them compete on an industrial level. Thankfully, the versatility of OSCs allow innumerable ways of engineering the components of an organic device, as well as great flexibility in the methods used in their construction [23]. However, much of the research methodology in the field still revolves around trial and error, even in the relative mature field of OLEDs [24], i.e. a "top-down" approach of constructing devices and measuring their properties to find optimal combinations. With a near infinite number of combinations, a "bottom-up" approach could accelerate the rate which commercial competitive devices are realised, by developing targeted designs based in scientific theory [25].

An element common to all organic devices (and in fact electronic devices in general) is the existence of interfaces between different materials. With a combination of the surface properties of each material (which are often different to the bulk) and the interaction between two different species, much of the most complex physics can be found at the interface [26, 27, 28, 29]. This is especially so for organic/inorganic interfaces, as the materials on either side have very different properties. The mechanisms for the interaction at the interface also depend on a wide range of factors such as preparation conditions, morphology and adsorption mode [27, 30, 31]. With

highly variable characteristics and incompatible morphologies, the organic/inorganic interface is often a limiting factor in the performance of organic devices [26, 23]. Therefore, the engineering of more favourable interfaces is a promising route to more efficient device operation [32, 26], and can be achieved through a better understanding of the science behind the processes that occur at the interface. Indeed, the importance of the interface in determining the efficiency of spin injection and operating performance of an organic spintronic device has led to the widely-used term "spinterface" [33, 34].

An established method of studying interfaces is photoemission spectroscopy. This uses the energy of ultraviolet and x-ray photons to induce the emission of electrons from a surface. The result of this is a kinetic energy spectrum that contains features reflecting the electronic and chemical properties of the sample. With different frequencies (and therefore energies) of photons, both the core and valence electronic states of a material can be measured [35]. By studying the changes to the electronic structure as a layer of organic molecules is introduced to the surface, a wealth of knowledge regarding the interfacial properties can be gained. To facilitate the unimpeded detection of emitted electrons, these experiments have to be undertaken in ultra high vacuum (UHV) conditions, and a goal of this project was to construct an UHV system capable of both core and valence level spectroscopy measurements.

A lesser known electron spectroscopy technique involves the use of the energy associated with metastable helium atoms to induce the emission of an electron from the surface [36]. This is known as metastable de-excitation spectroscopy (MDS) and produces a kinetic energy spectrum much like valence level photoemission. A more detailed explanation of the technique will be outlined in Chapter 3. The helium atoms do not penetrate into the surface, and this makes the technique incredibly surface sensitive. While conventional photoemission spectroscopy is also very surface sensitive, there is always some level of penetration into the sample and therefore includes a mixing of the contributions from the bulk and surface states. With MDS, the signal from the topmost layer can be isolated from the rest of the sample and this complementary data can contain crucial information not available in photoemission. The extraction and interpretation of this extra information obtained from organic interfaces is one of the primary aims of this project.

The electron spectroscopy techniques listed above are all surface analysis techniques

and therefore are sensitive to contamination of samples exposed to air. To combat this, the UHV system is equipped with a preparation chamber for the growth and cleaning of samples to be measured in-situ. With the apparatus in place, organic/inorganic interfaces for study need to be chosen. For a "bottom-up" approach to probe the electronic properties at the interface, the constituent materials should be well studied and relatively simple to allow easier interpretation of results, both as a test to the new UHV system and to build a foundation for further research. For these reasons, the molecule chosen for study was carbon-60 (C_{60}), also known as buckminsterfullerene. Although technically not an organic molecule, this allotrope of carbon is well studied, possesses many useful properties and is one of the materials used in the first organic photovoltaics [37]. On the other side of the interface, inorganic substrates paired with C_{60} in this project were silicon, the ubiquitous semiconducting material, and $La_{1-x}Sr_xMnO_3$ (LSMO), a ferromagnetic oxide used in the earliest organic spintronics devices [16]. The use of MDS to probe the C_{60}/Si and C_{60}/LSMO interface is an entirely new endeavour and it is one that yielded interesting results which will be revealed in the following thesis.

1.1 Thesis Overview

Chapter 2 covers a general overview of the background literature on organic interfaces, with a focus on the concepts relevant to the experiments carried out in this project. This will begin by introducing organic semiconductors, followed by a discussion of the factors that affect the interaction at organic interfaces.

Chapter 3 is focussed on the technique of metastable de-excitation spectroscopy. The theory behind it will be described, including the available scattering mechanisms. The apparatus used in the MDS beamline is then described, which covers He beam generation, collimation and spin polarisation.

Chapter 4 contains a description of the UHV system built for this project. The chapter starts with a description of the chambers and pumping arrangements. The individual measurement techniques used are then described (apart from MDS which is covered in the previous chapter). Special focus is given to x-ray photoemission spectroscopy (XPS) as XPS studies undertaken in collaboration during this project had contributed to publications.

Chapter 5 starts with a growth study of magnetite. This was partly used to test the capabilities of the preparation chamber, and also finds a way to reliably grow a complex magnetic oxide surface that is both well studied and has many applications. The latter part of the chapter details results of a study into the Fe/Fe_3O_4 interface with MDS.

Chapter 6 covers the first organic interface studied: C_{60}/Si(111) 7×7. A brief outline of the existing literature on this interface is first included. This is followed by the details of the experiment and then the results obtained. Discussion of the results are placed at the end.

Chapter 7 covers the second organic interface studied: C_{60}/LSMO. This also includes a brief outline of the relevant literature followed by results and discussions.

Finally, some suggestions are given for possible directions to take for further work building on the results obtained in this project.

Chapter 2

Organic Interfaces

2.1 Organic Semiconductors (OSCs)

Many properties of organic compounds make them attractive for use in electronic and spintronic devices. These include various characteristics that improve the practicality of their use, such as cost and compatibility with flexible substrates [8, 3]. Chemically, the lack of dangling bonds make organics generally quite stable at room temperature, and molecular properties can be approximately designed based on the molecular moiety, which stems from little intermolecular overlap of orbital wavefunctions as a result of weak Van der Waals forces [38]. From this property, there is a huge number of possible configurations to try out, with designs tailor-made for purpose [23]. Certain organic dyes also display incredibly high absorption coefficients in the visible range, making them ideal for photodetector and photovoltaic applications [39]. This is compounded by a strong red-shift in the emission of certain dyes, reducing re-absorption in light emitting devices [40].

OSCs also display low spin-orbit interaction, where electron spin is coupled to its orbital motion around a nucleus. In the rest frame of the electron, it experiences a magnetic field due to the charge of the nucleus and the relative motion. This can cause irreversible changes to the spin polarisation over time and the strength of the spin-orbit interaction is greater for heavier atoms (more charged nuclei), approximately proportional to Z^4 [13]. Carbon-based molecules are made from very light elements, mostly C, H, N and O and there is very little spin-orbit coupling in organic materials. Elements such as C and N also have relatively low nuclear magnetic dipole

moments (although somewhat offset in many OSCs by the high magnetic moment of the H nucleus), which reduces the hyperfine interaction between the nuclear and electronic magnetic moments. Therefore OSCs have long spin relaxation times that far exceed most metals and semiconductors [12, 33], making them an interesting option for spintronics applications, such as spin valves and tunnel junctions [17, 18]

2.1.1 Molecular Orbitals

The sp^n nomenclature for orbital hybridisation in molecules arises from the linear combination of atomic orbitals (LCAO) method of describing bonds between atoms, where orbitals are constructed from a linear combination of the basis set of atomic orbitals. For carbon, the hybrid orbitals formed are sp, sp^2 and sp^3, which are formed from a combination of the valence orbitals of carbon ($2s$, $2p_x$, $2p_y$ and $2p_z$). In sp^3 hybridisation, all four valence orbitals hybridise to form four equivalent hybrid orbitals. These form four σ bonds with neighbouring atoms in a tetrahedral arrangement, leading to the diamond structure. sp^2 hybridisation is responsible for many structures such as graphene and fullerenes, as well as the conduction properties in organic semiconductors. sp^2 is a result of the $2s$ orbital hybridising with the $2p_x$ and $2p_y$ orbitals of carbon. These form three σ orbitals in a planar configuration with the remaining $2p_z$ orbital forming a π orbital lying perpendicular to the plane. While the electrons in the σ orbitals are localised in the bonds, the electron in the π orbital can propagate throughout the molecule, which is the origin of conduction in organics. sp hybridisation results in linear molecular structures. Two π orbitals are formed from the hybridisation of two $2s$ orbitals with two $2p$ orbitals which then leaves the remaining $2p$ orbitals in a linear configuration. sp hybridisation occurs in triple bond structures such as ethyne. A diagram of the different hybridisation orbitals is shown in figure 2.1.

2.1.2 Charge Injection and Intermolecular Hopping

Electrical carriers in OSCs are provided by external electrodes as the density of intrinsic charge carriers in them is very low, on the order of 10^{-4} to 10^{-5} per site in PPV based polymers used in OLED applications [15, 42]. Charge is injected into the OSCs at the interface with the inorganic conductor and is easily accepted by

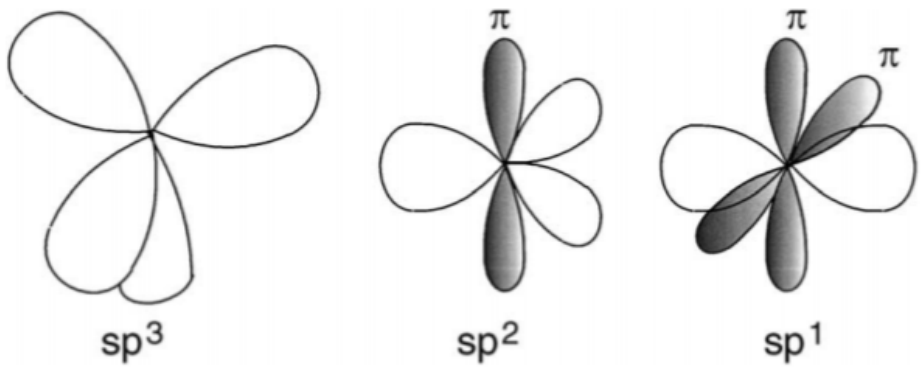

Figure 2.1: Schematic taken from [41] of the sp^n hybridised orbitals in carbon.

molecules. Charge carriers in OSCs generally propagate via hopping between nearest neighbour atomic sites (though other mechanisms are possible, such as variable range hopping in low temperature C_{60} FETs [43]) and the direction is guided by the potential applied at the electrodes. Transport properties depend heavily on the order of the molecules and structural defects [15]. Thermal energy is required to overcome the barriers for hopping to occur. The conductivity σ in an organic material is therefore dependent on all of these factors and in the case of low charge carrier concentration in OSCs, the Mott formula can be applied [44]:

$$\sigma \propto e^{(T_0/T)^{-\frac{1}{4}}} \tag{2.1}$$

Where T is the temperature and T_0 is Mott's temperature and is inversely proportional to the localisation length (raised power of three for the number of dimensions), and is therefore dependent on the level of disorder in the system. The $-\frac{1}{4}$ exponent on the temperature arises from the dimensionality of the system (i.e. the exponent generalises to $\frac{1}{d+1}$ for d dimensions). Due to the hopping transport process the electron mobility in OSCs is much lower than inorganic semiconductors.

The physics behind charge injection and transport in organic devices add to the complexity of the systems, as the charge transport between molecules is heavily affected by the weak intermolecular interaction. This complexity could lead to the transport performance being space-charge-limited (due to an abundane of injected charge carriers causing charge carrier mobility to become the limiting factor), injection-limited (due to energy barriers at the interface causing charge carrier density to become the limiting factor) or trap-limited (due to defects/impurities) [31];

and which limiting factor becomes dominant is dependent on the experimental conditions and applied fields. Therefore, only taking measurements of the transport (such as simple current-voltage data) will lead to difficulties in pinpointing the exact origins and mechanisms of the bottleneck in the device. To fully understand the electronic structure and thus the injection barriers, an isolation of the interface is necessary. An avenue for these studies is the combination of photoemission spectroscopy (PES) and inverse photoemission spectroscopy (IPES), the former of which is the central family of experimental techniques used in this project.

2.1.3 C_{60} Buckminsterfullerene

A majority of the results presented in this thesis are directed towards investigating organic-electronic interfaces using C_{60} as the "organic" component. C_{60} has found widespread use in organic electronics applications due to a multitude of useful properties. C_{60} has a high electron affinity of 2.65 eV (attributed to a reduction in the strain energy when an electron is added) and is easily reduced, with the molecule able to accept up to six electrons to form the C_{60}^{6-} anion [45, 46]. This, when combined with the low HOMO-LUMO gap of 1.68 eV [47], makes C_{60} an excellent electron acceptor with a relative low-lying LUMO. In addition, C_{60} has a reasonable electron mobility value of 11 $cm^2/(Vs)$. These properties have resulted in the use of C_{60} as a charge carrier in a number of organic devices such as organic photovoltaics [48] and organic field effect transistors [49].

C_{60} molecules also share other organic semiconductors' advantage of low spin orbit coupling, and therefore long spin lifetimes, which stems from the small atomic number of carbon [13]. Different to other OSCs, C_{60} is comprised only of carbon, with no hydrogen, and therefore avoids a major mechanism in spin scattering: hyperfine interaction with the proton in the hydrogen nuclei (which has a large nuclear magnetic moment) [50]. In addition, the most common isotope C, ^{12}C (other isotopes are very rare naturally, with ^{13}C having a natural abundance of less than 2%), only has a spin singlet in the nuclei and therefore no hyperfine interaction. These properties result in a long spin lifetime in C_{60} films and, when combined with a relatively high electron mobility of 11 cm^2/Vs [51], give a long spin diffusion length, which is at the order of 100 nm at room temperature [52].

More recently, there has been a revival of interest in C_{60}/ferromagnetic interfaces. C_{60} molecules have been found to become ferromagnetic due to spin doping at the interface with Co, and a loss of majority spin electrons result in a weakened magnetic moment in the ferromagnet [51]. Also, the deposition of C_{60} on Cu and Mn, normally non-ferromagnetic materials, can cause ferromagnetic states to appear in the metal [53], which is attributed to charge transfer at the interface. From these results it can be seen that the deposition of organics can affect the magnetic properties at the interface and that C_{60} is an excellent candidate for these spinterface engineering purposes.

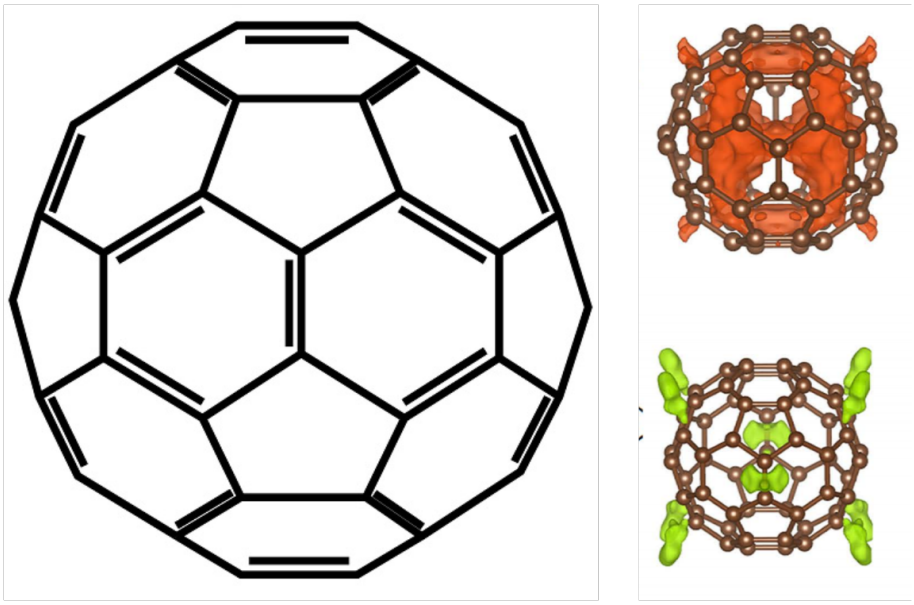

Figure 2.2: Left: Schematic of the C_{60} cage. Right: Diagram of calculated C_{60} HOMO (top) and LUMO (bottom), taken from [54].

C_{60}, or buckminsterfullerene or buckyballs, was first synthesised and characterised by Kroto, Curl and Smalley in 1985 [55], for which they won the Nobel Prize for chemistry in 1996. They discovered the formation of this remarkably stable carbon molecule after vaporising graphite and allowing clusters to form. The name buckminsterfullerene was given due to the similarity to the geodesic domes designed by Buckminster Fuller. The structure of C_{60} is a truncated icosahedron formed by 60 carbon atoms at the vertices each bonded to three others in a spherical structure with 20 hexagonal and 12 pentagonal faces and can be found in figure 2.2. In order for all four valence band electrons to be used in forming covalent bonds, each carbon atom is connected on average by two single bonds and one double bond, giving a total of 60 single bonds and 30 double bonds. In the lowest energy configuration,

the bonds between a pentagon and hexagonal face, or $[5,6]$, are single bonds, and those between two hexagonal faces, or $[6,6]$, are double bonds. The double bonds are shorter, with a length of 1.40 Å and the single bonds 1.45 Å[56]. The resulting diameter of the molecule in its gas phase is 7.1 Å[57]. The lack of hydrogen in the C_{60} molecule means that it is technically not an organic compound, but it does share many important properties with other OSCs and therefore shares many of the same applications.

The formation of sp^2 hybridised orbitals in C_{60} results in an average of one π orbital per carbon atom. With 60 π electrons in the molecule, there are a huge number of individual possible resonance structures, and therefore the electrons can be delocalised over the C_{60} cage. By considering the π electrons as particles delocalised on a sphere, it is possible to build a simple electronic structure of the valence band of the molecule, with two quantum numbers l and m_l (corresponding to the two degrees of freedom when moving on a sphere). However, filling up the electronic states in this manner according to Pauli's exclusion principle starting from $l = 0$ with $-l \leqslant m_l \leqslant l$ yields 10 unpaired electrons in the $L = 5$ states, which would be a paramagnetic material, as it contains unpaired electrons. Instead, due to the lower symmetry of the truncated icosahedron structure [58], the degeneracy is broken at the higher energy states, and the $L = 5$ states are split into three separate levels. The lowest energy state is the five-fold degenerate h_u state, which is fully filled, resulting in a diamagnetic molecule [59, 51]. A schematic of this simple model involving only the π electrons is shown in figure 2.3 alongside an image of the calculated energy levels in gaseous C_{60} molecules involving all 360 electrons inside the buckyball [59]. From the comparison, it can be seen that near the Fermi energy, the simple model is a decent approximation to the full electronic structure. The calculated band gap of the isolated molecule is 1.7 - 1.9 eV between the h_u and t_{1u} states (figure 2.3) [59, 60].

Progressing from isolated molecules to the bulk, C_{60} crystallises into a FCC configuration as a structural transition occurs to form a single crystal just below room temperature [61]. Assuming a weak Van der Waals interaction, at the interface to a surface, C_{60} molecules form a 2D close packed hexagonal structure [62, 63] and has a nearest neighbour distance of 9.5 to 10 Å [64]. DFT calculations have found that for this configuration at room temperature, the C_{60} molecules on the surface can fluctuate in all degrees of freedom (translational and rotational) and there is no

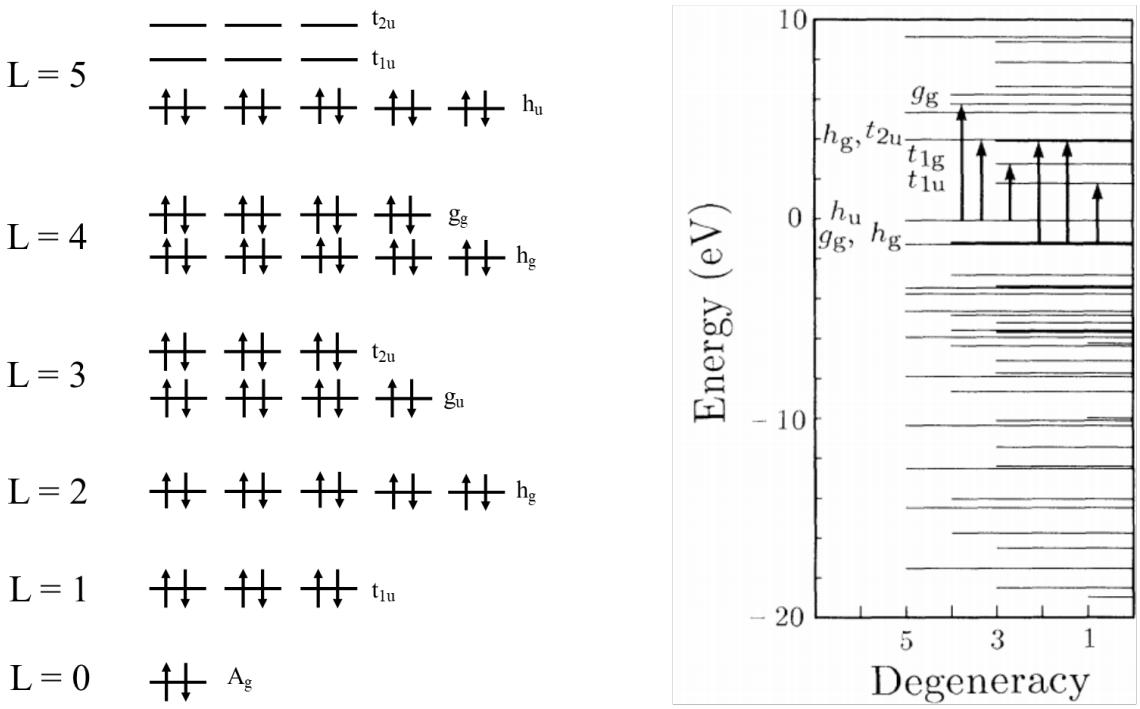

Figure 2.3: Left: simple model of the electronic structure in the valence band of a C_{60} molecule modelled as 60 delocalised electrons in the truncated icosahedral cage. Right: calculated C_{60} electronic structure taken from [59]. The simple model makes a reasonable prediction for the occupation and symmetry of the highest occupied states.

preferred orientation [54]. The same calculations have shown that these fluctuations do not affect the stability of the 2D layer until a temperature of 600 K is reached, and that, for a non-infinite film, the 2D configuration is stable for temperatures below 150 K. Above these temperatures, a 3D cluster is formed [54].

2.2 Interface Engineering

A variety of factors affect the performance of organic devices. These include (but are not exclusive to) the choice of organic and electrode material, the preparation conditions, the morphology and the device configuration [65, 9, 30, 23, 31]. A common element of the device affected by all of these properties is the interface between the electrode and the organic. The interfaces are key to the injection and transport properties in a device and are often the bottlenecks that limit performance [31, 66]. Many of the results in the literature are related to or can be explained by effects of or differences in the interfaces inside a device. For instance, it has

been found that in organic field effect transistors (OFETs), placing the gate and source/drain contacts on different sides of the semiconducting organic layer generally produces better performance than placing them on the same side [9], which has been attributed to the better contact between OSC and electrodes in these configurations [67]. There is a wealth of literature on the fundamental physics of these interfaces, often with specific applications in mind, such as for OFETs [68, 69], light emitting devices [70, 71] and photovoltaics [65]. It is important to understand the mechanisms behind the interaction at the surface in order to design higher performance devices.

2.2.1 Interfacial Dipole and Energy-Level Alignment

The simplest assumption when building a picture of the energy levels at an interface is to follow the rule of vacuum level alignment, also known as the Schottky-Mott limit. This allows a calculation of the hole or electron injection barrier from the work function of the electrode surface, the electron affinity of the organic and the ionisation energy of the HOMO [31]. A schematic of this is shown in figure 2.4. While this may seem valid for molecular interfaces where no strong interactions occur, evidence against vacuum level alignment very quickly began to appear in the literature [71, 26]. A dipole barrier forms at the interface and offsets the electronic structure of the two materials. An example of this is the interface between a Au surface and α-NPD molecules, where the Schottky-Mott predicts hole injection into the HOMO; but the vacuum level offset causes the hole barrier to rise from 0.2 - 0.3 eV to 1.4 eV, changing the nature of the interaction at the interface. This effect is present to some extent in the majority of organic-metal interfaces and the dipole can be positive or negative. The formation of the dipole can be attributed to three factors [31]: charge transfer across the interface, dependent on the work function of the substrate, as well as the electron affinity and the ionisation energy of the organic; formation of a chemical (covalent) bond and gap states which pins E_F at the interface; and changes induced by the proximity of the molecule to the electron density that tails into the vacuum from the metal surface.

When the work function of the substrate is less than the electron affinity of the organic, such as the case with PTCBI on Ag [72], a transfer of electrons from the metal into the LUMO of the molecule can occur. The dipole barrier that results from this is an upwards step in the vacuum level going from the metal to the organic.

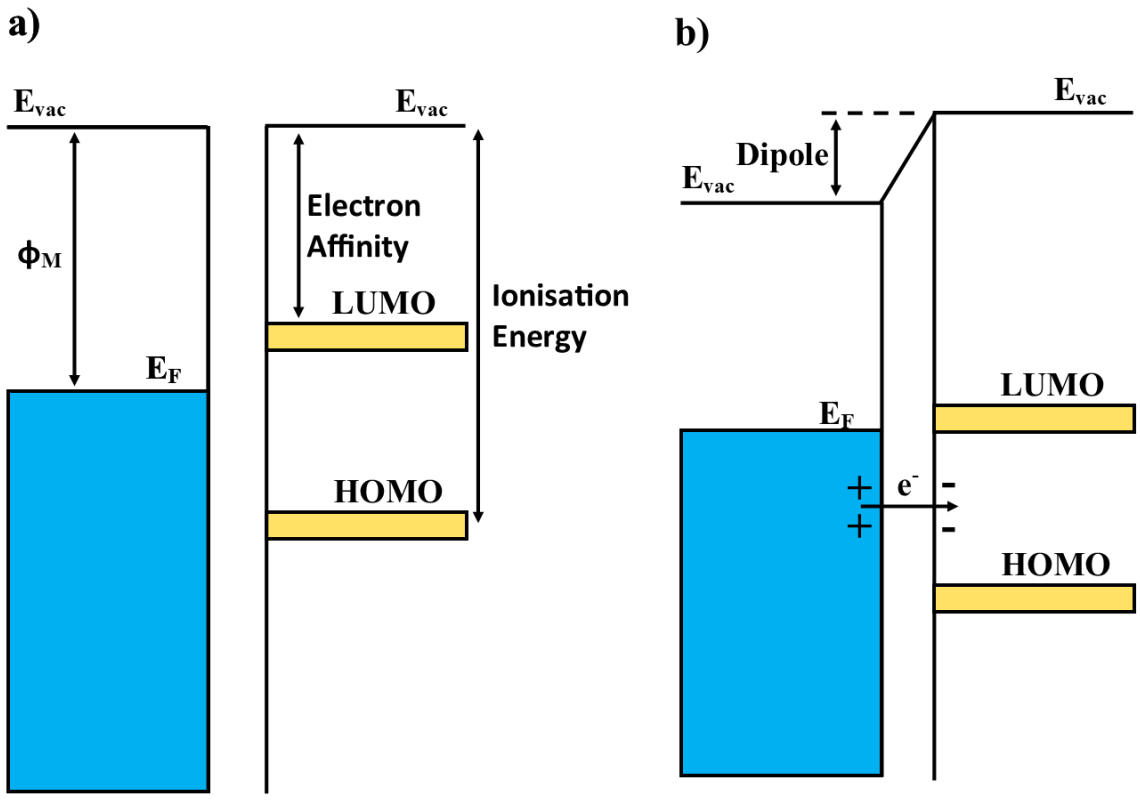

Figure 2.4: a) Diagram illustrating the electronic structure at an organic interface following the Shottky-Mott rule with values of interest labelled. b) Diagram showing the effect of a dipole barrier on the energy level alignment. In this case the alignment is caused by charge transfer due to the surface work function being lower than the electron affinity of the molecule.

A diagram of this can be found in figure 2.4b. This raises the energy level until the net transfer of charge is stopped. The electrons in the now partially occupied LUMO are now at an energy within the band gap and forms a state between the new LUMO and the Fermi energy. This charge is localised at the interface since photoemission measurements show the attenuation of the gap state emission signal with further layers of deposition [72]. The "step-up" dipole of the interface is also seen in other interfaces such as Fe_{16}CuPc/Mg, which can be attributed to the charge transfer mechanism as described above, but the formation of covalent bonds also plays a role in the interfacial electronic structure.

For the case of covalent bond formation, the interfacial alignment is controlled by the formation of a chemisorption induced electronic state. One example is the interface between Alq_3 and Mg, where the Mg work function falls inside the band gap of the Alq_3 and therefore there is little drive for charge transfer. However, a dipole barrier

nevertheless forms with a "downward" magnitude of 0.5 eV [73]. Investigations into the core levels of this interface [74] and first principles dynamics calculations [75] uncovered the formation of a three-dimensional organometallic complex involving the bonding of an Mg atom to two Alq_3 molecules through the formation of Mg-O and Mg-C bonds. The appearance of such chemisorption induced states in the gap leads to the pinning of the Fermi level at that energy. In order to align the Fermi levels, charge transfer is required to create the necessary dipole barrier. This charge originates from the interface state and in the case of Alq_3/Mg, the charge flows into the metal surface to create a negative dipole barrier.

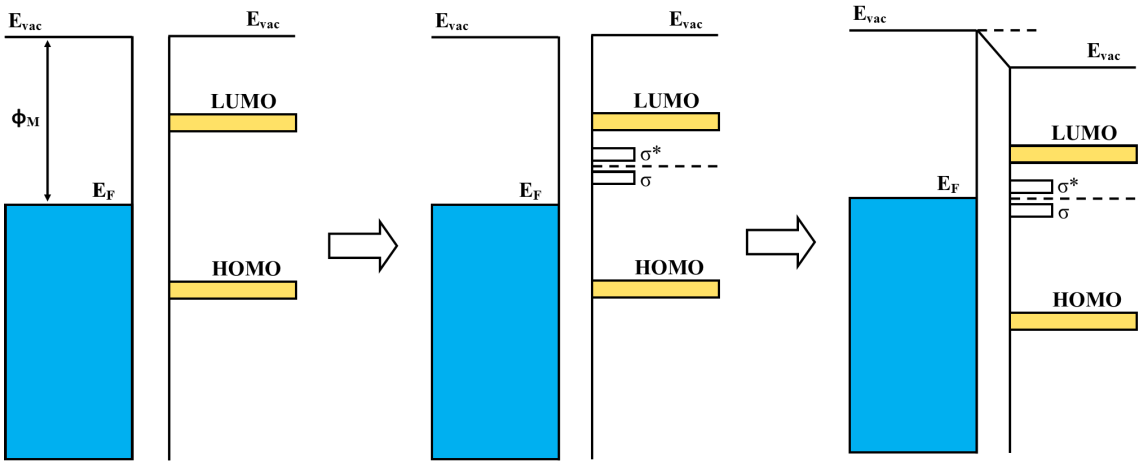

Figure 2.5: Diagram showing the steps leading to the formation of a dipole barrier due to a covalent bond between the surface and the molecule. The interface bonding states (where σ and $\sigma*$ in the diagram represent the bonding and anti-bonding orbitals) pin the Fermi level (i.e. force alignment of Fermi levels) and this forces a transfer of electrons that introduces a dipole barrier.

In a number of interfaces, such as TPD and α-NPD on Au, a lowering of the metal work function is observed upon adsorption of the molecules [40, 76, 77]. This results in the formation of an apparent dipole barrier, with an effect localised to the interfacial layer and is typical of physisorptive systems such as molecules on noble metals. The work function of a material is dependent on its bulk chemical potential as well as a surface dipole effect [78]. The surface dipole effect is dependent on the surface structure and the configuration of atomic orbital "tails" which point into the vacuum. When an adsorbate, such as a molecule is introduced, the repulsion between the molecular orbitals and the surface compresses these electron tails. This causes a reorganisation of the electron density tailing away from the surface in order

to accommodate a molecule in proximity, as though the molecule "sinks" in, causing an indent in the "pillow" of electrons. This is known as the "pillow" effect and lowers the work function of the surface [79]. This then in turn causes a drop in the molecular energy levels and therefore an increase between the HOMO and the Fermi level in the surface, increasing the hole injection barrier but reducing the electron injection barrier into the LUMO. The magnitude of this effect is dependent on the work function of the surface and for low work function surfaces, such as Sm ($\Phi = 2.7$ eV) [80], the resultant interface dipole is relatively small (0.2 eV for pentacene/Sm [81]).

Overall, alignment of the electronic structure at the organic/substrate interface takes place with a variety of mechanisms dependent on the nature of the interaction between the molecules and the surface. The presence of the dipole barrier in both chemisorbed (including ionic- and covalent-natured bonding) and physisorbed regimes contributes to the transport properties across the interface. It is therefore important to identify the interaction at the surface and understand the underlying mechanisms in order to find avenues of engineering more desirable properties.

2.2.2 Morphology and Interface Contacts

The effect of morphology of a sample on the interface properties is dependent on the materials used. One way of directly observing the effect morphology has on an interface is by comparing the difference between an interface where the organic is deposited on an inorganic substrate and where the inorganic is deposited on the organic. With the same materials used, the main difference is in the morphology at the contacts.

Early investigations of this manner were performed on the Alq_3/Mg and Mg/Alq_3 system. Although initial results found an overwhelming advantage of having an Mg top electrode [82], this was quickly found to be due to the contamination of a bottom Mg electrode under non-UHV conditions (10^{-6} - 10^{-7} mbar) rather than a proper comparison [83]. The same experiment performed under UHV [31] found that the photoemission data and therefore the gap states, core state shifts, HOMO position relative to the Fermi energy and the electronic barriers were all the same regardless of whether the Mg electrode was on top [74]. However, the morphology was quite

different between the two configurations. In the case of a bottom Mg electrode, the interface was abrupt, corresponding to the flat Mg substrate, while when Mg was deposited on the organic, the metal atoms penetrated quite deeply into the organic.

However, this does not hold true for all systems, an instance of which is the Fe_{16}CuPc /Au interface [84]. In this case, the substrate is very inert and there is no strong interaction between the molecule and the Au. When Au is evaporate onto the Fe_{16}CuPc film, the Au atoms diffuse into the organic lattice and there is a decrease in the Fermi energy of 0.5 - 0.6 eV compared to Fe_{16}CuPc on Au. The origin of this lies in the different interactions that take place at each interface. For Fe_{16}CuPc on Au, there is an abrupt interface where the interaction is controlled by the relative work functions (the pillowing effect is minimised due to similarity of the Au work function to the Fe_{16}CuPc electron affinity). Whereas in the reverse case, there is a doping effect as the Au atoms that diffuse into the organic act as p-type dopants that affect the balance of charges [84].

The issue of morphology is perhaps more crucial in the case of organic-organic interfaces [30]. Photoinduced electron transport between MEH-PPV (poly[2-methoxy-5-(2'-ethylhexyloxy)-p-phenylene vinylene]) and C_{60} kick-started the field of polymer solar cells [37] and organic photovoltaics soon adopted the bulk heterojunction concept [48, 85]. Naturally in these cases the morphology was important as a key advantage of bulk heterojunction is in the increased surface area, but at the same time, a greater complexity is present in the 3D structure in the bulk heterojunction. A general idea of an optimal morphology is present from theoretical calculations [86], involving a strongly intermixed blend of electron donors and acceptors while maintaining a network of paths to each electrode. But since the morphology is dependent on a great number of actors, such as blend composition, solution concentration, annealing and the structure of the materials [30], creating an optimal self assembled configuration is a great challenge. Since the samples under study for this project are 2D organic/inorganic interfaces, the author will not include too many details here.

2.2.3 Preparation Conditions

In the earlier example regarding the Alq_3/Mg interface, it was found that contamination plays a large role in the performance of devices [83]. This is a point of note in that the preparation conditions can also affect the final device performance. Given that the final goal is in widespread industrial applications, where the use of an UHV system is not available (due to cost, practicality and expertise available), some level of contamination of reactive surfaces is unavoidable. It has been shown that electron injection is much lower in cases where the substrate is somewhat contaminated (10^{-6} Torr) [83]. Therefore this could have an impact on the selection of electrode materials as many elemental metals are very reactive when compared to noble metals or oxides. It also limits time frame for experimentation, even when taking measurements in UHV conditions.

2.3 Organic Spintronics

The above discussion has mostly been limited to charge transport across organic interfaces. While these are still relevant for spintronic devices, there are a number of transport mechanisms that are applicable specifically for electronic spin.

2.3.1 Spin-dependent tunnelling

Tunnelling is a quantum mechanical effect arising from the wave nature of electrons. As the electron wavefunctions do not vanish at a conductor/insulator interface, there is a finite possibility for an electron to move across a narrow gap between two conducting layers when a potential is applied. This process is dependent on the density of states of both electrodes at any particular energy.

Spin-dependent tunnelling occurs across two ferromagnetic electrodes separated by a thin insulator layer, also known as a magnetic tunnel junction. In this case, the charge carriers are spin-polarised and the resistance across the junction is dependent on the relative orientations of magnetisation between the two ferromagnetic layers. More specifically, the conductivity is increased when the magnetisations are aligned parallel compared to when they are aligned anti-parallel [18]. This effect is

known as tunnelling magnetoresistance (TMR) and was first observed in the 1970s [87]. The cause of this phenomenon is the spin-dependent density of states and the conservation of spin. Since electrons from one spin sub-band in one electrode can only tunnel to the same spin sub-band in the other electrode, we can consider the total tunnelling current as two separate currents for each spin state. This is known as Mott's two current model, shown in figure 2.6. From this, it can be seen that the tunnelling current is proportional to the product of the density of states of each spin sub-band in the two electrodes creating a difference in the resistances of the two configurations.

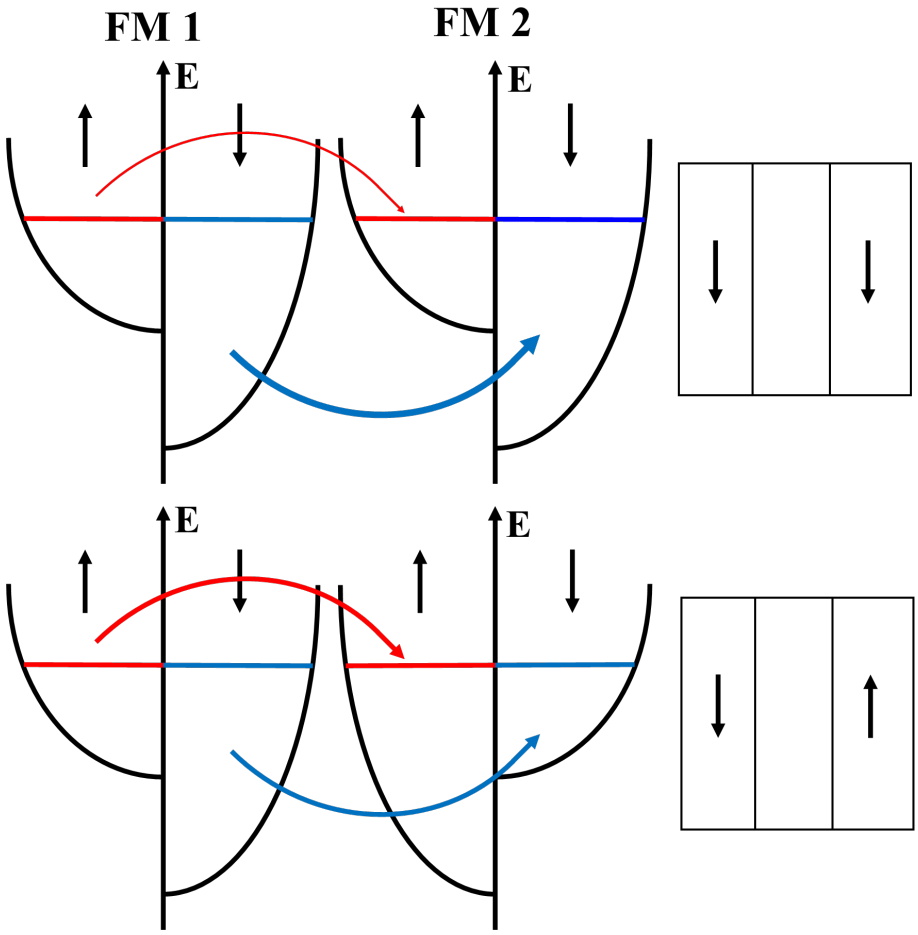

Figure 2.6: Diagram showing the Mott two current model for the parallel (top) and anti parallel (bottom) configurations.

The tunnel magneto-resistance is defined as the ratio of difference between the resistance in the antiparallel and parallel alignments to the resistance of the parallel configuration, i.e.:

$$TMR = \frac{R_{AP} - R_P}{R_P} \tag{2.2}$$

Where R_{AP} and R_P are the resistances of the antiparallel and parallel configurations

respectively. This can be rearranged into a function of the spin polarisation of the two ferromagnetic layers at the Fermi level using the expression for spin polarisation of each layer:

$$P = \frac{N^{\uparrow}(E_F) - N^{\downarrow}(E_F)}{N^{\uparrow}(E_F) + N^{\downarrow}(E_F)} \tag{2.3}$$

Where $N^{\uparrow}(E_F)$ and $N^{\downarrow}(E_F)$ are the density of states at the Fermi level of the up and down spin channels respectively. Then using the relationship between the density of states in each spin channel to the resistance, an expression in terms of the spin polarisation of each layer is obtained:

$$TMR = \frac{2P_1P_2}{1 - P_1P_2} \tag{2.4}$$

Where P_1 and P_2 are the spin polarisations of the two layers. Which allows a simple prediction of the TMR of a particular tunnel junction from the properties of the two magnetic layers. If the values for P_1 and P_2 both approach unity, i.e. the surface is fully spin polarised, the TMR of the junction goes to infinity. This was used to show half metallicity in LSMO through the measurement of the TMR in a LSMO - $SrTiO_3$ - LSMO junction [88].

The ability to control electrical resistance in a device through its magnetisation is used in many applications. In spin valves, the magnetic orientation of one ferromagnetic layer is pinned using an antiferromagnetic material through exchange bias [89]. The resistance of the device can then be controlled with the magnetisation of the other, free ferromagnetic layer. Due to this, the development of spin valves had a transformative effect on applications such as magnetic recording and memory, and helped to launch the field of spintronics [17].

2.3.2 Organic Spinterfaces

The above discussions into spintronics applications are relevant for both inorganic and organic devices. There are, however, some properties that are only present at organic interfaces. Examples include: a strongly spin polarised state was found in the HOMO-LUMO gap of the Fe/Alq_3 interface [90]; spin polarised STM found that the placement of one H_2Pc phthalocyanine molecule on Fe was enough to reverse the local spin polarisation [91]; and the spin doping and formation of ferromagnetic states in non-magnetic metal due to charge transfer into C_{60} molecules mentioned earlier [51, 53]. These unusual properties are unique to organic spinterfaces and have

allowed them to become competitive to their inorganic counterparts [34]. Therefore, understanding the mechanism underlying processes at the interface is crucial to the further development of the field.

Chapter 3

Metastable De-excitation Spectroscopy

A key electron spectroscopy technique used in this project is metastable de-excitation spectroscopy (MDS). This is a novel technique which uses excitation from a metastable noble gas atom to supply the energy required to eject an electron from a material's surface [36]. This technique has also been referred to in the literature as metastable atom electron spectroscopy (MAES), metastable quenching spectroscopy (MQS) and metastable impact electron spectroscopy (MIES). It should also be noted that there are also techniques which use ions to bombard the surface, such as Penning ionisation electron spectroscopy (PIES) and ion neutralisation spectroscopy (INS) and that the use of ions rather than metastable atoms change the de-excitation processes which occur. Since MDS is employed by very few researchers and is thus not well known, this chapter will try to give a review of its advantages, the theory of operation and how the technique can be modified to probe spin-polarised materials (spin polarised metastable de-excitation spectroscopy, or SPMDS).

3.1 Advantages of MDS

When a metastable noble gas atom approaches a sample surface to within a few Ångströms, an overlap of the surface and atomic orbitals allows electrons to tunnel from one to the other. This induces a transition into the ground state and the released energy liberates an electron from either the sample surface or the metastable

atom. The emitted electrons have a range of kinetic energies and the spectrum of intensity against kinetic energy can be analysed to obtain information regarding the density of states in the sample valence band. This is similar in principle to conventional valence band photoemission techniques (e.g. ultraviolet photoemission spectroscopy).

In contrast to photoemission techniques, the metastable atoms have zero penetration into the bulk and therefore probe only the outermost layer while other techniques provide information averaged over multiple atomic layers on the surface. This surface sensitivity allows MDS to be used for the study of a variety of surface and interface systems. Due to no contribution from the bulk material, MDS is well suited to studying adsorbed molecules and can observe the orientation of such molecules [92] and therefore MDS is a useful method for scrutinising the electronic states associated with changes at organic/metal and organic/semiconductor interfaces [36]. The technique is also non-destructive, as the kinetic energy associated with an atom travelling at thermal-velocities is small (A helium 2^3S atom travelling at 1000 ms^{-1} has an associated kinetic energy of 21 meV). This allows MDS to be used for the study of biomaterials [93]. The helium beam can also be spin polarised and the resulting beam can be used to probe magnetic systems, such as the organic/magnetic oxide samples grown for this project.

3.2 The Metastable Helium Atom

A suitable metastable atom needs to be selected for use in MDS. Noble gas atoms are typically used for their inert nature and suitability for use in vacuum systems. The metastable species also needs to be relatively stable, i.e. it needs to stay in the excited state for a relatively long period of time.

The excited 2^3S_1 state of helium (from here also referred to as the 2^3S state or the triplet state) is chosen for its suitability. The de-excitation from this metastable state into the ground state releases an energy of 19.8196 eV [94], which is the highest of all rare gas atoms. In this state, one electron occupies the helium $1s$ state and the other the helium $2s$ state, and the two electrons have the same spin angular momentum (both spin-up or both spin-down). Transitions from this state into the 1^1S_0 ground state, which is also the only lower state, is forbidden by selection rules.

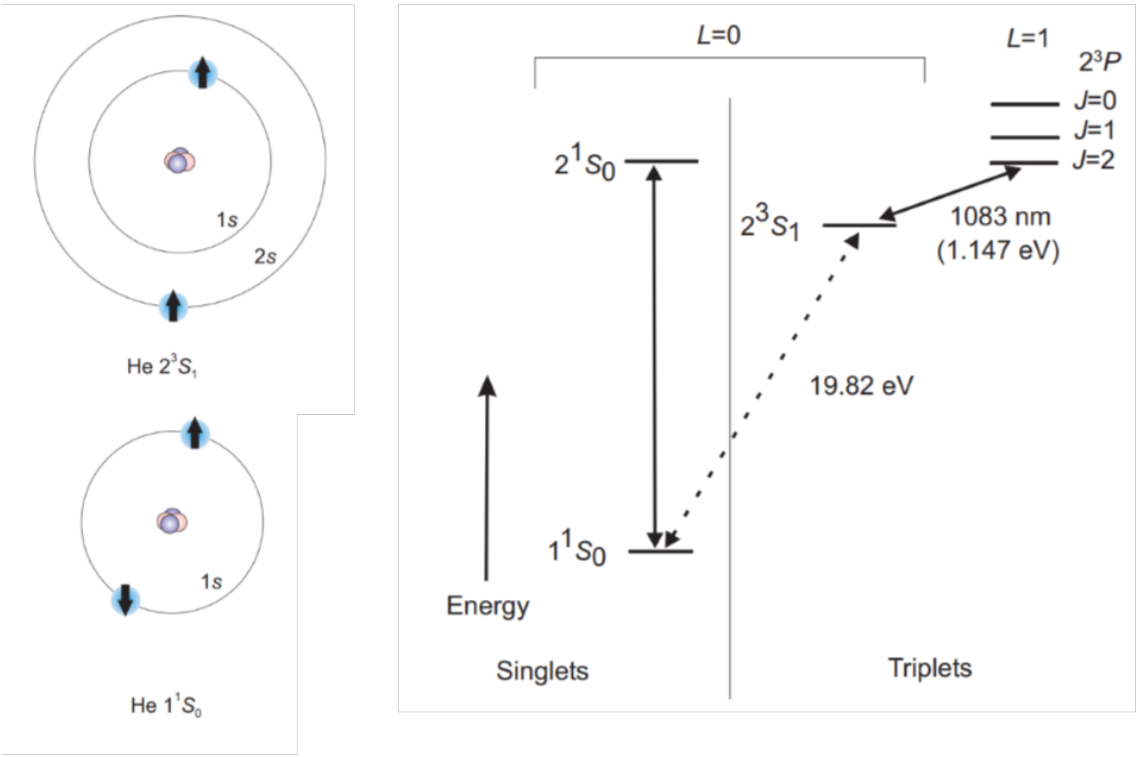

Figure 3.1: Illustration showing a schematic (left) and energy diagram(right) of the ground state of a helium atom and the 2^3S_1 metastable state with an excitation energy of 19.82 eV. The metastable state has a long half life due to the doubly forbidden nature of the transition down into the ground state.

Since the ground state consists of a spin-up and a spin-down electron in the ground state due to Pauli's exclusion principle, the transition would have to have an integer change in the total spin from +1 to 0, which is forbidden as ΔS must equal 0. In addition, the total orbital angular momentum is the same in both states ($l = 0$) and the selection rules for LS coupling state that any transitions must change this quantum number by +1 or -1.

The doubly forbidden transition causes the 2^3S state to have an extremely long half life of 8000 - 9000 s [94, 95]. Decay to the ground state requires a two-photon process, which in turn requires the emission of radiation from a source such as an oscillating magnetic dipole. An illustration of the metastable and ground states are provided in figure 3.1. There is also an undesired singlet 2^1S state with the same electron occupation, with a similar energy of 20.62 eV and a half life of only approximately 20 ms [95].

The 2^3S atom is suitable for MDS in many ways. There is only one state with lower

energy, and therefore the energy released from induced de-excitation is constant. The long half life mentioned above means that the majority of the metastable atoms are able to reach the sample still in an excited state. The energy stored in the transition is also large when compared to that of other noble gases, allowing a broader range of energies to be probed, comparable to the 21.22 eV used in He (I) UPS. The spin states of the metastable can also be flipped via optical pumping tuned to a transition frequency of helium. This property allows the helium beam to be polarised and is crucial to the development of spin-polarised metastable de-excitation spectroscopy (SPMDS).

However, due to the same limitations on the transition de-excitation, the 2^3S metastable state cannot be easily achieved using optical pumping. Electrical discharge at an energy higher than the excitation energy is used instead to create a source of metastable helium. This is a simple process, but has the disadvantage of also possibly promoting the helium atoms into a different excited state with the same electron occupation. The 2^1S singlet state also has one electron in each of the helium $1s$ and $2s$ states, but the two electrons are of opposite spin (parahelium). It has an energy of 20.62 eV and a half life of approximately 20 ms [95]. While this state is less likely to be produced (1:10 ratio) and has a much lower half life when compared to the 2^3S state, there is a contribution to the ejected electron energy spectra due to the creation of a second species of metastable atoms. Also, since the 2^1S contains one spin up and one spin down electron, it cannot be spin polarised. The final energy spectrum obtained will therefore be a combination of the spectra due to the two states, with the 2^3S metastable providing the dominant part. To prevent the convolution of features arising from 2^1S and 2^3S atoms, it is desirable to remove the former from the helium beam. A laser cooling technique to selectively collimate only the desired triplet state metastable helium atoms is used in the laboratory at York in order to increase the proportion of the 2^3S atoms that reach the sample surface [96].

3.3 De-excitation Mechanisms

Unlike photoemission techniques, different electron tunnelling processes can occur when a metastable atom approaches a sample surface. This is dependent on the work function, Φ, of the surface and the energy distribution of surface orbitals.

In the case of most metal and semiconductor surfaces, the dominant mechanism is de-excitation though resonant ionisation (RI) followed by Auger neutralisation (AN). For insulating materials, Penning ionisation (PI) is more likely to occur when probing atoms or molecules, which is also referred to as Auger de-excitation (AD) when the sample is a solid surfaces.

The electron yield of these de-excitation events varies depending on the material and surfaces under investigation, but are typically between 0.3-0.95 electrons per metastable incident on the sample surface [94].

3.3.1 Penning Ionisation

Penning ionisation occurs when a metastable atom approaches another atom or molecule. This is a basic process where the collision will ionise the target species as described below:

$$M + He^* \rightarrow M^+ + He + e^- \tag{3.1}$$

where M is the target atom or molecule. As the metastable approaches from infinity, the interaction is initially dominated by Van der Waals forces; and as the distance shortens, the Pauli repulsion term between them becomes a more significant factor. The overall interaction can be described by a Lennard-Jones (or 6-12) potential. The Pauli repulsion forces at close proximity occur due to an overlapping of molecular orbitals, and this allows an electron to tunnel from the target into the $1s$ state of the metastable. Energy is released from this transition, which is transferred to the excited $2s$ electron in the helium which is then ejected in an Auger-type process. The probability of this transition occurring is dependent on the separation distance, and there is an approximately inverse exponential relationship between the transition probability and the separation[36].

3.3.2 Auger De-excitation

Auger de-excitation occurs between a metastable atom and a solid surface. The mechanisms are similar to Penning ionisation, but with subtle differences due to the broadening of electronic states in solids into bands. This process takes place when the surface Fermi level is at a higher energy than the excitation energy of the

metastable atom. The sample material therefore either has a relatively small work function or a large band gap. And since the Fermi level is higher than the energy of the excited electron, there are no empty states in the surface near that energy for the electron to tunnel into. Therefore Auger de-excitation occurs only when the metastable is relatively close to the sample, at around 3-5 Å [97], i.e. when there is a direct overlap of an occupied state with the $1s$ hole of the helium atom. When probing samples made from an insulating material, the primary de-excitation mechanism is Auger de-excitation since the work functions are generally small or band-gaps are present at the Fermi level.

The resulting mechanism is much like that of Penning ionisation - an electron tunnels from the sample surface into the metastable $1s$ which releases energy and liberates the electron from the He $2s$ state. The de-excitation process is illustrated in figure 3.2. With enough energy, the electron can reach the vacuum level and the remaining energy will be converted into kinetic energy E_k, which can be calculated by:

$$E_k = E_i^{'} - \alpha - \beta \tag{3.2}$$

where $\mathrm{E}_i^{'}$ is the effective ionisation potential of the He atom in its ground state; α is the energy difference between the vacuum level and the initial state of the tunnelling electron; and β is the energy required to promote the He $2s$ electron up to the vacuum level (as labelled in figure 3.2). Since the initial state of the emitted electron is constant, we can write:

$$E_i^{'} - \beta \approx 19.82\, eV \tag{3.3}$$

where 19.82 eV is approximately the excitation energy of the metastable helium state. The term α can be substituted as the sum of the binding energy E_b of the tunnelling electron's initial state and the surface work function Φ. This gives (and rearranging for the binding energy):

$$E_k \approx 19.82\, eV - E_b - \Phi \tag{3.4}$$

$$E_b \approx 19.82\, eV - E_k - \Phi \tag{3.5}$$

This is a simple expression directly relating the kinetic energy of the ejected electron and the binding energy of the electron in the sample as the other terms for constants for a given sample. As a quasi-one-electron process (the emitted electron is always from the He $2s$, and is therefore has constant initial energy), this produces sharp

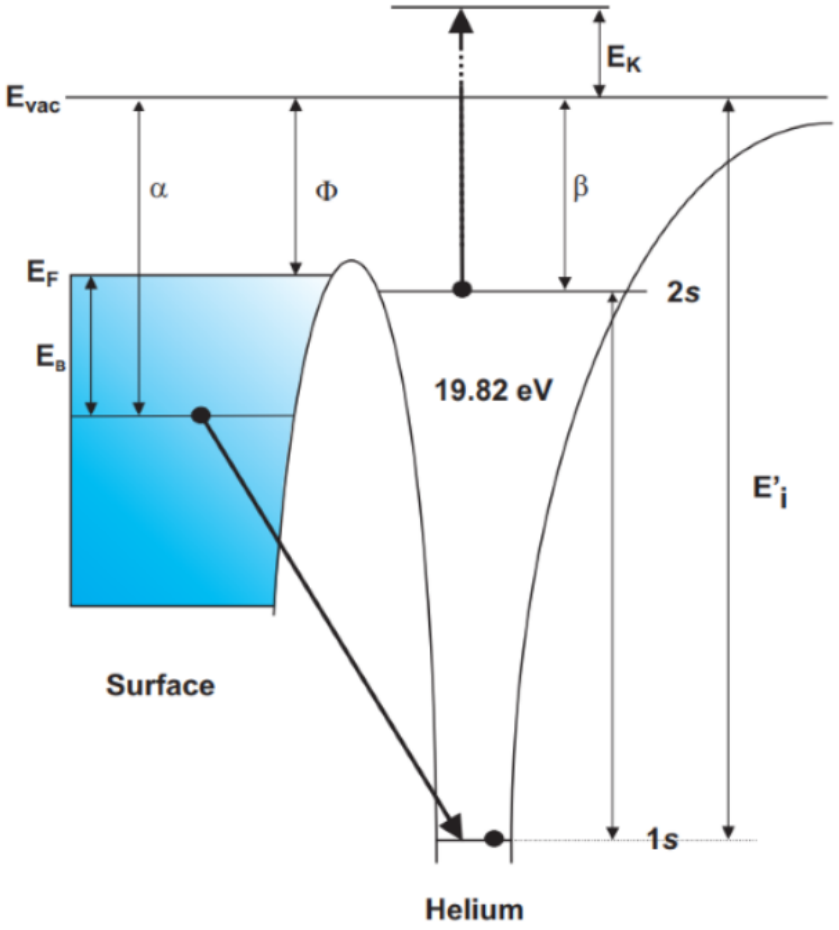

Figure 3.2: Illustration showing the Auger de-excitation process. An electron located at an energy E_B below the Fermi level (and at an energy α below the vacuum level) tunnels from the sample surface into the 1s of the approaching metastable helium atom. The electron in the He 2s state gains energy from this transition and is ejected. Φ is the work function of the sample surface, β is the energy required to promote the He 2s electron to the vacuum level and E'_i is the effective ionisation potential of the helium atom. The kinetic energy E_k of the emitted electron can be calculated by $E_i - \alpha - \beta$

features that are directly comparable to valence band photoemission, though with some broadening inherent to the Auger process [98].

3.3.3 Resonance Ionisation and Auger Neutralisation

When the Fermi level of a sample surface lies energetically below the excited level of an approaching metastable atom ($2s$ state for helium), there are empty states at

a similar energy in the surface for the excited electron to tunnel into (provided the band gap of the sample is not too large). This process is called resonance ionisation (RI) and is the first step of a two-stage de-excitation process involving resonance ionisation and Auger neutralisation (AN). This process is illustrated in figure 3.3.

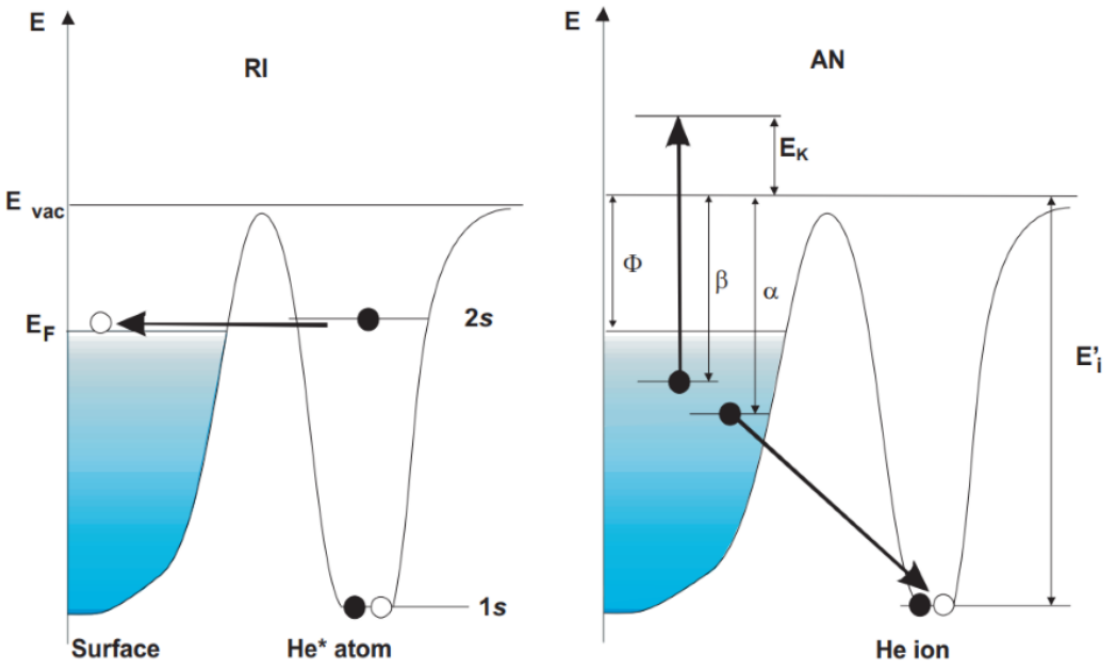

Figure 3.3: Illustration showing the two-step resonance ionisation + Auger neutralisation process. An electron tunnels from the 2s state of the approaching metastable helium atom into an empty state at the sample surface in the resonance ionisation step. This is followed by Auger neutralisation, where an electron tunnels from the sample into the 1s hole of the helium ion and another electron is simultaneously ejected from the valence band. Φ is the work function of the sample surface, α and β are the energies required to promote the neutralising and emitted electron to the vacuum level from their initial states and E'_i is the effective ionisation potential of the helium atom.

Resonance ionisation takes place at around 9 Å from the surface and results in the formation of a He^+ ion which continues to approach the sample surface [99]. After reaching a particular distance (typically around 5 Å[97]), an electron will tunnel from the surface into the helium $1s$ state, neutralising the helium ion into a helium atom in its ground state. This is the Auger neutralisation step. The energy released is equal to $E'_i - \alpha$ where E'_i is the effective ionisation energy of helium, and α is the initial energy of the neutralising electron. This energy then transfers to another

electron in the solid, and can cause the emission of an electron provided there is sufficient energy and direction of motion. The emitted electron will have a kinetic energy equal to the difference between the effective ionisation energy and the sum of the initial energies of the two electrons: $E'_k = E'_i - \alpha - \beta$. The maximum kinetic energy is acquired by an emitted electron when both electrons originate from the Fermi level of the solid ($\alpha = \beta = \Phi$):

$$E_{k,max} = E'_i - 2\Phi \tag{3.6}$$

The spectrum of kinetic energies obtained from the emitted electron will contain information about the density of states at the surface, much like in photoemission spectroscopy. However, since the two electrons do not originate from a set energy, there are two variables in the kinetic energy and the initial energy of the emitted electron cannot be directly calculated. Since both electrons originate from the same solid surface, the result is a self-convoluted spectrum which can be described by the self-convoluted integral:

$$F(\epsilon) \propto \int_{-\epsilon}^{\epsilon} |H_{fi}|^2 N(\epsilon - \Delta\epsilon) N(\epsilon + \Delta\epsilon) d(\Delta\epsilon) \tag{3.7}$$

where F(ϵ) is the transition probability (i.e. the intensity of the spectrum at a particular energy, ϵ), H_{fi} is the matrix element of the transition and $N(\epsilon)$ is the local density of states. This results in spectral features that are "smeared out" when compared to standard photoemission spectra.

The RI + AN de-excitation takes precedence over Auger de-excitation if there are empty states near the energy level of the He $2s$ state, since it takes place at a greater distance from the sample surface, and will, if possible, occur before the approaching metastable helium atom reaches the range needed for Auger de-excitation. The probability of occurrence is inversely proportional to the exponential of the distance. It is possible for both mechanisms to occur at the same time if a saturation point is reached with the RI + AN process and metastables are allowed to approach to the 3-4 Å distance needed for Auger de-excitation.

Image Potential

The interpretation of the kinetic energy spectra obtained in MDS experiments relies on knowledge of the effective ionisation potential $E_i^{'}$ of the helium atom. In the case of Auger neutralisation, $E_i^{'}$ is dependent on the image charge potential felt by the approaching He^+ ion, which is a function of the distance between it and the surface. In the gas phase, the value of $E_i^{'}$ for a He^+ ion is 24.6 eV. As the ion approaches a surface, it experiences a force due to its image charge which reduces the value of $E_i^{'}$:

$$\Delta E_i = -\frac{3.6}{R-d} \tag{3.8}$$

where ΔE_i is the change in the ionisation potential, R is the distance from the centre of the ion to the surface measured in Å and d is a corrective distance to account for the image force (approximately 0.6 Å) [100]. Therefore, when Auger neutralisation occurs at a greater distance from the surface, the change in the ionisation potential will be smaller and emitted electrons will be ejected with greater kinetic energy.

Resonance Neutralisation

Resonance neutralisation is a competing process where an electron from the surface tunnels into the excited state of the helium ion in the neutralisation step after resonance ionisation. This can occur if the Fermi level of the surface is higher than the empty excited state of the He^+ ion and is a competing process to Auger neutralisation. The resulting metastable atom can then undergo Auger de-excitation to induce emission. This has a low probability of occurring and is unlikely to play a significant role in the majority of systems under study.

3.4 The Metastable Helium Beamline

3.4.1 Metastable Helium Source

Efficient generation of metastable helium atoms to produce a high-flux beam is crucial to achieving the best signal-to-noise ratios in MDS data acquisition. Metastable atom beams have been developed for research applications such as scattering cross-section measurements [101] and crossed molecular beam experiments [102]. The

most common method is via direct current (DC) discharge through electron collisions, which is both relatively simple and can achieve good intensities of up to 10^{14} atoms $s^{-1}sr^{-1}$ [103]. There are other approaches such as collisions with a coaxial electron beam [104, 105], but these cases are neither easier to implement nor produce higher beam intensities. The helium source used at York is a cold cathode DC discharge source based on the one developed by Swanson et al. at the Australian National University [106].

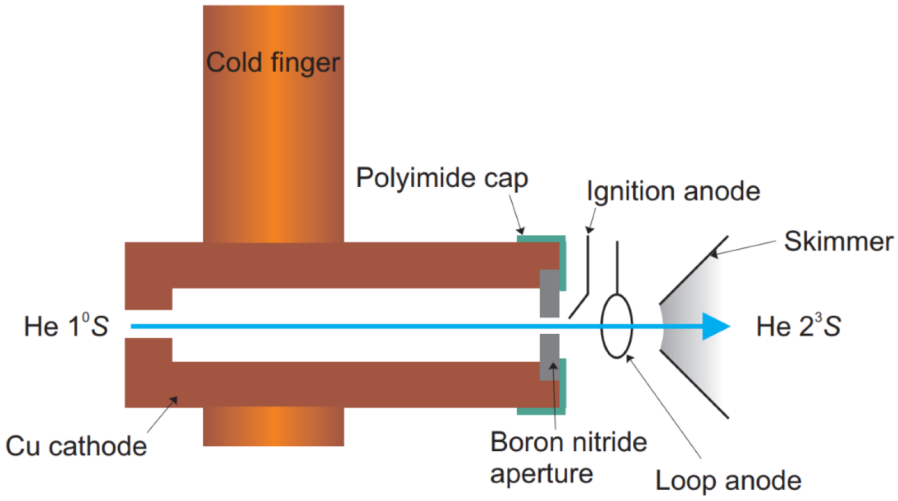

Figure 3.4: A schematic of the helium source used to generate metastable helium. Ground state He gas is injected at the rear of the cooled tubular Cu cathode. A discharge is struck and maintained by voltages on the two anodes. A skimmer separates the source and the flight chamber.

The helium used for MDS is supplied by 99.999% (i.e. grade He 5.0) He gas fed into the system from a regulated gas bottle through a leak valve. The cathode is a hollow cylindrical copper tube (length 60 mm, diameter 20 mm, inside diameter 10 mm), shown in figure 3.4. This is mounted on a copper cold finger cooled via a connected dewar outside the beamline filled with liquid nitrogen (LN_2). The cooled cathode slows the atoms exiting the source to 1000 ms^{-1}, allowing better beam manipulation and less impact on sample surfaces. A hollow design has advantages over a needle cathode due to its greater surface area (which allows lower pressure), stability and cooling efficiency. One end of the cathode is fitted with a boron nitride exit aperture with a diameter of 0.3 mm and thickness 12 mm. Boron nitride is used for its durable nature, allowing a longer lifetime on the aperture even under repeated electron bombardment. It also has good thermal conductivity for better

velocity control of exiting helium atoms. A polyamide cap is screwed on the end of the cathode to provide insulation from the anodes. Two anodes are fitted: the first is an ignition anode made from a piece of wire used to start the discharge; the second is a ring anode used to maintain a stable discharge and draw the discharge away from the source. A skimmer is placed approximately 20 mm from the source, and is used to reduce the profile of the discharge such that only a relatively narrow beam directed at the sample exits the source.

3.4.2 Beamline Operation and Apparatus

A discharge is struck in the source by applying 5.0 kV to the ignition anode, 1.4 kV to the loop anode and -500 V to the skimmer. Helium gas is then allowed into the source until discharge strikes. The ignition anode is current limited to $\sim$3 mA at this point (voltage reduces to $\sim$600 V) to reduce photon generation and unnecessary heating. A high helium pressure >60 mbar is required to strike the source, but is not necessary to maintain the discharge. A compromise is required as too low a pressure cannot maintain a discharge but too high a pressure causes collisions between meatstable atoms that cause them to de-excite before reaching the sample. The relationship of this driving pressure with the resulting metastable beam flux is a log-normal function, with a maxima flux occurring at 11-12 mbar as determined by previous experiments in the group [96].

The gas pressures used at the source to strike the discharge are very high, but a low pressure is required in the beamline to maximise the number of metastable helium atoms reaching the sample by reducing collisions (and therefore de-excitation events) of the metastable atoms with themselves and other gases. A Varian NRC diffusion pump with a pumping speed of 4000 ls^{-1} is placed behind the source to deal with the gas load when the beam is under operation. The beamline itself is pumped with two turbomolecular pumps: an Edwards EXT 250 with a pumping speed of 240 ls^{-1} and a Leybold Turbovac 360 CSV, with a pumping speed of 345 ls^{-1}. These are placed at roughly evenly spaced locations on the long flight chamber and both are backed by a large two-stage Edwards M40 rotary pump. A diagram of the beamline is shown in figure 3.5. A less permanent fixture of the MDS setup is the connection between the beamline and the analysis chamber, which is removed during bakeouts of the analysis/preparation chamber system. This is made from a four-way CF

connector of appropriate length in one direction with a bellows section to allow some flexibility. It is pumped by its own small Leybold Turbovac 50 turbomolecular pump with pumping speed of 33 ls^{-1}, which is backed by an Edwards RV12 rotary pump, and can reach a pressure in the 10^{-7} mbar range. As the pressure in this tube (and the rest of the beamline) is not at UHV, there is a small 2 mm aperture (drilled into a solid copper gasket) between the tube and the analysis chamber. This serves the purpose of both limiting the profile of the incident helium beam as well as reducing the effect on the base pressure in the analysis chamber.

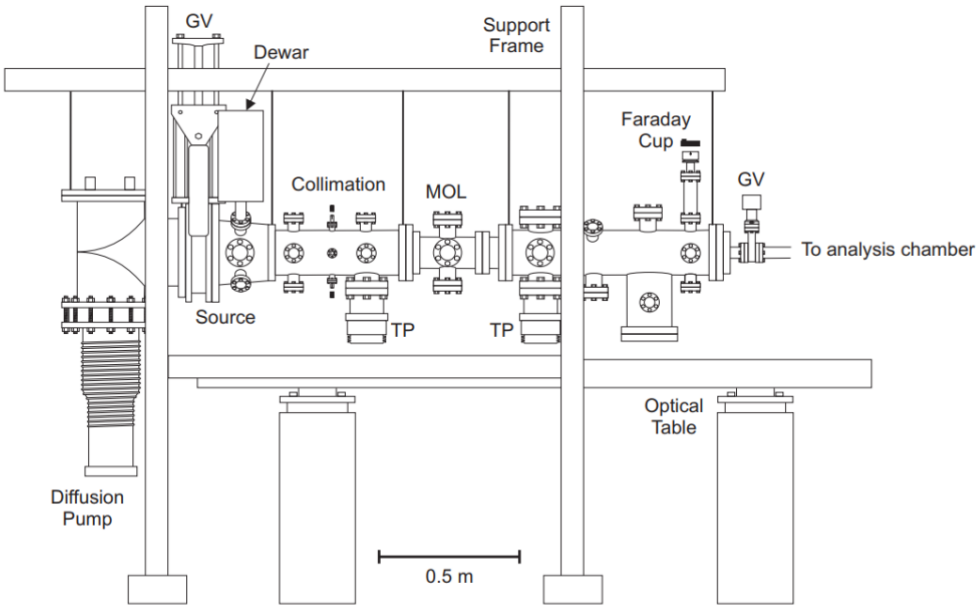

Figure 3.5: A schematic of the MDS beamline. The connection section to the analysis chamber is not shown. The beamline hangs from a supporting frame which reduces vibrations from the pumps affecting the optical table below.

When the beamline is not in use, the pressure in the flight chamber of the beamline is in the order of 10^{-7} mbar, and the large pneumatic gate valve that separates the diffusion pump from the source stays closed. Before starting operation, the valve is opened to allow the diffusion pump to pump away the high gas load. The skimmer acts as an aperture to the rest of the beamline and the pressure in the flight chamber is kept below 10^{-5} mbar when the source is being struck. Since the initial burst of helium required to strike the discharge causes a high pressure in the source and an accompanying increase in the photons produced, the source is allowed to stabilise for at least 10 minutes prior to experiments and reach an equilibrium. The pressure in the flight chamber recovers down into the 10^{-7} mbar range during normal operation.

The beamline also includes a simple Faraday cup apparatus, which can be wound into the path of the He beam via a rotational drive. This is placed at the end of the flight chamber and is used to monitor the intensity of metastable atoms via a current created from de-excitation events against the cup. Collimation apparatus will be discussed separately in the next section. To isolate the collimation optical apparatus from the vibrations of the pumps, the beamline hangs from a support frame instead of being supported from below, eliminating contact with the optical table entirely.

3.4.3 Collimation

Under normal conditions, metastable helium atoms created via DC discharge expand outwards from the source, yielding a $1/r^2$ relationship between the intensity and the distance r between the source and the sample. This reduction in intensity is prevented using a collimation technique on the beamline here at the University of York that utilises laser cooling principles and the spontaneous force [96]. The technique also results in an improved purity of He 2^3S atoms impinging on the sample, as He 2^1S atoms are not collimated.

Spontaneous Force

He in the 2^3S state can be excited into the 2^3P_2 state through illumination by light with a wavelength corresponding to the energy of the transition, in this case ∼1083 nm, corresponding to a transition of 1.147 eV (section 3.1). The 2^3P_2 then decays quickly back into the 2^3S state due to its short half life (98.8 ns) and a photon of the same energy is emitted in a random direction. If the incident photons all originate from a particular direction and the emitted photons all radiate in random directions, a net momentum will be imparted onto the helium atom over multiple absorption/emission events. This resulting force is referred to as the spontaneous force and this principle is applied in laser cooling and atom trapping applications [107]. This illumination can be provided by a laser, and each photon will give a change in momentum Δp:

$$\Delta p = \hbar k = \frac{h}{\lambda} = m\Delta v \tag{3.9}$$

Where k is the magnitude of the wave vector and λ is the frequency of the photon. Rearranging for the change in momentum Δv and substituting in the relevant values for this He 2^3S to 2^3P_2 gives a velocity change of 9.2 cms^{-1}. Changes in the velocity induced by the photons will induce a Doppler shift in the frequency felt by the atom, and therefore affect the force imparted by the laser. This follows a Lorentzian function of the atom's velocity and therefore the effect is only present over a certain velocity range and decays rapidly. This issue can be solved by detuning the laser so that the maximum force is always felt by the atoms as they change in velocity in the direction of laser propagation. To achieve this, four curved mirrors are placed along the path of the propagating helium beam. In each direction, a laser beam is reflected multiple times to form a network of counter-propagating laser pairs, which will force deviating atoms onto a straight path by reducing their transverse momentum. The curvature of the mirror changes the angle at which the laser hits the beam. Near the source the laser hits the beam at an angle and is therefore detuned to (i.e. perpendicular to the direction of motion of) atoms with a relatively large transverse velocity. As the mirror curves the laser is detuned to atoms with smaller deviations in their direction of motion. This has the effect of gradually collimating the metastable helium beam. An illustration of this set-up is shown in figure 3.6.

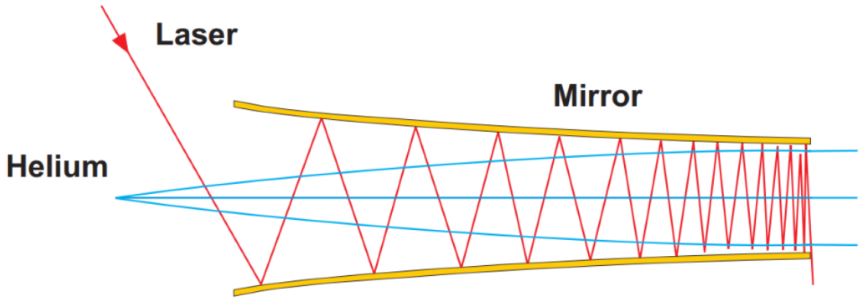

Figure 3.6: A diagram showing how collimation of the helium beam is achieved in the MDS beamline. The curvature of the mirror slowly changes the angle of the laser and therefore the laser is resonant with atoms with different transverse velocities.

Frequency Locking of the Diode Laser

The frequency of the diode laser used to drive the 2^3S_1 - 2^3P_2 transition can drift due to thermal fluctuation. The linewidth of the transition is 1.6 MHz, the linewidth of

the laser is 1.0 MHz and the thermal drift can be up to 100 MHzK^{-1}. Therefore the frequency of the laser needs to be locked for stable operation. This is also necessary for the spin polarisation of the beam via optical pumping. To do this, a saturated absorption spectroscopy set-up using a helium discharge cell was utilised [108]. A schematic of the discharge cell apparatus is shown in figure 3.7.

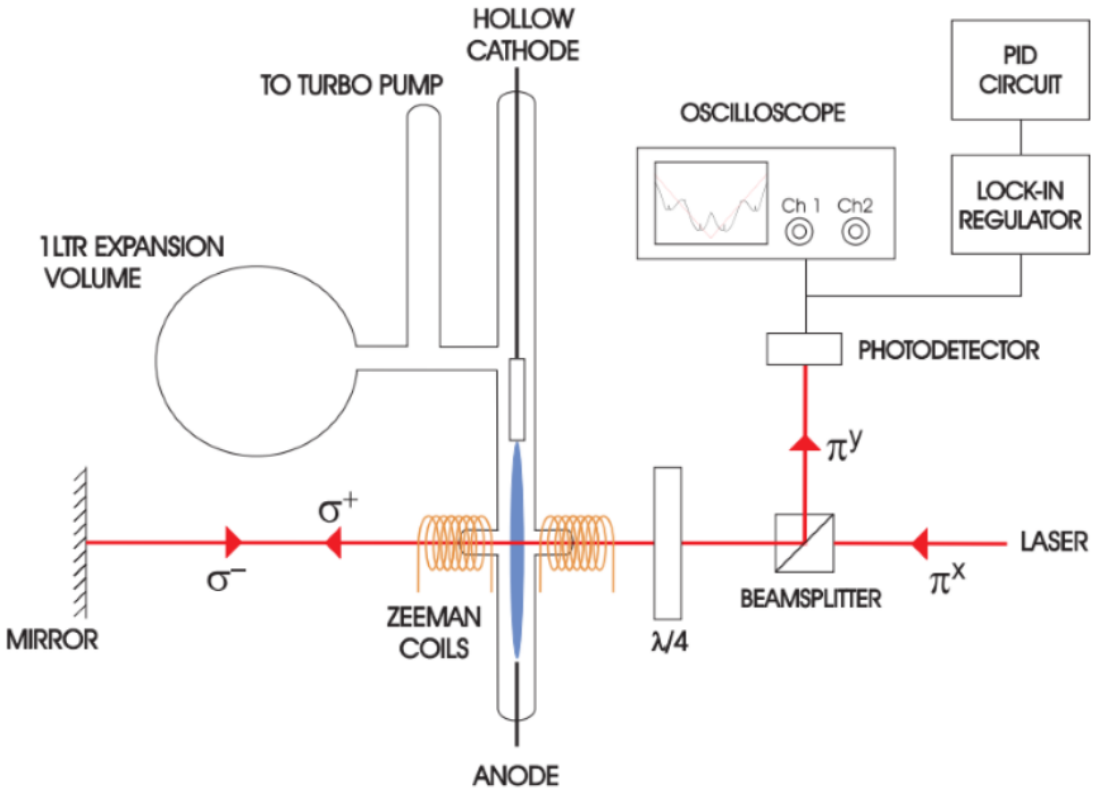

Figure 3.7: A schematic of the saturated absorption spectroscopy apparatus. The frequency of the laser is scanned around the 2^3S_1 - 2^3P_2 transition to create a saturated absorption signal at the transition frequency. This is fed into the laser diode control system to stabilise the frequency.

A helium discharge cell was pumped using a 50 ls^{-1} turbomolecular pump and baked to reduce the amount of other gases inside the the cell before filling with He gas. The 1 litre expansion volume also served to increase the amount of He gas and reduce the proportion of contaminants. The cell is filled up to 0.9 mbar of He and a discharge is struck through the tungsten needle anode and a grounded cathode with a voltage of 600 V. The pressure used is a compromise between maintaining the discharge and reducing pressure broadening effects. A hollow design for the titanium cathode was used to maximise surface and allow operation at low pressures. The cell excites the He atom into the 2^3S metastable states through collisions with electrons, much like

the metastable beam source.

A lock-on signal is generated using this set-up to tune the laser to the exact frequency of the transition. The narrow linewidth of the transition makes this difficult to do with current and temperature controls alone, and therefore the frequency of the laser is scanned using a piezoelectric transducer element attached to the diffraction grating of the laser diode. The laser beam is circularly polarised and passed through the discharge cell, and as it does so, photons with frequency corresponding to the 2^3S_1 - 2^3P_2 transition are absorbed to drive the transition. Thermal distribution of velocities of He atoms in the cell cause a range of frequencies to be absorbed, due to Doppler shifting of the resonant frequency. This manifests itself as a broadened feature in the absorption frequency spectrum of the laser.

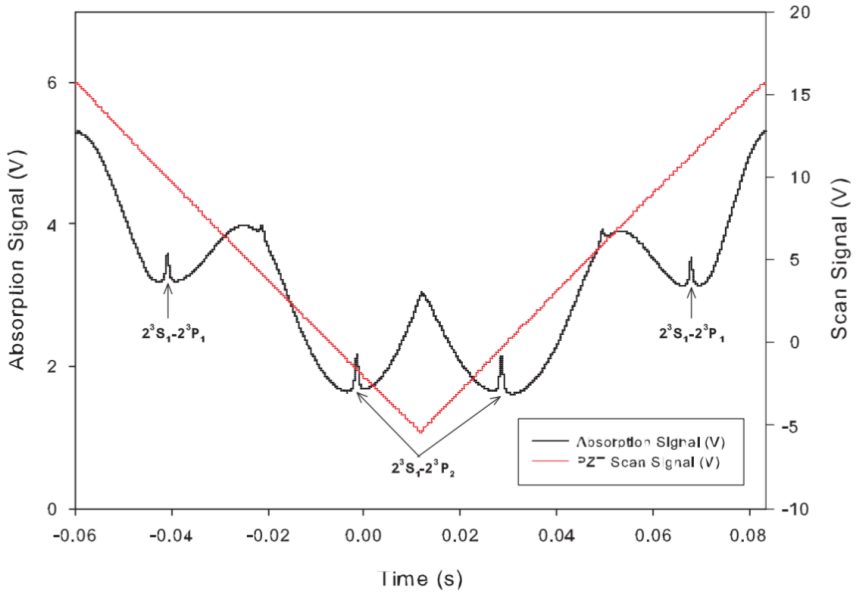

Figure 3.8: Graph taken from [96] showing the saturated absorption spectrum. The small peaks inside the larger troughs correspond to the transitions. The transition from the 2^3S_1 to both the 2^3P_1 and 2^3P_2 states can be seen due to the large scan amplitude.

However, the signal from the single absorption spectrum is too broad for the purpose of frequency locking. To obtain a more defined frequency, the laser is reflected back through the discharge cell. Atoms that move in the direction parallel to the initial beam are moving in the opposite direction to the returning beam and therefore the Doppler shift is reversed. Therefore, the returning beam will interact again with the atoms moving in the opposite direction, increasing the absorption signal. For atoms

that have no component of velocity in the direction of the laser, there is no Doppler shift and both the initial beam and the returning beam can interact with these atoms. However, since the lifetime of the 2^3P_2 state is much longer than the time it takes for the laser beam to reflect off the mirror and return, the atoms excited by the initial beam will still be in their excited state when the returning beam passes through. Therefore at this frequency the returning beam cannot interact with as many of the He atoms and there is a narrow peak at the exact position of the non-shifted transition in the frequency corresponding to a drop in the absorption. An example of this is shown in figure 3.8. The width of this saturated peak is given by [109]:

$$\Gamma_s = (\Gamma_n + \Gamma_c)\sqrt{1 + s_0} \tag{3.10}$$

Where Γ_n is the natural linewidth, Γ_c is a collisional broadening parameter and s_0 is the saturation parameter. The returning laser beam is then directed into a photodiode and the saturated absorption signal is used by the lock-in regulator of the Toptica Photonics diode laser system to lock the frequency to the transition using a phase-locked feedback loop.

3.5 Spin Polarised Metastable De-excitation Spectroscopy (SPMDS)

One the aims of this project was to create a spin-polarised MDS set-up similar to the one used by the group of Y. Yamauchi and M. Kurahashi at the National Institute of Materials Science (NIMS) in Tsukuba, Japan. The author gathered some expertise with the apparatus there while working at NIMS for 3 months in order to replicate it in York. The section below will outline the principles behind spin-polarising the helium beam and the theory of SPMDS. Extra parts of the experimental apparatus constructed for this purpose will be described later in Chapter 4.

3.5.1 Spin Polarisation of the Helium Beam

The metastable helium source produces helium atoms in the 2^3S state with electrons in both the spin up and spin down configurations. In order to perform SPMDS, the helium atoms in the beam must all be in either the spin up ($S = 1$) or spin down

($S = -1$) state. This is performed by optically pumping the helium with polarised light tuned to the 2^3S - 2^3P_2 transition.

For the case of excitation due to an incident photon, only transitions with $\Delta m = -1, +1$ are allowed as photons are massless ($\Delta m \neq 0$). The angular momentum eigenstates of the photon are σ^+ ($m_j = +1$) and σ^- ($m_j = -1$ which correspond to right circularly polarised and left circularly light respectively. Therefore illumination of atoms via right circularly polarised light tuned to the correct resonant frequency will only induce transitions with $\Delta m = +1$ due to selection rules.

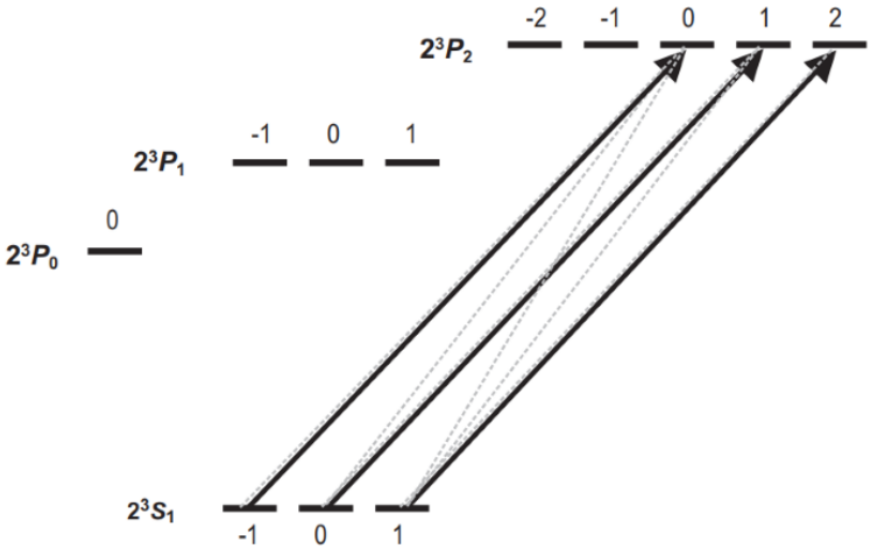

Figure 3.9: A diagram showing the transitions between the different He sub-level induced by irradiation of right circularly polarised light. The dotted lines represent possible decaying transitions. Repeated absorption/decay events eventually lead to occupation of the $m_j = +1$ state.

By applying a weak magnetic field, the degeneracy in the 2^3P_2 state is lifted with the levels ordered by the quantum number m_j. 2^3S - 2^3P_2 transitions induced by right circularly polarised light will cause $\Delta m = +1$ while decays are occur with all allowed transitions $\Delta m = +1, 0, -1$. Over many excitation/decay cycles, the electron will move to the state with the highest m_j. In the case of metastable helium this is the $m_j = 1$ level of the 2^3S_1 state, which has a total spin $S = 1$. At this point the beam is polarised in the direction of the weak magnetic field. A diagram of this is shown in figure 3.9. The reverse occurs with left circularly polarised light, which pumps the helium atoms into the $m_j = -1$ state.

3.5.2 Spin-Polarised Measurements

The spin-resolved density of states is not symmetric in many materials, i.e. the density of states in each spin channel is not equal, leading to majority and minority spin states. This occurs in ferromagnetic materials (due to the exchange interaction), which are often metallic and de-excite through the two stage process of resonance ionisation followed by Auger neutralisation. As described in section 3.3.3, in the second AN stage, an electron tunnels from the surface of the material into the He $1s$ state to create an atom in its ground state. Due to Pauli's Exclusion Principle, this electron can only have spin opposite to that of the electron already present in the He^+ ion. With a spin-polarised metastable helium beam, the neutralising electrons must therefore all originate from states with spin opposite to the polarisation of the beam.

The neutralisation step is accompanied by the emission of an electron. While this electron can originate from any state, it has been observed that the emitted and neutralising electrons are more likely to have anti-parallel spins [110]. Aside from a possible contribution from the Auger de-excitation process, the proposed explanation for this is that a two-hole singlet state is preferred in the surface, which is consistent with Pauli's Exclusion principle and the effect is stronger when the surface electrons probed are close to the Fermi energy [111, 112]. The likelihood of this differs depending on the surface and varies with energy. A diagram showing the process is shown in figure 3.10.

However, this is not a desirable characteristic. As mentioned in section 3.3.3, the resulting spectrum from RI+AN is a convolution of the states from which the neutralising and emitted electrons originate. When the two electrons originate from the same spin state, the spectrum will be a self-convolution of the density of states for that one spin state. But if the electrons originate from different spin states, the spectrum will be a convolution of both and therefore contain no useful information distinguishing the spin-resolved density of states. Both cases occur in practice, and although the two electrons involved are more likely to have anti-parallel spins, there will be a contribution from emitted electrons with the same spin and some information is retained regarding the spin asymmetry in the surface. Following from this, the spin asymmetry values calculated from any results are less than the actual asymmetry and the proportion of the spin resolved contribution varies with the material.

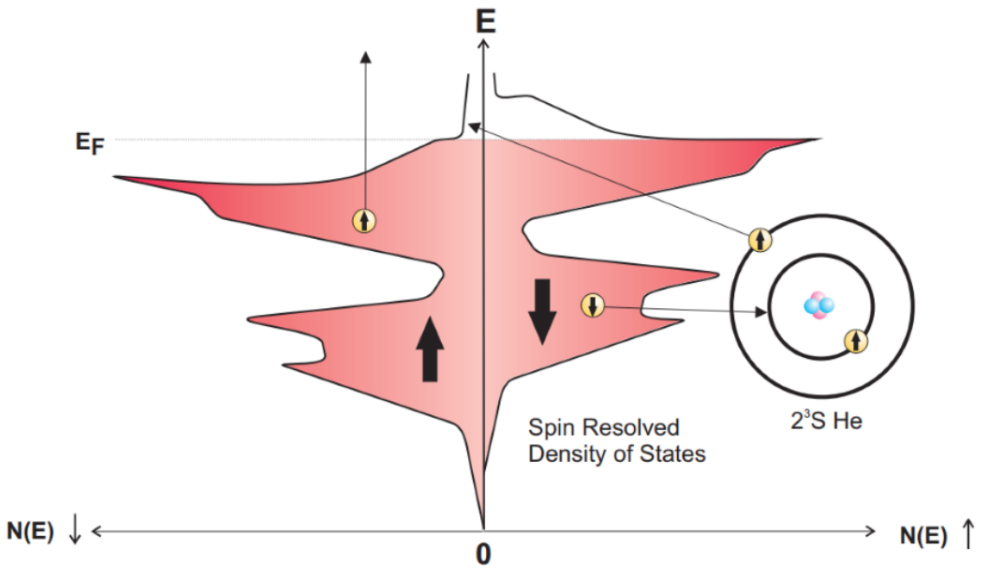

Figure 3.10: A diagram showing the resonance ionisation + Auger neutralisation process for a spin polarised helium beam probing a magnetic sample (where the majority spin at the Fermi level is in the spin down channel). The emitted electron is depicted as originating from a spin state opposite to that of the neutralising electron, which is more likely to occur.

Therefore only qualitative information is obtained in the cases where the He beam de-excites via RI+AN.

For insulating magnetic materials, the de-excitation mechanism is Auger de-excitation. This is more relevant for studying the spin polarisation of organic molecules deposited on the ferromagnetic surface. The only surface electron involved is the one that tunnels into the He $1s$ state, which will have anti-parallel spin to the one already present. A spin polarised helium beam will only probe the spin states opposite to that the beam polarisation and will yield a greater intensity when the majority spin state is anti-parallel to the beam. In theory, when the beam polarisation is aligned to the magnetisation of the sample, only the opposite state will be probed and the electron released from the metastable will all have the same spin polarisation, yielding a reliable representation of the the spin-resolved states. In practice, the secondary electron released means this is not entirely the case [112]. This will lead a slight variation in the measure spin asymmetry parameter, but the value is much closer to the actual asymmetry than in the case of metallic ferromagnetic surfaces.

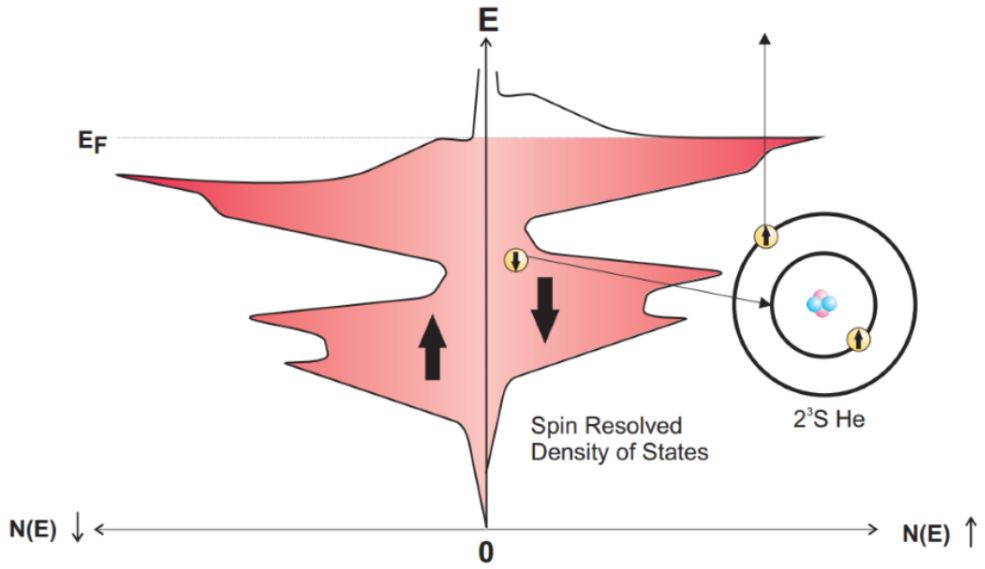

Figure 3.11: A diagram showing the Auger de-excitation process for a spin polarised helium beam probing a mostly insulating magnetic sample. The electron that tunnels in the He 1s state must have opposite spin to the electrons in the helium atom.

The spin asymmetry parameter, A, measured by the beam can be calculated using the proportion of spin up and spin down electrons collected by the analyser:

$$A = \frac{1}{|P_z|}\frac{N(E)\uparrow - N(E)\downarrow}{N(E)\uparrow + N(E)\downarrow} \tag{3.11}$$

Where P_z is the polarisation of the beam:

$$P_{z\pm} = \frac{R\uparrow \mp R\downarrow}{R\uparrow + R_0 + R\downarrow} \tag{3.12}$$

$N(E)\uparrow$ and $N(E)\downarrow$ are the numbers of electrons collected by the analyser when the helium beam is polarised to the spin up and spin down configurations respectively. $R\uparrow$ and $R\downarrow$ are the count rates for the helium atoms in each respective polarisation state while R_0 is the rate for the unpolarised atoms (2^1S).

Chapter 4

Experimental Methods

4.1 The Vacuum System

The UHV electron spectroscopy facility that was developed during this PhD is the only one in the world capable of performing metastable de-excitation spectroscopy (MDS), ultraviolet photoemission spectroscopy (UPS) and x-ray photoemission spectroscopy (XPS) all on the same system. This allows a huge amount of information to be gathered in a reasonably short span of time from the same sample, revealing complementary information on its electronic, magnetic and chemical properties, as demonstrated later in this thesis. The system consists of two connected chambers seated on the same table top: a preparation chamber to clean substrates and grow films; and an analysis chamber to take measurements using spectroscopy techniques. The setting up of a UHV system is a significant undertaking and therefore was a major part of the PhD project.

As well as the aforementioned UHV chambers, the beamline which generates the metastable helium atoms needed for MDS is also connected to the analysis chamber. A fast entry lock for the transfer of fresh samples is connected to the preparation chamber. A detailed schematic of the system is shown in figure 4.1, and in the following chapter, key components of the system will be described in detail and further explained where necessary. Pumping arrangements for the individual chambers are described in the relevant sections and those for the analysis and preparation chambers are shown in figure 4.2.

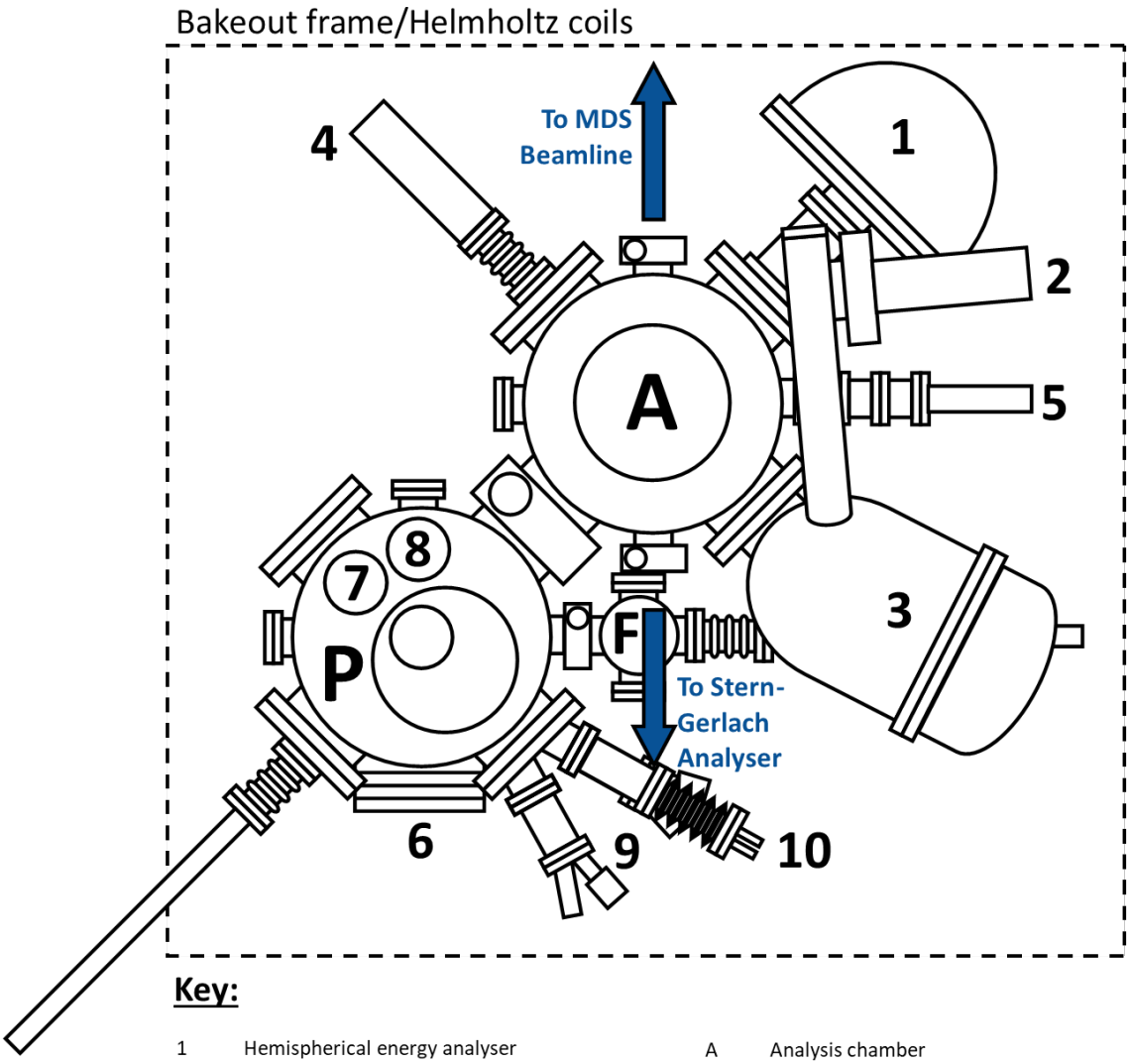

Key:

1	Hemispherical energy analyser	A	Analysis chamber
2	X-ray source for monochromated XPS	P	Preparation chamber
3	X-ray monochromator	F	Fast-entry lock
4	Dual-anode x-ray source		
5	UV source for UPS		
6	LEED screen		
7	Residual gas analyser		
8	Pulse magnet		
9	EFM3 and organic deposition sources		
10	Gas doser		

Figure 4.1: Schematic of the vacuum chamber built to grow and analyse samples, including the main instruments attached.

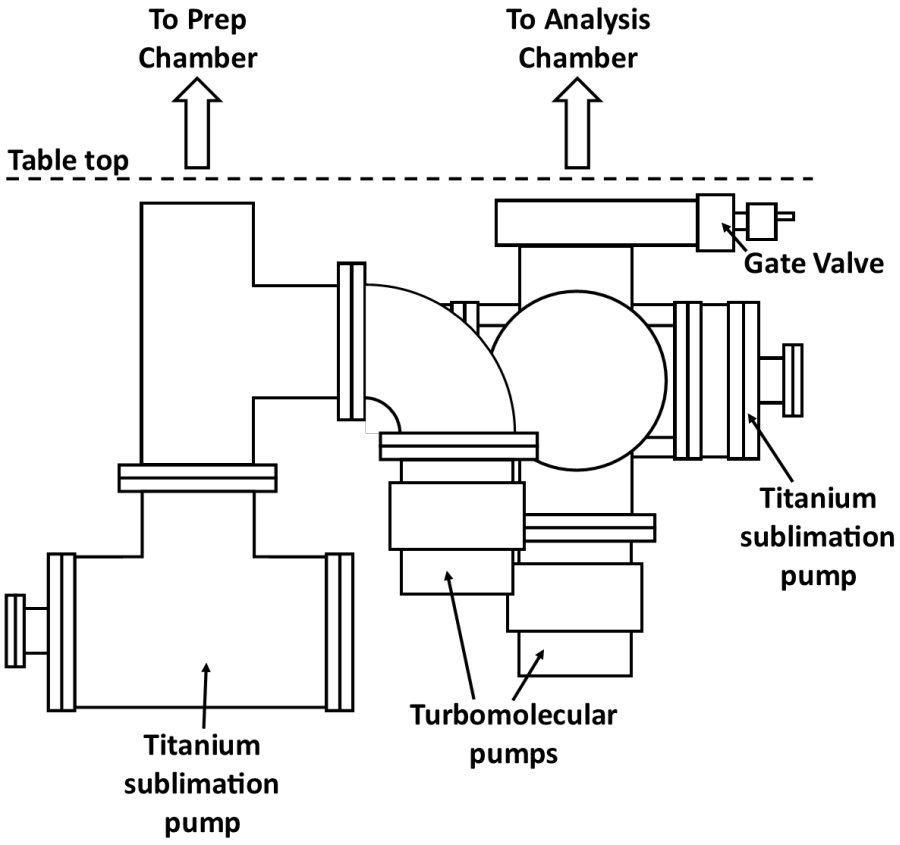

Figure 4.2: Schematic of the pumping arrangement underneath the table of the analysis and preparation chambers. Two extra smaller turbomolecular pumps for the UPS source and the fast entry lock are not pictured for clarity. The figure is a view of the arrangement from the side opposite to the MDS beamline.

4.1.1 Preparation Chamber

The components in the sample preparation chamber are mostly placed on two distinct vertical levels. Samples are moved between the two levels with a manipulator that allows for large vertical movement and rotations around the vertical axis. The sample holder is an Omicron GA02-1661-2 sample stage with e-beam heater and direct current heating capabilities when used with standardised Omicron sample plates. A thermocouple feedthrough is available on the preparation chamber manipulator, however, for the purposes of sample growth/preparation, more accurate readings are taken with an infra-red pyrometer instead. A quartz crystal microbalance is fixed at the top of the sample stage to monitor the deposition rate of films prepared in the prep chamber, see section 4.4.2.

The preparation chamber is connected to the fast entry lock (FEL) via a 38 mm CF

flange with a gate valve. The connection through to the analysis chamber is made through a larger 152 mm flange with a large gate valve. The preparation chamber can accommodate multiple deposition sources through 38 mm CF flanges and for the majority of this project, an Omicron EFM3 source was used for the deposition of Fe films and a MBE-Komponenten NTEZ low temperature effusion cell was used for depositing organic molecules. A retractable gas doser was attached to allow a gas inlet to approach at very close proximity to the sample, which can then create higher local gas pressures near the sample without compromising the base pressure of the whole preparation chamber. A more detailed description of deposition processes for the samples prepared will be discussed in the relevant chapters later in this thesis. A second gas inlet valve is also attached to the chamber for venting the chamber and handling gases needed at a lower pressure. An SmartLAB residual gas analyser was also attached to the preparation chamber to monitor the partial pressures of remnant gases in the chamber.

The preparation chamber is also equipped with an Omicron SPECTALEED low energy electron diffraction (LEED) apparatus to check the surface reconstruction of samples after they are prepared. A brief description of the technique is given in section 4.4.1. Magnetic samples can also be magnetised with a pulsed magnet set-up in the preparation chamber.

The pumping arrangement for the prep chamber hangs underneath the table on which it sits. The chamber connects to a T-piece via a 203 mm flange on the bottom. On one end of this, another T-piece re-purposed into a titanium sublimation pump (TSP) is connected directly underneath the prep chamber. The other end of the T-piece is connected to a pipe bend, which in turn is connected to a Seiko Seiki STP-400 turbomolecular pump with a pumping rate of 420 ls^{-1}. The backing for the turbomolecular pump is provided by an Edwards RV3 rotary pump. The backing pressure is monitored by a pirani gauge and the chamber pressure via an ion gauge connected to a 38 mm flange on the chamber. The base pressure in the preparation chamber is 8×10^{-10} mbar and the backing pressure is kept at 1×10^{-2} mbar or lower.

4.1.2 Analysis Chamber

The analysis chamber is equipped with a variety of electron spectroscopy techniques for the surface analysis of samples transferred in through the preparation chamber. Sample position can be changed with multiple degrees of freedom via the sample manipulator. It is equipped to move the sample in all three of the x, y and z directions as well as rotations around the vertical axis and the sample normal axis. The manipulator is also equipped with feedthroughs for direct current and electron beam capabilities when holding standardised Omicron sample plates. A pyrolytic boron nitride (PBN) heater is also attached to the sample stage to allow more gentle heating (when compared to direct current or e-beam heating) of samples up to 200 °C. A thermocouple is attached to the end of the sample stage to monitor the temperature. The use of an infra-red pyrometer is difficult due to the need for lead lining on all windows in order to use x-rays in the analysis chamber. Because of this, and to preserve the pressure as much as possible in the analysis chamber, cleaning procedures with the need to monitor and control the temperature of the sample at higher temperatures (for example flashing silicon) are not performed in the analysis chamber. The sample stage can also be cooled via liquid nitrogen through a pipe running down the manipulator.

An Omicron EA 125 hemispherical energy analyser is used to take data measurements for the various spectroscopic techniques connected to the analysis chamber. The theory of operation for the analyser will be covered briefly in the section focussing on electron spectroscopy (specifically section 4.2.1). The analyser is equipped with a 7-channel detector with a reported energy resolution of better than 10 meV over a range of up to 2000 eV, and a maximum count rate of 10^7 s^{-1}. This allows it to be used for both XPS (high energy range) as well as UPS/MDS (high count rate) with great precision.

The monochromated x-ray source is connected perpendicular to the analyser through a 152 mm CF flange (see figure 4.1). An adapter piece with a 5° offset is used to connect the monochromator to stop the x-ray source from physically impinging on the analysis chamber. X-ray radiation is generated via bombarding an aluminium anode with electrons emitted from one of two filaments. The power dissipated in standard operating conditions can be up to 300 W; therefore the source is cooled with a recirculating temperature controlled cooling system driven by a ATC KT1 chiller

pumping deionised water at 18 °C. De-ionised water is used to reduce leakage current. The x-rays emitted are aligned via the port aligner, redirected onto the quartz crystal in the monochromator and the resulting monochromated beam is focussed towards the sample stage. The theory behind monochromated x-ray generation will be discussed in further detail in a later section 4.2.3. Due to pumping difficulties arising from long tubular sections with many corners, an extra set of bellows were used to connect a 38 mm flange near the x-ray source to a flange on the analysis chamber. This allows quicker pumping of gas near the source and port aligner.

The ultraviolet source for UPS is connected to the analysis chamber though a 38 mm flange at 45° to the analyser and monochromator. Helium I α photons (21.22 eV) are produced via cold cathode capillary discharge. Helium gas is introduced into the source near its end through a needle valve. This part of the source is connected to the chamber through a thin glass capillary, and thus the pumping throughput is highly inadequate when using only the main turbomolecular pump under the analysis chamber. A smaller Leybold Turbovac 50 turbomolecular pump, with a pumping speed of 33 ls^{-1} was added to pump the UV source to remedy this. A roughing line was also connected to the source to pump away excess helium during normal operation. This pumping is done by a Edwards RV12 rotary pump. This rotary pump is also used when flushing out the helium line after bakeouts. The UV source is cooled by running tap water through a cooling shroud built around the source.

The pumping arrangement for the analysis chamber is also located underneath the table. Below the analysis chamber is a large gate valve (203 mm nominal tubular diameter), which can separate the chamber above the table from the the pumping arrangement and is used to preserve some measure of cleanliness when the pumps have to be stopped for alterations and power outages. Monitoring the pressure reading after cutting off the chamber from the pumping is also a method of checking for leaks. Below the gate valve hangs an eight-way 203 mm CF connector section. An Edwards nEXT 400 turbomolecular pump with a pumping speed of 400 ls^{-1} is connected to the flange directly underneath the chamber and is protected from falling samples by a mesh above the pump. The backing to the turbomolecular pump is provided by an Edwards RV3 rotary pump similar to the preparation chamber. The pumping arrangement also includes a titanium sublimation pump, which is again made from a 203 mm CF T-piece repurposed into a small chamber for the

titanium sublimation pump (TSP) to fire in. The TSP chamber is connected to one of the horizontal connections on the eight-way connector. The base pressure of the analysis chamber is 2×10^{-10} mbar and the backing line is kept at a pressure of 1×10^{-2} mbar or lower. When the chamber is opened to the MDS beamline and when UPS is under operation, the pressure rises above 1×10^{-8} mbar. But since the gas causing this pressure rise is helium in both cases, it is pumped away quickly and does not easily adsorb and the chamber recovers rapidly after use.

4.1.3 Bakeout

Bakeout is required for vacuum systems to reach UHV pressure ranges of 10^{-9} mbar and below within a reasonable time frame. This is due to the adsorption of water onto the chamber walls when the vacuum system is vented. The vapour pressure of water is high in the chamber as a result due to a the slow rate of desorption of water. With no leaks, the pressure would eventually drop into UHV levels but a long time would be needed. Baking the system accelerates this process.

The bakeout apparatus was specially designed for the vacuum chambers and constructed in the departmental workshop. This consists of a series of bakeout panels which are affixed to a cuboid shaped frame made from KJN aluminium profile. The frame also houses a set of coils designed to function as Helmholtz coils to control the magnetic field around the chamber, mainly to cancel out the earth's magnetic field. More details regarding the Helmholtz coils will be outlined in section 4.4.4. The panels are made of aluminium and are hollow for better heat insulation. A hole is present in the appropriate panel to allow for the transfer arm between the preparation and analysis chambers, which was heated using a separate heating sheath. The inside of the bakeout "oven" is heated using two heaters fixed to the panels, with fans attached to allow air circulation and more even heating. The pumping arrangements underneath the table are heated via heating tapes. The heating tapes provide less even heating compared to bakeout "oven" above the table, but since the pumps below the table cannot be baked, the tapes were used as an alternative.

The bakeout procedure involves baking the system at 130 °C for 24 hours. The temperature limited by the quartz crystal housing in the x-ray monochromator, which cannot be heated above this for extended periods of time. Prior to bakeout,

the chamber is allowed to pump down to the low 10^{-7} mbar range, where the pressure drop slows down due to water vapour. After the heaters are switched off, the TSP filaments are degassed and fired while the chamber is still hot to obtain a better base pressure after the chamber cools down.

4.2 Electron Spectroscopy Techniques

The theory behind photoemission spectroscopy techniques lies in Einstein's photoelectric effect, where irradiation with photons of sufficient frequency on a surface induces the emission of electrons. The emitted photoelectrons will have a range of kinetic energies as they are emitted from various electronic states with different binding energies. In the case of an photoelectron ejected from a state with binding energy E_b, the process can be described by the following equation:

$$E_k = h\nu - E_b - \phi_s \tag{4.1}$$

Where E_k is the kinetic energy of the emitted photoelectron, $h\nu$ is the energy of the photon and ϕ_s is the work function of the sample material. The kinetic energies of the photoelectrons therefore form a spectrum with high intensity peaks corresponding to the discrete energy states from which they are ejected. The maximum kinetic energy is determined by the energy of the photon and the work function of the surface.

4.2.1 Hemispherical Energy Analyser

Before diving into the explanations regarding the various electron spectroscopy techniques available, it is instructive to first mention a common element between them: the hemispherical energy analyser used to collect the data.

At the entrance to the analyser, an electrostatic input is used to collect electrons from a larger solid angle and to change the energy of the beam with respect to the pass energy of the analyser. The lens consists of a series of cylindrical electrodes held at different potentials. Potential gradients are located at the gaps between the cylindrical electrodes, which refract charged particles passing through the lens, a simple diagram of this shown in figure 4.3. It is possible to accelerate or slow

down the electrons without changing the focussing properties by using a system of 3 electrodes. The acceleration and deceleration of electrons is controlled by the ratio of the potentials between the front and end lenses and the relative magnitude of the potentials between them. The middle lens controls the focus. The profile of the beam is controlled by an input aperture, which is chosen from a set of built-in choices (of which the most commonly used in experiments are the 1 mm and 6 mm diameter circular apertures). The exit apertures are automatically set in the instrument depending on the entrance aperture used.

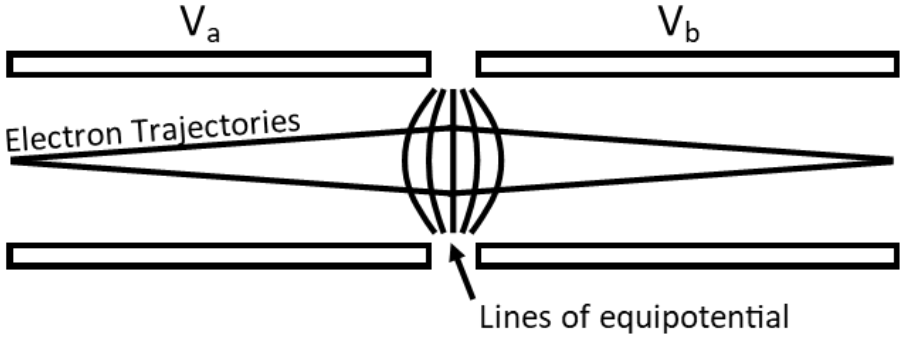

Figure 4.3: Trajectories of electrons passing through 2 cylindrical electrodes in the analyser lens. The potential gradient in the gap between the electrodes deflects the electron.

The electrons are then deflected through two hemispherical shells with a voltage applied between them. A schematic of this is shown in figure 4.4. Electrons of a particular pass energy are deflected around the shells along a semi-circular path with radius close to the mean radius of the two shells, and into a detector. A large semi-circular path is used, as the error in the pass energy is proportional to the ratio between the detector size to the radius of the passing electrons, and therefore the energy resolution ΔE of the instrument is improved with a larger radius. Specifically, the relationship can be described by the following equation:

$$\Delta E = E_p(\frac{d}{2R_0}) \tag{4.2}$$

Where d is the diameter of the exit aperture, R_0 is the mean radius of the two hemispherical shells and E_p is the pass energy. There is also another term proportional to the square of the solid angle of electrons passing through the entrance aperture, but this is much smaller than the exit aperture and therefore can be neglected. The Omicron EA 125 analyser used has an R_0 value of 125 mm and the exit aperture of width 2 mm was chosen for experiments. With a pass energy setting of 10.00 eV

(for valence band spectra), the resolution of the instrument is 0.08 eV, and for a pass energy setting of 50.0 eV (for core state spectra), the instrument resolution is 0.4 eV (i.e. the resolution is 0.8

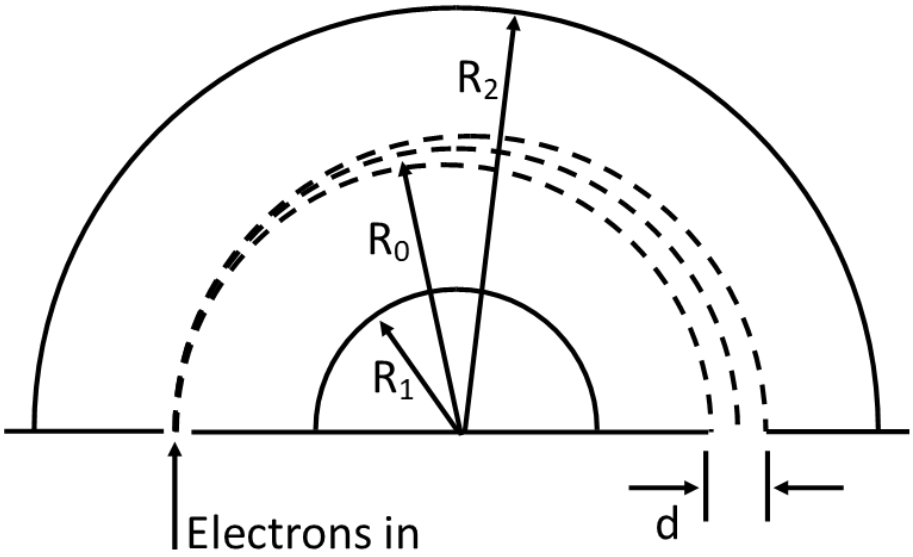

Figure 4.4: Figure showing the trajectories of electrons passing deflected around the hemispherical shells in the analyser.

The detectors used in the analyser are channeltron electron multipliers. When an electron is incident on the channeltrons, secondary electrons are generated and accelerated further into the detector with a voltage bias. These then progress and produce additional electrons until a cascade of 10^7 to 10^8 electrons reach the output, which produces a sufficiently large current to be detected. Since this process takes a finite amount of time, the detector has a maximum count rate which can be exceeded if the bias voltage or incident electron intensity is too high. The instrument used has 7 detector channels, which are placed at different positions in the exit plane. This multiplies the count rate by a factor of 7.

4.2.2 Ultraviolet Photoemission Spectroscopy

Ultraviolet photoemission spectroscopy (UPS) is a technique used to probe the occupied density of states in the valence band of a material's surface. The UV photons are generated with a cold cathode discharge source which operates by filling a glass capillary with He gas and then inducing breakdown by applying a high voltage (1 kV). The discharge source used generates He I α photons with an energy of 21.22

eV, which are directed at the sample under investigation. The low energy of the photons means that the core levels of the atoms in the sample material are not accessible and the spectrum is limited to the valence band region. A schematic of the photoemission process in UPS is shown in figure 4.5. The intensity spectrum of the emitted electrons at different kinetic energies will match the density of states at corresponding binding energies and therefore the spectrum provides a measurement of the density of states in the valence band.

The induced photoemission is also composed of electrons with low kinetic energy, which in turn results in a low inelastic mean free path. Therefore the "information depth" of UPS is relatively shallow as only electrons near the surface can escape and be detected. This results in UPS exhibiting high surface sensitivity, doubly so because of the especially low energy of the He I α discharge line when compared to others such as He II α (40.81 eV). However, there will still be some level of penetration in the bulk and therefore some bulk electronic states will also be probed as well as the surface states.

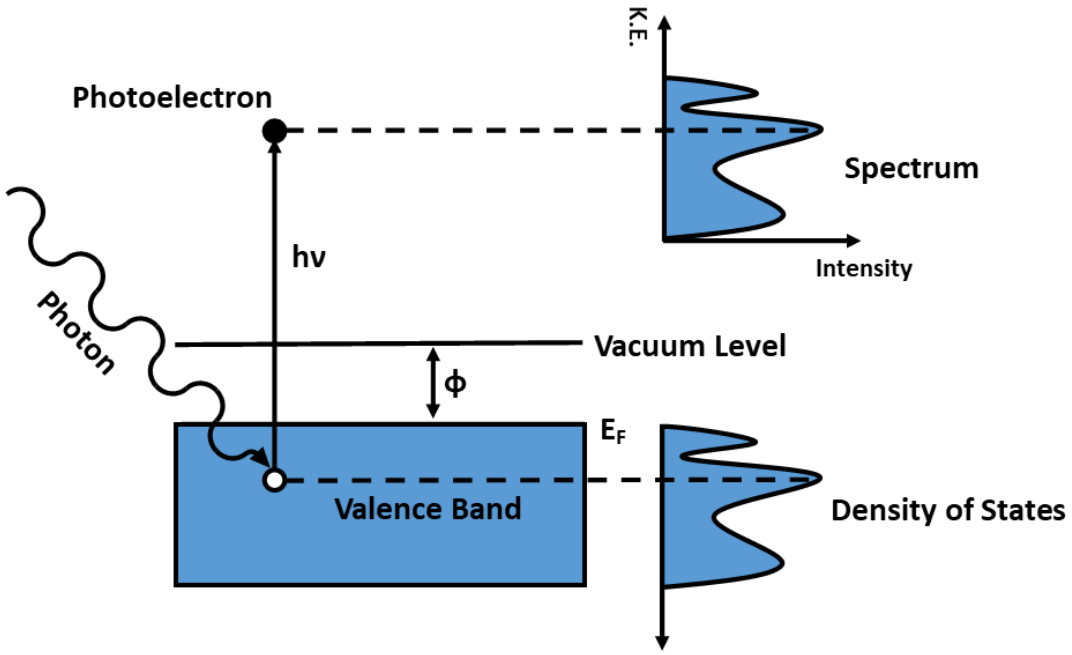

Figure 4.5: Schematic of ultraviolet photo-emission spectroscopy. The UPS spectrum gives a direct measurement of the density of states in the valence band up to a binding energy maximum dictated by the photon energy and the surface work function.

The UV photon energy used in the laboratory is close to the excitation energy of the metastable helium atoms used in MDS. This allows UPS to become a useful

complementary technique in conjunction with MDS, since the UPS and MDS spectra probe a very similar range of energies. Depending on the de-excitation mechanism of the metastable atoms (which is in turn dependent on the sample surface), the two spectra can exhibit corresponding features for comparison.

Another useful aspect of UPS is the ability to use the spectrum to measure the sample work function. The electronic work function of a material is the difference in energy between the Fermi level and the vacuum level, and is an important property for the development of devices in cases such as when valence band matching is a concern. The work function is sensitive to the surface structure and therefore this could be used to probe changes in the surface due to surface preparation procedures and deposition. UPS is able to measure the surface work function with a single spectrum by measuring the difference between the Fermi level and the low kinetic energy cut off in the spectrum and subtracting this from the total energy of the UV photon (21.22 eV). To deconvolute the sample work function from the internal work function of the analyser, we bias the sample to 15 V, and therefore raise the sample electron emission to a higher kinetic energy.

During data collection,samples are placed directly facing the analyser (-45° to the UV source. Because of the high intensity irradiation from the UV source (and therefore high intensity photoemission), the smallest circular entrance aperture is used on the analyser (1 mm diameter). This is so the channel electron multipliers are not saturated from the number of incident photoelectrons.

4.2.3 X-ray Photoemission Spectroscopy

The XPS instrument was installed on the UHV system near the beginning of this project. Unlike UPS and MDS, there was no prior experience in the research group with this technique and therefore it was necessary to dedicate much time to test its capabilities. XPS was central to much of the earlier work in this project, before the preparation chamber was added to grow samples in situ. A publication following a XPS study as a part of a collaboration will be discussed later in the chapter. Compared to UPS, more quantitative data can be obtained from XPS and details of the technique will be outlined in the following section.

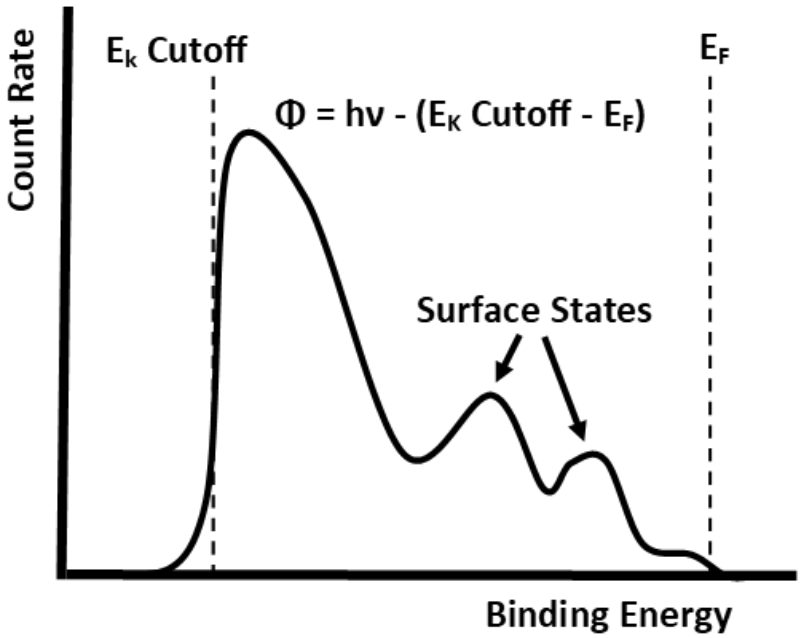

Figure 4.6: Diagram illustrating how to calculate a sample's surface work function using UPS. The spectrum depicted is obtained from a sample held at a negative voltage to isolate the sample work function from the analyser - leading to high secondary electron emission and a sharp kinetic energy cutoff. The cutoff energy is the lowest possible kinetic energy of the emitted electrons - on a unbiased sample, where the emitted electrons are not accelerated away from the surface, the kinetic energy would be zero.

Theory of XPS

Illuminating a surface with photons of higher energy will allow electrons to be liberated from more strongly bound states. X-ray photons with energies above 1 keV are used in XPS, which is used to probe the core states of atoms on a surface, as shown in figure 4.7. Unlike the valence bands probed by UPS, the atomic orbitals of core states do not overlap with their neighbours and form quantised states with distinct energies corresponding to each element. Therefore, by comparing spectra taken with known peak positions for specific elements, XPS can be used identify the composition of a surface.

Just identifying the elements present is only a small part of the capabilities of XPS. Information regarding the relative abundance of each element component of the surface can also be gleaned from the spectra. To calculate this, we can consider the variables which affect the amount of emission from a particular state, i.e. the

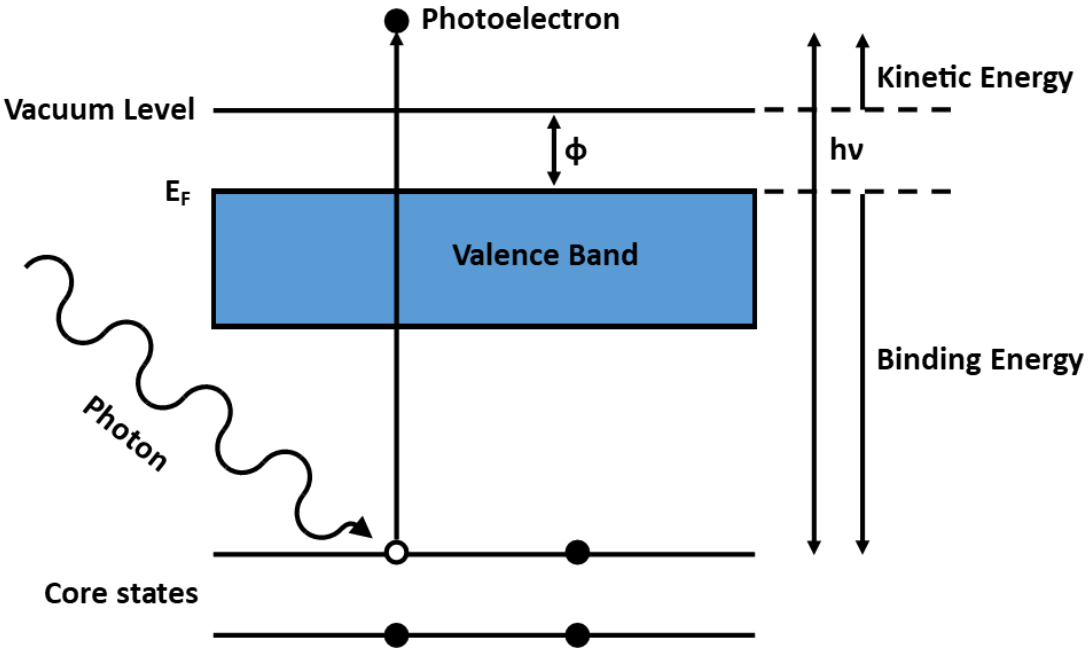

Figure 4.7: Schematic of x-ray photo-emission spectroscopy. The XPS shows peaks in emission at binding energies where core states lies in the sample.

formula for the intensity I_i of a peak i in an XPS spectrum:

$$I_i \propto N_i \sigma_i \lambda_i \tag{4.3}$$

where N_i is the average concentration of the element responsible for peak i in the sample surface; σ_i is the photoionisation cross section for the state i; and λ_i is the inelastic mean free path for the emitted electron. Other factors which may affect the intensity of detected electrons are generally constant for samples taken under the same experimental conditions, such as angle of emission, analyser transmission function and vacuum chamber pressure. Therefore XPS can measure not only the elements present, but also their relative compositions.

The inelastic mean free path (IMFP) of the electron also determines the sampling depth of the technique. The IMFP λ of an electron with a particular kinetic energy in a material and the intensity I of said electrons escaping from a depth d inside the surface in a direction normal to the surface is related by the Beer-Lambert law:

$$I = I_0 e^{-d/\lambda} \tag{4.4}$$

More than 95% of electrons are emitted within 3λ of the surface and this is considered the sampling depth of XPS. For most materials λ falls in the range of 1 - 3.5 nm for electron emission due to x-ray photoemission [113]. Therefore the sampling depth, or

"information depth", of XPS is approximately 3 - 10 nm, making it still a relatively surface sensitive technique, but probes more of the bulk than UPS or MDS.

The binding energy of the core states of an atom is affected by electrostatic shielding of the nuclear charge, which is contributed to by all electrons, including those in the valence band. Addition and subtraction of electrons due to bonding will alter this shielding effect and cause a change in the binding energy. More specifically, removal of electrons (oxidation) will lead to less shielding and increase in the binding energy, and vice versa. Therefore, the bonding environment for elements present in a sample can also be inferred from shifts in the XPS spectrum.

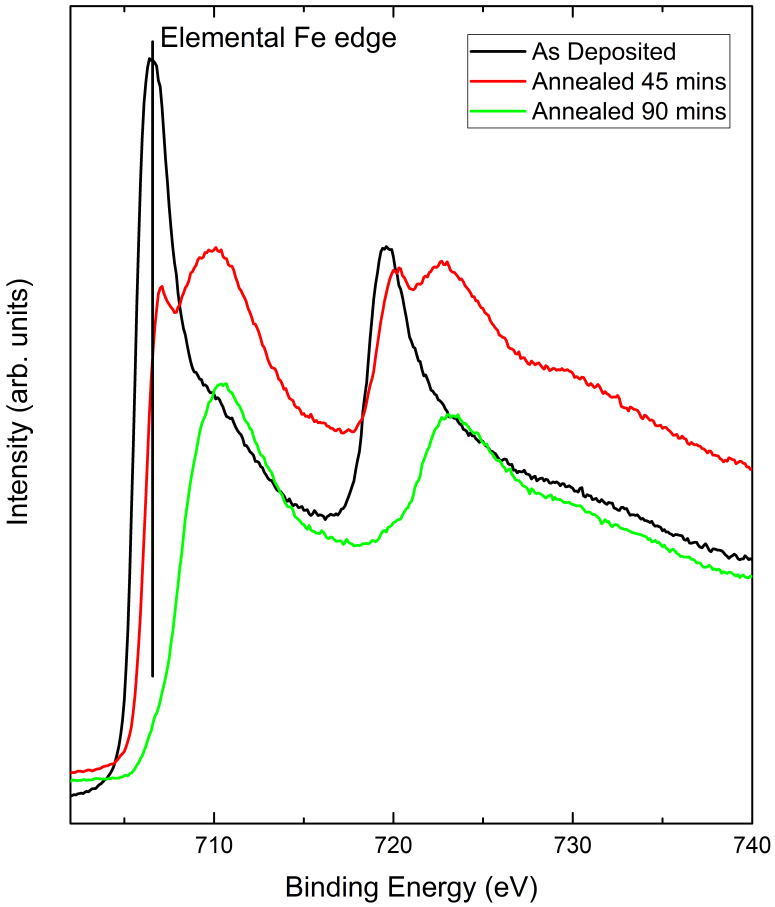

Figure 4.8: XPS spectra of an Fe-rich iron oxide film as desposited and after annealing in oxygen. The sharp edge at 706.5 eV associated with elemental iron disappears after the surface is oxidised and the spectrum moves to a higher binding energy.

An example of this is shown in figure 4.8. The black line is the XPS of the Fe $2p$ peak for a Fe-rich iron oxide film. The red and green lines are the XPS spectra for the same sample after successive annealing in oxygen. The as-deposited spectrum shows a sharp peak at around 706.5 eV, which is associated with elemental Fe. As the sample is oxidised, there is a loss of electrons in the Fe atoms and the shielding reduces, increasing the binding energy. The spectrum after oxygen roasts therefore loses this elemental Fe feature as Fe atoms becomes oxidised and the core state becomes dominated by a broad feature at around 710 eV.

The above features described are all associated with the initial state of atoms on the sample prior to the emission of an electron. Emission is also affected by the response of the atom to the creation of the hole/photoelectron and these "final state" effects lead to extra features on the spectrum intrinsic to the photoemission process. Extrinsic losses such as energy loss during transport and plasmon excitation can also cause changes in the spectrum. These effects do not directly correspond to the structure and bonding configuration of sample (although information can nevertheless still be garnered from these features), and therefore will not be covered at length here. Theory behind them are well understood and, if interested, the reader is directed to textbooks for further reading, such as the one by Feuerbacher, Fitton and Willis [35], from which the author has gleaned much knowledge.

X-Ray Sources and the Monochromator

Two x-ray sources are fitted on the analysis chamber. The first is a dual anode x-ray source, fitted with two x-ray anodes capable of generating x-ray radiation with frequency corresponding to the Mg Kα and Al Kα spectral lines with photon energies equal to 1253.6 ($\pm$0.70) and 1486.6 ($\pm$0.85) eV respectively (wavelengths of 0.9890$\pm$0.0002 and 0.8340$\pm$0.0002 nm). These particularly wavelengths have suitable energies for inducing core level emission whilst also having relatively low line widths. The anodes consist of a thin layer of Mg and Al placed side by side at the end of a conducting substrate rod. A thoriated tungsten filament is placed in front of each anode. During operation, a current flows through the filament, which heats up and emits electrons. These electrons are then accelerated towards the nearest anode by a high voltage. The irradiation of the anode material with electrons of sufficient energy generates x-rays at the characteristic frequency, which

travels to the sample through an aluminium window, used to reduce contamination and contain the electric fields in the source. The dual anode source is mounted on a linear drive and can be placed very close to the sample, allowing a high count rate. However, this also exposes the sample to the full range of radiation, including high energy Bremsstrahlung rays which are potentially destructive for the sample. Another issue is the presence of both Kα_1 and Kα_2 (and other) spectral lines, which causes a broadening of the spectral resolution with extra features. Therefore, the dual anode source was mostly only used before the monochromated source was fitted.

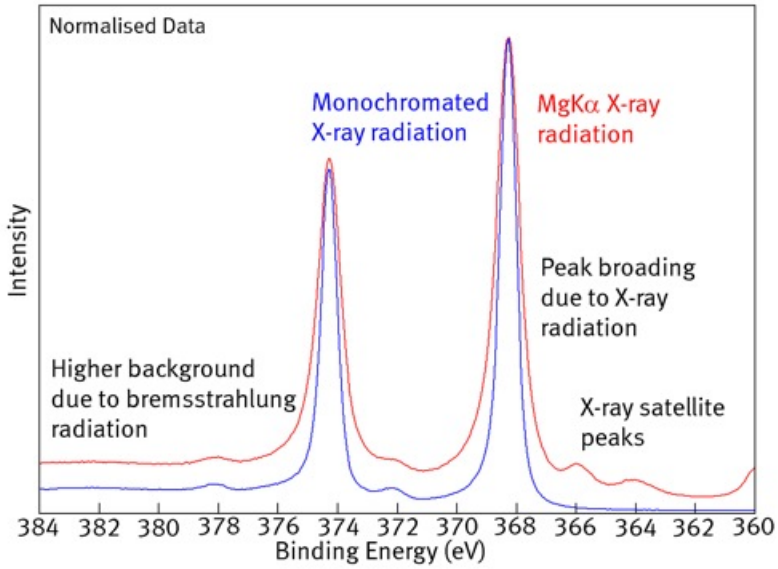

Figure 4.9: XPS spectra of the Ag 3d peak taken from [114] showing the improvements due to a x-ray monochromator on the spectrum obtained.

The x-ray source for monochromated XPS generates x-rays in much the same way as the dual anode source. An aluminium anode is used for this purpose, as the wavelength corresponding to the lattice spacing of quartz crystal acting as a "grating" in the monochromator. The x-ray radiation is directed towards a quartz crystal back plane and is diffracted, with constructive interference occurring according to Bragg's law:

$$n\lambda = 2dsin(\theta) \tag{4.5}$$

Where lambda is the wavelength of the x-ray, d is the crystal spacing and theta is the angle between the incident ray and the plane, or the Bragg angle. This constrains the wavelength of diffracted radiation using the crystal spacing in the quartz crystal, which matches the Al Kα spectral line [115]. Only radiation in a

narrow band can satisfy this condition and the line width of the x-ray is reduced to 0.25 eV, improving the energy resolution. This also eliminates other unwanted radiation such as ghost lines, Al Kβ and Bremsstrahlung. The quartz crystal is also curved to better focus the diffracted x-rays to a smaller spot on the sample, allowing better control of photoemission source on smaller samples. The apparatus at York was calibrated (by moving the quartz crystal using dials on the monochromator and seeing the effect on the fluorescent sample) such that a spot of size < 5 mm was achieved at the sample position. A graph showing how these improvements manifest on the spectrum is shown in figure 4.9.

4.3 XPS Study of Graphene Oxide

A good example of an in-depth XPS study demonstrating the capabilities of the technique was carried out in collaboration with the group of Rahul Nair from the University of Manchester. The data contributed to one publication [38] and another pending review at the time of writing [116]. The study revolved around the permeation and molecular sieving properties of graphene oxide (GO) films and XPS was used to probe the surface stochiometry and bonding environments present in graphene oxide flakes prepared under different conditions.

4.3.1 Permeation of Organic Solvents Through Graphene Oxide Membranes

Efficient separation processes utilising partially permeable membranes have important applications such as water purification and green energy [117, 118]. Graphene oxide has been shown to possess the potential to develop into a useful material for these applications [119, 120], and has displayed useful properties such as tunable pore size [121] and ultimate permeance [122]. It is also a fairly robust material and therefore practical for industrial use [119, 120].

While graphene oxide has been shown to be highly permeable to water, previous literature have reported the membrane to be impermeable to organic solutions [123, 119], thus limiting its use in pharmaceutical applications [124]. The purpose of this particular study by Nair and colleagues aimed to create a GO laminate which

was permeable to organic solvents, and this was achieved with ultrathin, highly laminated membranes where organic filtration occurred through capillaries forming in the film [38]. The XPS apparatus here at York was used to study differences in the chemistry of the sample through detailed deconvolution of the C 1s peak. This supplied knowledge of the changes in the bonding environments, which allows a better understanding of the mechanisms that facilitated the improved permeability.

XPS Spectra

The first set of XPS studies performed involved comparisons between graphene oxide films prepared in different ways - a conventional GO film (CGO) and a highly laminated film (HLGO). The detailed preparation methods can be found in [38]. The main difference in the preparation is that the HLGO flakes underwent a 3 minute ultrasonic exfoliation with a stepwise separation method, while the CGO flakes were exfoliated for 24 hours in the ultrasonic bath. The HLGO exhibits a superior laminar structure [38] with better aligned layers and a stronger interlayer interaction [125]. This would also serve to reduce the wrinkles found in CGO [119], and therefore improve the formation of 2D capillaries in the membrane.

Samples were provided as flakes of varying sizes. These were cut down to an appropriate size (approximately 8×8 mm in size) and stuck to a 10×10 mm piece of Ta foil using an Ag epoxy adhesive. The Ag base adhesive is both vacuum compatible and conducting, reducing charging effects in the sample. The Ta foil holding the sample is then affixed into a modified Omicron sample plate using clips spot welded onto the plate. The Ag epoxy is allowed to fully dry (>4 hours) before the sample is transferred into the UHV system.

Survey scans were first taken to ensure that the sample only has carbon and oxygen present, mainly to check that the Ag epoxy had not migrated onto the surface (not shown). The C 1s spectra taken for the CGO and HLGO are shown in figure 4.10. The peak was deconvoluted into four components corresponding to the main bonding environments found in graphene oxide: C-C (284.5-284.8 eV), C-O (285.2-285.4 eV), C=O (286.8-287.2 eV), and C(=O)-(OH) (288.1-289.1 eV) [123]. The areas underneath the fitted peaks were used to calculate the proportion of carbon in each bonding environment and from that C:O ratios in the membranes. This found a C:O ratio of 3.3±0.3 and 3.6±0.3 for the HLGO and CGO respectively - the two

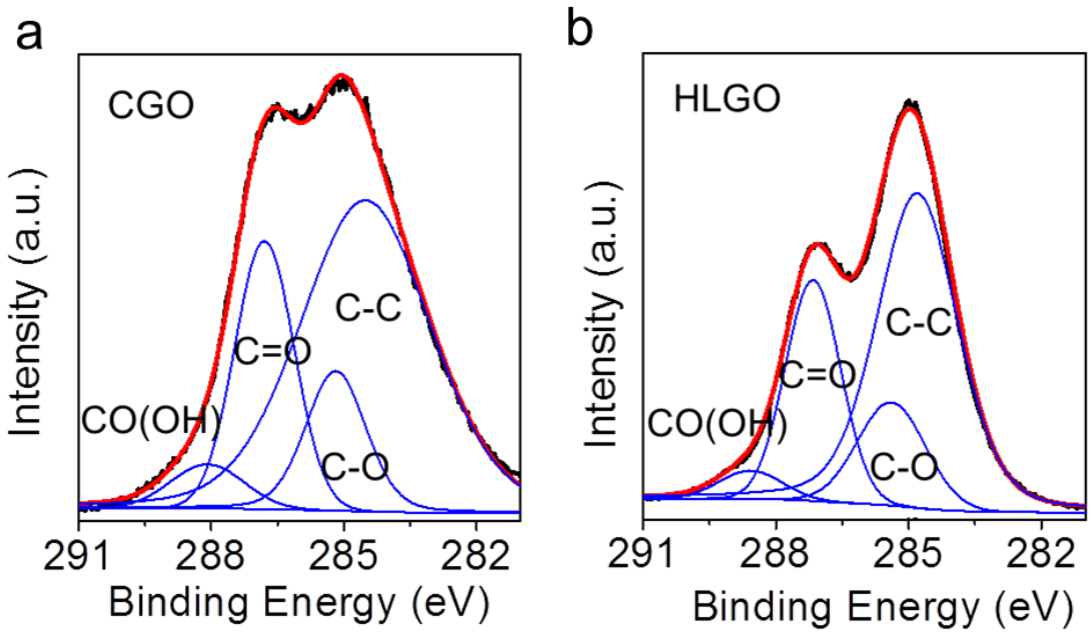

Figure 4.10: C 1s XPS spectra for CGO (a) and HLGO (b) samples, taken from [38]. There is a clear change in the bonding environment due to different preparation methods, even though the overall change in the O:C ratio was largely unchanged.

are the same within error. This gave an oxygen ratio of 23±2% and 22±2% for the two films and is consistent with previous findings that the exfoliation time is not correlated with the oxygen content [126]. There is, however, a shift in the relative proportions of the carbon environments. For the CGO, the C-C, C-O, C=O and CO(OH) have areas of 61±3%, 13±2%, 22±2% and 4±1% respectively; and for the HLGO, the C-C, C-O, C=O and CO(OH) have areas of 58±3%, 14±2%, 25±2% and 3±1% respectively. The difference in proportions are within error - there is no difference between the two, which is expected as the bonding configurations do not change much. However, there is a visible change in the overall shape of the C 1s peak and this is indicative of a difference in the width of the peaks (for each carbon bonding environment) and their positions. This can be attributed to the difference in the interlayer interactions between the HLGO and CGO causing minute changes in the energies of the core levels of the carbon atoms, while the bonding configurations remain the same.

4.3.2 Electrically Controlled Water Permeation

The second study performed in collaboration with Nair and colleagues involved research into the reversible control of water permeability through graphene oxide membranes. This naturally has applications to life sciences and is a significant boost to the versatility of inorganic membranes [116]. Previous attempts to modulate the water permeation properties of membranes involved varying conditions such as the pH and temperature to induce a physical response in the structure [127, 128]. Manipulation of permeation through electrical fields is more tricky, but allow faster response times and much easier integration into control systems. The use of graphene oxide for this purpose was studied and XPS was again used to check the bonding environment of the carbon atoms, this time between a pristine GO flake and one treated with an electric field, in order to check that changes in the GO flake are reversible and cause little to no chemical changes. This was contrasted to the effect of heat treating, which also affects the water permeability, but at the cost of causing irreversible chemical changes.

Samples supplied as flakes and prepared in the same way as described in the previous section. After taking the XPS spectrum of an as-inserted sample, the sample is heat treated at gradually increasing temperatures using the PBN heater (50, 75, 100 and 150 °C). XPS spectra were taken after each heat treatment and the C 1s peaks were deconvoluted. The peak positions used for this were: hydrogenated (sp^2) carbon (C=C/C-C/C-H, 284.6-285.1 eV), hydroxyl groups (C-OH, 285.9 eV), epoxy groups (C-O-C, 286.9 eV), carbonyl groups (C=O, 288.2 eV), and carboxyl groups (C=O(OH), 289.3 eV) according to literature [129]. An extra feature is observed in the spectra post 150 °C anneal, which was attributed to $\pi - \pi*$ shake up satellites. As before, survey scans were also taken to ensure no migration of the Ag epoxy onto the surface, which is not shown here.

C 1s XPS spectra are shown in figure 4.11, with the pristine GO spectrum on the left and the electric field treated samples on the right. The figure shows the spectra for the room temperature as inserted samples (bottom) and for the post final 150 °C anneal (top). The inset of Figure 4.11 shows the relative number of sp^2 C, C-OH, and C-O-C bonds present in each sample as calculated from the integrated spectral intensities of each peak weighted according to their stoichiometry. The amount of sp^2-bonded C is very similar for pristine GO and for GO after exposure to an electric

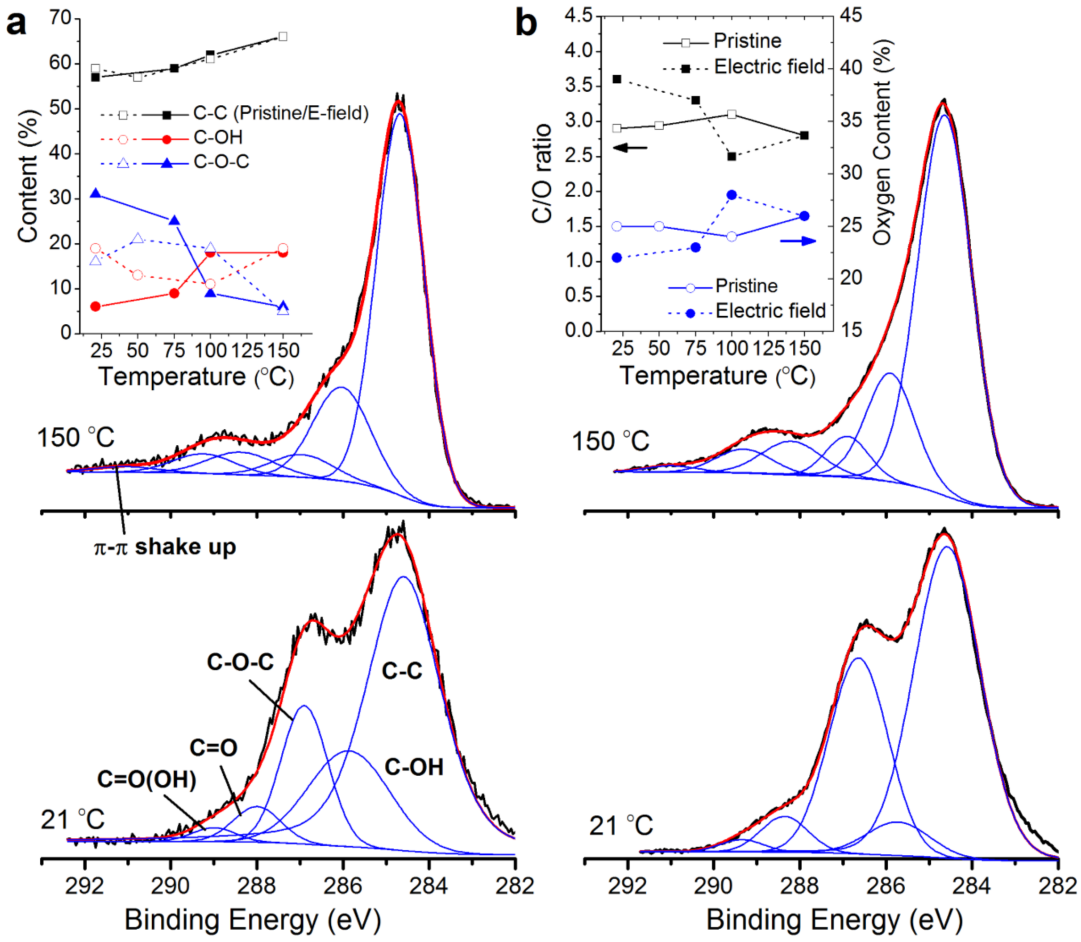

Figure 4.11: C 1s XPS spectra for pristine GO (a) and electric field treated samples (b), with the graphs for the as inserted samples at the bottom and the 150 °C annealed data at the top. The inset shows the evolution of the contribution attributed to each peak as the annealing temperature is increased.

field with both displaying a content of 57±3% at room temperature rising to 66±3% at 150 °C, the onset of thermal reduction. At 150 °C, a much greater number of proportion of sp^2 bonds are present and this corresponds to the desorption of water and would mean greater electrical conduction properties.

At room temperature, the sample exposed to an electric field has a much larger C-O-C content (31%) relative to C-OH (6%) when compared to pristine GO (16% and 19%, respectively). This suggests that the application of the electric field stimulates dehydrogenation of the C-OH bonds allowing the subsequent formation of C-O-C bonds. This in turn results in a change in chemical environment with a slight reduction in the sample, which could correspond to the formation of conduct-

ing channels in the flakes as an electric field was applied [116]. This would cause a rearrangement in the membrane but no chemical changes as drastic as heat treatment. Overall, lingering effects of the electric field remains in the graphene oxide membranes, but does not affect them as much as heat treatment up to 150 °C. The lack of a drastic change suggests that the effects of this electric field treatment may be reversible (unlike heat treatment) and therefore could potentially facilitate the control of other properties that are changed by an electric field treatment(such as permeability) through an external field.

4.4 Other instruments

Many of the instruments (other than the apparatus for electron spectroscopy) were mentioned in passing in the description of the vacuum chamber at the beginning of the chapter. However, many of these are used just as often and a few merit some extra details regarding their theory and operation, which will be covered in the following section.

4.4.1 Low Energy Electron Diffraction (LEED)

Low energy electron diffraction (LEED) is a technique used to investigate the surface structure of a material. The surface reconstruction of a sample is crucial to its properties, varies greatly depending on the stoichiometry and preparation conditions and is often characteristic of the material. Therefore LEED is another way to check the growth process of samples, which is quicker than XPS and provides complementary data to the electron spectroscopy techniques. This is advantageous as although UHV conditions slows the degradation of samples, some material surfaces, such as Si(111) and elemental metals, are highly reactively and relatively fast ways to check the sample are necessary.

LEED was first used by Davisson and Germer in 1927 to demonstrate the wave nature of electrons [130]. Electrons have a de Broglie wavelength dependent on their momentum and therefore their kinetic energy, given by the expression:

$$\lambda = \frac{h}{\sqrt{2mE_k}} \tag{4.6}$$

Electrons with kinetic energy in the range of 20 - 400 eV have wavelengths corresponding to atomic spacings, and therefore diffraction effects can occur upon an electron beam illuminating a well ordered sample similar to when light illuminates a grating of appropriate spacing. The diffraction pattern formed shows the reciprocal lattice of the sample surface. Since the penetration of these low energy electron is low, within tens of monolayers for many materials, the technique is very surface sensitive, as illustrated in the graph of penetration depth against electron energy in figure 4.12 [113].

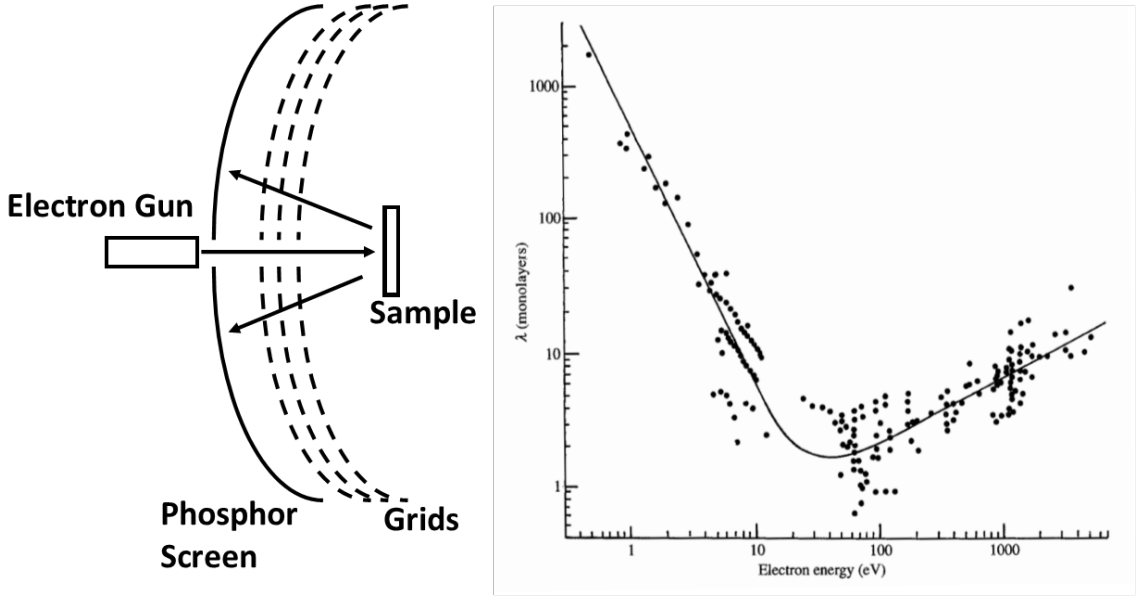

Figure 4.12: Left: a schematic of the LEED instrument. Right: Plot shown the relationship between electron penetration depth for a large number of materials. The electrons between the 10-100 eV kinetic energy range are especially surface sensitive. Graph adapted from [113]

In the LEED instrument, an electron beam is generated via thermionic emission from a thoriated tungsten filament and projected towards the sample with a relatively low kinetic energy (up to 250 eV in the SPECTALEED instrument). The beam is diffracted at the surface and some are backscattered towards a phosphor screen. The inelastically scattered electrons are screened out using a series of grids, and the elastically backscattered electrons form a diffraction pattern on the screen. A diagram illustrating the set-up is shown in figure4.12

The surface overlay structures as interpreted by the diffraction patterns are classified by Wood's notation [131]. This is valid for cases where the overlayer structure and bulk planar structure have the same symmetry; more specifically, the angles between

the lattice vectors of the surface unit cell in the bulk, $\mathbf{a}_1$ and $\mathbf{a}_2$ are equal to the angle between the same for the overlayer $\mathbf{b}_1$ and $\mathbf{b}_2$. The first part of the notation specifies to the length of the overlayer lattice vectors in terms of the bulk vectors, i.e. $\mid \mathbf{b}_1 \mid / \mid \mathbf{a}_1 \mid$ and $\mid \mathbf{b}_2 \mid / \mid \mathbf{a}_2 \mid$. For example, the Si(111) 7×7 reconstruction has $\mid \mathbf{b}_1 \mid = 7 \mid \mathbf{a}_1 \mid$ and $\mid \mathbf{b}_2 \mid = 7 \mid \mathbf{a}_2 \mid$. Rotations in the overlay cell relative to the bulk are specified after the length notation. For example, for the $Fe_3O_4(001)$ surface, the reconstruction is (2×2)R45°, signifying a rotation in the surface unit cell of 45° from the bulk (as well as an increase in the size).

4.4.2 Quartz Crystal Microbalance

The deposition rate for all samples deposited was measured using the quartz crystal microbalance (QCM) in the preparation chamber. Since the quartz crystal used in the laboratory for these experiments was fresh with only a small amount of deposition (< 2

$$\Delta f = -\frac{2f_0^2}{A\sqrt{\rho_q \mu_q}}\Delta m \tag{4.7}$$

Where the change in oscillation frequency of the crystal (Δf) changes linearly with the change in deposited mass (Δm) and the constants ρ_q, μ_q and f_0 are the density and shear modulus of quartz and the resonant frequency of the crystal respectively. Since the oscillation frequency of the crystal used was >5.8 MHz and the resonant frequency is 6 MHz with zero load, the condition $\Delta f / f_0 < 0.02$ is satisfied and the Sauerbrey Equation can be used. A tooling factor was not needed as the QCM is mount just above the sample stage and can be moved into the same spot as the sample when calibrating deposition rate.

When the assumptions for the Sauerbrey equation fail, the film thickness can be calculated with the Z-match equation:

$$\frac{\Delta m}{A} = \frac{N_q \rho_q}{\pi Z f_L} arctan[Z \cdot tan(\pi \frac{f_U - f_L}{f_U})] \tag{4.8}$$

Where f_U and f_L are the unloaded and loaded frequencies, N_q is a frequency constant for AT-cut quartz (1.668×10^{12} Hz·nm). Z, also known as the Z-factor, is equal to

$\sqrt{\frac{\rho_q \mu_q}{\rho_f \mu_f}}$, where ρ_f and μ_f are the density and shear modulus of the film material respectively.

The Sycon Instruments STM-100 QCM crystal driver used is equipped with the means to calculate the deposition rate automatically. However, the deposition rate is monitored with low precision (0.1 $\mathring{A}s^{-1}$), which is unsuitable for the purpose many samples grown in the project - in these cases the growth rate is better calibrated by calculating the thickness change corresponding to a particular change in frequency.

A final point of note is that these calculations, irrespective of the method, require certain parameters, such as the material density, which may differ greatly between the bulk structure and a thin film. This is especially the case for many large molecules, where the first monolayer (and beyond) may arrange themselves in ways dissimilar to the bulk configuration. The bulk values are used in deposition rate calibration in all cases to avoid making unfounded assumptions about the adsorption characteristics - discrepancies with the actual thickness deposited are likely to arise.

4.4.3 Stern-Gerlach Analyser

The polarisation of the helium beam must be confirmed before use in SPMDS. This was done using apparatus applying the principles of the Stern-Gerlach experiment in 1922. This was a landmark experiment in quantum physics which showed that silver atoms directed through an inhomogeneous magnetic field are split into 2 beams, therefore confirming the quantisation of the direction of angular momentum. Using the same principles, we can direct the helium beam through an inhomogeneous magnetic field and expect to see the deflection of the beam according to its spin polarisation.

A Stern-Gerlach analyser was added to the system in order to assess the polarisation of the helium beam. This was added to the analysis chamber, on the opposite side to the beam line and in direct line of sight to the helium source. The apparatus was aligned such that the helium will first pass through a narrow vertical rectangular aperture upon exiting the analysis chamber. The helium atoms will then continue through a narrow rectangular flight tube of 300 mm in length, where it will be subject to a non-uniform magnetic field. This will be applied via a horseshoe magnet with magnetically soft Fe pole pieces as illustrated in figure 4.13. The inhomogeneous

magnetic field causes a splitting of the helium beam along the direction of the field gradient according to the spin of the atoms. The incoming atoms are detected via a micro-channel plate held at a potential of 3 kV. The micro-channel plate requires a working pressure of $<10^{-7}$ mbar and therefore it is housed inside a small vacuum chamber made from a CF collar piece and it is pumped via a Pfeiffer TPU 060 turbomolecular pump with a pumping speed of 56 ls^{-1}.

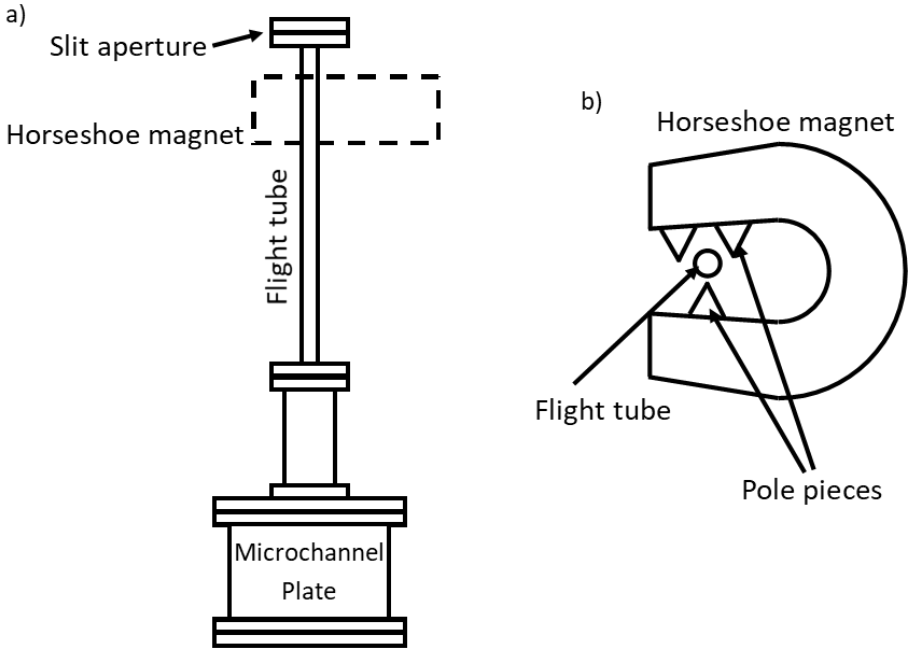

Figure 4.13: a) A schematic of the Stern-Gerlach apparatus. a) A top down view of the flight tube and chamber. b) An illustration of how an inhomogeneous mangetic field was applied using a horseshoe magnet.

The phosphorescence from the microchannel plate is captured using a computer interfaced CCD camera. This was mounted just outside the small Stern-Gerlach chamber in front of the microchannel plate. By polarising the helium beam and reversing the polarisation, a shift in the glow on the phosphor screen can be observed.

4.4.4 Controlling the Ambient Magnetic Field

When an atom with spin, such as in the case of the He 2^3S state with total spin $S = 1$, moves through a magnetic field, the spin will precess around the direction of the magnetic field and quickly align with it. The magnetic field of the earth is therefore enough to affect the direction of the spin in the metastable helium beam. In order for SPMDS to only probe the majority spin state in a sample, the

spin polarisation of the helium beam needs to align with magnetisation axis of the sample. A way to ensure this is to create a magnetic field in the vicinity of the sample, which will cancel out the earth's magnetic field as well as generating a net field (>0.1 Gauss) in the direction of the sample magnetisation. To this end, a set of coils were designed and made to fit around the UHV system. While these coils do not make Helmholtz pairs, they will nevertheless henceforth be referred to as the "Helmholtz" coils for want of a better name.

To make the "Helmholtz" coils as unintrusive as possible, they were fitted inside the bakeout frame (inside the inner channels of the KJN aluminium frame). Three pairs of coils were wound, with for each rectangular face of the frame, with sizes corresponding to the size of the frames, which is 158 × 166 × 140 cm. Due to the position of the frame, the coils roughly centre on the analysis chamber, and therefore the sample position is quite central within the coils. Since the net field applied only needs to be reasonably constant over a small vicinity around the sample when compared to the large size of the coils, the inhomogeneity of the field due to having a square coil in non-optimal positions becomes less of an issue.

However, one important property of the coils that needs to be satisfied is its ability to overcome the earth's magnetic field and apply a net field around the sample. Due to the size of the channels in the frame, the number of turns in the coil was severely limited. Insulated copper wire with diameter 0.8 mm was used, which had a maximum current rating of 5 A, but since the wires are wound in a tight bundle a maximum working current of 3 A was assumed as it displayed no significant warming. 30 loops of the coils were fitted in each face of the frame. To calculate whether the field generated is sufficient, consider the field in one of the directions acted on a pair of coils as the field generated by 8 lengths of straight wire, each applying a field:

$$B = \frac{\mu_0 I}{2\pi r} \tag{4.9}$$

Where r is the radial distance from each wire. The greatest radial distance is just under 115 mm, using this to calculate a lower bound the field generated gives a field of 1.26 Gauss. Given that the earth's magnetic field is <0.7 Gauss at the surface, the minimum field generated by the coil is enough to overcome the earth's magnetic field and apply a field >.1 Gauss in the vicinity of the sample as required.

Chapter 5

Growth and Characterisation of Fe_3O_4 Thin Films and Interfaces

5.1 Background

Magnetite, or Fe_3O_4, is the oldest mangetic material known to man. It is a naturally occurring magnet, with stable room temperature magnetic properties facilitated by a high Curie temperature and, in theory, has 100 % spin polarisation at the Fermi level in the bulk. However, even though it is a well known and well studied material, atempts to use it in spintronic devices have been met with limited success [132], which has been attributed to surface effects. The surface preparation of Fe_3O_4 has been well studied but obtaining the correct reconstruction is nevertheless still a challenge, making this an appropriate system to test the capabilities of the preparation chamber developed during this project.

5.1.1 Crystalline and Electronic Structure of Fe_3O_4

Fe_3O_4 is a metal oxide that crystalises into the Spinel structure, which is based on an FCC lattice of O^{2-} anions. In a normal Spinel structure, with a formula of AB_2O_4, the A^{2+} ions occupy 1/8 of the tetrahedral interstices and the B^{3+} ions occupy 1/2 of the octahedral interstices. In the case of Fe_3O_4, the A^{2+} cation has a large crystal field stabilisation energy [133] and the material forms what is known as an "inverse" Spinel structure, where the Fe^{2+} cations take up half of the octahedral interstitial

sites and the Fe^{3+} cations displaced by these occupy the tetrahedral interstitial sites. Many of the material's properties stem from the presence of both Fe^{2+} and Fe^{3+} in the octahedral sites [132]. The Curie temperature of Fe_3O_4 is very high, at 858 K [134]. At a temperature of 125 K the crystal transitions to a monoclinic phase, as well as a shift in the magnetic easy axis from $\langle 111 \rangle$ to $\langle 001 \rangle$. These changes are accompanied by a sudden drop in the conductivity by 2 orders of magnitude [135] and is known as the Verwey transition. The Verwey transition is a defining characteristic of magnetite and is one of the main reasons that the material is so well studied. However, since the present project is not particularly related to this or low temperature measurements, the 70+ years of literature will not be covered here and the reader is directed to a summary by Walz [136] for more details.

Though initially classified as a ferromagnet, in 1948, Néel proposed that the tetrahedral and octahedral sublattices are aligned antiferromangetically [137] and therefore the Fe^{3+} ions cancel out, leaving the Fe^{2+} responsible for the net magnetic moment. This gives a net magnetic moment of $+4\ \mu_B$ per formula unit, which is in agreement with experimental results of $4.07\ \mu_B$ [138]. The origin of this can be explained using a simple model of the d electrons in the Fe ions. A simple schematic can be found in figure 5.1. An exchange splitting of $\approx$3.5 eV is present between the majority and minority spin states [139]. The energy levels are further split in each band by the crystal field, which leads to 3 degenerate t_{2g} and 2 degenerate e_g bands. In the case of the Fe^{2+} ion, which is responsible for net magnetic moment, there are 6 electrons and the majority spin states are filled with 1 electron in the minority spin state. This results in a net moment of $4\ \mu_B$ as expected. The partially filled minority spin band is also responsible for the conduction properties in the material. For the Fe^{3+} ion, there are 5 electrons and no occupation of the minority spin states, leaving a net magnetic moment of $5\ \mu_B$.

From the electronic structure described above, there is a band gap in the majority spin states at the Fermi energy of the Fe^{2+}, and a partially occupied band that crosses the Fermi energy in the minority spin channel [140]. This property, where the material is 100% spin polarised at the Fermi level is called half metallicity. And as a predicted half-metallic ferrimagnet [141, 142], Fe_3O_4 is an attractive material for use in spintronics devices as a source of spin polarised current [143]. However, the devices made using magnetite have not displayed performance that matches a fully spin polarised electrode [144]. The origin of this has been attributed to effects

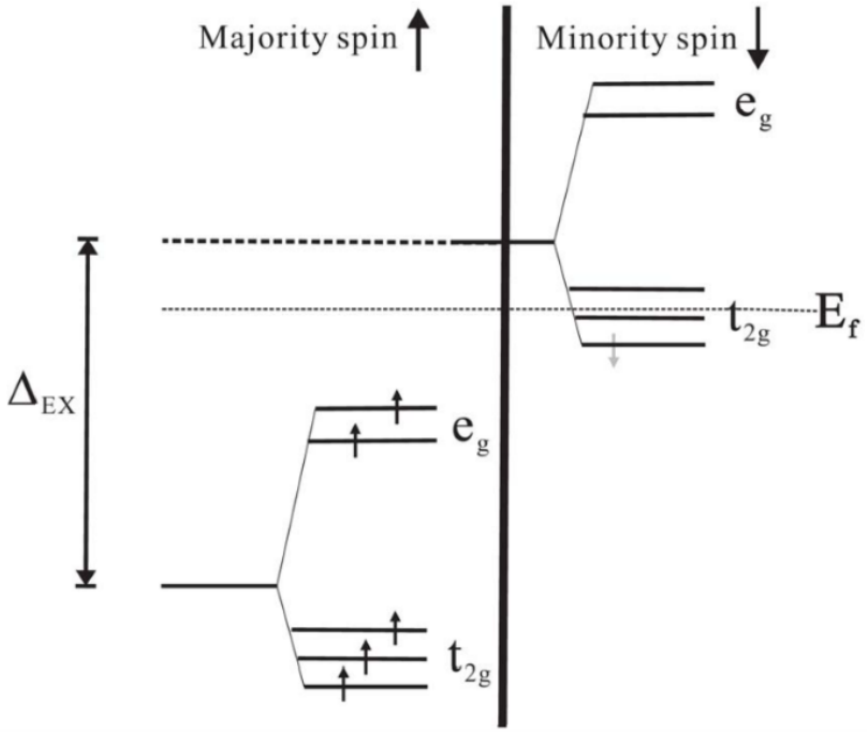

Figure 5.1: Schematic taken from [139] of the energy levels in the d state of Fe^{2+} ions in magnetite. The majority and minority states are split by the exchange energy and these are further split by the crystal field into the t_{2g} and e_g levels.

at the surface, and it has been found that the spin polarisation as measured by spin-polarised photoemission (which is relatively surface sensitive) is worst for the (100) surface (at approximately 50% compared to 80% for the (111) face) [145, 146], as distortions from the surface reconstruction stretches many layers into the bulk. However, photoemission still nevertheless penetrates the sample to an extent, cause a mixing of the bulk and surface signals. SPMDS measures have been taken of Fe_3O_4 surfaces by Pratt, Yamauchi and colleagues [147]. They found that the (111) surface was positively spin polarised rather than the strong negative polarisation expected in the bulk, and that the (100) surface exhibited a weak negative spin polarisation. This could be attributed to the difference in surface sensitivity compared to photoemission, and that the outermost layer was very different to the bulk. SPMDS studies also found an enhancement of spin polarisation from 5% to 50% when the surface was treated with atomic hydrogen by exposure to cracked hydrogen molecules in a vacuum; which was attributed to the adsorbate-induced elimination of surface dangling bonds [148]. Similar effects were also found for benzene [146] and boron [149] as well as being predicted for other group IV elements [150]. Overall, the surface

effects of the material are crucial to its properties and performance in devices. SP-MDS is an excellent tool for understanding the mechanisms at the surface and for exploring new avenues for engineering better surface properties.

5.1.2 The Fe_3O_4(100) Surface

The model of the Fe_3O_4(100) $(\sqrt{2}\times\sqrt{2})$R45° reconstruction has been developed over time in the literature. A number of early models were eventually dismissed due to not being consistent with all properties of the surface [151, 152, 153, 154]. The distorted bulk truncation (DBT) model was proposed by Pentcheva et. al. which suggests that the reconstruction originates from a lattice distortion that is coupled to the subsurface charge order [155, 156]. This model gave a good qualitative explanation for undulating rows observed in STM, and was in general agreement with LEED-IV and SXRD measurements [156, 132], which gave a better fit than other competing models at the time [155].

However, issues with the DBT model arose upon investigations into metal adatoms on Fe_3O_4. Au atoms deposited at room temperature displayed a preference for one of two available tetragonal Fe sites [157], which was not reproducible with DFT+U calculations [158]. Co atoms deposited at room temperature display a similar preference, but also quickly incorporate themselves into the lattice [159]. This indicates the existence of vacancies in the cation lattice. All surface cations are visible in STM and therefore the vacancies must be below the surface. The deposition of 1 Co atom per unit cell also causes the $(\sqrt{2}\times\sqrt{2})$R45° spots to disappear from the LEED pattern [159], suggesting a filling of the vacancy that leads to a bulk truncation-like structure.

These results led to the development of the subsurface cation vacancy (SCV) model of the surface [158]. This is consistent with experimental observations and has an improved Pendry R-factor from LEED experiments (0.125) when compared to the DBT model (0.34) [132]. The SCV model involves a rearrangement of atoms in the subsurface layers, involving an extra tetragonal site Fe in the second layer replacing two octahedral site Fe ions in the third layer. This results in the net loss of one cation per unit cell. This extra interstitial Fe ion blocks the adsorption of metal atoms on the tetragonal bulk continuation sites, which explains the preferential adsorption

displayed by Au and Co [157, 159]. The surface stoichiometry of the octahedral site Fe and O ions is maintained in the SCV model, but the structure is distorted to form the undulations seen in STM [132]. The goal of the sample growth procedure outlined later in this chapter is a surface with octahedral Fe termination and the SCV structure.

Other reconstructions of the Fe_3O_4 (100) surface are possible, dependent on the preparation conditions. An array of bright oval shaped protrusions become visible when a natural mangetite sample is argon ion sputtered and subsequently annealed in UHV [160]. These were seen in early STM images and have been resolved further into pairs of protrusions between the octahedral Fe rows [161]. This is known as the Fe dimer surface, and they form as a result of non-stoichiometry in the film after sputter anneal cycles, which preferentially remove oxygen [154]. Despite being called as such, there is no evidence of an actual Fe-Fe bond between the two Fe adatoms [132]. As the surface is reduced further, from sputter-anneal cycles without oxygen or deposition of Fe on the surface, the Fe dimer structures will become more abundant. These structures will contain an increase in the number of Fe^{2+} cations, which should be apparent in XPS. The ultimate limit for this will be an $Fe_{1-x}O$-like film [161] which is highly defective. Overall, there is a dependence of the film termination on both the growth conditions in thin films and the annealing conditions in post deposition heat treatment. Therefore, sample growth methods suitable for the UHV chamber are required to produce good quality Fe_3O_4 surfaces.

5.2 Fe_3O_4 Growth and Preparation

5.2.1 Fe_3O_4 Single Crystal

The surface preparation and characterisation of a Fe_3O_4 crystal cleaved along the (001) plane was carried out prior to the thin film growth. This served as a comparison for the growth data which can be used to check the quality of the films. The preparation method for these single crystals have been well studied and a procedure outlined in [132] will be followed in order to obtain a good octahedral Fe termination with the SCV structure.

Surface Cleaning and LEED

The surface termination of stoichiometric Fe_3O_4 (001) single crystal samples depend greatly on the in-situ preparation method used [132]. In order to prepare a clean surface, the Fe_3O_4 single crystal first underwent cycles of Ar ion sputtering followed by annealing. The Omicron ISE 10 ion sputter gun was set to operate at a beam energy of 1000 V, a focus voltage of 840 V and an emission current of 10 mA. Ar gas with a purity >99.999% was was let into the sputter gun until the pressure in the preparation chamber read 3.0×10^{-6} mbar. This yields a broad and relatively low powered ion beam profile according to the manufacturer's test sheet, and was used to reduce the adverse effect on the crystal surface as repeated sputter/anneal cycles introduces roughness over time [132, 162]. Each sputter-anneal cycle involves sputtering at the aforementioned settings for 15 minutes followed by an anneal at 600 °C for 20 minutes. Initial anneal attempts with lower annealing temperatures yielded poor LEED patterns with very weak spots, which shows little improvement over the as-inserted crystal with no pattern at all (shown in figure 5.2). 3-4 anneal-sputter cycles are needed to clean a fresh single crystal.

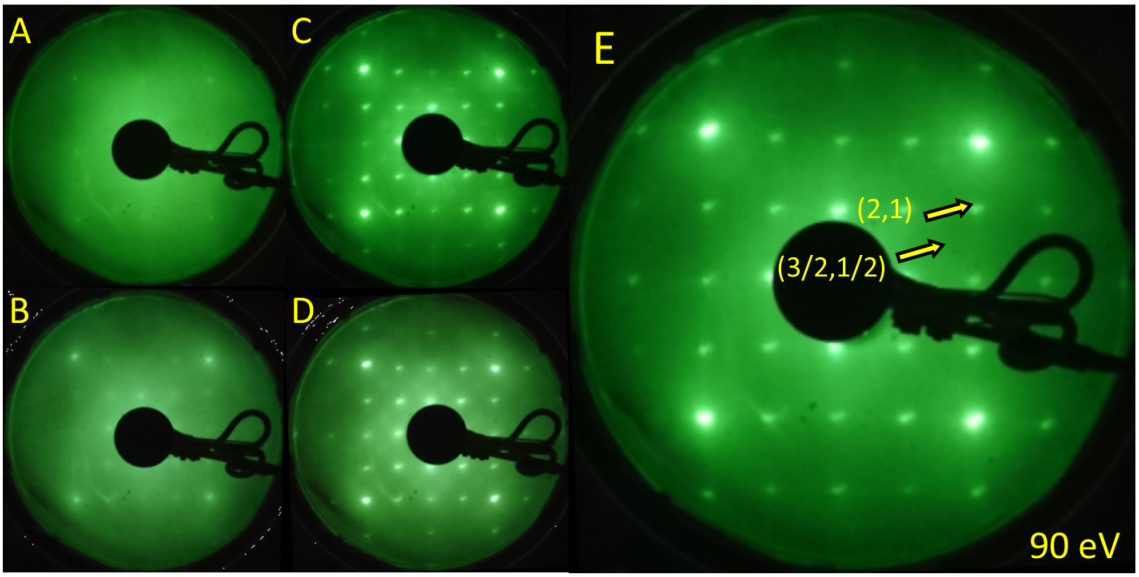

Figure 5.2: LEED patterns taken at 90 eV for various stages of Fe_3O_4 single crystal preparation. A: after sputter-anneal at 350 °C, B: after sputter-anneal at 450 °C, C: after sputter-anneal at 600 °C, D: after heating in oxygen with sample held at 500 °C and E: after oxygen roast with final annealing without oxygen at 500 °C.

The sputter-anneal cycle results in an Fe-rich termination as the Ar ion sputtering preferentially removes oxygen ions [158, 157]. The ideal subsurface cation vacancy

(SCV) structure can then be produced by a final anneal in oxygen to oxidise the reduced surface [162]. The oxygen doser was advanced to within 1 cm of the sample for this and oxygen was introduced to the chamber until the chamber pressure read 5×10^{-8} mbar, which yields a higher local pressure around 1×10^{-6} mbar needed for the oxygen anneal as stated in the literature [132]. The sample was held at 500 °C for the oxygen anneal. In order to obtain the optimal surface reconstruction, an extra 15 minute anneal at 500 °C was added at the end in accordance to the literature [146], although the effect is not clear in the LEED patterns obtained. This yielded a LEED pattern where the $(\sqrt{2}\times\sqrt{2})$R45° spots are rather weak (figure 5.2, which suggests a reduced surface where the cation vacancies are filled[132], but the overall LEED pattern is quite clear.

Spectroscopy Data

XPS, UPS and MDS spectra were taken at several points during the preparation of the Fe_3O_4 single crystal surface. XPS scans over a large binding energy range (1000 to 0 eV) were taken first. These "survey scans" on the sample are used to check that any adventitious carbon on the surface of the as-inserted sample is been cleaned away with the sputter-anneal cycle. An eradication of the C 1s peak was observed (figure 5.3), along with an overall increase in intensity for the Fe 2p and O 1s peaks as the surface contamination layer is removed.

XPS provides a further check of whether the SCV structure has been obtained by comparing the relative magnitude of the contributions from the Fe^{2+} and Fe^{3+} ions to the spectrum. The reduced Fe "dimer" structure described in section 5.1.2 has a greater proportion of Fe^{2+} ions near the surface, and the corresponding features in the XPS spectrum are enhanced. The XPS spectra in figure 5.4 for the Fe 2p peaks show a visible increase in intensity for the Fe^{2+} satellite feature at a binding energy of 716 eV for the sample post sputter-anneal cycles when compared to the as-inserted crystal; and a decrease in the satellite peak for Fe^{3+} ions at 718.5 eV. The as-inserted sample is expected to have more Fe^{3+} ions as the surface is heavily oxidised from being exposed to air for a prolonged period of time. The shake-up satellites are used to distinguish the different surfaces as the changes are much more pronounced than those for the Fe^{2+} and Fe^{3+} peaks at 709 and 711.4 eV. The spectrum for the sample after the final oxygen anneal shows a decrease in the Fe^{2+} shake-up satellite

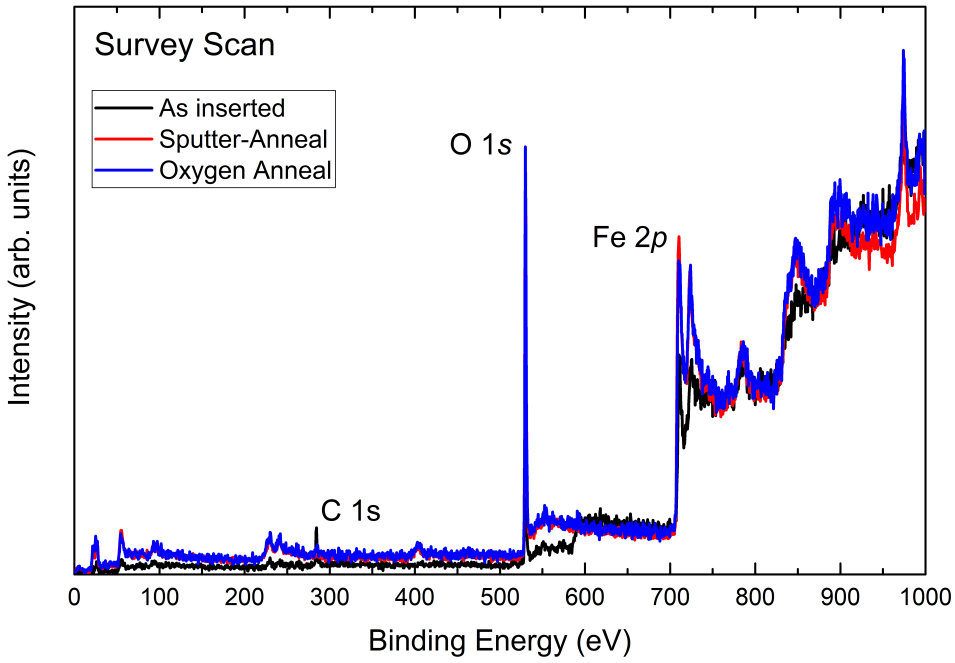

Figure 5.3: XPS survey spectra over a binding energy range of 0-1000 eV. The C 1s peak disappears after the sputter-anneal cycles and the Fe 2p and O 1s peaks increase in intensity.

as expected after the surface is oxidised. The SCV structure has been shown to be Fe^{3+} rich at the surface by angular resolved XPS measurements [158], as the Fe^{3+} satellite feature is enhanced when spectra are taken from emission at glancing angles to the sample surface. The spectrum taken after the oxygen anneal agrees with the spectrum for the SCV structure taken at 45°, where the contributions from the Fe^{2+} and Fe^{3+} features form a relatively symmetric region between the Fe $2p_{1/2}$ and Fe $2p_{3/2}$ peaks.

XPS spectra for the oxygen $1s$ peak were also taken at the same points, also shown in figure 5.4. Although the oxygen peaks are very similar in shape before and after the oxygen anneal, there is a small but perceptible shift in the binding energy to a slightly higher energy after the anneal, which also been seen in the literature [132].

UPS and MDS spectra were taken after sputter-anneal cycles, initial oxygen anneal and the final preparation step figure 5.5. Spectra were not taken for the as-inserted samples as the sample surface were likely too contaminated before cleaning to obtain a reasonable spectrum. The UPS spectra taken are very similar, peaking at 4.8 eV

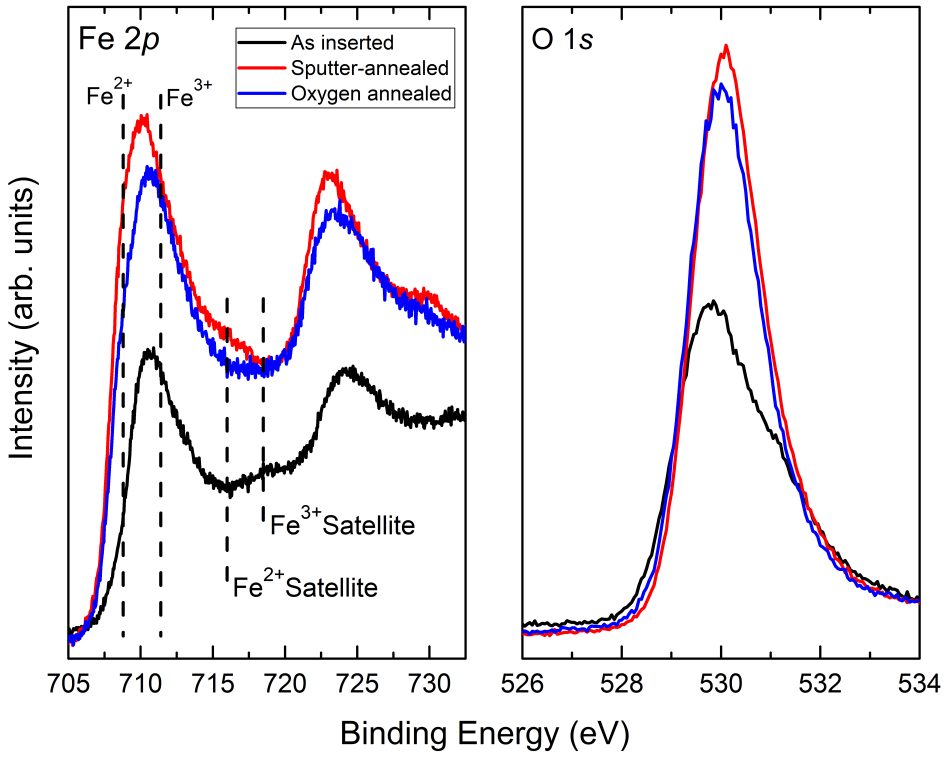

Figure 5.4: XPS spectra for the Fe 2p (left) and O 1s (right) peaks for the as-inserted sample, the sample post sputter-anneal cycles and after the final oxygen roast. The increase and decrease in relative contributions from the Fe^{2+} and Fe^{3+} satellite features suggests the formation of a Fe-rich termination prior to annealing in oxygen. A small shift is visible in the oxygen spectra.

below the Fermi energy and a broad feature is visible at 2.8 eV with very weak Auger features at approximately 10.5 eV and 12.5 eV. These agree well with Fe_3O_4 UPS spectra in the literature [163]. The one clear difference between the spectra is for the post anneal sample, the Fermi Edge is sharper than the later spectra, which is also indicative of an Fe rich surface, where there are more Fe $3d$ band electrons present near the Fermi energy.

The MDS spectral features (also found in 5.5) are present at kinetic energies of 7.0 eV, 9.0 eV, 14.2 eV and 16.0 eV. Comparing these to the UPS peaks, the MDS peaks at kinetic energies of 16.0 and 14.2 eV correspond to the UPS peaks at 2.8 eV and 4.8 eV below the Fermi level; and the MDS peaks at kinetic energies of 9.0 eV and 7.0 eV correspond to the two UPS peaks at 10.5 eV and 12.5 eV below the Fermi level. While it is difficult to pinpoint the exact contributions, there is a very clear

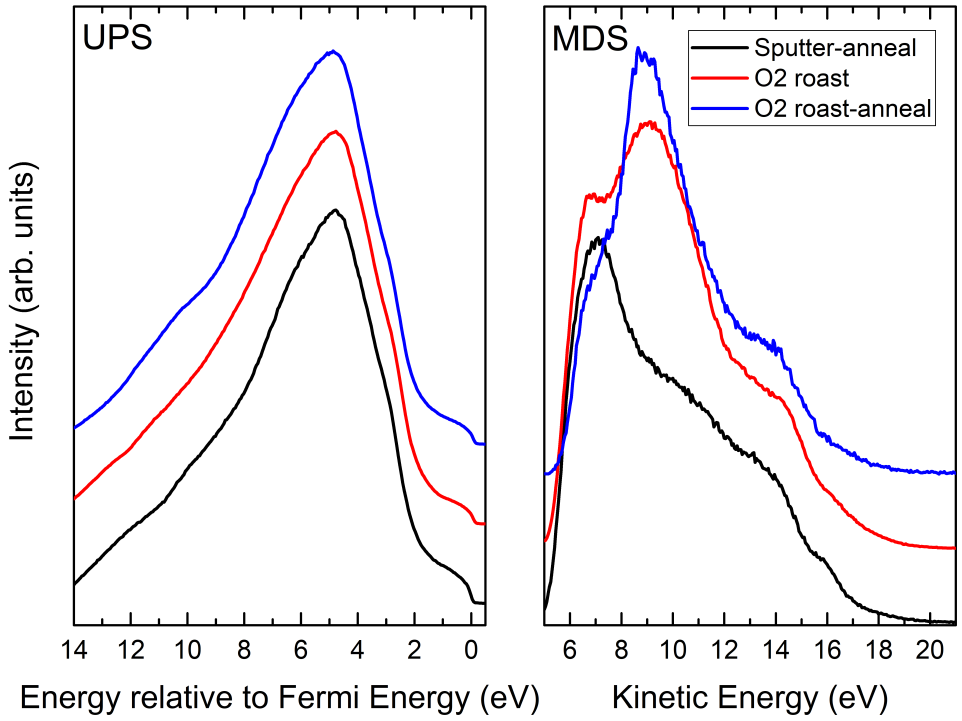

Figure 5.5: UPS and MDS spectra for the Fe_3O_4 Single Crystal at various stages of sample preparation. UPS spectra shapes are all very similar, with minute changes, but the MDS spectrum shows very prominent changes at each step in the features at 7 and 9 eV.

change from a dominant peak at 7.0 eV for the sputter-annealed surface to a more intense peak at 9.0 eV for the oxygen-annealed and final surfaces. This presents an interesting contrast to the UPS spectrum, where the features are not very sensitive to the difference in the Fe "dimer" and the SCV terminations. Therefore the MDS spectrum of a prepared Fe_3O_4 surface could be used to further check for subtle differences in the surface preparation.

However, the presence of features at all is a point of concern. Since the de-excitation mechanism on the Fe_3O_4 surface should be the two electron process of resonance ionisation and Auger neutralisation, the spectrum will be a convolution of the electronic states of the two electrons involved in the process. This should lead to very broadened and weakened features in the Fe_3O_4 spectrum [146], whereas the most prominent feature at 14.2 eV is still quite clear. This could be an indication of some contribution of the Auger de-excitation mechanism, which suggests that the

surface is more insulating. This could result from issues with the stoichiometry at the surface as well as defects. The SCV structure is terminated with a layer of octahedral site Fe cations, with a mix of 2+ and 3+ charge. Incorrect termination and increased oxidation could reduce the proportion of 2+ cations which are responsible for conduction.

Sputter-anneal-oxygen roast cycles have helped to clean the surface, which has affected the photoemission data. But the MDS could indicate that the surface may not be as pristine as possible (and is supported by the LEED pattern), which may stem from the fact that the crystal is not cleaved inside the vacuum, but inserted into the UHV system and then cleaned, and therefore has been exposed to heavy contamination (such as carbon particulates and oxygen in the air) and has a less controlled history than films grown in-situ.

5.2.2 Fe_3O_4 on MgO (001)

Growth

A co-deposition method for growth of Fe_3O_4 on MgO(001) substrates was also used to prepare a magnetic surface on top of which organic molecules could be grown. This has an advantage over Fe_3O_4 single crystals as the repeated cleaning of single crystal samples can cause surface roughness and the growth of Fe_2O_3 regions from dislocations [132], therefore the use of newly grown samples eliminates the effects of the sample history on the properties of the organic-ferromagnetic interface. Therefore, the experiments described later in this chapter were all performed on samples using thin film Fe_3O_4 grown in-situ. The analysis of the single crystal was still a necessary step, however, to verify the results of surface preparation steps taken for the thin film; to ensure that clean, stoichiometric Fe_3O_4 samples were grown to a satisfactory standard.

MgO (001) was chosen as its lattice constant (0.42 nm) is almost exactly half of that of Fe_3O_4 (0.84 nm). This allows smooth epitaxial growth in the Frank-van der Merwe (FM) mode. However, because the Fe_3O_4 growth is equally as likely to nucleate on sites with integer or half integer lattice constant lengths apart, domains form as the film covers the surface, which greatly affects its magnetic properties [132]. MgO is also an insulating material, and given that many of the techniques used to probe

the sample involves the bombardment or loss of electrons, charging effects on the data become an issue. This problem was alleviated by affixing the sample onto the OMICRON sample plates via a firm conducting contact on the top surface, which will form a path to ground for the magnetic film, when the conducting Fe_3O_4 film is deposited on both the substrate and the contact. Although there are issues with its use, MgO is nevertheless still a prime substrate candidate for the preparation of a clean Fe_3O_4 $(\sqrt{2} \times \sqrt{2})R45^\circ$ surface as the preparation of magnetite films on the substrate is relatively simple and reliable.

MgO(001) substrates measuring 10 × 10 mm were affixed onto Omicron sample plates for e-beam heating, where a hole in the centre of the plate is present at the sample location (such that the e-beam can reach the sample being heated more directly). The MgO substrate can then be cleaned in-situ by an oxygen anneal. The oxygen doser is advanced to within 1 cm of the sample and O_2 gas allowed into the chamber until the chamber pressure reads 5×10^{-8} mbar. The sample is then heated to 750 °C for 45 minutes to obtain a clean surface. The surface is then checked with LEED (figure 5.6). Unfortunately, as the MgO surface is insulating, any attempts to verify that all residues of carbon had disappeared from the sample with in-situ XPS shows unmanageable amounts of charging effects and the results are entirely inconclusive for their purpose. An electron gun to neutralise the sample during the process would be able to help, but nothing was available on hand to allow this.

Fe_3O_4 is then grown on the MgO substrate via co-deposition, or reactive sputtering. This is done through sputtering Fe onto the sample while exposing the sample to oxygen. An oxygen pressure of 1×10^{-7} mbar is required and the oxygen doser was advanced to within 1 cm of the sample to allow a high local pressure. Iron was deposited using an Omicron EFM3 source. The deposition rate of iron was calibrated to 1 $\text{Å}\text{min}^{-1}$ using a QCM and the rate was maintained by intermittently advancing the iron rod to keep a constant sample flux reading on the source controller. The deposition rate was checked mid-way and at the end with the QCM to ensure that it had stayed constant. 90-minute depositions were used to grow approximately 13.7 nm of Fe_3O_4, accounting for the increase of film thickness per unit mass of iron between Fe_3O_4 from pure Fe due to a lower density (5.17 g/cm^3 when compared to 7.87 g/cm^3 of iron) and the addition of oxygen atoms. Sample is held at 350 °C throughout the deposition procedure, which was chosen as the surface reconstruction is unstable with prolonged exposure above this temperature [132].

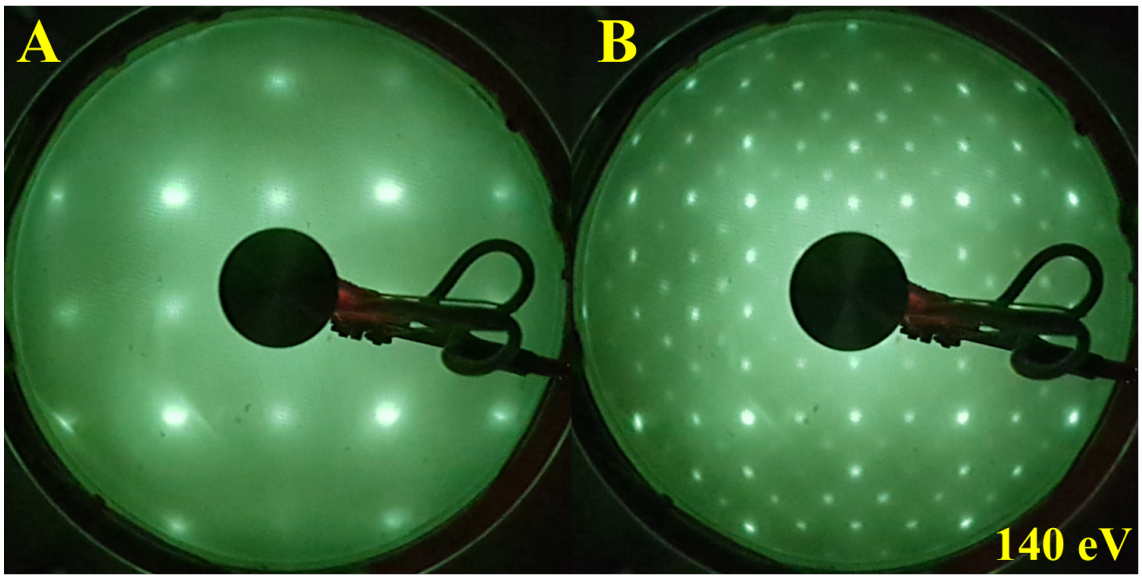

Figure 5.6: LEED images of the cleaned MgO surface (A) and the deposited Fe_3O_4 film (B) after annealing in oxygen. The $\sqrt{2} \times \sqrt{2}$ spots are clearly visible for the Fe_3O_4 film, and is much clearer than that of the single crystal. A higher LEED energy was required to view the LEED pattern compared to the single crystal, as charging effects due to the insulating substrate affected the LEED pattern.

Spectroscopy Data

XPS spectra taken immediately after deposition show an iron-rich surface, with a pronounced Fe 2^+ feature in the Fe $2p$ core peak, including an indistinct iron feature at a binding energy of approximately 706 eV. The LEED pattern is also quite poor, with quite diffuse spots. This was rectified by further annealing in oxygen at 350 °C for 45 minutes. Clear improvements show after anneal, with the $(\sqrt{2}\times\sqrt{2})$R45° spots becoming more visible (figure 5.6). In the XPS, the Fe edge disappears entirely and the balance of the Fe 2^+ and Fe 3^+ peaks become similar to that of the magnetite single crystal. However, the overall shape of the spectrum between the Fe $2p$ 1/2 and Fe $2p$ 3/2 peaks is a little more similar to that of the Fe "dimer" structure than the SCV, suggesting that even after annealing, the surface still has a relatively Fe rich termination when compared to the single crystal samples, albeit the difference is minor. A comparison of the Fe $2p$ XPS spectra with that of the single crystal can be found in figure 5.7

While the issue of an initial iron-rich surface could be taken as an indication that the deposition rate of iron was set too high relative to the oxygen pressure (or the tem-

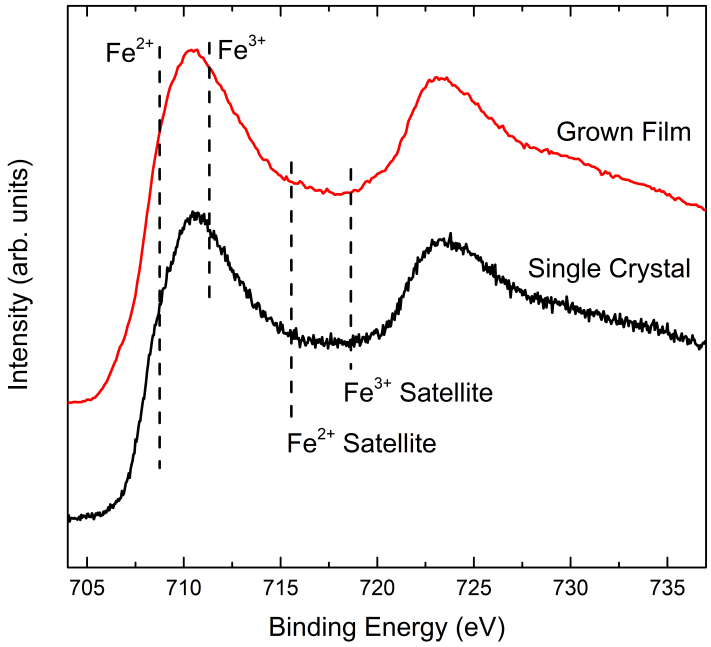

Figure 5.7: A comparison of the Fe 2p XPS spectra for the deposited Fe_3O_4 film and the single crystal. The spectra are largely similar, with a slight shift in the weighting of the 2+ and 3+ satellites, signifying a small change in the stoichiometry.

perature), further samples prepared with a considerably lower iron deposition rate still showed a similar iron-rich spectrum immediately after the deposition (though the effect is less pronounced). The final LEED images and XPS spectra can be taken as a good indication of a well prepared Fe_3O_4 $(\sqrt{2} \times \sqrt{2})$R45° surface. In fact, the $\sqrt{2} \times \sqrt{2}$ spots in the LEED are much more visible than those from the single crystal, indicating a surface reconstruction that is more in line with the SCV reconstruction described earlier, which is an advantage of the sample being prepared in-situ.

UPS and MDS spectra comparing the Fe_3O_4 film to the single crystal are displayed in figure 5.8. There are visible differences in both. The UPS spectrum for the film shows a large peak consisting of two features at 4.5 and 5.5 eV from E_F, with the stronger feature at 5.5 eV. A very weak features is seen at approximately 2.4 - 2.8 eV. The positions of these are not too far removed from those of the single crystal spectrum, but there is a shift in the relative intensities of these peaks. The peak at 4.5 eV is stronger than the one at 5.5 eV in the single crystal but is vice versa in the film and the feature at 2.8 eV is much stronger in the single crystal. There is

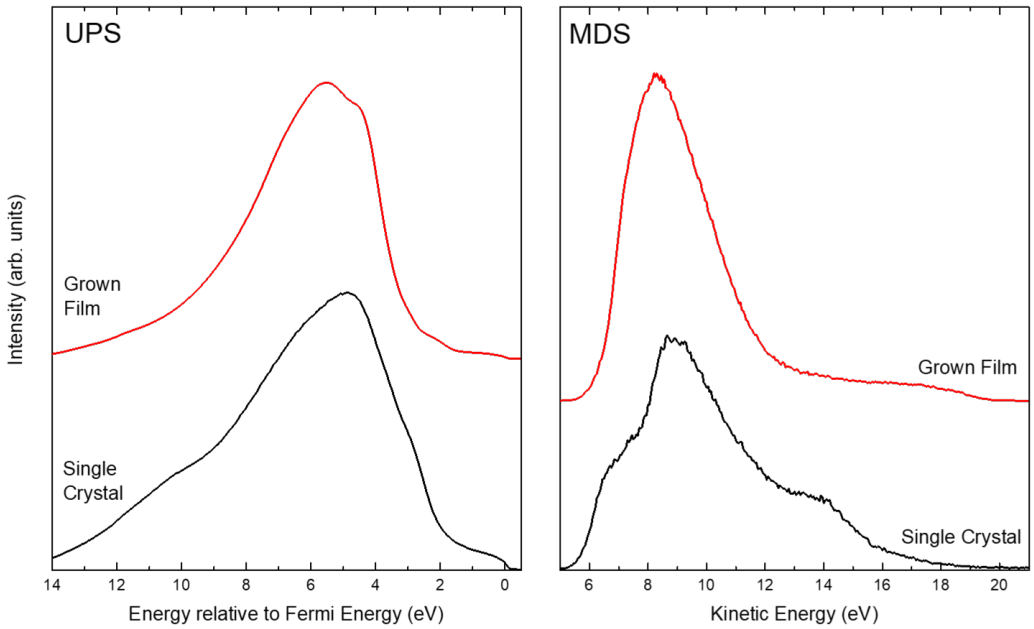

Figure 5.8: A comparison of the UPS and MDS spectra for the Fe_3O_4 film and the single crystal.

also a considerably less sharp edge at E_F. While the features on the UPS spectrum for the single crystal match well to those in the literature for similar samples [163], there is also valence level photoemission data on magnetite films that is similar to the film grown here [164], specifically for the relative intensity of the features at 4.5 and 5.5 eV and the size of the shoulder at 2.5-3.0 eV. And since it is difficult to extract good quantitative data from UPS and the overall similarity of the peaks, a clear conclusion cannot be drawn from the UPS alone.

The MDS spectrum shows very clear changes. The spectrum is largely featureless, aside from a peak at a kinetic energy of 8.3 eV and a broadened feature near the maximum kinetic energy at approximately 18 eV. Compared to the single crystal spectum, this is much more in-line with expectations due to the de-excitation mechanism and better agrees with previous MDS spectrum taken of $Fe_3O_4(001)$, where there are no clear features at around 14 eV [146]. This is compounded by the clear LEED pattern showing the $\sqrt{2} \times \sqrt{2}$ R45 reconstruction. The UPS and XPS spectra both displayed discrepancies to that of the single crystal, which may indicate, to an extent, issues with the surface; but these are difficult to quantify and are markedly less distinct than the changes in the MDS and LEED data that suggest a better sur-

face has been prepared using in-situ growth. Overall, from the spectroscopy study presented, it is reasonable to conclude that a decent $Fe_3O_4(001)$ film was grown in the UHV chamber built here at York and the replication of the co-deposition technique is a success.

5.3 Antiferromagnetic coupling at the Fe/Fe_3O_4 interface

Exchange coupling between magnetic multilayers is one of the key mechanisms for controlling magnetization alignment in device structures at the heart of magnetic recording, sensing, and MRAM technologies [165]. If the interlayer exchange coupling (IEC) is strong enough, adjacent ferromagnetic layers may align antiferromagnetically leading to a reduction in detrimental stray fields due to a suppression of magnetostatic energy. This is made use of in synthetic antiferromagnets (SAF), often used as a reference layer in magnetic tunnel junctions (MTJs) and typically consisting of two ferromagnetic (FM) layers separated by a non-magnetic layer [166]. Dipolar coupling between the FM layers leads to an antiparallel alignment of their magnetization directions thereby reducing the interaction with the free layer of a device when compared to magnetically hard-pinned layers [2]. SAF-based devices also produce a more symmetric reversal of a free layer and a reduced shift in the free-layer hysteresis loop allowing two stable resistance states at zero field [167]. As such, SAF-based devices are better, not only for in-plane MTJs, but also for MRAM using perpendicular magnetic anisotropy.

Yanagihara *et al.* previously showed that the exchange coupling between Fe and Fe_3O_4 in $Fe/MgO/Fe_3O_4$ tri-layer structures is antiferromagnetic (AFM) and increases as the thickness of the MgO spacer layer decreases [168] (see Fig. 5.9). For no MgO layer at all, an exchange coupling as strong as -2.2 $ergcm^{-2}$ was measured which compares favourably to that of Co/Ru/Co structures typically used as SAFs in MTJ stacks [165]. First-principles band structure calculations for $Fe/Fe_3O_4(001)$ junctions suggested an extrinsic mechanism for antiparallel magnetization alignment that is mediated by impurity-like states of Fe atoms at the interface [169]. The observed AFM coupling was attributed to direct exchange between Fe atoms in neighbouring Fe(001) and $Fe_3O_4(001)$ with superexchange via oxygen ions ruled out

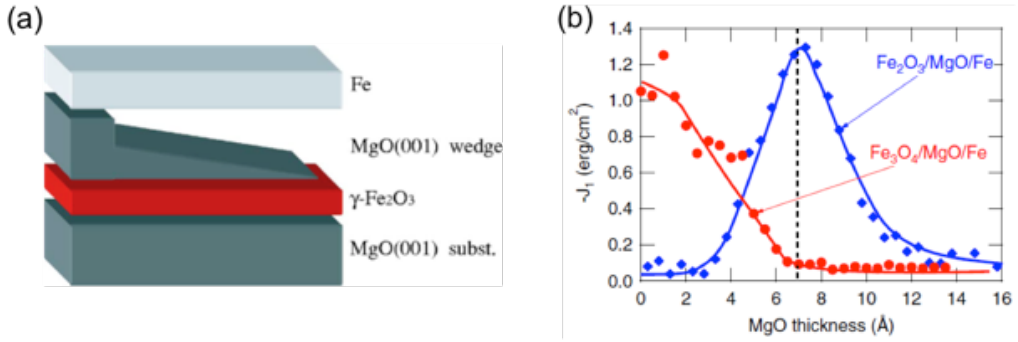

Figure 5.9: (a) Experimental methodology employed by Yanagihara et al. *[168] in probing exchange coupling in epitaxial MgO(001)/γ-Fe_2O_3/MgO/Fe(001) multilayers with different MgO spacer layer thicknesses. For similar experiments with Fe_3O_4, it was found that the exchange coupling between Fe and Fe_3O_4 was maximum when no MgO layer was present at all (b). The two layers are antiferromagnetically coupled, as indicated by the negative value of* J.

based on the assumption that the interfacial electronic structure of $Fe_3O_4(001)$ is bulk-like [170]. However, as we have previously shown, relaxation and reconstruction at the surface of Fe_3O_4 leads to the appearance of significant electron density in the previously-empty majority band gap meaning that the Fermi-level spin polarisation of Fe_3O_4, predicted to be -100% in the bulk, is drastically reduced [171]. As such, a much more detailed understanding of this system is needed in order to address its potential use as a synthetic antiferromagnet in spintronic device structures.

5.3.1 Spin-polarised metastable de-excitation spectroscopy study of Fe/Fe_3O_4 interfaces

To address the formation and properties of the Fe/Fe_3O_4 interface, spin-polarised metastable de-excitation spectroscopy (SPMDS) experiments were performed at the National Institute for Materials Science (NIMS) in Tsukuba, Japan using a growth procedure similar to that described earlier in this chapter. The SPMDS set-up employed at NIMS to obtain the following results was similar in principle to the arrangement at York with some key differences. To produce the He 2^3S beam, a pulsed nozzle-skimmer discharge source was used with the kinetic energy of emitted electrons measured using a simple retarding field analyzer. He atoms were spin polarised through optical pumping of the 2^3S_1–2^3P_2 transition at 1083 nm and a

quantization axis was then imposed on these atoms to align them either parallel or antiparallel to the in-plane sample magnetization direction. See Ref. [172] for full details of the He 2^3S beamline used at NIMS.

Samples were prepared in an ultrahigh vacuum system with a base pressure of $< 3 \times 10^{-10}$ mbar by first growing Fe_3O_4 thin films approximately 20 nm thick on clean MgO(001) single crystal substrates through electron beam evaporation of 99.99% pure Fe in an elevated O_2 pressure of $\sim 3 \times 10^{-6}$ mbar. The growth procedure followed, as shown in earlier in this chapter, is known to produce high-quality Fe_3O_4 films in the modified B orientation which has a surface terminated with a $(\sqrt{2} \times \sqrt{2})R45°$ structure as verified in the previous section using low energy LEED and elsewhere using Auger electron spectroscopy [172]. $Fe_3O_4(001)$/Fe(001) interfaces were then formed by sequentially depositing further amounts of Fe in an oxygen-free environment. The samples were then pulse magnetized in the in-plane direction before the acquisition of SPMDS spectra. Spin asymmetry was calculated using equation 2.3.

Figure 5.10(a) shows the spin-summed MDS spectra obtained from a clean $Fe_3O_4(001)$ surface and after subsequent deposition of Fe up to a coverage of 1 monolayer (ML) at which point the spectra saturate. The featureless spectrum of the clean surface is characteristic of the RI+AN de-excitation mechanism and reflects emission from the high kinetic energy features corresponding to the O $2p$ and Fe(B) $3d$ states, located in the $(\sqrt{2} \times \sqrt{2})R45°$ reconstruction [174, 171]. Adsorption of just a small coverage (0.05 nm) of Fe leads to marked changes in the MDS spectrum with a clear peak present at $\sim$8.5 eV and stronger emission at higher kinetic energies. O $2p$ and Fe $3d$ states, centred at kinetic energies of $\approx$9 and 13 eV respectively, are now much clearer possibly suggesting that the de-excitation mechanism has switched to the one-electron process of Auger de-excitation which occurs for insulating surfaces. The strength of the oxygen peak is somewhat unexpected given that additional iron has been deposited and is possibly due to the segregation of excess oxygen atoms from the $Fe_3O_4(001)$ surface to form an insulating FeO precursor layer. Further deposition of iron reduces the sharpness of both the O and Fe features until the spectra saturate at a coverage of approximately one monolayer, or somewhere between 0.15 and 0.20 nm. For higher coverages, the spectra are relatively featureless, indicating that RI+AN is again the dominant de-excitation mechanism as expected for transition metal surfaces.

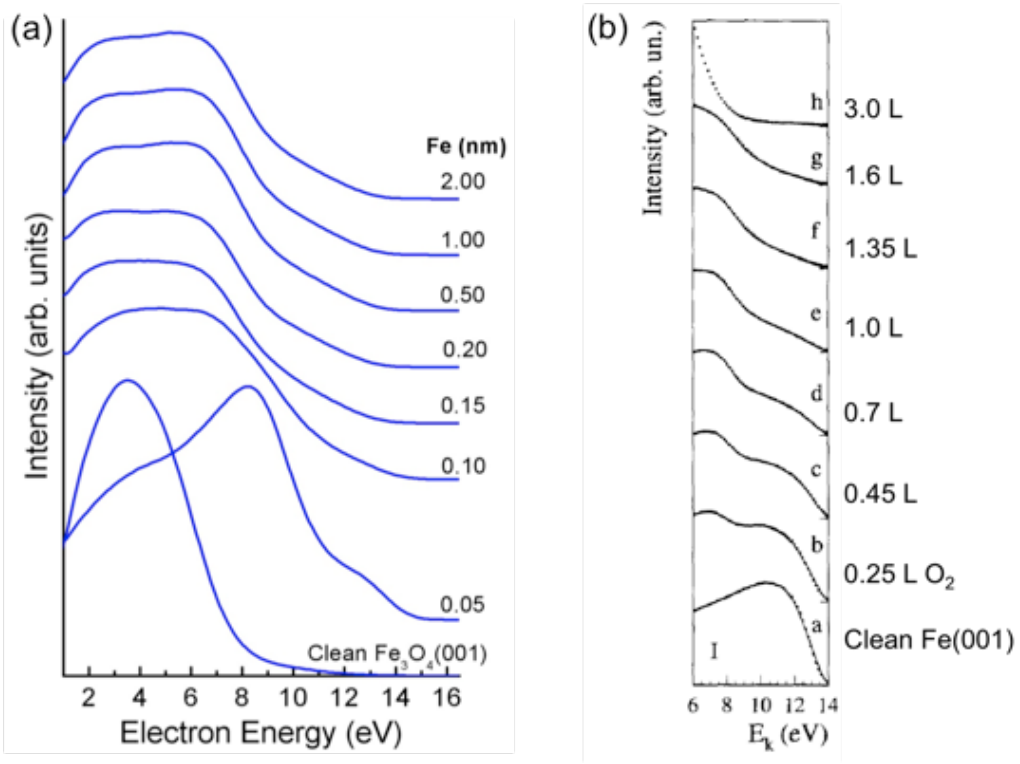

Figure 5.10: (a) Spin-summed MDS spectra from a clean $Fe_3O_4(001)$ surface and for coverages of Fe up to 2.0 nm. A one monolayer Fe coverage corresponds to approximately 0.15-0.20 nm after which point the features in the spectra remain consistent. (b) A figure reproduced from Ref. [173] showing MDS spectra for a clean Fe(001) film before and after exposure to small amounts of oxygen, expressed in units of Langmuirs (L), which is equal to 1 second of exposure at 1×10^{-6} torr.

It is notable in the MDS spectra for higher iron coverages that emission at high kinetic energies, i.e. close to the Fermi energy, is lower than would be expected given the density of $3d$ states near to E_F. This is especially apparent when comparing the spectra obtained here to previous MDS data from clean iron films, where the there is a much stronger peak at higher kinetic energy, an example of which is shown in the bottom plot of Fig. 5.10(b), taken from a study by Moroni *et al.* [173]. In that study, the authors exposed the clean Fe(001) film to small doses of oxygen, as indicated in the series of spectra in Fig. 5.10 (b). Note that the kinetic energy scale used in this figure is over a smaller range than presented with our data in Fig. 5.10(a). Comparing the two sets of data, it is apparent that the spectra for iron coverages of 1 ML (0.15 nm) and above in Fig. 5.10(a) are very similar to the spectra in Fig. 5.10 (b) for an iron film exposed to between 1.0 and 1.6 Langmuirs of oxygen. This strongly suggests that the 'clean' Fe films grown in this study actually

have a very small amount of oxygen present at the surface. This is an interesting finding and leads to the questioning the origin of the oxygen. Despite the reactivity of iron, previous studies of the growth of iron films in the same system on different substrates to $Fe_3O_4(001)$ show strong emission close to the Fermi energy, indicative of a clean Fe surface [172]. Hence, contamination of the analysis chamber or the helium beamline as being the source of oxygen can be ruled out. It is therefore probable that the small amount of oxygen present on the Fe films originates from the $Fe_3O_4(001)$ substrate, always remaining at the topmost surface even as more and more Fe is deposited. In other words, oxygen is acting as a surfactant in the growth of $Fe/Fe_3O_4(001)$ interfaces. The driving mechanisms behind this effect need further investigation and it is sufficient for the purposes of this study to state that Fe films of a certain thickness have been prepared on $Fe_3O_4(001)$ which allows us to discuss the spin polarisation of this system.

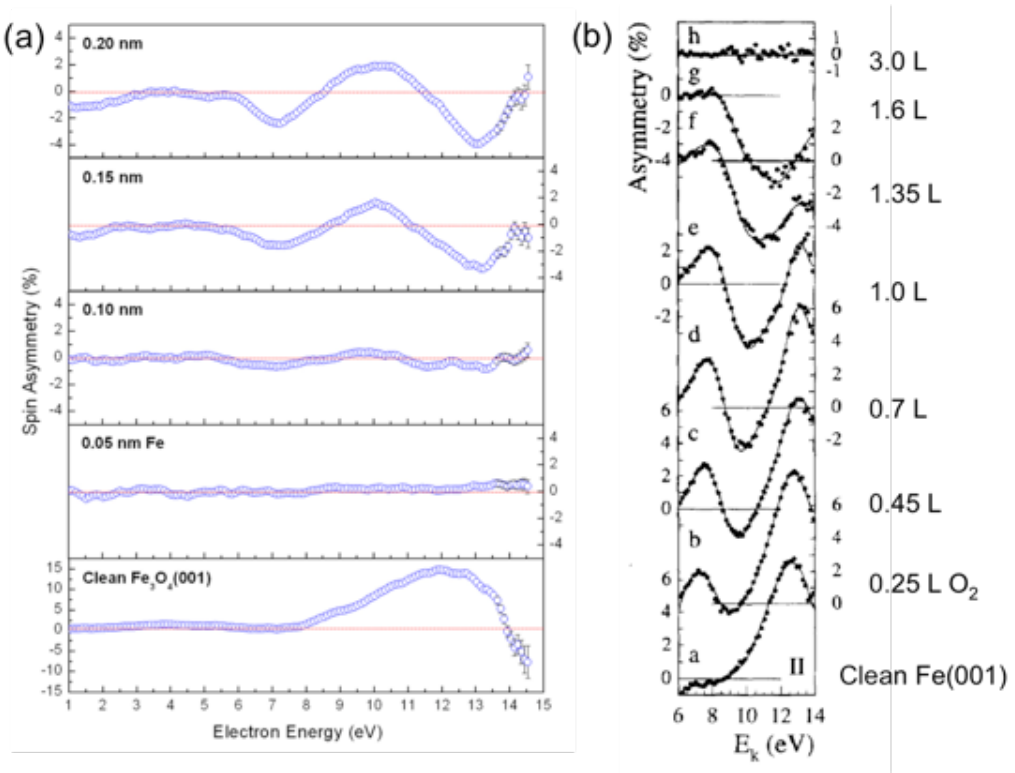

Figure 5.11: (a) Spin asymmetry data for a clean $Fe_3O_4(100)$ surface and after exposure to increasing amounts of Fe, up to the formation of a film approximately 1 ML thick. (b) A figure reproduced from Ref. [173] showing spin asymmetry data for a clean Fe(001) film before and after exposure to small amounts of oxygen, expressed in units of Langmuirs (L). Note the anticorrelation between the features in the 0.20 nm spectrum in (a) and the 1.0 L spectrum in (b)

Figure 5.11(a) shows the spin asymmetry calculated from the spin-resolved spectra that were combined in Fig. 5.10(a). The spin asymmetry of the clean $Fe_3O_4(001)$ is slightly negative at high kinetic energies where emission is mainly due to states around the Fermi level. A negative spin asymmetry in SPMDS implies a positive spin polarisation in the surface density of states of $Fe_3O_4(001)$ due to the dynamics of the spin-dependent de-excitation process, which must satisfy Pauli's exclusion principle. A small positive spin polarisation in the surface DOS of $Fe_3O_4(001)$ is in sharp contrast to predictions of a Fermi-level spin polarisation of -100% for this material and the origin of this change has been attributed by Pratt *et al.* to the presence of oxygen dangling bond surface states appearing in the bulk majority band gap [171]. A very small amount (0.05 nm) of Fe deposition leads to the disappearance of spin asymmetry altogether. The formation of a magnetically-dead layer supports the assertion that an FeO-like structure has formed. Spin asymmetry returns for higher coverages of Fe with strong features emerging for a coverage of approximately one monolayer (0.20 nm). Two negative 'dips' in spin asymmetry are observed at kinetic energies of approximately 7 eV and 13 eV separated by a positive peak at 10 eV. To make sense of these features, comparison is again made to the study by Moroni *et al.* who presented spin asymmetry data for the same oxygen-exposed Fe on Ag system for which MDS data are shown in Fig. 5.10(b). Fig. 5.11(b) shows this asymmetry data. A large positive asymmetry is observed around the Fermi level for the clean Fe surface, expected as minority spin states dominate in the spin-resolved band structure of Fe close to E_F. When the Fe film is exposed to small amounts of oxygen, the spin asymmetry changes such that two clear positive peaks are present for an oxygen dose of 1.0 L separated by a negative dip. The energetic positions of these features align very closely to those for the Fe film grown on $Fe_3O_4(001)$, as shown in Fig. 5.11(a) again suggesting that the films grown in this study have a trace level of oxygen present at their surface. Interestingly though, the polarity of the features is reversed. For example, the negative dip at 13 eV for the 0.20 nm Fe film on $Fe_3O_4(001)$ appears as a positive peak at 13 eV for the 1.0 L spectrum from the oxygen-exposed Fe study. But the spectra in Fig. 5.11 for the clean $Fe_3O_4(001)$ and Fe surfaces have the same respective polarisation, this striking anti-correlation can be taken to mean that the majority spins of the Fe film grown here are aligned in the opposite direction to the underlying $Fe_3O_4(001)$ substrate. In other words, the Fe and $Fe_3O_4(001)$ layers either side of the Fe/$Fe_3O_4(001)$ are antiferromagnetically coupled. This interesting observation supports the earlier work of Yanagihara *et al.*,

described above, which only observed bulk magnetisation effects.

Further work is needed to clarify the exact origin of this exchange coupling effect but it would seem that the formation of the insulating, and magnetically-dead, FeO precursor layer is key. Previously, Kida *et al.* noted that frustration effects at such an insulating interface would prevent intrinsic exchange coupling between Fe atoms in the two layers and most ferromagnetic bilayers display ferromagnetic coupling [169]. Hence, in keeping with the unique and interesting properties of Fe_3O_4, a more intricate mechanism must account for the observed AFM coupling. Clarification of this mechanism is likely to require theoretical support to the experimental data presented here, specifically, density-functional theory (DFT) calculations that build on earlier work for the clean Fe_3O_4 surface [171, 175].

Chapter 6

The C_{60}/Si(111) 7×7 Interface

6.1 Introduction

The C_{60} on Si organic-semiconductor interface was selected to test the characterisation techniques described in the previous chapters. As the quintessential semiconductor material, silicon was a natural choice of substrate with its well studied surface reconstructions and ease of preparation. On the organic side, C_{60} was the first fullerene molecule to be discovered and is a good electron acceptor for use in charge transfer applications such as organic electronic devices. Together, the C_{60}-Si system can be considered an "archetypal" organic-semiconductor interface on which to test the capabilities of the new vacuum system.

Naturally, such an organic-semiconductor combination will be well studied, and there is in fact a great amount of research that has been carried out, starting in the early 1990s, not long after the discovery of the C_{60} molecule in 1985 [55]. However, there has been great debate with regards to the nature of the interfacial bonding and, even now, some of the underlying mechanisms are still not entirely understood [176]. Evidence both for and against exists concerning whether there is charge transfer from the silicon surface into the C_{60} cage. It is important to resolve this issue in order to gain a better understanding and engineer organic electronics interfaces with enhanced efficiency and more control over transport properties for use in organic electronic devices. For example, low charge mobility and extraction in organic photovoltaics can be improved with easier transport across organic/organic and organic/electrode interfaces [177]. The MDS technique offers a novel way to di-

rectly characterise the electronic structure of the C_{60} cage, while being more surface sensitive than conventional valence band photoemission using UPS. The literature concerning the C_{60}-Si(111) 7×7 interface will be examined at the start of this chapter, followed by presentation and discussion of the results obtained.

6.2 Background

6.2.1 Deposition, structure and STM

Initial studies of C_{60} deposited on the Si(111) 7×7 reconstruction were conducted using STM [178, 179]. Individual fullerene molecules adsorbed on the surface were found to stay isolated and showed no evidence of island formation, unlike what was previously observed for C_{60} on metal surfaces such as Au(111) [180]. This suggested that there was a strong interaction and provided initial evidence that the C_{60} molecules bind strongly to the Si surface[178]. Changes in the appearance at different sample/tip biases show the presence of different bonding configurations and the apparent heights of the molecule change depending on the adsorption site, with the molecule having "sunk" deepest at the corner hole sites and overall showing lower apparent height than the diameter of the C_{60} molecule [178, 179, 181]. At sub-monolayer coverages, no obvious preferred bonding site can be seen. An STM image taken from the literature [179] at sub-monolayer coverage is shown in figure 6.1. Statistical analyses of the STM images have yielded mixed results [179, 181], which could be attributed to difficulties in precisely determining the adsorption site of such a large molecule from STM images alone, as well as discrepancies arising from changes in preferred site as coverage increases towards 1 ML.

An ordered structure emerges when a full monolayer is deposited [182, 181], with the C_{60} molecules adsorbed on two sites: the corner hole site (where the molecule sits above the corner hole of the reconstruction) and at sites bridging a centre adatom and corner adatom (where the molecule sits in the "triangle" between three corner holes). It was proposed that pinning of fullerene molecules adsorbed at the corner site, where it "sinks" into the hole, forced the ordered structure as the coverage increased [181]. Given two sets of equivalent adatom bridge sites available on the Si(111) 7×7 reconstruction, two different domains are present on the surface with

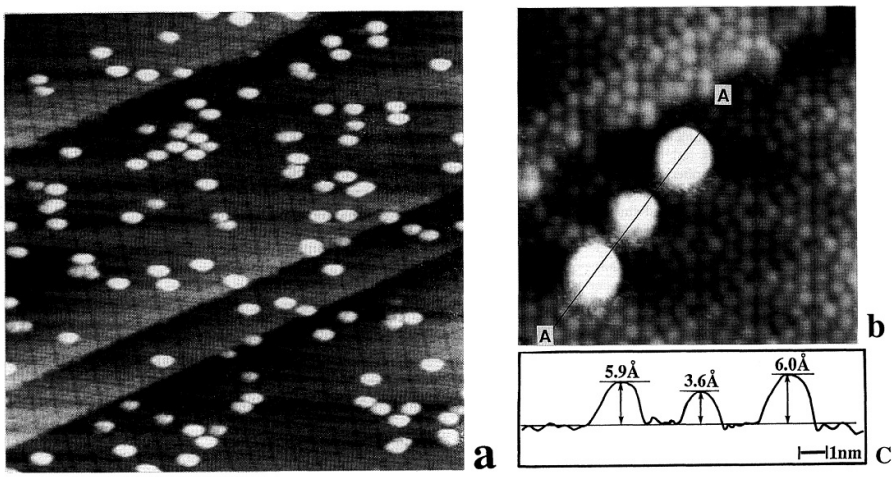

Figure 6.1: (a) STM image of C_{60} on Si(111) at sub-monolayer coverage. (b) Image illustrating the "large" and "small" molecules observed, where the "small" molecules are intially theorised as due to being sunk inside a corner hole site, and (c) a plot showing the scan across the molecules along the line drawn in (b). Images taken from [179].

an offset of approximately 22° from each other [182] and, in Wood notation, the description is $\sqrt{7} \times \sqrt{7}$ R19.1° [183]. A schematic of this structure is shown in figure 6.2.

6.2.2 Adsorption character

The observations described above suggest the presence of significant bonding between the carbon and silicon atoms. At low coverages, valence level photoemission spectra show a clear broadening or splitting of peaks when compared to the spectra of bulk fullerite [184, 185]. This was attributed to a change in bonding nature of the C_{60} molecule to the surface by eliminating other possibilities [184]: STM images did not show dimerisation or polymerisation of the C_{60} [182]; high-resolution electron energy loss spectroscopy (HREELS) data did not find vibrational modes corresponding to C_{60} dimers; and the energies measured of > 1.50 eV from the Fermi level are rather higher value than that of a filled C_{60} LUMO when bonded to an alkali metal [186]. In this framework, the origin of a splitting in valence band photoemission, as in the literature and later in this chapter, could be due to both a breaking of symmetry in the molecule when covalently bonded, and the formation of a bonding orbital [184]. By comparing to the valence level spectra of C_{60} dimers, it can be seen

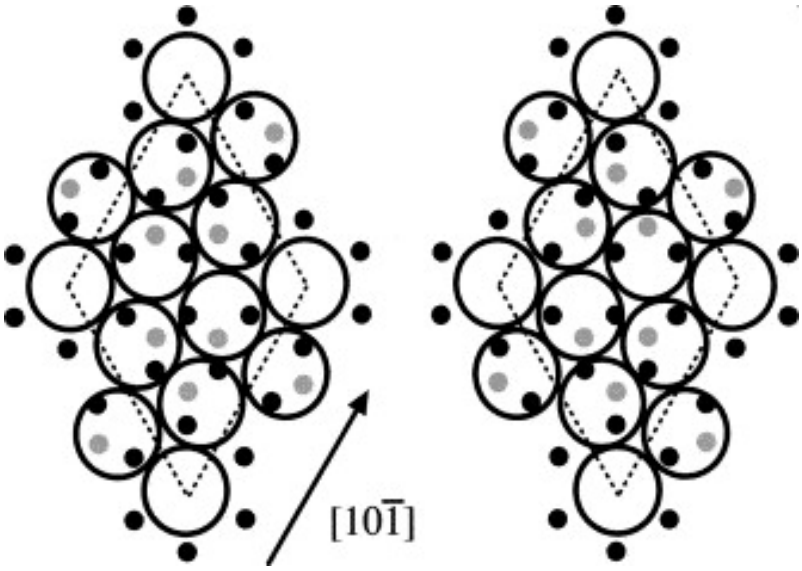

Figure 6.2: Schematic of the two different domains' arrangements of an epitaxial C_{60} film grown on Si(111) taken from [183]. The open circles represent C_{60} molecules while the black and grey dots represent the adatoms and rest atoms of Si respectively.

that the split HOMO due to a change in symmetry only yields a small shoulder on the HOMO peak [187, 188], and therefore the formation of a bonding state is more likely the main contributor. More specifically, the sp^2-like hybridisation is changed to a sp^3-like character when a carbon double bond is broken to form an Si-C bond with the surface. A reasonably straightforward DFT calculation of C_{60} molecules bonded to SiH_3 groups yields very similar predictions for the valence band spectra of C_{60} on Si [189], which show the formation of Si-C bonds.

After establishing that Si-C bonds exist between the C_{60} molecules and the Si(111) surface, a point of controversy arose from the debate over whether the molecules are all chemisorbed on the surface or only partially so. Initial photoemission data in the literature over a range of coverages up to 1 ML showed a change in the line shape of the HOMO and HOMO-1 peaks: the peaks, which at low sub-monolayer coverages showed a high degree of splitting, became more symmetrical [190]. This led to the conclusion that, at 1 ML, many of the molecules are physisorbed on the Si surface, since the presence of the Si-C bonding state has diminished. A mixed physisorbed-chemisorbed state was also used to explain differences in individual C_{60} molecules observed in STM [191] - where the more weakly adsorbed molecules seem larger in the STM images (as seen in figure 6.1) due to more molecular movement (induced by tip proximity). After annealing at 600 °C, the larger molecules in the

STM image, corresponding to weak bonding, evolved into smaller ones [191], which indicates that they have become more strongly bound.

However, later work called into question the deposition coverage as calibrated by the quartz crystal microbalance (QCM) [176]. A comparison of the UPS spectra for 1.0 ML deposited as calibrated by QCM shows a striking resemblance to the spectra for bulk fullerite, or very thick films, with the peaks being much more symmetrical and the "valley" between the HOMO and HOMO-1 peaks having depth of a similar size to the peak heights. As well as this, from STM studies, it has been found that annealing the sample to 300 ^{o}C does not cause the first monolayer to desorb [181], but merely for the molecules to migrate on the surface. This means that by annealing, one can return to a coverage of 1.0 ML after a large amount of deposition, and doing so yielded a spectrum that was similar to that of sub-monolayer coverages obtained from QCM calibrated data [185]; with a more split HOMO peak and a less distinct separation between the HOMO and HOMO-1 peaks. From this data, the conclusion is that the C_{60} molecules are in fact all chemisorbed upon deposition onto the Si(111) surface. Later work combining STM and valence level photoemission on annealed samples also confirmed this conclusion, which is now generally accepted [189].

First principles calculations of C_{60} on Si(111) were performed to find the adsorption geometries of C_{60} at the interface [192, 193]. The results found no evidence for a physisorbed precursor state, but instead explained the 'large' and 'small' molecules observed in STM (shown in figure 6.1) as being bound with different numbers of Si-C bonds [192]. In this interpretation, less strongly adsorbed C_{60} molecules are chemisorbed via just a few covalent bonds, while for strongly adsorbed molecules, silicon adatom bonds to the surface are broken to form additional Si-C bonds if given enough energy to overcome a kinetic barrier, such as when the sample is annealed. A diagram illustrating this is shown in figure 6.3. These findings support the consensus that, at 1 ML and below, all C_{60} molecules adsorbed on the Si(111) surface are chemisorbed upon deposition.

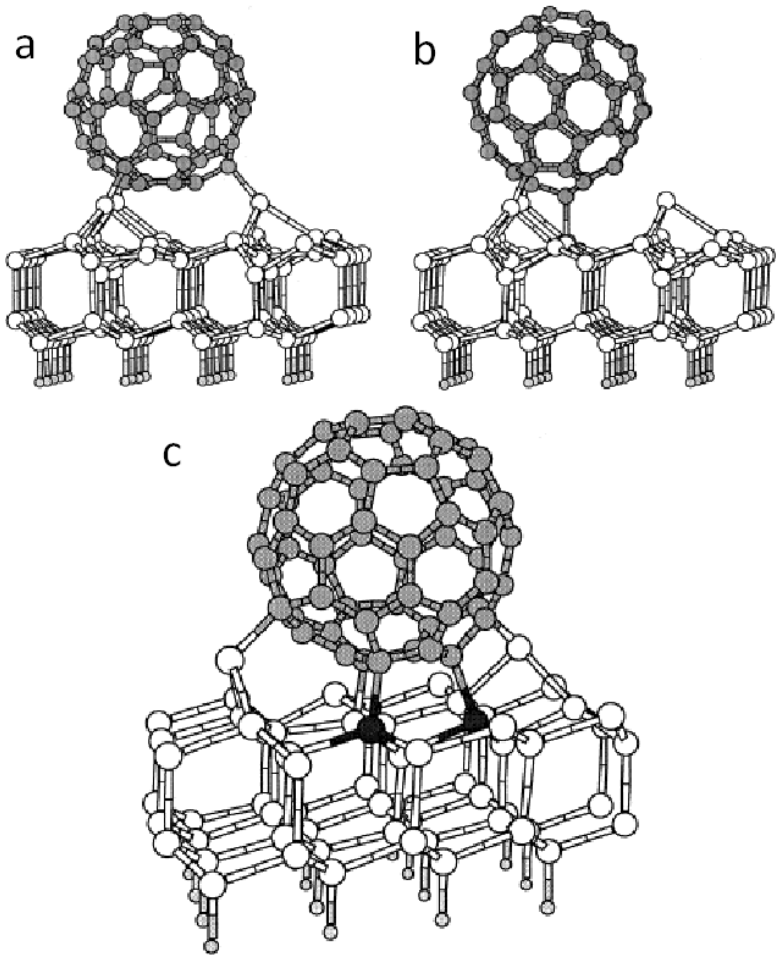

Figure 6.3: Schematic of C_{60} molecule adsorption on Si(111) for weakly (a, b) and strongly (c) adsorbed states taken from [192]. Additional bonds are formed between C_{60} molecules and Si adatoms when energy is supplied to break bonds between adatoms and the surface.

6.2.3 Charge transfer

In addition to the disputes over the type of adsorption at the interface, the nature of the chemical bond formed is also the subject of conflicting theories. The possibility of charge transfer across the interface (from the Si dangling bonds into the LUMO of the C_{60}) has been the subject of heated debate in the literature [176]. Electron donation from the dangling bonds has been proposed since the first STM studies of C_{60} deposition onto Si(111) [179, 181]. In those STM images, the adatoms neighbouring C_{60} adsorption sites appear darker than adatoms elsewhere on the surface. This darkening is caused by a reduction in filled electronic density of states in those adatoms, and was attributed to the donation of charge into the C_{60} LUMO. A more direct measurement of this charge transfer was taken with HREELS [194, 195] and

an estimate of the amount of charge transferred across the interface was obtained. Specifically, the estimate was carried out by using a method proposed earlier for alkali-metal-doped C_{60} [196], where a linear softening effect in the T_{1u} mode of a A_xC_{60} molecule (where A is the alkali metal) is predicted to be proportional to x. The initial results of this calculation predicted stronger charge transfer at sub-monolayer coverages (approximately 0.25 ML) with 3 ± 1 electrons per C_{60} molecule [195] and a smaller amount at 1.0 ML with approximately 1 ± 1 electrons. These initial results depict a very unrealistic picture and, naturally, further evidence for charge transfer has been pursued in the literature with other measurements.

The most direct measurement of the density of states is with photoemission spectroscopy. If electrons are transferred into the C_{60} LUMO, then this should be observable as an extra occupied state near the Fermi level. However, valence level photoemission spectroscopy taken using ultraviolet photons yielded no observable density of states near the Fermi level [197, 184]. Initially, this was attributed to the fact that the >100 eV photons used [197] were at too high an energy [185], but later experiments with UV photons generated with the He I spectral line (21.2 eV) showed similar results [184]. This new data also drove renewed discussion into the validity of the interpretation of previous HREELS data [190, 184, 185], and a new conclusion was reached: that due to covalent bonding at the surface, the C_{60} would be more strongly distorted, which would in turn affect the vibrational modes of the molecule on the surface. This would mean that the method used to estimate the amount of charge transferred for C_{60} - alkali metal interfaces can no longer be reliably applied.

However, probing the core electronic states using XPS paints a contradictory picture. After sub-monolayer deposition and subsequent annealing, a shift to a lower binding energy is observed for the C $1s$ peak. This has been attributed to a final-state screening effect from charging as electrons move from the Si surface into the C_{60} LUMO [184]. The proportion of contribution from image charge screening and charge transfer screening is difficult to separate from XPS data alone, but the data gives evidence of charge transfer across the interface. One theory put forward to reconcile the opposing evidence for charge transfer is that the injected charge is not uniformly distributed in the C_{60} cage [198, 192]- more specifically, the electrons are localised to the carbon atoms closest to the Si surface. In this case, there would be a charge redistribution over the C_{60} cage that photoemission measurements

are not sensitive to due to the signal being averaged over a finite depth. MDS could provide a possible avenue to probe these subtle changes. Another crucial point is that the charge transferred does not occupy the LUMO states, but instead arises from hybridisation of the molecule with the surface [192]. While this is more consistent with the valence band photoemission measurements, it is yet to be verified experimentally and theoretical calculations still predict a measure of ionic character in the chemical bonds [199, 193]. The issue of charge transfer is still unresolved for the C_{60}-Si(111) 7×7 interface.

6.2.4 Si(111) 7×7 surface

Si(111) 7×7 was the substrate chosen for the initial experiments with C_{60} deposition. It is well studied and is an easy-to-prepare surface used extensively in a variety of research fields. When a silicon crystal is cleaved across the (111) plane, a 2×1 structure is produced. When heated above 873 K, the surface irreversibly reconstructs into the 7×7 structure [200]. The surface reconstruction is explained by the dimer-adatom-stacking-fault (DAS) model, which is shown in figure 6.4. The key features of the reconstruction are the dimers along the dotted line in the diagram; the adatoms, which are the largest circles; and the corner hole sites where the bulk silicon is exposed. The unit cell also has a faulted and an unfaulted side, where on the faulted side there is a stacking fault in the atomic layers.

The dangling bonds and back bonds of the surface form electronic states in the band gap of bulk silicon. There surface states are only localised at the surface and have been studied by UPS and AES [201, 202]. UPS and MDS spectra of the clean Si(111) surface will be included with the results for the C_{60}/Si(111) 7×7 interface.

6.3 Experimental and Results

6.3.1 Si surface preparation and growth of C_{60}

The Si(111) 7×7 reconstruction was prepared inside the vacuum system by an established procedure of flashing the sample using direct current heating. Sample strips approximately 12×5 mm^2 were cut from a 0.5 mm thick n-type Si wafer and

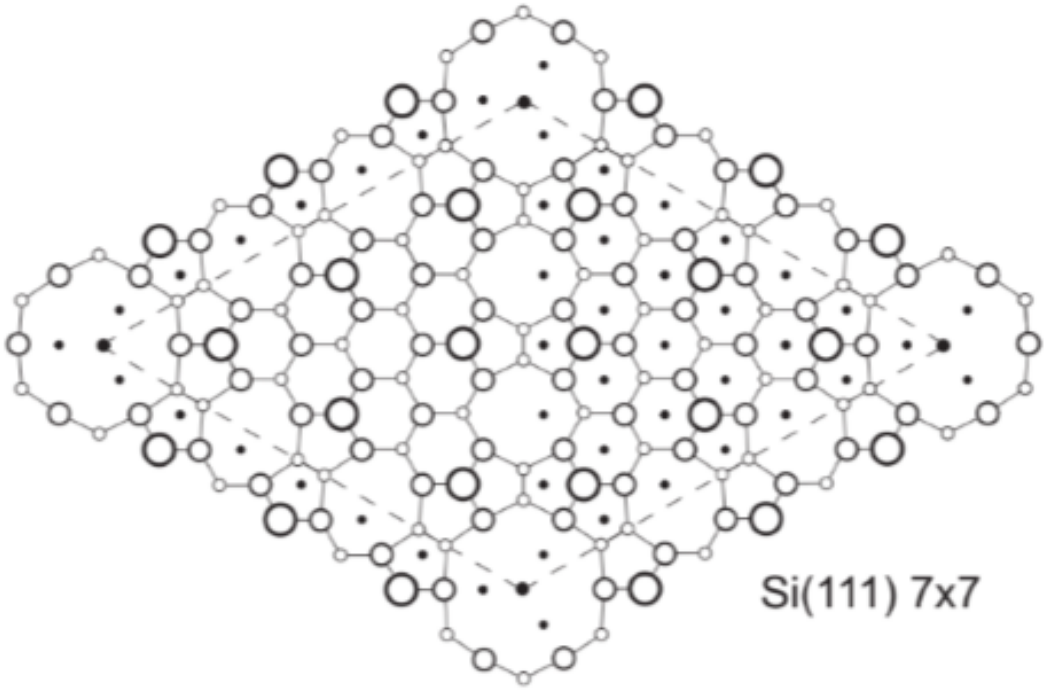

Figure 6.4: Diagram of the Si(111) 7×7 reconstruction, the unit cell is marked by the dotted line. Large circles are the adatoms. The pairs of small circles, such as those on the dotted line, are the dimers. The dots distinguish the faulted and unfaulted sides of the unit cell.

mounted in an Omicron direct current heating sample plate. Samples were then degassed at a temperature of approximately 500 °C for several hours, usually overnight. Samples were brought to 900 °C for 10 minutes before flashing three times to 1200 °C, allowing the chamber pressure to recover down to the low 10^{-9} mbar range between each flash. This was followed by ten more minutes at 900 °C. Finally samples underwent slow cooling down to room temperature at a rate of roughly 1 °Cs^{-1}. The surface cleaning procedure was carried out prior to all measurements and deposition involving Si samples.

The resulting 7×7 surface reconstruction was then checked with LEED and UPS to ensure a good quality surface. Examples of the 7×7 LEED pattern and UPS spectrum for clean Si are shown in figure 6.5. In the UPS spectrum, three Si surface states are present at -0.2 eV, -0.8 eV and -1.8 eV, which correspond to the dangling bonds of the adatoms, the rest atoms and the backbonds of the adatoms respectively [203]. If a clear LEED pattern or surface state peaks were not observed, then the sample would be flashed again until a satisfactory clean substrate was obtained.

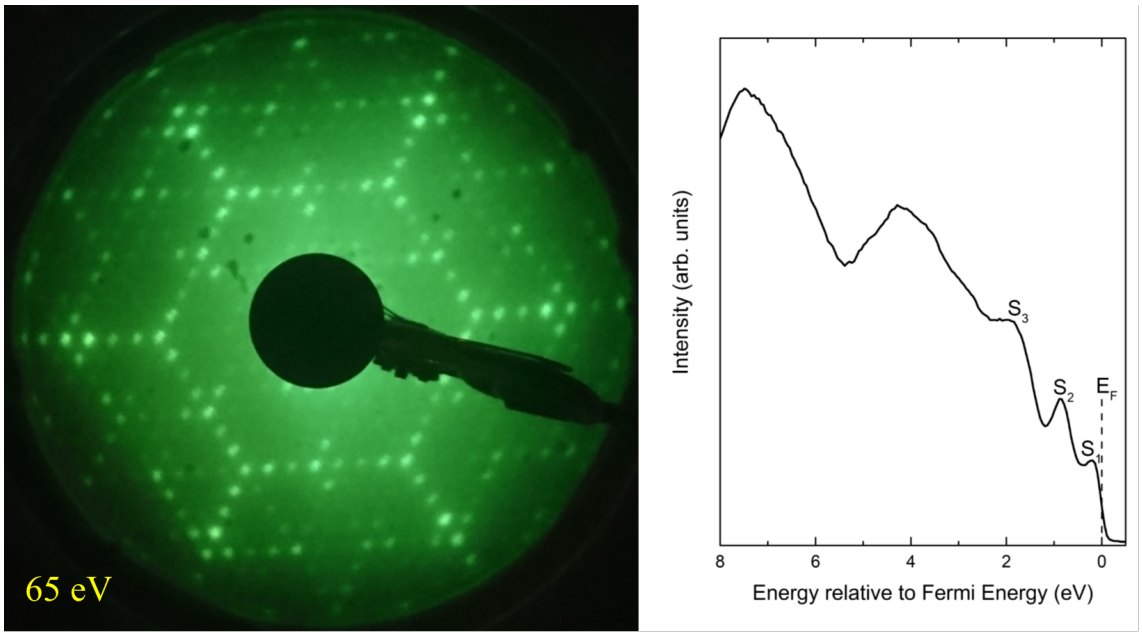

Figure 6.5: Left: LEED pattern of the Si(111) 7×7 surface taken at a beam energy of 65 eV. Right: UPS spectrum of the clean Si(111)7×7 surface. The surface states labelled S_1, S_2 and S_3 correspond to the dangling bonds, underlying free atom/corner hole sites and back bonds respectively.

C_{60} films were then sputtered onto prepared substrates by heating the C_{60} powder (with a purity of 99.8%) using the MBE-Komponenten NTEZ low temperature effusion cell. The deposition rate was monitored using a quartz crystal microbalance. An ideal deposition rate of 0.2 nm per minute was aimed for, since this has previously been shown to form no islands on the surface for a 1.0 ML film [176]. A suitable deposition temperature of approximately 350 °C, as measured by the thermocouple attached to the crucible of the instrument, was determined after calibration using the QCM. From the QCM measurements, the C_{60} sublimation in the cell seems to start around this temperature as a drop of only 10 °C below causes no appreciable deposition even over long periods of time. Since the deposition rate is very sensitive to small changes in temperature at around 350 °C, calibration is carried out prior to all deposition.

After growth in the preparation chamber, the samples are transferred into the analysis chamber for measurement. For UPS and MDS, samples are placed normal to the analyser (45° to the UPS source and the MDS beamline). For XPS, the sample is placed 45° to both the monochromated x-ray source and the analyser as the best compromise. The largest circular analyser entrance aperture is used (6 mm) for

XPS and MDS measurements to maximise count rate and a smaller, 1 mm circular aperture is used for the UPS due to saturation of the channel electron multipliers.

6.3.2 Core and valence level photoemission

UPS

Valence level photoemission data were taken via UPS for a range of nominal C_{60} coverages - from 0.2 ML to 1.0 ML in 0.2 ML increments. The spectra obtained are displayed in figure 6.6. The peaks corresponding to the molecular orbitals of the C_{60} immediately becomes dominant on deposition, even at low coverages. The peak at -2.0 eV from the Fermi energy is assigned to the HOMO, the peak at -3.2 eV to the HOMO-1. Further peaks appear at -5.1, -5.5, -6.8 and -8.0 eV from the Fermi energy. These values are in line with values reported in the literature [184]. The surface states of the substrate are visible at low coverages but disappear completely by 0.6 ML, contrary to C_{60} deposited on metal surfaces, where substrate electronic states can be observed at 1 ML [204, 205]. The disappearance of the surface states shows interaction of the C_{60} with the Si dangling bonds.

The form of the molecular orbitals also changes with deposition. At low coverages, the HOMO peak is initially broad and, from the shape, it is clearly split into two (or more) peaks. As the coverage increases, the HOMO peak narrows into a symmetrical, single peak. The "valley" between the HOMO and HOMO-1 also inceases in depth to a size comparable to the peaks themselves. As mentioned in the previous section, this peak form is more similar in shape to the spectrum for bulk fullerite [176]. Therefore the nominal coverages fall under suspicion, as the 1.0 ML spectrum is close to that of others in the literature where the QCM calibration has fallen under scrutiny. This is further strengthened by the consensus that all C_{60} molecules in the first monolayer are chemisorbed on deposition, but a strong chemical interaction of the C_{60} with the Si would cause a large breaking of symmetry in the molecules and cause a splitting in the peaks [190]. This is observed only until a nominal coverage of 0.4 ML and indicates that above this, the coverage extends beyond the first monolayer.

Therefore, another way to be sure that 1 ML of C_{60} has been deposited is desirable. By taking advantage of the fact that the first monolayer of molecules (which are

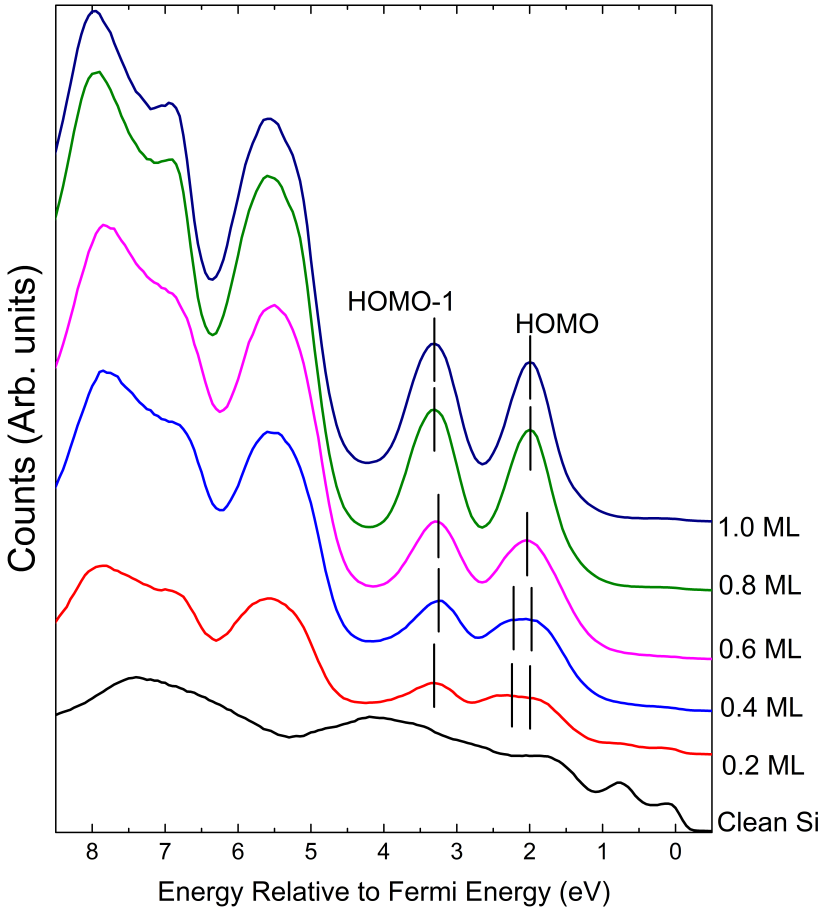

Figure 6.6: UPS spectra of C_{60} grown on Si(111) taken at different nominal sub-monolayer C_{60} coverages. Lines are drawn at rough maxima positions as a guide to better see the shifts.

chemisorbed) do not desorb on annealing [181], samples with many layers of C_{60} can reliably return to a coverage of 1 ML by heating the sample up to a suitable temperature. However, heating can introduce possible changes in the film, shown in figure 6.3, and these changes should be noted. Thick C_{60} films (>1 ML nominal) were grown on clean Si substrates and then subsequently annealed. UPS spectra were taken after annealing at 550 K, 650 K, 750 K and 1100 K for 10 minutes each. The data are plotted in figure 6.7. After the initial anneal at 550 K, the size of the C_{60} molecular orbital peaks falls drastically and a visible shift of around 0.3 eV is observed in all peaks. The HOMO peak also splits, indicating a breaking of symmetry [190]. This is expected as the physisorbed upper layers of C_{60} desorb

by 550 K, leaving only molecules that strongly interact with the Si surface [176]. As the annealing temperature rises to 750 K, there is little-to-no change in peak positions. There is, however, a slight but perceptible shift in the split HOMO peak: the weight of the peak shifts towards a higher binding energy with the higher temperature anneal. This could indicate that additional chemical bonds have formed between the C_{60} molecules and the Si adatoms as more energy was supplied [192]. Furthermore, the shift towards a higher binding energy occurs mostly between 650 K and 750 K, rather than uniformly across the whole range, which suggests that an energy barrier was overcome by 750 K to give a discrete change in the bonding configuration, which could correspond to the breaking of Si-Si bonds to form more bonds with the C_{60}. Finally, at 1100 K, the spectrum changes drastically as the C_{60} molecular orbitals disappear. At this temperature, the C_{60} cage has been broken. New peaks are observed at -2.1, -5.2 and -7.6 eV relative to the Fermi energy and these have similarities to an Si-rich 3C-SiC(001)-(2×1) surface [184].

Comparing these results to the graph shown in figure 6.6, the UPS spectrum taken post anneal (and therefore corresponding to a ML coverage) best matches the spectrum taken at 0.4 ML of nominal coverage in terms of relative peak size. While the HOMO peak shape is more similar in the case of 0.2 ML nominal coverage, the remnant presence of Si surface states indicates that the coverage is sub-monolayer. Therefore a tentative conclusion can be drawn that QCM calibration overestimated the deposition rate by 2-3 times. This can be attributed to the incompatibility of C_{60} films with the assumptions made for the QCM calibrations, specifically linear viscoelasticity, and large differences in the density of an ultrathin C_{60} when compared to the bulk value used in the calculations. There are however, subtle differences between the results. The splitting of the HOMO peak is more visible in the UPS spectra taken post anneal and crucially, the HOMO peak of the as-deposited sample is weighted more towards a lower binding energy. This suggests a stronger interaction at a similar coverage, which is in line with the results of DFT calculations that showed a greater number of covalent bonds forming between C_{60} and the Si adatoms when given a suitable activation energy (corresponding to annealing at temperatures of 670 - 879 K) [192]. Overall, the UPS data agrees well with the literature and gives confidence in the prepared 1 ML C_{60} on Si(111) samples.

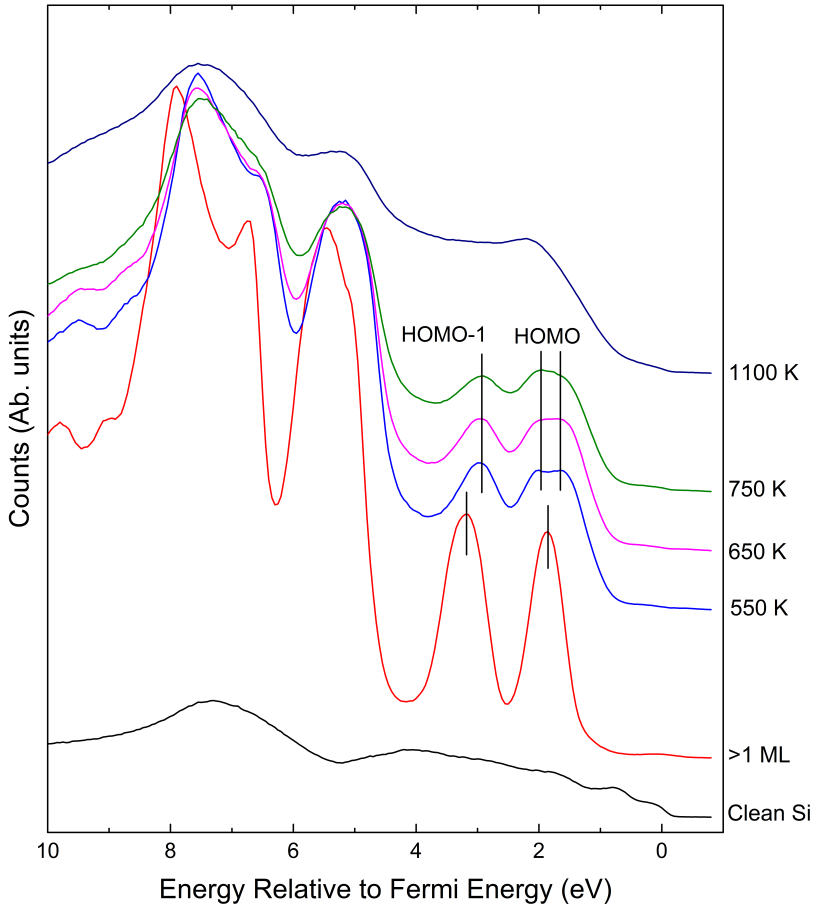

Figure 6.7: UPS spectra of C_{60} grown on Si(111) taken after annealing at a range of temperatures. Lines are drawn at rough maxima positions as a guide to better see the shifts.

XPS

Core level spectra were also taken with XPS to study changes in the chemical environment due to annealing. XPS spectra for C 1s and Si 2p peaks before and after annealing are shown in figure 6.8. The peaks were fitted using Voigt profiles - a Gaussian-Lorentzian convolution. Initially, the as-deposited C 1s peak is located at 284.9 eV, and shows a single, relatively symmetric peak. The line profile changes on annealing, and an extra feature appears at a lower binding energy at 283.1 eV. The "main" peak also shifts slightly towards a lower binding energy of 284.5 eV. Since the annealing process caused outer layers of C_{60} to desorb, a corresponding

reduction in the size of the C 1s is also observed.

The Si 2s peak shows less pronounced changes before and after annealing. In both there is a main component feature and a tail at +3 eV. There is a general shift of the Si 2s peak to a lower binding energy, much like the C 1s and UPS peaks. This slight global change of the binding energy in the XPS towards the Fermi level could suggest a change in the surface work function induced due to band bending at the interface, but the core levels of a 1 ML C_{60} film (where all molecules are chemisorbed) on metallic surfaces are always situated lower than that of a thick film [204, 205]. So a dependence on the work function can be ruled out. It is also possible that a thicker C_{60} film causes a charge accumulation effect due to its higher resistivity, but this can be mostly ruled out due to a conducting substrate, only still having a very thin film and the reasonable electron mobility of C_{60}. The peaks were only crudely fitted due to the high noise and relatively low intensity, and qualitative conclusions are more reliable than the small quantitative changes in the Si 2s peak. The relatively small changes in the Si is in contrast to the larger changes in the C 1s, but since the information depth of XPS is quite high, the spectra are averaged over multiple layers and therefore any changes to the surface would be averaged out.

The results taken here are largely in line with core level XPS spectra in the literature [184, 176]. The extra feature observed at 283.1 eV suggests a change in the bonding environment. This would be an initial state effect, caused by the hybridisation of the atoms in the C_{60} cage that interact with Si adatoms. A lower binding energy implies a gain in electrons, as the screening of the nucleus increases. The presence of this feature also reinforces the theoretical calculations predicting a localised transfer of charge [192], since not all of the C atoms are affected. An overall shift of 0.5 eV in the remaining "main" peak could be explained by a non-localised image charge screening effect, which would indicate a small amount of charge transfer into the unoccupied states of the molecule. The de-convolution of initial and final state effects is a difficult task that is dependent on the system studied [206] and was not performed here. However, considering the possibilities, the changes in the XPS spectra can be interpreted as pointing towards some amount of charge transfer into the unoccupied states in the C_{60}.

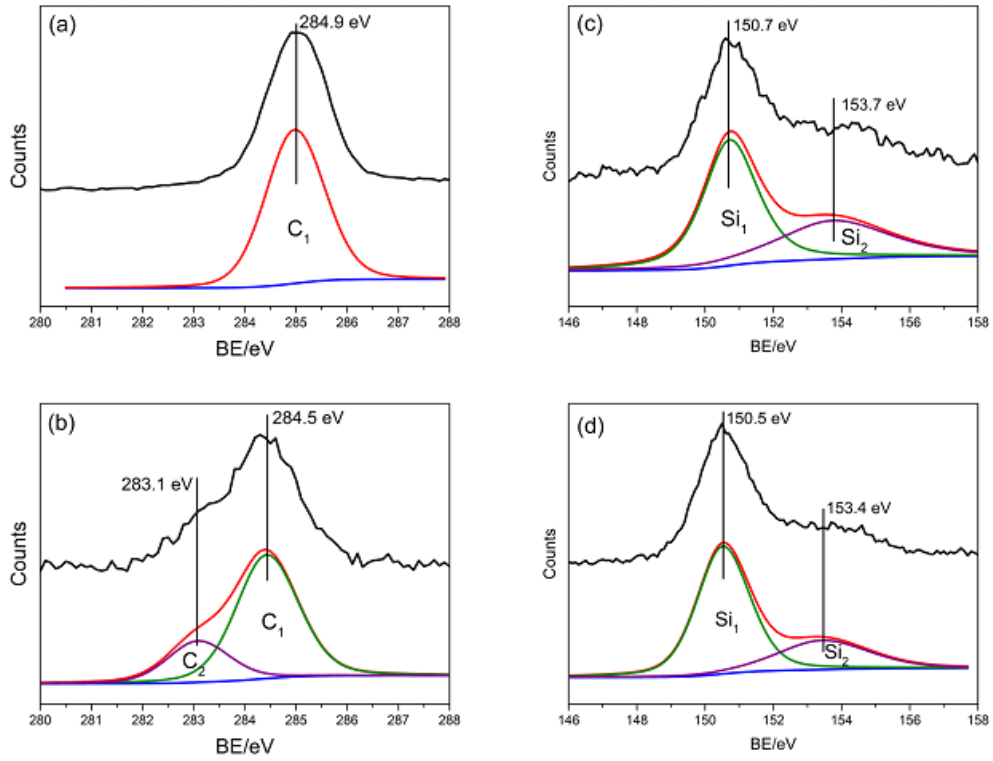

Figure 6.8: XPS spectra of C_{60} grown on Si(111) taken before and after annealing at 750 K for 10 minutes. (a) As deposited C 1s, (b) Annealed C 1s, (c) As deposited Si 2s and (d) Annealed Si 2s

6.3.3 MDS spectra

To possibly shed more light on the nature of the adsorption, MDS spectra were taken. As MDS would only probe the topmost atoms on the topmost layer of molecules, effects that diminish in UPS due to averaging over the entirety of the C_{60} cage are likely to be detected. MDS spectra were taken for a range of nominal sub-monolayer coverages with the spectra taken shown in figure 6.9. As a semiconductor with a high work function, the two-electron de-excitation process of resonance ionisation followed by Auger neutralisation occurs and a convolved spectrum is obtained. The three separate surface state peaks observed in the UPS spectra are replaced with two broad features located at kinetic energies of 17.2 eV and 15.2 eV. The higher kinetic energy peak is attributed to the Si surface state peaks s_1, s_2, s_3 [207] mentioned earlier in the chapter and the overall form of the spectrum is similar to that of INS and core-valence-valence Auger spectroscopy [208, 209]. These features remain dominant at a nominal coverage of 0.2 ML, which is in contrast to the UPS at the same thickness

where the peaks for the C_{60} molecular orbitals are more visible. Since the two step process is favoured, there are states present at the surface for the metastable $2s$ electron of the He 2^3S atom to tunnel into. This therefore confirms that there are still significant portions of the substrate exposed and a QCM-calibrated nominal thickness of 0.2 ML is below full monolayer coverage.

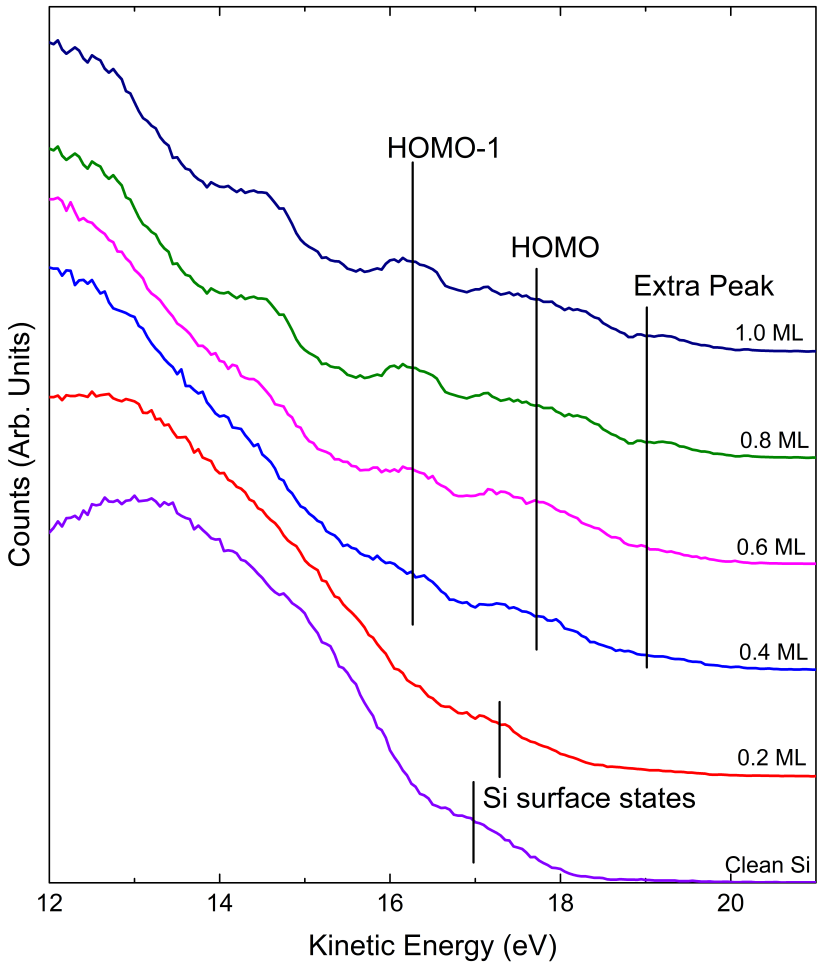

Figure 6.9: MDS spectra of C_{60} grown on Si(111) taken at different nominal sub-monolayer C_{60} coverages. Lines are drawn at very approximate positions due to the large broadening/splitting effects.

The form of the spectrum changes from a nominal coverage of 0.4 ML onwards. Two broad features are visible at approximately -2.1 eV and -3.2 eV from the maximum kinetic energy and can be attributed to the HOMO and HOMO-1 molecular orbitals

respectively. Although the exact positions are much harder to estimate due to the spectrum displaying much stronger splitting, the overall peak positions correspond well to the UPS spectra. This suggests a change in the de-excitation process when compared to the Si surface, from a two-electron scheme to the one electron Auger de-excitation mechanism. Therefore at this point the surface is likely covered in C_{60} molecules and further confirms the suspicion that a QCM-calibrated coverage of 0.4 ML is already close to a full monolayer of C_{60}.

While the MDS features are broadened in general when compared to the UPS peaks, splitting of the HOMO peak clearly exceeds this and suggests a lifting of the degeneracy in the h_u states in the C_{60}. Interestingly, unlike the UPS spectrum, the splitting in the MDS increases with greater coverage. For UPS, which probes the entirety of the atom, a splitting at low coverages is seen due to symmetry breaking effects at the interface such as dipole formation (breaking the symmetry in the molecule) as well as electrons becoming located in bonding states. However for MDS, since much of these effects are localised at the bottom of the molecules, the molecular orbitals at the top are less affected and there is little impact from this on the spectrum. The splitting of the MDS peaks at higher coverage can instead be explained via orientation. The orientation of the C_{60} molecule is often ignored in spectroscopy studies due to the high symmetry and electron mobility in the molecule allowing it to be treated as a sphere. But as discussed in chapter 2, the difference between the icosahedron and a sphere has a great impact on the electronic structure. For MDS this is especially so, since at only the top of the molecule, there is a greater variation possible in the geometry, i.e. the arrangement of pentagon/hexagon faces, and would create large differences in the electronic states probed. Therefore the narrow HOMO peaks in the MDS spectra at coverages up to 1.0 ML suggests good ordering in the film, with set orientations, which is likely since C_{60} has preferred bonding sites [183, 210] and site dependent orientations [199]. As the coverage increases, the interaction of the molecule-molecule Van der Waals forces is weak and therefore more orientations become possible due to thermal movement. This leads to a greater variety of geometrical states at the top of the molecule probed by the MDS and therefore a more pronounced splitting of the HOMO peak.

An extra feature not found in the UPS spectra is also present at a kinetic energy of approximately 19.4 eV, or -0.4 eV from the maximum kinetic energy. This would correspond to electron density at an energy level inside the HOMO-LUMO gap

of C_{60} molecule. Such a peak is not observed in UPS. Electron density present inside the HOMO-LUMO gap of the molecule has been theorised to exist in the anti-bonding state arising from the hybridisation of the C_{60} molecules with the Si surface [184]. However, there are several issues with this interpretation. Firstly, the charge transferred in the hybrid orbitals would be localised to the C atoms closest to the Si adatoms [192], and since the He* beam used in MDS has zero penetration into the sample, it is unlikely for the electrons detected to originate from hybrid orbitals located at the bottom of the molecule. Secondly, since the observed peak is located at an energy level of 1.7 eV above the HOMO level, and the HOMO-LUMO gap is close to this difference in energy (also 1.7 eV) [176], this electron density is originating from the LUMO level of the molecule, rather than an anti-bonding orbital at an energy slightly above the HOMO. Finally, the size of the extra peak increases in intensity with deposition up to 1.0 ML of nominal coverage, which is an estimated 2-3 ML of actual thickness. This suggests that the source of the extra density of states is not due to the interaction between the molecule and the surface, because the He* atoms would probe the physisorbed topmost layers only.

Another difference between the MDS and UPS spectra is in the shape of the HOMO peak. In the UPS, at higher coverages when compared to a single monolayer, the HOMO peak becomes narrower, taller and displays a single peak. On the other hand, the MDS peak remains at roughly the same intensity but is split into a broader range of peak energies. The source of discrepancy lies in the coverage of C_{60} for thicker films. Above 1 ML, the C_{60} molecules are physisorbed onto the first layer and no longer uniformly cover the surface [176], instead forming clusters. Although with much more C_{60} molecules deposited the clusters will eventually cover the surface, with the coverages shown here (<5 ML), much of the first monolayer will still be exposed. In the case of the UPS, the spectra will be the result averaged between all of the molecules probed by the UV light, which will overwhelmingly be the C_{60} in the physisorbed clusters. Therefore the spectrum shows a single, non-split peak similar to that of bulk fullerite [211], as even though it will probe a greater number of the molecules on the bottom layer, the signal from those will be averaged out by that from the clusters. In the case of MDS, the He* atoms only probe the topmost layer and therefore much of the first monolayer will still contribute to the spectrum, as long as significant clustering occurs and the majority of the first monolayer is not covered. The spectrum will then be a combination of the signal corresponding to

the first monolayer that is still exposed and the signal from the top few molecules in each cluster and the peak intensity will not increase by a large amount.

6.4 Discussion

6.4.1 Hybridisation-driven charge transfer

One theory put forward for the mechanism of charge transfer is via localised hybrid interface states [176, 184]. When the C_{60} molecule approaches the Si(111) surface, covalent bonds form: the molecular orbitals overlap with the dangling bonds of the Si to form sp^3 hybridised states. As the orbitals overlap, due to Pauli's exclusion principle forbidding the electrons from having the same quantum numbers, they split into two bonding and anti-bonding orbitals. This is part of the contribution to the splitting of HOMO peak in the UPS spectra for low coverages (along with broken symmetry due to a dipole forming at the interface).

Partial filling of the LUMO can then come about due to hybridisation of the LUMO with another dangling bond state. This creates a bonding state consisting of a filled orbital which is brought below the Fermi level and an unfilled anti-bonding state. A schematic of the proposed electronic structure is given in figure 6.10. This would correspond to the softening of certain HREELS vibrational modes as the occupation of the LUMO would soften C-C bonds [190] (i.e. the acceptance of electrons reduces strain in the cage). This process would also create an occupied state at just below the Fermi energy, which is at around the same energy as the extra peak in the MDS spectrum. It is not seen on the UPS spectra as the cross-section for partially-filled LUMO states is generally low, as seen in photoemission data for C_{60} on Au [212] and CO on transition metals [213]. Due to the relatively large distance between dangling bonds [184] (as a proportion of the radius of the C_{60} molecule), the hybrid orbitals are not necessarily located at the bottom of the C_{60} cage, but on the side, where the metastable helium atoms can reach.

There is, however, one major problem which is that the extra peak in the MDS is present at far higher coverages of C_{60}. In fact, the intensity of the peak increases at greater coverage, which indicates that the peak is not due to an interface effect. This does not invalidate the model for hybridisation driven charge transfer, but does

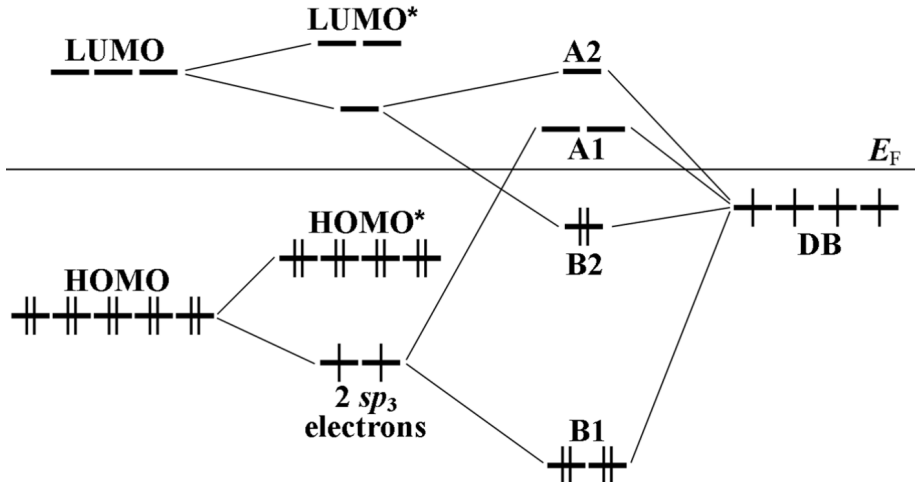

Figure 6.10: Diagram of the proposed energy levels for an adsorbed C_{60} molecule on the Si(111) surface adapted from [184]. A split occurs in the HOMO and the LUMO states upon adsorption and parts hybridise with the dangling bond (DB) states on the Si surface. B1, B2 are the bonding states and A1, A2 are the anti-bonding states. Hybridisation of the LUMO with the DB states creates a filed bonding state B2 just below the Fermi level and results in the partial filling of the LUMO.

mean that the origin of the extra peak in the MDS spectra likely lies elsewhere.

6.4.2 Physical effects of He* beam on C_{60}

The presence of the extra peak in the MDS spectra near the Fermi level is not easily explained by present models. If charge transfer is not used to explain the new peak, then one can turn to the possibility that the He* beam is able to cause a physical change in the C_{60} molecules. This change must be reversible, or only present in the presence of the He* atoms as UPS spectra taken after the MDS do not show a change. Therefore major changes to the shape and bonding of the cage can be ruled out.

However, it is possible to reversibly and temporarily break individual bonds in the cage with enough energy, which is a property used in the production of endohedral fullerenes [214]. Any changes occurring due to the helium beam impinging on the sample surface will have to be both reversible and short-lived, since UPS measurements taken after do no detect the changes; as well as having a relatively low energy barrier as the only energy available for such a change is the low kinetic energy of

the helium atoms, which have thermal energies in the meV range. When comparing to the experimental conditions used when creating endohedral fullerenes [215], the probability of temporarily breaking C-C bonds at UHV and room temperature is too low to have an appreciable effect on the spectra.

Nevertheless, it is prudent to confirm that no physical changes have taken place due to the helium beam with an experiment. A simple experiment was carried out to check this by performing UPS scans while the sample is subjected to the metastable helium beam. The experimental conditions were identical to the separate experiments, with the sample facing the analyser and positioned such that it can be subject to both the ultraviolet radiation and the metastable helium beam. The individual spectra were taken first in this position for comparison and then with both beams on at the same time. Since the emission due to the ultraviolet light is orders of magnitude greater than that of the helium beam, the resulting spectra can be thought of as the UPS spectrum for a C_{60}/Si sample under bombardment by a metastable helium beam.

The results are presented in figure 6.11. The MDS spectrum in the figure has been scaled with a multiplicative constant so it is visible on the graph for comparison. It has also been shifted so that the maximum kinetic energy (19.81 eV) lines up with that of the UPS (21.22 eV), i.e. lining up the Fermi level at 0 eV. From the graph, the peaks in the MDS corresponding to the C_{60} molecular orbitals line up nicely with those in the UPS spectrum. However, the key result is that the spectrum taken with the metastable helium beam on shows little difference to that of normal UPS. In particular, there is no presence of the extra peak near the Fermi level. This immediately rules out the possibility of a physical change due to the metastable helium beam.

6.4.3 Summary

The origin of the extra peak now has significantly fewer possibilities. First is an unconsidered quantum mechanical interaction between C_{60} and He*, which causes electrons to occupy a higher energy state. However, the dominant de-excitation mechanism is one electron Auger de-excitation, since the overall spectrum shape matches that of the UPS spectrum. In this case, further movement of electrons

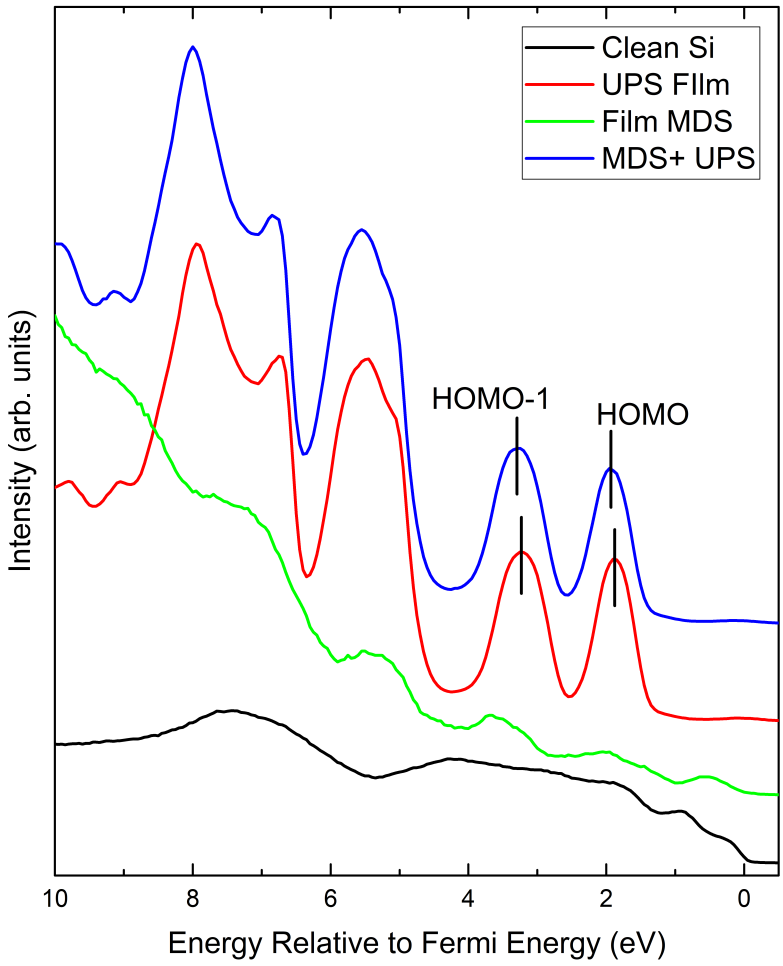

Figure 6.11: Graph comparing the UPS and MDS spectra with the UPS spectrum taken while the He beam was impinging on a sample of a high coverage (nominally 3 ML) of C_{60} on Si(111). The MDS spectrum has been scaled up for clarity due to a lower count rate when compared to UPS.*

between the surface and He* atoms will result in a convoluted spectrum as more electrons in the sample become involved, all originating from different energies in the valence band. Electrostatic interactions are also ruled out since the He atom does not form an ion at any point in the Auger de-excitation process.

Another possibility is that of contamination. A very thin layer would not be easily detected by UPS, but the MDS spectrum could change drastically. This is very unlikely due to the fact that all experiments were performed in situ inside a UHV

system. While the Si surface is very reactive and will pick up contaminants not long after cleaning, the probability of a C_{60} molecule doing the same is very low. The only possible source of possible contamination would be through the deposition process, if the source or evaporant was not sufficiently clean. But since this would yield a layer of roughly constant thickness (with random variations) on top of the C_{60} film after each deposition, and the peak in the MDS spectrum shows clear development with more deposition, the effect of contamination can be ruled out.

Since the intensity of the extra peak rises with extra coverage, this suggests that the peak is due to the C_{60} molecule itself, or an unknown interaction which occurs just between the C_{60} and the metastable helium atoms. This is very interesting as it seems to imply that there is somehow a filling of the LUMO band in thick C_{60} films at the surface. Interaction with the substrate also seems to affect this as the peak intensity is lower at 1 ML. To look for the origin of this, the next step would be to study a C_{60}/substrate where the interaction is weak and the molecules are chemisorbed. Despite not being able to pinpoint the origin of the extra feature in the MDS spectrum, this data was able to complement UPS data regarding the electronic structure and bonding at the surface. And due to the extreme surface sensitivity, the MDS spectrum was able to pick up the differences between orientations of fullerene molecules averaged over the sample, shown by the strongly split HOMO peak. This can be attributed to the changes in the interaction of the molecule with the helium atom, depending on the orientation of the molecule at the moment the metastable atom arrives.

Chapter 7

The C_{60}/LSMO Interface

7.1 Background

As a ferromagnetic oxide used in the earliest organic spintronic devices [16], $La_{1-x}Sr_xMnO_3$, or LSMO was chosen as the next substrate for C_{60} deposition. This material belongs to the family of perovskite manganites that have been studied extensively since a paper from Jonker and Van Santen in 1950 [216], which reported ferromagnetism in several manganese oxides with the general chemical formula $RE_{1-x}M_xMnO_3$, where RE is a trivalent rare earth cation and M is a divalent alkaline cation. Initial interest in these mixed valence manganites originally stemmed from their ability to display colossal magnetoresistance (CMR), but the requirement of very large magnetic fields (>1 T) vastly limited its practicality and widepread use. In 1998, Park et al. demonstrated that $La_{0.7}Sr_{0.3}MnO_3$ is a half-metallic material below its Curie temperature. Since then, LSMO has been included in a wide range of spintronic devices. Early organic spin valves made from LSMO and Co electrodes with an Alq_3 organic spacer layer reported high magnetoresistance (40%) at low temperatures [17]. And by depositing magnetic nanodots rather than individual atoms to reduce diffusion into the spacer layer, the MR of these devices can be further enhanced to around 300% [217]. Room temperature spintronic effects have also been demonstrated in organic spin valves employing an LSMO electrode [218].

Naturally, with two promising materials, the combination of C_{60} and LSMO has not gone unnoticed in the field, and a good amount of research has been funnelled into organic devices using this interface. For example, C_{60}-based organic spin valves

using LSMO and Co as electrodes have demonstrated MR at room temperature [219]. However, the performance of these devices have been lackluster in comparison to what their individual characteristics would suggest. Since hyperfine coupling has been identified as a limit to spin transport, an increase in spin diffusion length was expected with the use of C_{60} in organic devices, due to its minute hyperfine interaction. This was not observed in C_{60} based spin-valves [21]. The cause for this is not well understood and a variety of factors such as thickness and conductivity mismatch can affect the interfacial properties crucial to performance. Morphology induced disorders have also been found to affect the spin diffusion length in C_{60} films [220].

Therefore, in order to overcome the issues faced by the devices made thus, it is important to further investigate the electronic properties of the interface. A recent study performed photoemission measurements for C_{60} films ranging from 5 to 80 Ådeposited onto an LSMO substrate [221]. This study found a transition with increasing thickness from an n-type to a p-type organic semiconductor as the HOMO moves closer to the Fermi level for very thick films. An upwards band bending effect of 0.72 eV was found in the 80 Å film when compared to the 5 Å film, which becomes a barrier for the electrons moving from the molecules near the interface to the surface. Oxygen diffusion into the C_{60} film was also proposed, which explains a reduction in the LSMO surface (despite C_{60} being an electron acceptor) [221]. Electron spectroscopy therefore has the ability to greatly improve understanding in this field, but to study possible interfacial effects, a systematic study of the C_{60}/LSMO interface for lower coverages is required. To that end, UPS, XPS and MDS results for C_{60} films with a range of thicknesses (including submonolayer coverages) will be presented in the following sections.

7.2 $La_{1-x}Sr_xMnO_3$

7.2.1 Crystalline and Electronic Structure

As LSMO is a complex oxide system, it is useful to firstly summarise the structure and key characteristics of the material in order to better understand and interpret the data obtained. The crystalline structure of LSMO, like other manganites with

formula $RE_{1-x}M_xMnO_3$, has a structure close to that of standard cube perovskite crystals (figure 7.1). The larger RE and M ions occupy the A sites, which form the vertices of a cubic unit cell; the oxygen ions are located at the face centres of the unit cell and surround the A ions with 12-fold coordination; and the smaller Mn ions occupy the B sites, located at the centre of the unit cell, inside octahedral oxygen interstices. In the case of stoichiometric $RE_{1-x}M_xMnO_3$ oxide, the Mn^{3+} and Mn^{4+} exist in the structure with proportion $1-x:x$. For the case of manganites, there is a sizeable deviation from the perfect cubic structure into a rhombohedral or orthorhombic symmetry [222]. This is governed by a tolerance factor $t = (r_A + r_O)/\sqrt{2}(r_B + r_O)$, which is stable for $0.89 < t < 1.02$, with $t = 1$ in the perfect cubic case.

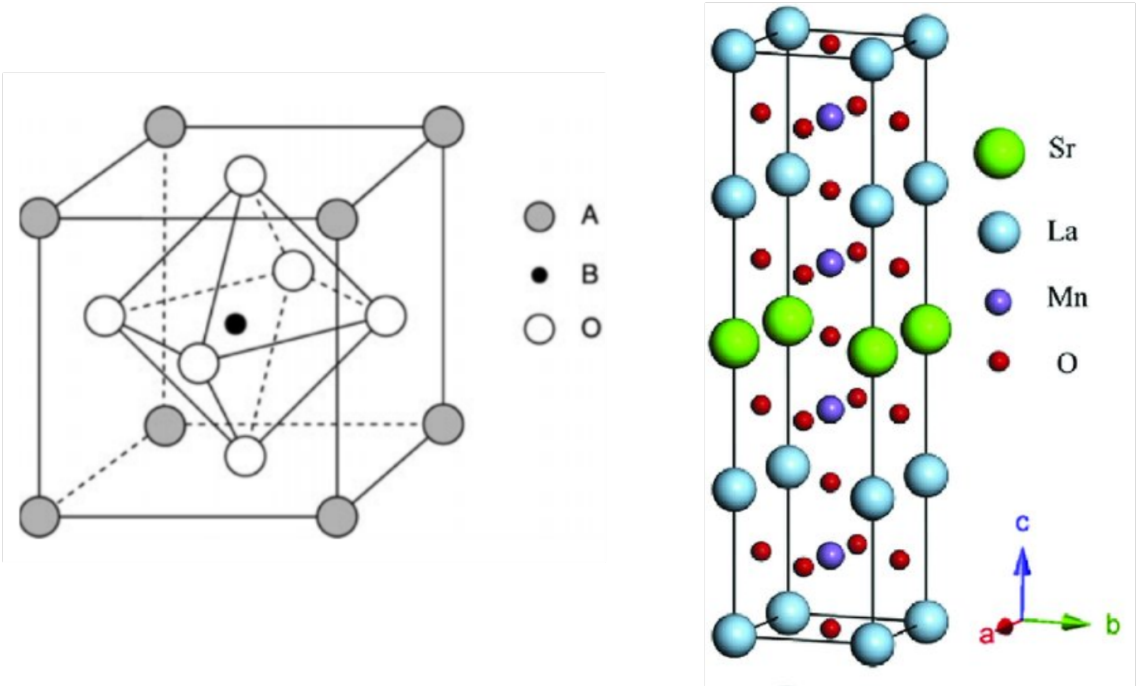

Figure 7.1: Diagram of the perfect cubic perovskite structure taken from [222] (left) and of $LaMnO_3$ (right) a diagram of the LSMO strcture, the system under study and a typical example of rare earth manganites. Figure taken from [223]

To describe the electronic properties of LSMO, we consider the $3d$ electron configuration of the Mn ion. Compared to the isolated $3d$ ion, which has five degenerate orbital states ($l = 2$), the octahedral MnO_6 in a cubic lattice causes a lifting of the degeneracy with three states at a lower energy level (d_{xy}, d_{yz}, d_{zx}), referred to as t_{2g}, and two states at a higher level ($d_{x^2-y^2}$, $d_{3z^2-r^2}$), referred to as e_g [224, 225]. The energy splitting between the lowest t_{2g} state and the highest e_g state is approximately

1.5 eV. Due to Hund's coupling, the three t_{2g} electrons are aligned parallel to form a 3/2 state. In the case of Mn^{3+} ions, the remaining $3d$ electron is also coupled to the t_{2g} state electrons as the exchange interaction energy is approximately 2.5 eV, much greater than the energy splitting [222]. In Mn^{4+}, there is no electron in the t_{2g} states.

In a non cubic-configuration, the degeneracy is further lifted by a Jahn-Teller distortion, caused by a coupling of the e_g electron with the displacement of surrounding oxygen ions, which further reduces the symmetry. Therefore, an abundance of Mn^{3+} ions will cause more elongation in the manganite crystal, the most extreme example of which is the parent compound $LaMnO_3$, which has its unit cell length approximately doubled. This is further enhanced as the individual effects from each Mn^{3+} ion are not independent from each other (cooperative Jahn-Teller effect). The crystal distortion can be controlled by doping the manganite, which changes the relative concentration of Mn^{3+} and Mn^{4+} ions. Alkaline metal dopants increase the number of Mn^{4+} ions in the structure, which in turn means holes are created at the e_g level. These are free to move within the lattice and they play the role of charge carrier. An illustration of the energy splitting relative to the distortion in the lattice is given in figure 7.2.

The magnetic properties of LSMO are also dependent on the interaction between the Mn ions' spins. The interaction is strong for two ions separated by an oxygen atom and is regulated by the overlap between the Mn $3d$ and O $2p$ orbitals. Generally, Mn^{3+}-O-Mn^{3+} interaction can be antiferromagnetic or ferromagnetic, Mn^{4+}-O-Mn^{4+} is antiferromagnetic, while the Mn^{4+}-O-Mn^{3+} can undergo an exchange in valence through a double exchange mechanism [226] to create a strong ferromagnetic interaction. Therefore, supposing the magnitude of the ferromagnetic (Mn^{4+}-O-Mn^{3+}) and antiferromagnetic (Mn^{4+}-O-Mn^{4+}) interactions are of the same magnitude (Mn^{3+}-O-Mn^{3+} can be disregarded as it can be both), we can roughly calculate the doping needed to aim for a ferromagnetic compound with highest T_C:

$$T_C \approx 2x(1-x) - x^2 \tag{7.1}$$

which yields a maximum at x $\approx$ 1/3. $La_{1-x}Sr_xMnO_3$ has been extensively studied due to its large T_C value at 370 K for x $\approx$ 1/3. It is also relatively easy to deposit from a single crystal [222] and $La_{0.7}Sr_{0.3}MnO_3$ has been shown to display half metallic nature at room temperature.

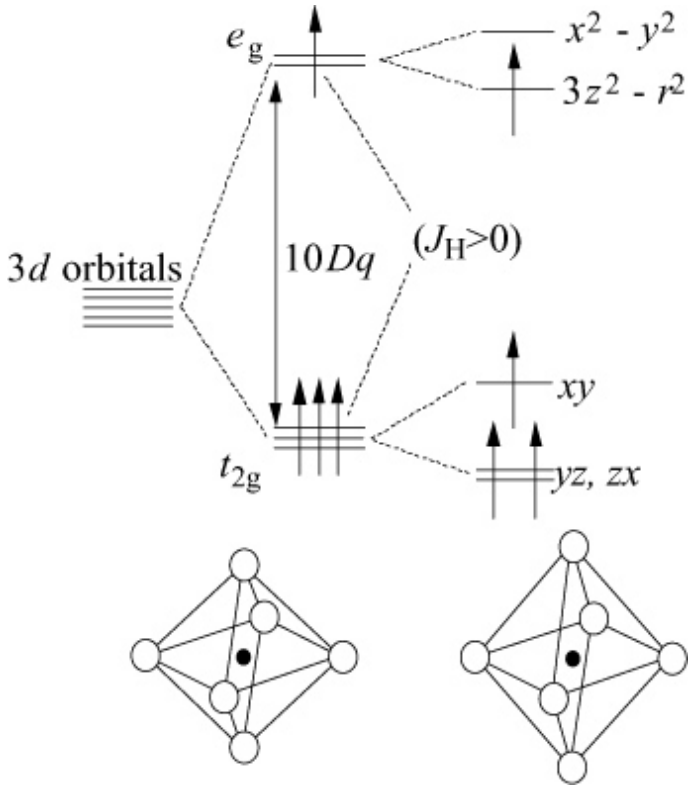

Figure 7.2: Illustration taken from [225] showing the splitting of the energy levels in the crystal and the corresponding crystal structures.

7.2.2 Surface Termination of LSMO

Before studying the properties of an interface between an LSMO thin film and an organic, the surface properties of the substrate need to be known. The surface cleaning procedures for LSMO have been shown to greatly affect the termination layer in manganites [13]. The stoichiometry of the surface can vary greatly from the bulk [227, 228], which, as detailed in the previous subsection, is crucial to the key magnetic properties of the material. It has been shown that the 100% spin-polarisation at the surface breaks down easily at low temperatures, and therefore causes the performance of devices employing LSMO to deteriorate even at room temperature, which is far from its Curie temperature of 370 K [229].

Studies in the literature have found a Sr-rich termination after cleaning for a range of oxygen pressures and temperatures [230, 231], mainly observed by x-ray photoemission techniques. A comparison of the relative intensities of La and Sr spectra at various emission angles shows an increase in the proportion of Sr at glancing angles - an indication of a Sr rich surface [232, 231]. These spectra also show little

change in the La $3d$ and Mn $2p$ peaks at different angles, while the Sr $3d$ peak shows a shift attributed to an increased in a surface contribution, suggesting that the surface segregation effect applies to the Sr ions only [232]. Figure 7.3 shows a set of XPS spectra illustrating this. This trend is seen for other manganites of the form $La_xA_yMnO_3$, where A = Ca, Pb [233, 234]. The extent to which the Sr segregation occurs does decrease with increasing temperature and partial pressure of oxygen [230], but the effect is still significant under all conditions and is seemingly an unavoidable property of these oxide systems.

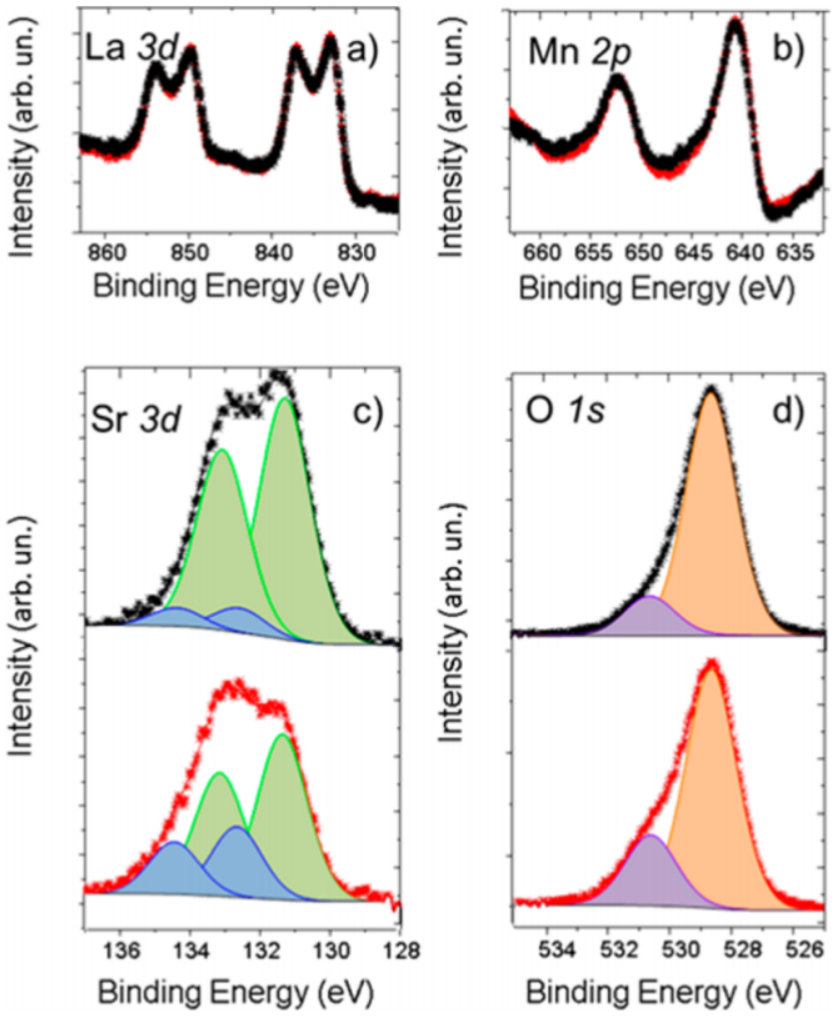

Figure 7.3: XPS spectra taken from [232] of the La 3d, Mn 2p, Sr 3d and O 1s peaks for the LSMO surface at different angles. La and Mn peaks were largely unchanged. For Sr and O data, top spectra were taken at normal emission and the bottom at 60°. A clear angle dependence is present and the component of the Sr peak attributed to the surface increases at glancing angles.

The LSMO thin films used in the experiments described below were supplied by Dr.

Ilaria Bergenti of the Institute for Nanostructured Materials at CNR-Bologna, as a part of collaborative work on organic spinterfaces. These samples were $La_{0.7}Sr_{0.3}MnO_3$ thin films with a thickness of 40 nm, grown on NGO(111) substrates via channel spark ablation (CSA). The process involves ablation of a stoichiometric polycrystalline target with a pulsed electron beam in an oxygen partial pressure of 4×10^{-2} mbar. More specific details of the growth process can be found in [235]. Thin films prepared using this method have demonstrated success as spin injection electrodes in spintronic devices, such as magnetically enhanced memristors and spin valves [236, 218]. AFM and XRD have been used to confirm the film thickness and shows a surface root-mean-square roughness of around 0.6 nm.

7.3 Experimental

Prior to putting the substrate into the vacuum system, the sample was first cleaned by sonication in acetone and ethanol for 5 minutes each. It was then gently heated in UHV at 500 K for 30 minutes by the PBN heater before taking data. This surface treatment method used to clean the surface has been shown to significantly reduce contamination, validated with XPS measurements [237]. Monochromated XPS measurements were taken before and after cleaning to verify that the process has cleaned the surface as expected. A comparison of these spectra is shown in figure 7.4. From the graphs, it is clear that the process of annealing has significantly reduced the intensity of the C 1s peak (though some still remain) while the other peaks of interest (La 3d, Sr 3d, Mn 2p, and O 1s) are mostly unchanged.

C_{60} molecules were then deposited onto the cleaned surface firstly for a range of sub-monolayer coverages, and then thicker films. The deposition was performed under the same conditions as for previous Si samples with the organic deposition source: 350 °C, which is the lowest temperature at which deposition occurs, or approximately 1.0 ML every 7 minutes. The deposition rate was calibrated using the QCM. The organic film was deposited in steps of 0.25 ML up to 1.0 ML. The thicknesses here were taken as half the nominal calculated values to reach a number closer to the true thickness, as discussed in the deposition of C_{60} on Si(111). MDS and UPS data was taken after each deposition and XPS was taken after reaching a thickness of 1.0 ML. Further data was then collected at 2.0 ML, 5.0 ML and 25

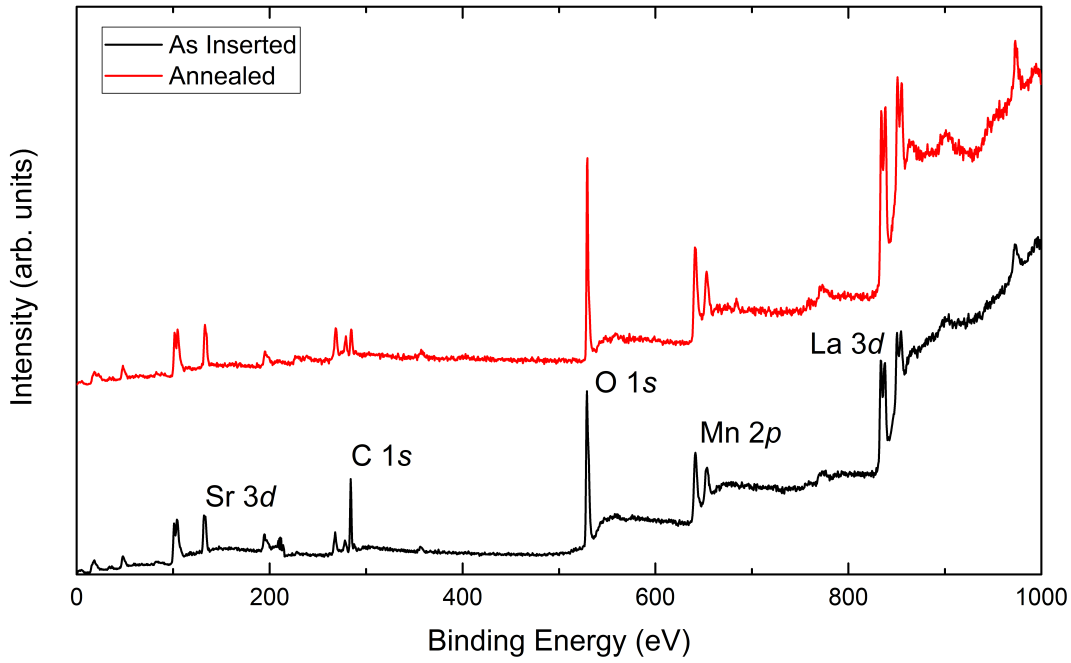

Figure 7.4: Graph comparing the XPS spectra of the LSMO substrate before and after annealing at 500 K for 30 minutes. The C 1s shows a significant reduction in intensity after annealing, while the other key features corresponding to elements in the sample remain largely unaffected.

ML thick films. At the maximum thickness, the sample was exposed to increasing amounts of oxygen gas (1, 10, 50 and 200 Langmuirs) and spectra obtained for each. This was done to check whether features of the spectrum could be attributed to oxygen migrating from the substrate into the organic layer. This oxygen exposure was done by increasing the pressure in the preparation chamber to 1.3×10^{-7} mbar (1×10^{-7} torr) for the appropriate amount of time (10 seconds per Langmuir). The gas doser is retracted in this case to keep the inlet far from the sample.

7.4 Results

7.4.1 Sub-MonoLayer C_{60} Coverages

The UPS and MDS spectra taken for the clean LSMO surface and after each 0.25 ML C_{60} deposition are shown in figures 7.5 and 7.6. In the UPS spectrum of clean

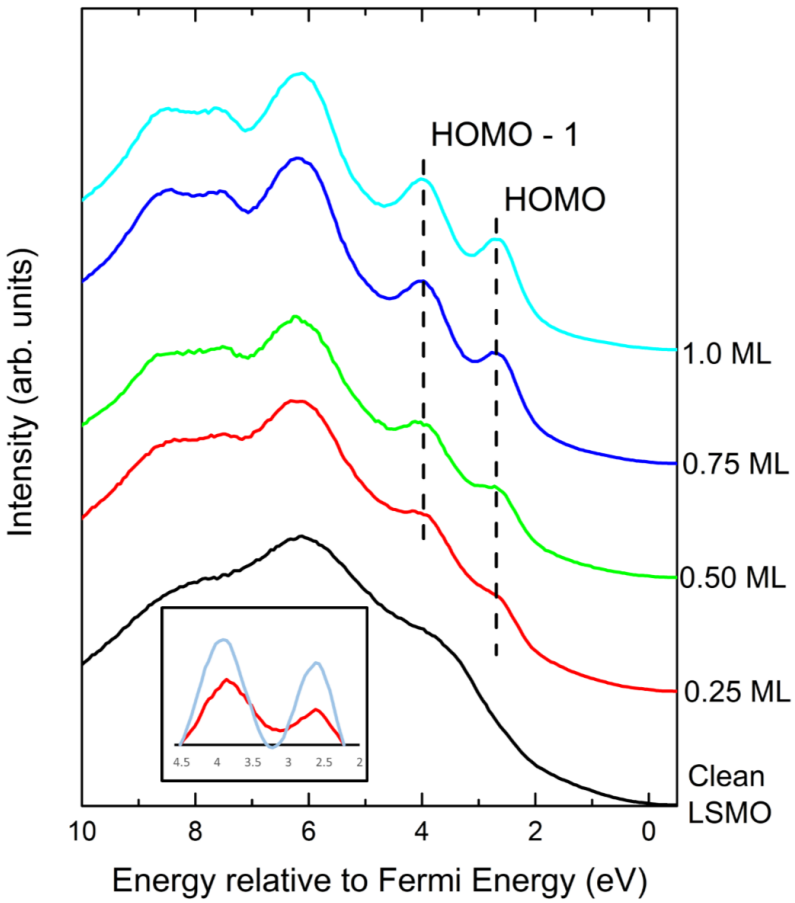

Figure 7.5: Graph of UPS spectra taken at various sub-monolayer deposition coverages. The HOMO and HOMO-1 peaks are labelled and dash lines were placed at the maxima of each peak in the 1.0 ML UPS spectrum. Inset: comparison of the HOMO and HOMO-1 peaks between 4.5 and 2.0 eV from the Fermi level after background has been subtracted. The "valley" between the two peaks in the 0.25 ML case is clearly shallower due to contribution from the broad LSMO peak, which causes the "valley" between the two peaks in the low coverage case to never dip down to background level.

LSMO, there are broad features at approximately 3.5 and 5.8 eV from the Fermi level. With deposition of C_{60}, the peaks corresponding to the HOMO and HOMO - 1 of the C_{60} appear at 2.7 and 4.0 eV from the Fermi energy respectively. These are located at a much higher binding energy than the same peaks for C_{60} deposited on Si, indicating a weaker interaction. In addition, the "background" for the UPS

spectra up to 1.0 ML shows a clear effect from the features of the clean LSMO surface. The broad LSMO peak at 3.5 eV from the Fermi energy manifests itself as a shoulder on the background between the HOMO and HOMO - 1 peaks; and the feature of the LSMO spectrum at 5.8 eV causes a broadening in the HOMO -2 peak. The effect is still present at 1.0 ML (although it diminishes with increased coverage), which indicates emission from LSMO and therefore incomplete coverage of the surface.

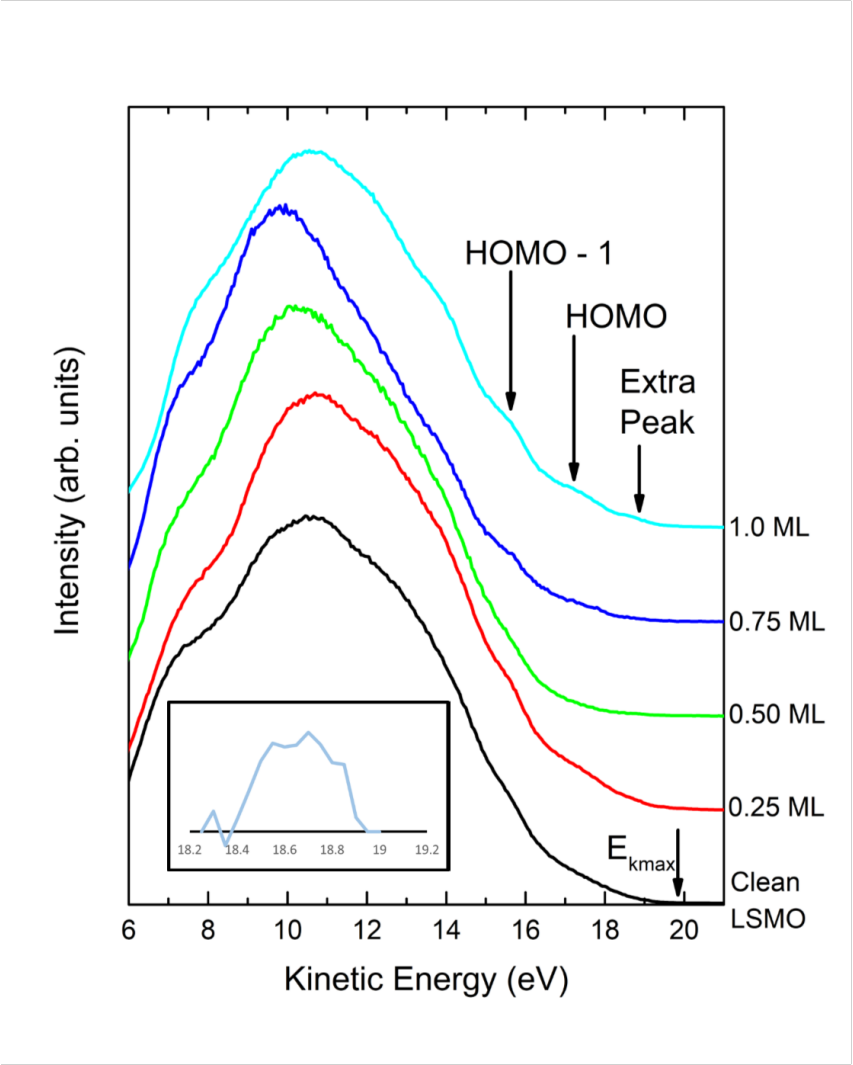

Figure 7.6: Graph of MDS spectra taken at various sub-monolayer deposition coverages. Only weak features are present, including the extra peak seen in the MDS spectra of previous C_{60} films. Inset: the extra feature in the MDS spectrum close to the kinetic energy maximum at 1.0 ML deposition.

Features are present in the MDS spectrum of clean LSMO at approximate kinetic energies of 14.5 ± 0.3 and 15.8 ± 0.3 eV. These features are very weak, owing

to the two-electron de-excitation mechanism that would occur on the manganite surface (work function 4.8 eV). Features corresponding to the deposition of C_{60} do not appear in the spectrum until 0.8 ML and above, located at approximately 17.2 $\pm$ 0.2 and 15.7 $\pm$ 0.2 eV. These peaks are very weak and it is therefore difficult to accurately pinpoint their locations, but the energies largely agree with the values obtained in UPS when aligning maximum kinetic energies. The extra feature near the Fermi level seen in earlier results is also present at a kinetic energy of 18.7 $\pm$ 0.2 eV (see inset on figure 7.6), although very weak. The weakness of the C_{60} features in the MDS spectra also suggests incomplete coverage. Stronger peaks are expected as the de-excitation process for C_{60} molecules is the one electron Auger de-excitation mechanism, and a weak signal means very few C_{60} molecules are being probed. This implies that the C_{60} molecules are forming clusters where only the top of the clusters can be probed by the metastable helium atoms. Overall, these spectra suggest a very weak interaction between the C_{60} molecules and LSMO surface, with the C_{60} - C_{60} interactions being more dominant, forming clusters of molecules on the surface and leaving much of the LSMO exposed.

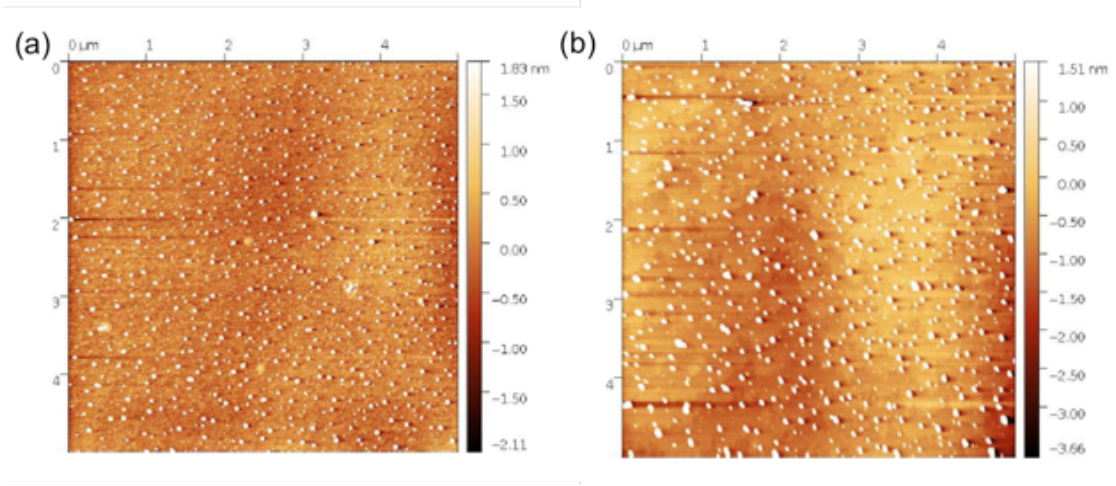

Figure 7.7: AFM images of C_{60} deposited on LSMO with thicknesses of (a) 0.5 nm and (b) 1.0 nm. Clustering is apparent at 1.0 nm which is above 1.0 ML in thickness.

Confirmation of this can be obtained through direct observation of the clustering of C_{60} on the LSMO at these coverages with microscopy techniques. Atomic force microscopy (AFM) data shown in figure 7.7 were provided by the group of I. Bergenti. These were performed on the same type of LSMO substrates (both synthesised by them) under very similar deposition rates. At 1.0 nm thickness film (which corresponds to >1 ML coverage), the molecules still aggregate into clusters and the

overall coverage of the surface is very low.

7.4.2 Thicker Films

The UPS and MDS spectra taken for C_{60} film coverages greater than (and including) 1.0 ML are shown in figures 7.8 and 7.9. At 2.0 ML, there is an significant change in the overall shape of the UPS spectrum. The effects on the spectrum that can be attributed to the LSMO surface largely disappear. There is also a perceptible shift in both the HOMO and HOMO - 1 peaks of 0.1 eV towards the Fermi energy. This suggests a much better coverage of C_{60} on the LSMO substrate. Judging from the shape of the 5.0 ML spectrum, however, the surface is likely not fully covered at 5.0 ML as the C_{60} peaks are still quite far from saturation (when compared to 25 ML). Most interestingly, at a 25 ML coverage, a small but clear feature is present close to the Fermi level at 0.7-0.8 eV. This would correspond to the extra feature found in the MDS at all coverages above 1.0 ML for this and previous samples.

The features on the MDS spectra are also much clearer from 2.0 ML onwards, supporting the UPS data in indicating a better surface coverage. The HOMO and HOMO - 1 peaks at 2.0 ML are located at 17.3 $\pm$ 0.3 and 15.5 $\pm$ 0.2 eV respectively. These are shifted from the approximate positions of the 1.0 ML spectrum, but since the features at 1.0 ML are faint and difficult to judge, it is hard to draw conclusions from the comparison. Unlike in the UPS spectrum, the shape of the MDS features clearly changes with deposition. The HOMO peak splits into a higher and lower component. At 5.0 ML, the HOMO peak begins to broaden when compared to 2.0 ML and at 25 ML, two separate features appear at 17.1 $\pm$ 0.2 and 17.7 $\pm$ 0.2 eV, with an overall intensity shift (and a shift of the HOMO onset) towards the Fermi level. The HOMO - 1 also undergoes broadening: a small shoulder begins to appear on the low binding energy side at 5.0 ML coverage (positioned at 15.8 eV), which increases in intensity at 25 ML. This trend of intensity shifting towards the Fermi level is also mirrored in the HOMO - 2 peak. Beyond that, there is a significant increase in the secondary emission at higher coverages which makes peak positions difficult to judge.

A possible avenue for the splitting in the MDS spectrum is the average distribution of orientations of the C_{60} molecule. The orientation is largely not considered in pho-

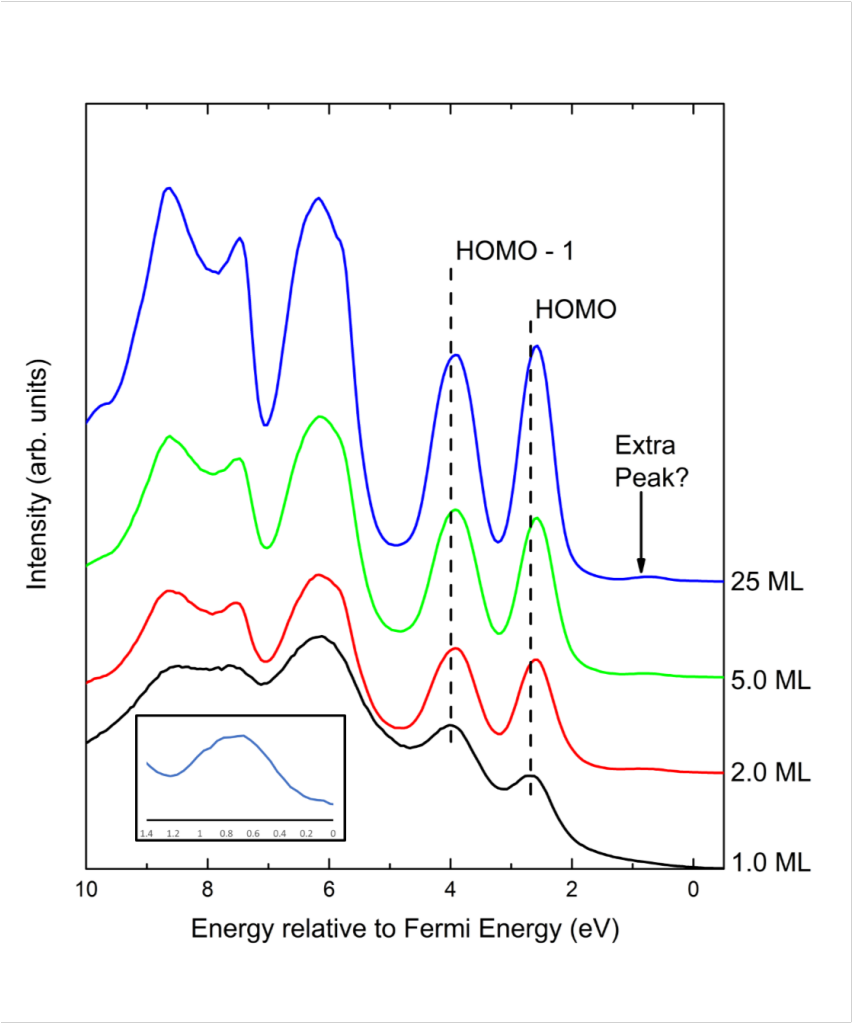

Figure 7.8: Graph of UPS spectra taken at various deposition coverages greater than 1.0 ML. Dashed lines were placed at the peak maxima points in the 1.0 ML UPS spectrum. An extra feature has appeared in the UPS spectrum close to the Fermi level (approximately 0.7 eV from E_F). Inset: an extra peak in the UPS spectrum close to the Fermi energy, which could correspond to the extra feature seen in the MDS.

toemission studies involving C_{60} due to its high symmetry and is generally treated as a spherical molecule. But as discussed in the case with C_{60} on Si, the surface sensitive nature of MDS means that the top face of the molecule is likely to have an effect. The final broadened features, much like in the case of C_{60} on Si, would be dependent on the orientation of the molecule at the moment when the interaction between the molecule and the helium atom occurs. Although we cannot identify any specific orientation as the molecule can rotate freely due to thermal energy [54], this is a possible contributor towards a more broadened peak in the MDS spectrum

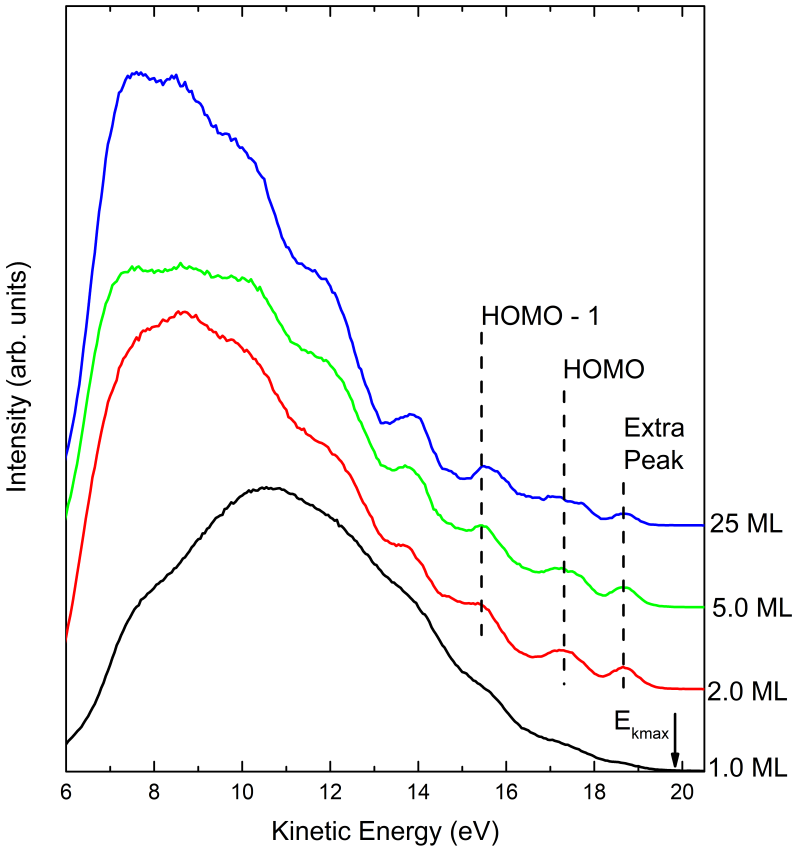

Figure 7.9: Graph of MDS spectra taken at various deposition coverages greater than 1.0 ML. Dashed lines placed at the peak maxima of the 2.0 ML MDS spectrum (1.0 ML features were too weak to accurately place).

as the helium atoms are probing a range of orientations at any given moment.

A confirmation of the coverage can once again be provided through AFM. AFM images for C_{60} film thicknesses on LSMO of up to 30 nm were provided by the group of I. Bergenti and are shown in figure 7.10. These show continued clustering of the C_{60} molecules up to 15 nm, which is greater than 5 ML. However at 30 nm, a continuous and relatively flat film is formed. This signifies that the formation of a regular bulk fullerite-like structure has become energetically favourable, and has overcome the amorphous aggregation. While the 25 ML coverage is less than 30 nm in thickness, the AFM images can be taken as confirmation that at very high coverages, a flat film is formed and this would agree with the changes in the MDS spectrum at 25 ML.

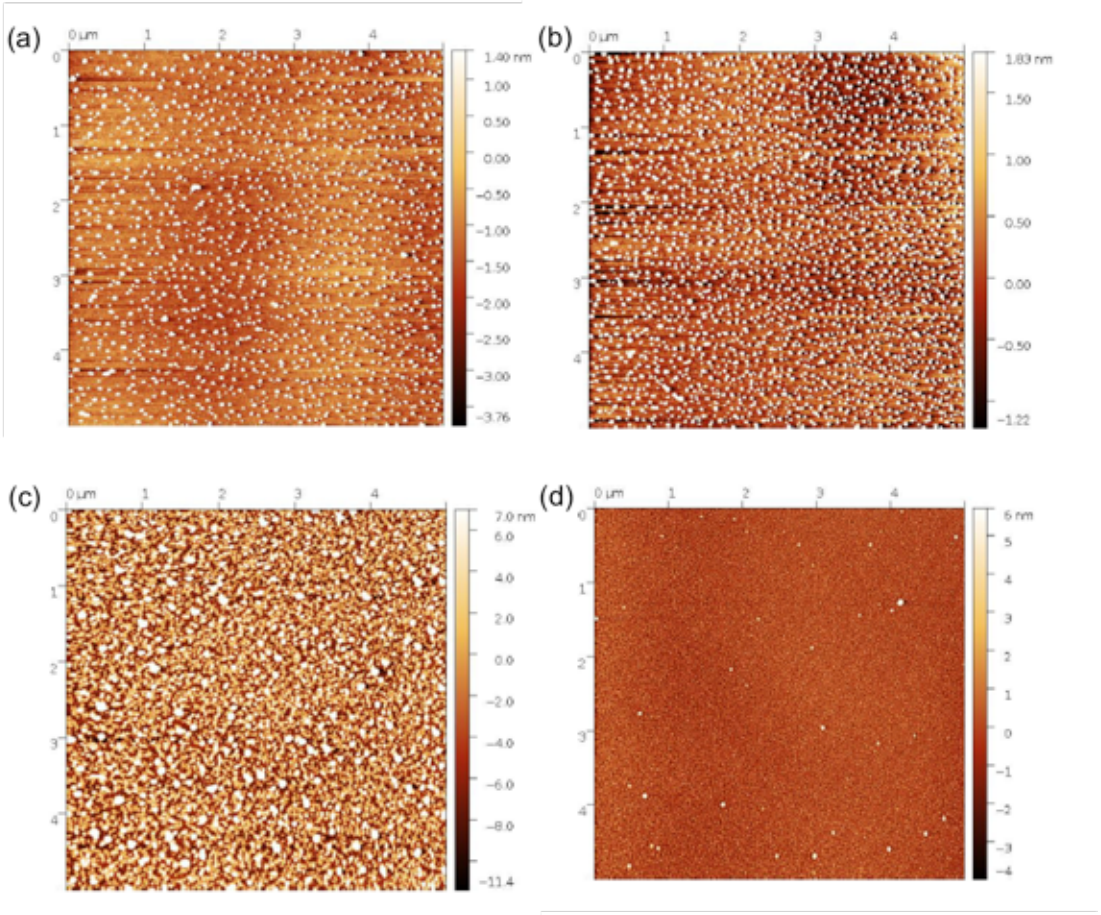

Figure 7.10: AFM images of C_{60} deposited on LSMO with thicknesses of (a) 2.0 nm and (b) 5.0 nm (c) 15 nm and (d) 30 nm. The surface is not fully covered even at 15 nm (approximately 20 ML) of deposition. At 30 nm, a relatively flat film of C_{60} is formed.

7.4.3 Oxygen Exposure

The UPS and MDS spectra of the thick C_{60} film taken for a range of oxygen exposures are shown in figures 7.11 and 7.12. In the UPS spectrum, there is also a slight but perceptible shift towards the Fermi energy at up to 10 L, and this increases to a bigger 0.1 eV shift at 50 and 200 L. This trend is mirrored in the HOMO - 1. Although there is a drop in the overall intensity, the peak shapes are largely the same. In the MDS spectrum, the exposure of oxygen caused an enhancement of the existing features. This effect is apparent at 1 L of oxygen and becomes very clear at 10 L and 50 L. Unlike the 25 ML spectrum, where the splitting of the HOMO is very vague, at 50 L of O_2 exposure, the HOMO is clearly resolved into two separate components. The HOMO - 1 peak is likewise enhanced relative to the background.

However, in contrast to the UPS, where there is an overall shift towards the Fermi level, the increase in intensity for the MDS features are more skewed towards a higher binding energy. The parts of the HOMO and HOMO - 1 peaks at 17.1 and 15.5 eV (as seen in figure 7.12) are more enhanced than the parts at 17.7 and 15.8 eV. This in turn means there is an overall shift in intensity away from the Fermi level. The extra peak is also enhanced with oxygen exposure, but no visible shift occurs. The trend in the MDS reverses at 200 L. There is a drop in the overall intensity of the features from 50 L of exposure. In addition, the intensity in the peaks shifts back towards the Fermi level. In the HOMO peak, the proportion of the 17.7 eV component increases visibly and in the HOMO - 1, there is a shift in the maxima accompanying an increase in the component at 15.8 eV.

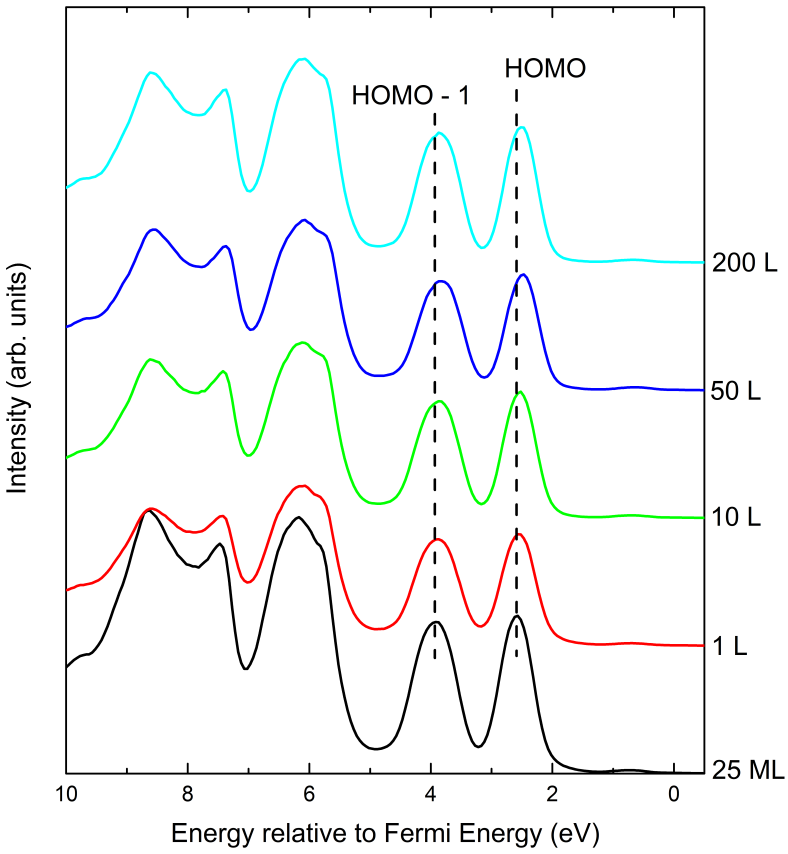

Figure 7.11: Graph of UPS spectra taken after different amounts of exposure to oxygen. Dashed lines were placed at the peak maxima points in the 25 ML spectra. The peaks show a perceptible shift towards the Fermi level as oxygen exposure increases.

Unlike photoemission scattering cross sections, the probability of a de-excitation event occurring when a metastable helium approaches a sample is unity. This seems to indicate that an enhancement in the signal has somehow caused an increase in the number of C_{60} molecules available for probing via MDS. One possibility to consider is that the exposure to oxygen has changed the morphology of the surface. An increase in the surface roughness would increase the surface area available for probing. However, since all atoms in the helium beam travel in roughly the same direction at the sample and the overall sample size has not increased, the greater surface area would not result in a noticeable increase in the yield as the solid angle of the beam which impinges on the sample has not increased.

Another possibility is that the yield has increased not because of more de-excitation events, but the number of electrons that reach the analyser has increased. The only possible avenue for this would be a change in the angular dependence of the emission due to Auger de-excitation. Any electrostatic effects due to an oxygen-doping related accumulated charge to dipole can be ruled out since that would cause an acceleration of the emitted electron and therefore a shift in the peak position, which is not present. Given that both the helium atom and the C_{60} molecules are fairly spherically symmetric species, the probability of an angular preference is rather unlikely and these effects would create an increase in the overall intensity rather than enhance the features.

A final consideration is the removal of contaminants on the surface from exposure to the oxygen gas. If there was some level of very thin and incomplete coverage of contamination on the surface of the deposited samples, that would attenuate the signal from the C_{60} molecules. If the contaminant layer is able to react with oxygen gas and then be carried away then it would explain the change. The most likely source of contamination is the deposition process, where the sample was exposed to the highest pressure. While this is the best explanation, there is no way to check it since previous XPS data did not indicate the existence and therefore there is only a trace amount; taking the sample out of the UHV system for other techniques would immediately subject it to much heavier contamination.

The dip in the feature sharpness at 200 L breaks the trend. While the shorter and broadened HOMO peak seems to suggest a reversal of previous oxygen exposure effects, upon closer inspection, the higher binding energy peaks are not less defined,

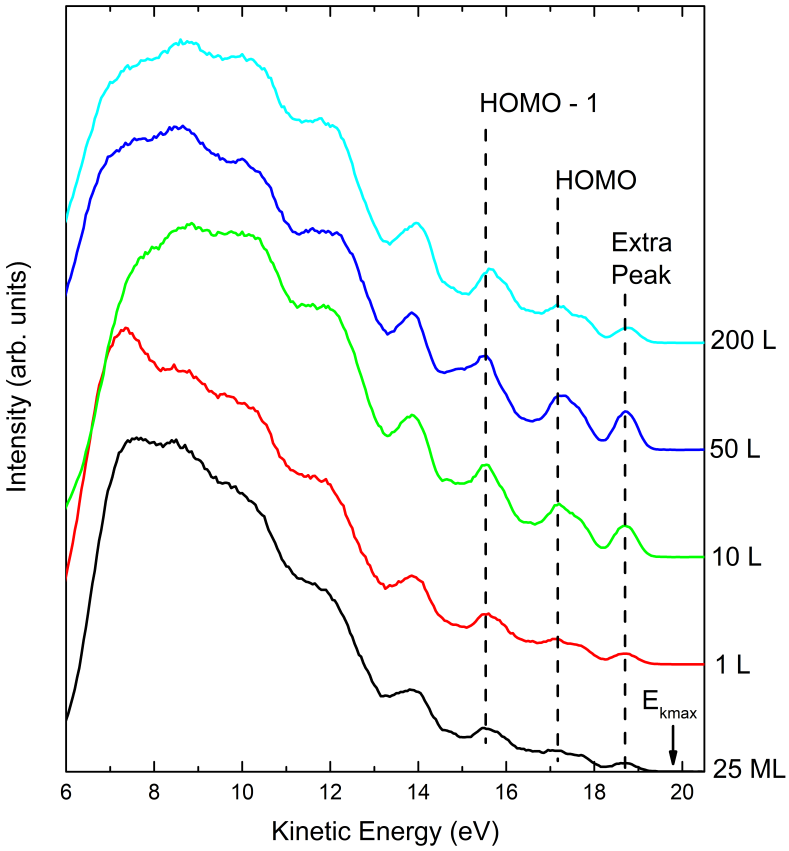

Figure 7.12: Graph of MDS spectra taken after different amounts of exposure to oxygen. Oxygen gas is allowed into the chamber at a pressure of 5 × 10^{-8} mbar and exposure of the sample to the oxygen is timed to the desired amount. The above graph shows MDS spectra taken after increasing amounts of oxygen dosage at various points from 1 Langmuir to 200 Langmuirs. The spectrum shows a change in peak shapes accompanied by an enhancement in the peak intensities.

such as in for the HOMO - 2 and HOMO - 3 peaks. The effect of the long oxygen exposure is therefore a change in the electronic structure rather than a diminuation of the overall signal. Since the oxygen molecules can diffuse between the gaps in the C_{60} lattice from the LSMO surface [221], then naturally one can assume that the reverse can also occur. The increased oxygen exposure could cause a build up of oxygen in the film and cause a doping effect that reduces the occupation of the least bound states. This would explain the clear diminishing in the HOMO and extra peaks, which is not shared by the peaks corresponding to the more tightly bound

states. If this were the case, a level of relatively permanent oxygen concentration in the sample would be required, which may be probed with XPS.

7.4.4 XPS Spectra

A graph of the XPS spectra taken for this system is shown in figure 7.13. As the thickness of the film increases, the signal from the La $3d$, Mn $2p$ and O $1s$ peaks corresponding to the LSMO surface diminish. The C $1s$ peak naturally increases in intensity as the amount of C_{60} increases. The features from the LSMO elements are still visible at 5 ML, which confirms the AFM images earlier that there is clustering in the surface and some of the LSMO surface is still exposed. At 25 ML all peaks except the C $1s$ peak disappear, signifying that a complete thick film has formed, and that there is nothing else within the information depth of the XPS that is able to be probed. After 200 L of oxygen exposure, there is no evidence of the presence of oxygen at the surface, which disagrees with the suggestion that there is oxygen doping at or near the surface.

The results from the graph are largely as expected and agree with the UPS, MDS and AFM data described above. However, the spectrum taken after 200 L of oxygen exposure comes as a surprise. The change in the MDS spectrum would suggest enough oxygen is present to cause a shift in the surface electronic structure but the XPS shows nothing. This indicates only a trace amount of oxygen is present at the surface. It is possible that the accumulation of oxygen decays over time and the presence of the oxygen is negligible by the time the XPS data was taken (the data was taken in the order of most-to-least surface sensitive: MDS, UPS then XPS). However, MDS also takes a fairly significant amount of time, and since decay through random processes is expected to follow an inverse exponential function against time, the MDS spectrum should visibly change over time. However, an examination of the spectra (15 total scans in series) shows that there was little-to-no change.

This leaves the possibilities of either the oxygen exposure causing irreversible physical changes to the sample, or trace oxygen on the surface being enough to cause a sufficiently strong interaction to alter the MDS. The former is somewhat unlikely as the oxygen pressure was not changed from the 50 L exposure, merely increasing the time. For the other possibility, it is somewhat supported by an almost imperceptible

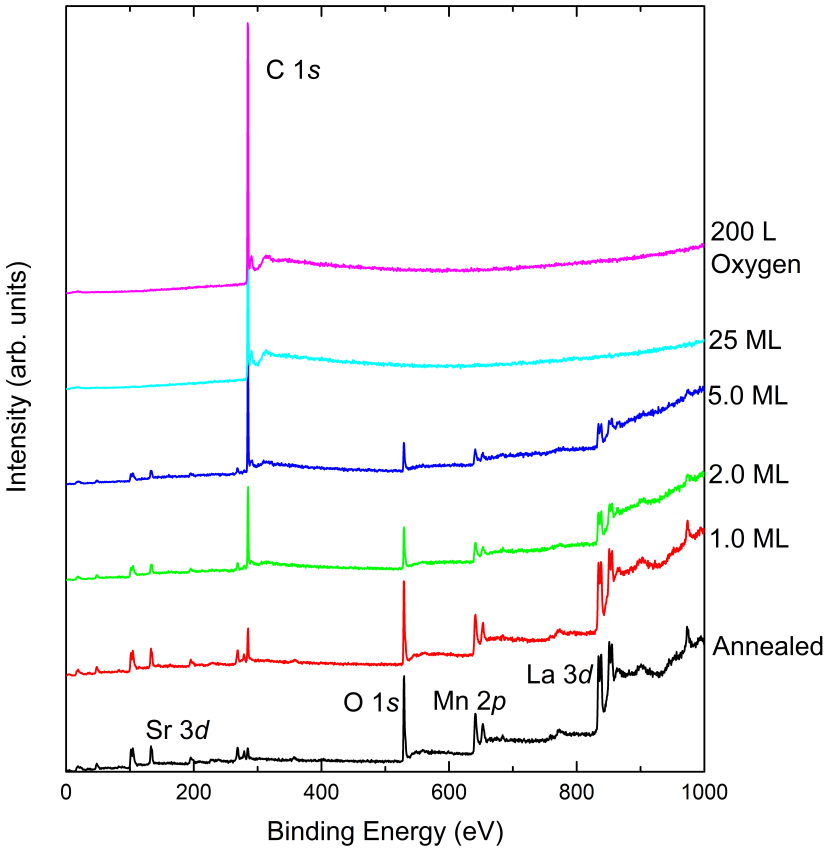

Figure 7.13: Graph of XPS data taken after various depositions coverages and after long oxygen exposure. The peaks of interest are marked. It is clear that at 25 ML deposition, there is a thick film of C_{60} on the surface with little else. After deposition to 25 ML, the sample is exposed to 200 Langmuirs of oxygen gas. No oxygen is present in the XPS spectrum even at 200 L of oxygen exposure.

shift in the UPS spectrum away from the Fermi energy, suggesting a more strongly bound state, which could come about from a loss of electrons from the C_{60}.

7.4.5 Extra Peak

The presence of the extra peak in the weakly C_{60}/LSMO interface conclusively rules out the theory that the feature is due to the formation of a hybridised orbital in the C_{60}/Si system. With a charge injection barrier of 0.61 eV [221], charge injection into the C_{60} from the LSMO is highly unlikely. If the sharpening of the MDS

spectrum after oxygen exposure is due to the removal of contaminants as discussed above, then the possibility of the peak being a result of contamination can also be excluded. From the discussion in the previous chapter, the remaining idea is that of partial LUMO occupation at the surface of the C_{60} film.

The results from the C_{60}/LSMO interface adds an interesting point to this discussion. There is an appearance of a very weak feature at the corresponding energy (to the extra peak) in the UPS spectrum for very high coverages (25 ML). Since the scattering cross section for partially filled LUMO states is very low [212], this small feature would correspond to a much bigger peak observed in the MDS spectrum, as the scattering cross section for surface states is unity for MDS. In the MDS spectrum after the 200 L oxygen exposure, the size of this feature falls visibly along with the intensity of the HOMO, while the more tightly bound states are less affected. This could indicate that the feature corresponds to real density of states in the sample, with a response to the high oxygen exposure, rather than a byproduct of the metastable de-excitation process. However, with no clear source of energy or extra charge, the author is unable to explain how the electrons are promoted into the LUMO of the C_{60}.

7.5 Summary

The electron spectroscopy and AFM results of the C_{60}/LSMO interface has shown that the C_{60} molecules do not form a uniform film at the surface even up to depositions significantly greater than 1 ML. This indicates that the interaction between the C_{60} molecules is stronger than between the C_{60} and the LSMO surface. Only at deposition up to 25 ML does a flat film appear. This could be a rather disappointing result for the potential performance of the interface in devices as the coupling between the magnetic surface and the molecule is poor.

The presence of the extra peak near the Fermi energy in the MDS spectrum of C_{60}/LSMO ruled out certain possibilities discussed in the previous chapter. The data points to the existence of a partially filled LUMO state at the surface of the C_{60} film, although with the data on hand it is difficult to pinpoint the origin of the charge and energy needed if this is the case.

The MDS data again demonstrates that the technique is able to probe differences in the rotational orientations of the C_{60} cage. The single HOMO peak from the corresponding UPS is resolved into multiple peaks in the MDS spectra, which can be assigned to different "sides" of the C_{60} cage pointing into vacuum. Oxygen exposure was found to enhance the features in the MDS spectrum but no evidence of lingering oxygen could be found in the XPS data.

Chapter 8

Conclusions and Further Work

8.1 Conclusions

This thesis describes the development and extension of an advanced facility for performing electron spectroscopy and its application to the study of various materials relevant to organic electronics and spintronics. Adding a monochromated x-ray photoelectron spectroscopy (XPS) source to pre-existing capabilities for performing ultraviolet photoelectron spectroscopy (UPS) and metastable de-excitation spectroscopy (MDS) has resulted in the only system in the world in which these three surface analysis techniques are combined on the same instrument. As demonstrated in the later chapters of this thesis, this approach allows a huge amount of data on the electronic, magnetic and chemical properties of a material to be obtained in a relatively short space of time from the same sample surface.

To validate the installation of the monochromated XPS source and gain experience in the technique, a dedicated study of graphene oxide samples prepared under different conditions and before and after the application of an electric field was performed, as described in Chapter 4. The results demonstrated the power of XPS in determining the rich carbon chemistry of graphene oxide and its sensitivity to chemical shifts of core electronic states. Determining the C/O ratio of various graphene oxide films, and whether they changed after different treatments, was an essential contribution to demonstrating the efficacy of this material in the filtration of organic solvents [38] and electric-field controlled water permeation [116].

As described in Chapter 3, the technique of MDS is extremely surface sensitive and therefore ideal for probing the adsorption of molecules on different substrates. Despite this applicability to materials systems relevant to the development of organic electronic and organic spintronic devices, MDS and spin-polarised MDS are not common techniques, largely due to the complexity in their operation and interpretation of the associated data. Indeed, the system developed at York is the only instrument for performing MDS in the U.K. and one of only a handful around the world. It has therefore been both novel and timely to apply it to the study of C_{60} on both semiconducting (Chapter 6) and ferromagnetic substrates (Chapter 7).

To gain experience in spin-polarised MDS (SPMDS), work was conducted in the Spin Characterisation Group of Dr. Yasushi Yamauchi at the National Institute for Materials Science (NIMS) in Tsukuba, Japan. As outlined in Chapter 5, a co-deposition growth method for producing high-quality $Fe_3O_4(100)$ films was established and used to prepare substrates for the study of Fe/Fe_3O_4 interfaces. SPMDS confirmed results from earlier studies which showed that the two ferromagnetic layers in these interfaces are antiferromagnetically coupled, suggesting their potential use as synthetic antiferromagnets in spintronic devices. The surface sensitive nature of SPMDS also revealed an interesting 'surfactant' effect in which a residual oxygen layer, presumably originating from the Fe_3O_4 substrate, is always present at the top of an Fe film growing on this substrate. Following this work at NIMS, the growth protocol was implemented in York allowing the production of high-quality Fe_3O_4 films, as verified using XPS, UPS, and MDS.

To test the growth and study of organic semiconductor interfaces, a study of C_{60} on Si(111) was performed. This system was chosen as a prototype for testing the developed instrument due to its ease of preparation and various uncertainties that still exist regarding its properties, for example the nature of charge transfer from Si to C_{60}. A systematic MDS study of sub-monolayer and multilayer C_{60} films on Si(111) revealed the presence of an extra feature close to the Fermi energy that is barely observable using UPS. This has been tentatively attributed to the filling of the C_{60} LUMO band although the exact origin of this effect requires further investigation. Additionally, the HOMO state was observed to split into multiple components using MDS becoming more pronounced with thicker coverages of C_{60}. Whereas the HOMO state in UPS splits due to the broken symmetry associated with adsorption of C_{60} at the Si(111) surface, the splitting in MDS is attributed

to resolution of states appearing on the different pentagonal and hexagonal faces of the C_{60} molecule. Distinction of these states is a very interesting observation that highlights the power of MDS in probing outermost molecule orbitals. It will help in efforts to understand and control the structure of C_{60} through functionalization for various applications.

Finally, C_{60} was deposited onto LSMO, one of the more device-relevant substrates available and a material that has attracted particular attention in the field of organic spintronics. The combination of electron spectroscopy techniques used, in addition to complementary scanning probe microscopy images, revealed that C_{60} grows in clusters on the LSMO surface suggesting that it is not suitable for use in organic spintronic devices. Only at relatively thick coverages of approximately 25-30 nm does a C_{60} film appear to form more uniform layers on LSMO. Such findings are significant as much attention has been paid to both C_{60} and LSMO and their possible combination in a device structure.

As a whole, this thesis demonstrates the need for complementary electron spectroscopy studies of technologically-relevant materials and interfaces in order to understand the critical relationship between properties and device performance.

8.2 Further Work

There are still further developments to the UHV chamber that need to be carried out in order for the system to work to its full capabilities. First and foremost is the completion of the SPMDS apparatus. In order for the technique to be fully functional, the spin polarisation of the helium beam needs to be optimised with a clear signal observed on the Stern-Gerlach analyser. The operating conditions of the technique will then need to be calibrated, which includes the finding optimal current settings for the Helmholtz coils and checking that the pulse magnet is producing a sufficiently strong field.

Another improvement on the existing UHV system would be the adding of the Mott polarimeter. The Mott polarimeter is used to measure the spin polarisation of emitted photoelectrons and therefore would add spin-polarised UPS capabilities to the system. As well as obtaining magnetic data on its own, this would also be used

to verify the findings from SPMDS.

For experiments, with an operational SPMDS, the spin-resolved data for C_{60}/LSMO would be the next step. The project covered the study of C_{60} molecules on a strongly interacting semiconductor substrate and a weakly interacting ferromagnetic substrate. A possible step forwards is to study interface between C_{60} a ferromagnetic $3d$ transition metal, such as Fe or Co to contrast with the weakly interacting LSMO substrate.

Moving beyond C_{60}. Next steps could include functionalised C_{60} molecules, with a radical group designed to enhance the interaction between the surface and the molecule. There is also a myriad of other OSCs that make good candidates for study. Flat molecules such as phthalocyanines and porphyrins could exhibit strong interactions with substrates if they lie flat on the surface. Conjugated polymers and aromatics, such as T6 (sexithiophene), have also been used in various electronic and spintronic applications. More exotic choices are also available, such as double decker molecules (e.g. $TbPc_2$).

Bibliography

[1] R. Das, K. Ghaffarzadeh, and X. He, "Printed, organic & flexible electronics forecasts, players & opportunities 2017-2027," *IDTechEx, Cambridge, UK, Tech. Rep*, 2017.

[2] T. Sekitani, H. Nakajima, H. Maeda, T. Fukushima, T. Aida, K. Hata, and T. Someya, "Stretchable active-matrix organic light-emitting diode display using printable elastic conductors," *Nature materials*, vol. 8, no. 6, p. 494, 2009.

[3] S. R. Forrest, "The path to ubiquitous and low-cost organic electronic appliances on plastic," *Nature*, vol. 428, no. 6986, p. 911, 2004.

[4] H. Sirringhaus, N. Tessler, and R. H. Friend, "Integrated optoelectronic devices based on conjugated polymers," *Science*, vol. 280, no. 5370, pp. 1741–1744, 1998.

[5] J. A. Rogers, T. Someya, and Y. Huang, "Materials and mechanics for stretchable electronics," *science*, vol. 327, no. 5973, pp. 1603–1607, 2010.

[6] T. Cramer, B. Chelli, M. Murgia, M. Barbalinardo, E. Bystrenova, D. M. de Leeuw, and F. Biscarini, "Organic ultra-thin film transistors with a liquid gate for extracellular stimulation and recording of electric activity of stem cell-derived neuronal networks," *Physical Chemistry Chemical Physics*, vol. 15, no. 11, pp. 3897–3905, 2013.

[7] D. Khodagholy, T. Doublet, P. Quilichini, M. Gurfinkel, P. Leleux, A. Ghestem, E. Ismailova, T. Hervé, S. Sanaur, C. Bernard, *et al.*, "In vivo recordings of brain activity using organic transistors," *Nature communications*, vol. 4, p. 1575, 2013.

[8] G. H. Gelinck, H. E. A. Huitema, E. van Veenendaal, E. Cantatore, L. Schrijnemakers, J. B. van der Putten, T. C. Geuns, M. Beenhakkers, J. B. Giesbers, B.-H. Huisman, *et al.*, "Flexible active-matrix displays and shift registers based on solution-processed organic transistors," *Nature materials*, vol. 3, no. 2, p. 106, 2004.

[9] C. Wang, H. Dong, W. Hu, Y. Liu, and D. Zhu, "Semiconducting pi-conjugated systems in field-effect transistors: A material odyssey of organic electronics," *Chemical Reviews*, vol. 112, no. 4, pp. 2208–2267, 2011.

[10] G. Li, V. Shrotriya, J. Huang, Y. Yao, T. Moriarty, K. Emery, and Y. Yang, "High-efficiency solution processable polymer photovoltaic cells by self-organization of polymer blends," in *Materials For Sustainable Energy: A Collection of Peer-Reviewed Research and Review Articles from Nature Publishing Group*, pp. 80–84, World Scientific, 2011.

[11] Y. Sun, G. C. Welch, W. L. Leong, C. J. Takacs, G. C. Bazan, and A. J. Heeger, "Solution-processed small-molecule solar cells with 6.7% efficiency," *Nature materials*, vol. 11, no. 1, p. 44, 2012.

[12] A. R. Rocha, V. M. Garcia-Suarez, S. W. Bailey, C. J. Lambert, J. Ferrer, and S. Sanvito, "Towards molecular spintronics," *Nature materials*, vol. 4, no. 4, p. 335, 2005.

[13] V. A. Dediu, L. E. Hueso, I. Bergenti, and C. Taliani, "Spin routes in organic semiconductors," *Nature Materials*, vol. 8, no. 9, pp. 707–716, 2009.

[14] S. Sanvito, "Molecular spintronics," *Chemical Society Reviews*, vol. 40, no. 6, pp. 3336–3355, 2011.

[15] I. Bergenti, V. Dediu, M. Prezioso, and A. Riminucci, "Organic spintronics," *Philosophical Transactions of the Royal Society A: Mathematical, Physical and Engineering Sciences*, vol. 369, pp. 3054–3068, jul 2011.

[16] V. Dediu, M. Murgia, F. Matacotta, C. Taliani, and S. Barbanera, "Room temperature spin polarized injection in organic semiconductor," *Solid State Communications*, vol. 122, no. 3-4, pp. 181–184, 2002.

[17] Z. Xiong, D. Wu, Z. V. Vardeny, and J. Shi, "Giant magnetoresistance in organic spin-valves," *Nature*, vol. 427, no. 6977, p. 821, 2004.

[18] J. S. Moodera, L. R. Kinder, T. M. Wong, and R. Meservey, "Large magnetoresistance at room temperature in ferromagnetic thin film tunnel junctions," *Physical review letters*, vol. 74, no. 16, p. 3273, 1995.

[19] T. Miyazaki and N. Tezuka, "Giant magnetic tunneling effect in $Fe/Al_2O_3/Fe$ junction," *Journal of Magnetism and Magnetic Materials*, vol. 139, no. 3, pp. L231–L234, 1995.

[20] S. Pramanik, C.-G. Stefanita, S. Patibandla, S. Bandyopadhyay, K. Garre, N. Harth, and M. Cahay, "Observation of extremely long spin relaxation times in an organic nanowire spin valve," *Nature nanotechnology*, vol. 2, no. 4, p. 216, 2007.

[21] R. Geng, H. M. Luong, T. T. Daugherty, L. Hornak, and T. D. Nguyen, "A review on organic spintronic materials and devices: II. magnetoresistance in organic spin valves and spin organic light emitting diodes," *Journal of Science: Advanced Materials and Devices*, vol. 1, no. 3, pp. 256–272, 2016.

[22] V. Coropceanu, J. Cornil, D. A. da Silva Filho, Y. Olivier, R. Silbey, and J.-L. Brédas, "Charge transport in organic semiconductors," *Chemical reviews*, vol. 107, no. 4, pp. 926–952, 2007.

[23] K. Walzer, B. Maennig, M. Pfeiffer, and K. Leo, "Highly efficient organic devices based on electrically doped transport layers," *Chemical Reviews*, vol. 107, no. 4, pp. 1233–1271, 2007.

[24] C. Groves, "Bright design," *Nature Materials*, vol. 12, no. 7, pp. 597–598, 2013.

[25] M. Mesta, M. Carvelli, R. J. de Vries, H. van Eersel, J. J. M. van der Holst, M. Schober, M. Furno, B. Lüssem, K. Leo, P. Loebl, R. Coehoorn, and P. A. Bobbert, "Molecular-scale simulation of electroluminescence in a multilayer white organic light-emitting diode," *Nature Materials*, vol. 12, no. 7, pp. 652–658, 2013.

[26] H. Ishii, K. Sugiyama, E. Ito, and K. Seki, "Energy level alignment and interfacial electronic structures at organic/metal and organic/organic interfaces," *Advanced Materials*, vol. 11, no. 8, pp. 605–625, 1999.

[27] S. L. James, "Metal-organic frameworks," *Chemical Society Reviews*, vol. 32, no. 5, p. 276, 2003.

[28] M. Galbiati, S. Tatay, C. Barraud, A. V. Dediu, F. Petroff, R. Mattana, and P. Seneor, "Spinterface: Crafting spintronics at the molecular scale," *MRS Bulletin*, vol. 39, no. 07, pp. 602–607, 2014.

[29] Y. Zhan and M. Fahlman, "The study of organic semiconductor/ferromagnet interfaces in organic spintronics: A short review of recent progress," *Journal of Polymer Science Part B: Polymer Physics*, vol. 50, no. 21, pp. 1453–1462, 2012.

[30] H. Hoppe and N. S. Sariciftci, "Morphology of polymer/fullerene bulk heterojunction solar cells," *J. Mater. Chem.*, vol. 16, no. 1, pp. 45–61, 2006.

[31] A. Kahn, N. Koch, and W. Gao, "Electronic structure and electrical properties of interfaces between metals and π-conjugated molecular films," *Journal of Polymer Science Part B: Polymer Physics*, vol. 41, no. 21, pp. 2529–2548, 2003.

[32] S. Shi, Z. Sun, A. Bedoya-Pinto, P. Graziosi, X. Li, X. Liu, L. Hueso, V. A. Dediu, Y. Luo, and M. Fahlman, "Hybrid interface states and spin polarization at ferromagnetic metal-organic heterojunctions: Interface engineering for efficient spin injection in organic spintronics," *Advanced Functional Materials*, vol. 24, no. 30, pp. 4812–4821, 2014.

[33] C. Barraud, P. Seneor, R. Mattana, S. Fusil, K. Bouzehouane, C. Deranlot, P. Graziosi, L. Hueso, I. Bergenti, V. Dediu, F. Petroff, and A. Fert, "Unravelling the role of the interface for spin injection into organic semiconductors," *Nature Physics*, vol. 6, pp. 615–620, jun 2010.

[34] S. Sanvito, "The rise of spinterface science," *Nature Physics*, vol. 6, no. 8, pp. 562–564, 2010.

[35] B. Feuerbacher, B. Fitton, and R. F. Willis, *Photoemission and the electronic properties of surfaces*. John Wiley & Sons, 1978.

[36] Y. Harada, S. Masuda, and H. Ozaki, "Electron spectroscopy using metastable atoms as probes for solid surfaces," *Chemical Reviews*, vol. 97, no. 6, pp. 1897–1952, 1997.

[37] N. S. Sariciftci, L. Smilowitz, A. J. Heeger, and F. Wudl, "Photoinduced electron transfer from a conducting polymer to buckminsterfullerene," *Science*, vol. 258, no. 5087, pp. 1474–1476, 1992.

[38] Q. Yang, Y. Su, C. Chi, C. T. Cherian, K. Huang, V. G. Kravets, F. C. Wang, J. C. Zhang, A. Pratt, A. N. Grigorenko, F. Guinea, A. K. Geim, and R. R. Nair, "Ultrathin graphene-based membrane with precise molecular sieving and ultrafast solvent permeation," *Nature Materials*, vol. 16, no. 12, pp. 1198–1202, 2017.

[39] C. W. Tang, "Two-layer organic photovoltaic cell," *Applied Physics Letters*, vol. 48, no. 2, pp. 183–185, 1986.

[40] C. W. Tang and S. A. VanSlyke, "Organic electroluminescent diodes," *Applied Physics Letters*, vol. 51, no. 12, pp. 913–915, 1987.

[41] J. Robertson, "Diamond-like amorphous carbon," *Materials Science and Engineering: R: Reports*, vol. 37, pp. 129–281, may 2002.

[42] M. Bouhassoune, S. L. M. van Mensfoort, P. A. Bobbert, and R. Coehoorn, "Carrier-density and field-dependent charge-carrier mobility in organic semiconductors with correlated gaussian disorder," *Organic Electronics*, vol. 10, no. 3, pp. 437 – 445, 2009.

[43] K. Horiuchi, S. Uchino, S. Hashii, A. Hashimoto, T. Kato, T. Sasaki, N. Aoki, and Y. Ochiai, "Variable range hopping in a C_{60} field-effect transistor," *Applied physics letters*, vol. 85, no. 11, pp. 1987–1989, 2004.

[44] A. E. Ela and H. Afifi, "Hopping transport in organic semiconductor system," *Journal of Physics and Chemistry of Solids*, vol. 40, no. 4, pp. 257–259, 1979.

[45] C. Jehoulet, A. J. Bard, and F. Wudl, "Electrochemical reduction and oxidation of C_{60} films," *Journal of the American Chemical Society*, vol. 113, no. 14, pp. 5456–5457, 1991.

[46] R. Taylor and D. R. M. Walton, "The chemistry of fullerenes," *Nature*, vol. 363, no. 6431, pp. 685–693, 1993.

[47] P. B. Shevlin, "Lecture notes on fullerene chemistry: a handbook for chemists," *Journal of the American Chemical Society*, vol. 122, no. 19, pp. 4846–4846, 2000.

[48] G. Yu, J. Gao, J. C. Hummelen, F. Wudl, and A. J. Heeger, "Polymer photovoltaic cells: Enhanced efficiencies via a network of internal donor-acceptor heterojunctions," *Science*, vol. 270, no. 5243, pp. 1789–1791, 1995.

[49] H. Li, B. C.-K. Tee, G. Giri, J. W. Chung, S. Y. Lee, and Z. Bao, "High-performance transistors and complementary inverters based on solution-grown aligned organic single-crystals," *Advanced Materials*, vol. 24, no. 19, pp. 2588–2591, 2012.

[50] P. A. Bobbert, W. Wagemans, F. W. A. van Oost, B. Koopmans, and M. Wohlgenannt, "Theory for spin diffusion in disordered organic semiconductors," *Physical Review Letters*, vol. 102, no. 15, 2009.

[51] T. Moorsom, M. Wheeler, T. M. Khan, F. A. Ma'Mari, C. Kinane, S. Langridge, D. Ciudad, A. Bedoya-Pinto, L. Hueso, G. Teobaldi, V. K. Lazarov, D. Gilks, G. Burnell, B. J. Hickey, and O. Cespedes, "Spin-polarized electron transfer inferromagnet/C_{60} interfaces," *Physical Review B*, vol. 90, no. 12, 2014.

[52] X. Zhang, S. Mizukami, T. Kubota, Q. Ma, M. Oogane, H. Naganuma, Y. Ando, and T. Miyazaki, "Observation of a large spin-dependent transport length in organic spin valves at room temperature," *Nature Communications*, vol. 4, no. 1, 2013.

[53] F. Al Ma'Mari, T. Moorsom, G. Teobaldi, W. Deacon, T. Prokscha, H. Luetkens, S. Lee, G. E. Sterbinsky, D. A. Arena, D. A. MacLaren, *et al.*, "Beating the stoner criterion using molecular interfaces," *Nature*, vol. 524, no. 7563, p. 69, 2015.

[54] C. D. Reddy, Z. G. Yu, and Y.-W. Zhang, "Two-dimensional van der waals C_{60} molecular crystal," *Scientific Reports*, vol. 5, no. 1, 2015.

[55] H. W. Kroto, J. R. Heath, S. C. O'Brien, R. F. Curl, and R. E. Smalley, "C_{60}: Buckminsterfullerene," *Nature*, vol. 318, no. 6042, p. 162, 1985.

[56] C. S. Yannoni, R. D. Johnson, G. Meijer, D. S. Bethune, and J. R. Salem, "Carbon-13 NMR study of the C_{60} cluster in the solid state: molecular motion and carbon chemical shift anisotropy," *The Journal of Physical Chemistry*, vol. 95, no. 1, pp. 9–10, 1991.

[57] K. Hedberg, L. Hedberg, D. S. Bethune, C. A. Brown, H. C. Dorn, R. D. Johnson, and M. D. Vries, "Bond lengths in free molecules of buckminsterfullerene, C_{60}, from gas-phase electron diffraction," *Science*, vol. 254, no. 5030, pp. 410–412, 1991.

[58] K. Yabana and G. F. Bertsch, "Electronic structure of C_{60} in a spherical basis," *Physica Scripta*, vol. 48, pp. 633–637, nov 1993.

[59] S. Saito and A. Oshiyama, "Cohesive mechanism and energy bands of solid C_{60}," *Physical Review Letters*, vol. 66, no. 20, p. 2637, 1991.

[60] R. Rivelino and F. de Brito Mota, "Band gap and density of states of the hydrated C_{60}fullerene system at finite temperature," *Nano Letters*, vol. 7, no. 6, pp. 1526–1531, 2007.

[61] M. C. Böhm and J. Schulte, "Electronic structure of C_{60}: from the molecular to the solid state," *Molecular Physics*, vol. 87, pp. 735–778, mar 1996.

[62] J. G. Hou, Y. Jinlong, W. Haiqian, L. Qunxiang, Z. Changgan, Y. Lanfeng, W. Bing, D. M. Chen, and Z. Qingshi, "Topology of two-dimensional C_{60} domains," *Nature*, vol. 409, no. 6818, pp. 304–305, 2001.

[63] J. Cho, J. Smerdon, L. Gao, Özgün Süzer, J. R. Guest, and N. P. Guisinger, "Structural and electronic decoupling of C_{60} from epitaxial graphene on SiC," *Nano Letters*, vol. 12, no. 6, pp. 3018–3024, 2012.

[64] X. Roy, C.-H. Lee, A. C. Crowther, C. L. Schenck, T. Besara, R. A. Lalancette, T. Siegrist, P. W. Stephens, L. E. Brus, P. Kim, M. L. Steigerwald, and C. Nuckolls, "Nanoscale atoms in solid-state chemistry," *Science*, vol. 341, no. 6142, pp. 157–160, 2013.

[65] J.-L. Brédas, J. E. Norton, J. Cornil, and V. Coropceanu, "Molecular understanding of organic solar cells: The challenges," *Accounts of Chemical Research*, vol. 42, pp. 1691–1699, nov 2009.

[66] H. Ma, H.-L. Yip, F. Huang, and A. K.-Y. Jen, "Interface engineering for organic electronics," *Advanced Functional Materials*, vol. 20, no. 9, pp. 1371–1388, 2010.

[67] C. an Di, Y. Liu, G. Yu, and D. Zhu, "Interface engineering: An effective approach toward high-performance organic field-effect transistors," *Accounts of Chemical Research*, vol. 42, no. 10, pp. 1573–1583, 2009.

[68] D. Braga and G. Horowitz, "High-performance organic field-effect transistors," *Advanced Materials*, vol. 21, no. 14-15, pp. 1473–1486, 2009.

[69] J. Zaumseil and H. Sirringhaus, "Electron and ambipolar transport in organic field-effect transistors," *Chemical Reviews*, vol. 107, no. 4, pp. 1296–1323, 2007.

[70] W. R. Salaneck, S. Stafstrom, and J. L. Brédas, *Conjugated polymer surfaces and interfaces: electronic and chemical structure of interfaces for polymer light emitting devices.* Cambridge University Press, 1996.

[71] W. R. Salaneck, K. Seki, A. Kahn, and J. J. Pireaux, *Conjugated Polymer And Molecular Interfaces: Science And Technology For Photonic And Optoelectronic Application.* CRC Press, 2001.

[72] I. Hill, J. Schwartz, and A. Kahn, "Metal-dependent charge transfer and chemical interaction at interfaces between 3, 4, 9, 10-perylenetetracarboxylic bisimidazole and gold, silver and magnesium," *Organic Electronics*, vol. 1, no. 1, pp. 5–13, 2000.

[73] C. Shen, I. G. Hill, A. Kahn, and J. Schwartz, "Organometallic chemistry at the magnesium- tris(8-hydroxyquinolino)aluminum interface," *Journal of the American Chemical Society*, vol. 122, no. 22, pp. 5391–5392, 2000.

[74] C. Shen, A. Kahn, and J. Schwartz, "Role of metal–molecule chemistry and interdiffusion on the electrical properties of an organic interface: The Al–F_{16}CuPc case," *Journal of Applied Physics*, vol. 90, no. 12, pp. 6236–6242, 2001.

[75] S. Meloni, A. Palma, J. Schwartz, A. Kahn, and R. Car, "Chemistry between magnesium and multiple molecules in tris(8-hydroxyquinoline) aluminum films," *Journal of the American Chemical Society*, vol. 125, no. 26, pp. 7808–7809, 2003.

[76] N. Koch, A. Kahn, J. Ghijsen, J.-J. Pireaux, J. Schwartz, R. L. Johnson, and A. Elschner, "Conjugated organic molecules on metal versus polymer electrodes: Demonstration of a key energy level alignment mechanism," *Applied Physics Letters*, vol. 82, no. 1, pp. 70–72, 2003.

[77] X. Crispin, V. Geskin, A. Crispin, J. Cornil, R. Lazzaroni, W. R. Salaneck, and J.-L. Brédas, "Characterization of the interface dipole at organic/ metal interfaces," *Journal of the American Chemical Society*, vol. 124, no. 27, pp. 8131–8141, 2002.

[78] M. Cardona and L. Ley, *Photoemission in Solids I: General Principles (Topics in Applied Physics)*. Springer, 2013.

[79] H. Vázquez, Y. Dappe, J. Ortega, and F. Flores, "Energy level alignment at metal/organic semiconductor interfaces:"pillow" effect, induced density of interface states, and charge neutrality level," *The Journal of chemical physics*, vol. 126, no. 14, p. 144703, 2007.

[80] N. Koch, E. Zojer, A. Rajagopal, J. Ghjisen, R. L. Johnson, G. Leising, and J.-J. Pireaux, "Electronic properties of the interfaces between the wide bandgap organic semiconductor para-sexiphenyl and samarium," *Advanced functional materials*, vol. 11, no. 1, pp. 51–58, 2001.

[81] N. Koch, J. Ghijsen, R. L. Johnson, J. Schwartz, J.-J. Pireaux, and A. Kahn, "Physisorption-like interaction at the interfaces formed by pentacene and samarium," *The Journal of Physical Chemistry B*, vol. 106, no. 16, pp. 4192–4196, 2002.

[82] V. Bulović, P. Tian, P. E. Burrows, M. R. Gokhale, S. R. Forrest, and M. E. Thompson, "A surface-emitting vacuum-deposited organic light emitting device," *Applied Physics Letters*, vol. 70, no. 22, pp. 2954–2954, 1997.

[83] C. Shen, I. G. Hill, and A. Kahn, "Role of electrode contamination in electron injection at Mg:Ag/Alq_3 interfaces," *Advanced Materials*, vol. 11, no. 18, pp. 1523–1527, 1999.

[84] C. Shen and A. Kahn, "Electronic structure, diffusion, and p-doping at the Au/F_{16}CuPc interface," *Journal of Applied Physics*, vol. 90, no. 9, pp. 4549–4554, 2001.

[85] J. J. M. Halls, C. A. Walsh, N. C. Greenham, E. A. Marseglia, R. H. Friend, S. C. Moratti, and A. B. Holmes, "Efficient photodiodes from interpenetrating polymer networks," *Nature*, vol. 376, no. 6540, pp. 498–500, 1995.

[86] K. O. Sylvester-Hvid, S. Rettrup, and M. A. Ratner, "Two-dimensional model for polymer-based photovoltaic cells: numerical simulations of morphology effects," *The Journal of Physical Chemistry B*, vol. 108, no. 14, pp. 4296–4307, 2004.

[87] M. Julliere, "Tunneling between ferromagnetic films," *Physics Letters A*, vol. 54, no. 3, pp. 225–226, 1975.

[88] M. Bowen, A. Barthélémy, M. Bibes, E. Jacquet, J. Contour, A. Fert, D. Wortmann, and S. Blügel, "Half-metallicity proven using fully spin-polarized tunnelling," *Journal of Physics: Condensed Matter*, vol. 17, no. 41, p. L407, 2005.

[89] H. N. Fuke, K. Saito, Y. Kamiguchi, H. Iwasaki, and M. Sahashi, "Spin-valve giant magnetoresistive films with antiferromagnetic Ir-Mn layers," *Journal of Applied Physics*, vol. 81, no. 8, pp. 4004–4006, 1997.

[90] Y. Zhan, E. Holmström, R. Lizárraga, O. Eriksson, X. Liu, F. Li, E. Carlegrim, S. Stafström, and M. Fahlman, "Efficient spin injection through exchange coupling at organic semiconductor/ferromagnet heterojunctions," *Advanced Materials*, vol. 22, no. 14, pp. 1626–1630, 2010.

[91] N. Atodiresei, J. Brede, P. Lazić, V. Caciuc, G. Hoffmann, R. Wiesendanger, and S. Blügel, "Design of the local spin polarization at the organic-ferromagnetic interface," *Physical Review Letters*, vol. 105, no. 6, 2010.

[92] K. Ohno, H. Mutoh, and Y. Harada, "Study of electron distributions of molecular orbitals by penning ionization electron spectroscopy," *Journal of the American Chemical Society*, vol. 105, no. 14, pp. 4555–4561, 1983.

[93] B. Heinz and H. Morgner, "A metastable induced electron spectroscopy study of graphite: the k-vector dependence of the ionization probability," *Surface science*, vol. 405, no. 1, pp. 104–111, 1998.

[94] F. B. Dunning and R. G. Hulet, *Atomic, molecular, and optical physics: Atoms and molecules*. Academic Press, 1996.

[95] H. Morgner, "Advances in atomic, molecular, and optical physics," 2000.

[96] A. Pratt, A. Roskoss, H. Ménard, and M. Jacka, "Improved metastable de-excitation spectrometer using laser-cooling techniques," *Review of Scientific Instruments*, vol. 76, no. 5, p. 053102, 2005.

[97] W. Sesselmann, B. Woratschek, J. Küppers, G. Ertl, and H. Haberland, "Interaction of metastable noble-gas atoms with transition-metal surfaces: Resonance ionization and auger neutralization," *Physical Review B*, vol. 35, no. 4, p. 1547, 1987.

[98] H. D. Hagstrum and Y. Takeishi, "Effect of electron-electron interaction on the kinetic-energy distribution of electrons ejected from solids by slow ions," *Physical Review*, vol. 137, no. 1A, pp. A304–A310, 1965.

[99] L. Salmi, "Theory of spin polarization in the metastable-He–metal interaction," *Physical Review B*, vol. 46, no. 7, p. 4180, 1992.

[100] J. Appelbaum and D. Hamann, "Variational calculation of the image potential near a metal surface," *Physical Review B*, vol. 6, no. 4, p. 1122, 1972.

[101] E. W. Rothe, R. Neynaber, and S. Trujillo, "Velocity dependence of the total cross section for the scattering of metastable He ($^3S_1$) by helium, argon, and krypton," *The Journal of Chemical Physics*, vol. 42, no. 9, pp. 3310–3314, 1965.

[102] E. Leasure, C. Mueller, and T. Ridley, "Hot,metastable atom, molecular beam source," *Review of Scientific Instruments*, vol. 46, no. 5, pp. 635–637, 1975.

[103] D. Fahey, W. Parks, and L. Schearer, "High flux beam source of thermal rare-gas metastable atoms," *Journal of Physics E: Scientific Instruments*, vol. 13, no. 4, p. 381, 1980.

[104] P. Johnson and T. Delchar, "A helium metastable source for surface spectroscopy," *Journal of Physics E: Scientific Instruments*, vol. 10, no. 4, p. 428, 1977.

[105] R. Rundel, F. Dunning, and R. Stebbings, "Velocity distributions in metastable atom beams produced by coaxial electron impact," *Review of Scientific Instruments*, vol. 45, no. 1, pp. 116–119, 1974.

[106] J. Swansson, K. Baldwin, M. Hoogerland, A. Truscott, and S. Buckman, "A high flux, liquid-helium cooled source of metastable rare gas atoms," *Applied Physics B*, vol. 79, no. 4, pp. 485–489, 2004.

[107] K. C. Neuman and S. M. Block, "Optical trapping," *Review of Scientific Instruments*, vol. 75, pp. 2787–2809, sep 2004.

[108] W. Lu, D. Milic, M. D. Hoogerland, M. Jacka, K. G. H. Baldwin, and S. J. Buckman, "A practical direct current discharge helium absorption cell for laser frequency locking at 1083 nm," *Review of Scientific Instruments*, vol. 67, no. 9, pp. 3003–3004, 1996.

[109] W. Demtröder, *Laser spectroscopy: basic concepts and instrumentation*. Springer Science Business Media, 2013.

[110] F. B. Dunning, P. Nordlander, and G. K. Walters, "Dynamics of metastable-atom deexcitation at metal surfaces," *Physical Review B*, vol. 44, no. 7, pp. 3246–3250, 1991.

[111] J. C. Lancaster, F. J. Kontur, G. K. Walters, and F. B. Dunning, "Dynamics of he^+ ion neutralization at clean metal surfaces: energy- and spin-resolved studies," *Physical Review B*, vol. 67, no. 11, 2003.

[112] M. W. Hart, M. S. Hammond, F. B. Dunning, and G. K. Walters, "Spin-polarized metastable-atom deexcitation spectroscopy: A new probe of the dynamics of metastable-atom–surface interactions," *Physical Review B*, vol. 39, no. 8, pp. 5488–5491, 1989.

[113] D. Briggs and M. P. Seah, *Practical surface analysis. Volume 1–Auger and photoelectron spectroscopy*. Wiley, Chichester, 1990.

[114] Thermo Scientific, *XR5: Microfocus X-ray Monochromator*, 2008.

[115] Y. Baer and G. B. P. Cohn, "Monochromatized x-ray source for high resolution electron spectroscopy," *Review of Scientific Instruments*, vol. 46, no. 4, pp. 466–469, 1975.

[116] K.-G. Zhou, K. S. Vasu, C. T. Cherian, M. Neek-Amal, J. C. Zhang, H. Ghorbanfekr-Kalashami, K. Huang, O. P. Marshall, V. G. Kravets, J. Abraham, Y. Su, A. N. Grigorenko, A. Pratt, A. K. Geim, F. M. Peeters, K. S.

Novoselov, and R. R. Nair, "Electrically controlled water permeation through graphene oxide membranes," *Nature*, vol. 559, no. 7713, pp. 236–240, 2018.

[117] J. Mulder, *Basic principles of membrane technology*. Springer Science Business Media, 2012.

[118] W. J. Koros and C. Zhang, "Materials for next-generation molecularly selective synthetic membranes," *Nature materials*, vol. 16, no. 3, p. 289, 2017.

[119] P. Sun, K. Wang, and H. Zhu, "Recent developments in graphene-based membranes: structure, mass-transport mechanism and potential applications," *Advanced Materials*, vol. 28, no. 12, pp. 2287–2310, 2016.

[120] G. Liu, W. Jin, and N. Xu, "Graphene-based membranes," *Chemical Society Reviews*, vol. 44, no. 15, pp. 5016–5030, 2015.

[121] J. Abraham, K. S. Vasu, C. D. Williams, K. Gopinadhan, Y. Su, C. T. Cherian, J. Dix, E. Prestat, S. J. Haigh, I. V. Grigorieva, *et al.*, "Tunable sieving of ions using graphene oxide membranes," *Nature nanotechnology*, vol. 12, no. 6, p. 546, 2017.

[122] K. Celebi, J. Buchheim, R. M. Wyss, A. Droudian, P. Gasser, I. Shorubalko, J.-I. Kye, C. Lee, and H. G. Park, "Ultimate permeation across atomically thin porous graphene," *Science*, vol. 344, no. 6181, pp. 289–292, 2014.

[123] R. Nair, H. Wu, P. Jayaram, I. Grigorieva, and A. Geim, "Unimpeded permeation of water through helium-leak–tight graphene-based membranes," *Science*, vol. 335, no. 6067, pp. 442–444, 2012.

[124] P. Marchetti, M. F. Jimenez Solomon, G. Szekely, and A. G. Livingston, "Molecular separation with organic solvent nanofiltration: a critical review," *Chemical reviews*, vol. 114, no. 21, pp. 10735–10806, 2014.

[125] X. Lin, X. Shen, Q. Zheng, N. Yousefi, L. Ye, Y.-W. Mai, and J.-K. Kim, "Fabrication of highly-aligned, conductive, and strong graphene papers using ultralarge graphene oxide sheets," *ACS nano*, vol. 6, no. 12, pp. 10708–10719, 2012.

[126] C. Cai, N. Sang, Z. Shen, and X. Zhao, "Facile and size-controllable preparation of graphene oxide nanosheets using high shear method and ultrasonic

method," *Journal of Experimental Nanoscience*, vol. 12, no. 1, pp. 247–262, 2017.

[127] C. Zhao, S. Nie, M. Tang, and S. Sun, "Polymeric pH-sensitive membranes—a review," *Progress in Polymer Science*, vol. 36, no. 11, pp. 1499–1520, 2011.

[128] Z. Liu, W. Wang, R. Xie, X.-J. Ju, and L.-Y. Chu, "Stimuli-responsive smart gating membranes," *Chemical Society Reviews*, vol. 45, no. 3, pp. 460–475, 2016.

[129] F. Perrozzi, S. Prezioso, and L. Ottaviano, "Graphene oxide: from fundamentals to applications," *Journal of Physics: Condensed Matter*, vol. 27, no. 1, p. 013002, 2014.

[130] C. Davisson and L. H. Germer, "Diffraction of electrons by a crystal of nickel," *Physical Review*, vol. 30, no. 6, pp. 705–740, 1927.

[131] K. Hermann, *Crystallography and Surface Structure: An Introduction for Surface Scientists and Nanoscientists*. John Wiley & Sons, 2017.

[132] G. S. Parkinson, "Iron oxide surfaces," *Surface Science Reports*, vol. 71, pp. 272–365, mar 2016.

[133] K. E. Sickafus, J. M. Wills, and N. W. Grimes, "Structure of spinel," *Journal of the American Ceramic Society*, vol. 82, pp. 3279–3292, dec 2004.

[134] R. M. Cornell and U. Schwertmann, *The iron oxides: structure, properties, reactions, occurrences and uses*. John Wiley Sons, 2003.

[135] E. J. W. Verwey, "Electronic conduction of magnetite (Fe_3O_4) and its transition point at low temperatures," *Nature*, vol. 144, pp. 327–328, aug 1939.

[136] F. Walz, "The Verwey transition-a topical review," *Journal of Physics: Condensed Matter*, vol. 14, no. 12, p. R285, 2002.

[137] M. L. Néel, "Propriétés magnétiques des ferrites : ferrimagnétisme et antiferromagnétisme," *Annales de Physique*, vol. 12, no. 3, pp. 137–198, 1948.

[138] E. Goering, S. Gold, M. Lafkioti, and G. Schütz, "Vanishing Fe 3d orbital moments in single-crystalline magnetite," *Europhysics Letters (EPL)*, vol. 73, pp. 97–103, jan 2006.

[139] K. Jordan, A. Cazacu, G. Manai, S. F. Ceballos, S. Murphy, and I. V. Shvets, "Scanning tunneling spectroscopy study of the electronic structure ofFe3o4surfaces," *Physical Review B*, vol. 74, aug 2006.

[140] A. Yanase and K. Siratori, "Band structure in the high temperature phase of Fe_3O_4," *Journal of the Physical Society of Japan*, vol. 53, pp. 312–317, jan 1984.

[141] A. Yanase and N. Hamada, "Electronic structure in high temperature phase of Fe_3O_4," *Journal of the Physical Society of Japan*, vol. 68, pp. 1607–1613, may 1999.

[142] Z. Zhang and S. Satpathy, "Electron states, magnetism, and the verwey transition in magnetite," *Physical Review B*, vol. 44, pp. 13319–13331, dec 1991.

[143] J. Coey and C. Chien, "Half-metallic ferromagnetic oxides," *Mrs Bulletin*, vol. 28, no. 10, pp. 720–724, 2003.

[144] G. Hu and Y. Suzuki, "Negative spin polarization ofFe3o4in magnetite/manganite-based junctions," *Physical Review Letters*, vol. 89, dec 2002.

[145] M. Taguchi, A. Chainani, S. Ueda, M. Matsunami, Y. Ishida, R. Eguchi, S. Tsuda, Y. Takata, M. Yabashi, K. Tamasaku, *et al.*, "Temperature dependence of magnetically active charge excitations in magnetite across the verwey transition," *Physical review letters*, vol. 115, no. 25, p. 256405, 2015.

[146] A. Pratt, M. Kurahashi, X. Sun, and Y. Yamauchi, "Adsorbate-induced spin-polarization enhancement of Fe_3O_4(0 0 1)," *Journal of Physics D: Applied Physics*, vol. 44, p. 064010, jan 2011.

[147] A. Pratt, M. Kurahashi, X. Sun, D. Gilks, and Y. Yamauchi, "Direct observation of a positive spin polarization at the (111) surface of magnetite," *Physical Review B*, vol. 85, may 2012.

[148] M. Kurahashi, X. Sun, and Y. Yamauchi, "Recovery of the half-metallicity of an Fe_3O_4 (100) surface by atomic hydrogen adsorption," *Physical Review B*, vol. 81, no. 19, p. 193402, 2010.

[149] X. Sun, A. Pratt, and Y. Yamauchi, "Half-metallicity induced by boron adsorption on an Fe_3O_4 (100) surface," *Physical Chemistry Chemical Physics*, vol. 17, no. 23, pp. 15386–15391, 2015.

[150] X. Sun, S. Li, B. Wang, M. Kurahashi, A. Pratt, and Y. Yamauchi, "Significant variation of surface spin polarization through group IV atom (C, Si, Ge, Sn) adsorption on Fe_3O_4 (100)," *Physical Chemistry Chemical Physics*, vol. 16, no. 1, pp. 95–102, 2014.

[151] C. Noguera and J. Goniakowski, "Polarity in oxide ultrathin films," *Journal of Physics: Condensed Matter*, vol. 20, p. 264003, jun 2008.

[152] J. Goniakowski, F. Finocchi, and C. Noguera, "Polarity of oxide surfaces and nanostructures," *Reports on Progress in Physics*, vol. 71, p. 016501, dec 2007.

[153] N. Mulakaluri, R. Pentcheva, and M. Scheffler, "Coverage-dependent adsorption mode of water on Fe_3O_4(001): Insights from first principles calculations," *The Journal of Physical Chemistry C*, vol. 114, pp. 11148–11156, jun 2010.

[154] G. S. Parkinson, Z. Novotny, P. Jacobson, M. Schmid, and U. Diebold, "Room temperature water splitting at the surface of magnetite," *Journal of the American Chemical Society*, vol. 133, pp. 12650–12655, aug 2011.

[155] R. Pentcheva, F. Wendler, H. L. Meyerheim, W. Moritz, N. Jedrecy, and M. Scheffler, "Jahn-teller stabilization of a "polar" metal oxide surface:Fe_3O_4(001)," *Physical Review Letters*, vol. 94, apr 2005.

[156] R. Pentcheva, W. Moritz, J. Rundgren, S. Frank, D. Schrupp, and M. Scheffler, "A combined dft/leed-approach for complex oxide surface structure determination: Fe_3O_4 (0 0 1)," *Surface Science*, vol. 602, no. 7, pp. 1299–1305, 2008.

[157] Z. Novotný, G. Argentero, Z. Wang, M. Schmid, U. Diebold, and G. S. Parkinson, "Ordered array of single adatoms with remarkable thermal stability:Au/Fe_3O_4(001)," *Physical Review Letters*, vol. 108, may 2012.

[158] R. Bliem, E. McDermott, P. Ferstl, M. Setvin, O. Gamba, J. Pavelec, M. A. Schneider, M. Schmid, U. Diebold, P. Blaha, L. Hammer, and G. S. Parkinson, "Subsurface cation vacancy stabilization of the magnetite (001) surface," *Science*, vol. 346, pp. 1215–1218, dec 2014.

[159] R. Bliem, J. Pavelec, O. Gamba, E. McDermott, Z. Wang, S. Gerhold, M. Wagner, J. Osiecki, K. Schulte, M. Schmid, P. Blaha, U. Diebold, and G. S. Parkinson, "Adsorption and incorporation of transition metals at the magnetite Fe_3O_4(001) surface," *Physical Review B*, vol. 92, aug 2015.

[160] G. Tarrach, D. Bürgler, T. Schaub, R. Wiesendanger, and H.-J. Güntherodt, "Atomic surface structure of Fe_3O_4 (001) in different preparation stages studied by scanning tunneling microscopy," *Surface science*, vol. 285, no. 1-2, pp. 1–14, 1993.

[161] J. Gaines, J. Kohlhepp, J. Van Eemeren, R. Elfrink, F. Roozeboom, and W. De Jonge, "The (001) surface of Fe_3O_4 grown epitaxially on mgo and characterized by scanning tunneling microscopy.," *MRS Online Proceedings Library Archive*, vol. 474, 1997.

[162] S. Nie, E. Starodub, M. Monti, D. A. Siegel, L. Vergara, F. E. Gabaly, N. C. Bartelt, J. de la Figuera, and K. F. McCarty, "Insight into magnetite's redox catalysis from observing surface morphology during oxidation," *Journal of the American Chemical Society*, vol. 135, no. 27, pp. 10091–10098, 2013.

[163] D. Schrupp, M. Sing, M. Tsunekawa, H. Fujiwara, S. Kasai, A. Sekiyama, S. Suga, T. Muro, V. A. M. Brabers, and R. Claessen, "High-energy photoemission on Fe_3O_4: Small polaron physics and the verwey transition," *Europhysics Letters (EPL)*, vol. 70, pp. 789–795, jun 2005.

[164] C. Brundle, T. Chuang, and K. Wandelt, "Core and valence level photoemission studies of iron oxide surfaces and the oxidation of iron," *Surface Science*, vol. 68, pp. 459–468, nov 1977.

[165] K. Li, Y. Wu, Z. Guo, Y. Zheng, G. Han, J. Qiu, P. Luo, L. An, and T. Zhou, "Exchange coupling and its applications in magnetic data storage," *Journal of nanoscience and nanotechnology*, vol. 7, no. 1, pp. 13–45, 2007.

[166] H. Sato, T. Yamamoto, M. Yamanouchi, S. Ikeda, S. Fukami, K. Kinoshita, F. Matsukura, N. Kasai, and H. Ohno, "Comprehensive study of CoFeB-MgO magnetic tunnel junction characteristics with single- and double-interface scaling down to 1x nm," in *2013 IEEE International Electron Devices Meeting*, IEEE, dec 2013.

[167] S. Bandiera, R. C. Sousa, Y. Dahmane, C. Ducruet, C. Portemont, V. Baltz, S. Auffret, I. L. Prejbeanu, and B. Dieny, "Comparison of synthetic antiferromagnets and hard ferromagnets as reference layer in magnetic tunnel junctions with perpendicular magnetic anisotropy," *IEEE Magnetics Letters*, vol. 1, pp. 3000204–3000204, 2010.

[168] H. Yanagihara, Y. Toyoda, and E. Kita, "Antiferromagnetic coupling between spinel ferrite and alpha-Fe layers in $Fe_{3-\delta}O_4$ /MgO/Fe(0 0 1) epitaxial films," *Journal of Physics D: Applied Physics*, vol. 44, p. 064011, jan 2011.

[169] T. Kida, S. Honda, H. Itoh, J. Inoue, H. Yanagihara, E. Kita, and K. Mibu, "Electronic and magnetic structure at the Fe/Fe_3O_4interface," *Physical Review B*, vol. 84, sep 2011.

[170] H. Yanagihara, Y. Toyoda, A. Ohnishi, and E. Kita, "Antiferromagnetic coupling at the interface between Fe and Fe_3O_4(001) epitaxial films," *Applied Physics Express*, vol. 1, p. 111303, oct 2008.

[171] A. Pratt, M. Kurahashi, X. Sun, D. Gilks, and Y. Yamauchi, "Direct observation of a positive spin polarization at the (111) surface of magnetite," *Physical Review B*, vol. 85, may 2012.

[172] Y. Yamauchi and M. Kurahashi, "Spin-polarized metastable deexcitation spectroscopy study of iron films," *Applied Surface Science*, vol. 169-170, pp. 236–240, jan 2001.

[173] R. Moroni, F. Bisio, M. Canepa, and L. Mattera, "Oxygen adsorption on a Fe/MgO(1 0 0) film: a surface magnetism investigation," *Applied Surface Science*, vol. 175-176, pp. 797–801, may 2001.

[174] A. Pratt, M. Kurahashi, X. Sun, and Y. Yamauchi, "Adsorbate-induced spin-polarization enhancement of Fe_3O_4(0 0 1)," *Journal of Physics D: Applied Physics*, vol. 44, p. 064010, jan 2011.

[175] X. Sun, S. D. Li, B. Wang, M. Kurahashi, A. Pratt, and Y. Yamauchi, "Significant variation of surface spin polarization through group IV atom (c, si, ge, sn) adsorption on Fe_3O_4(100)," *Phys. Chem. Chem. Phys.*, vol. 16, no. 1, pp. 95–102, 2014.

[176] P. J. Moriarty, "Fullerene adsorption on semiconductor surfaces," *Surface Science Reports*, vol. 65, no. 7, pp. 175–227, 2010.

[177] Y. Lin, Y. Li, and X. Zhan, "Small molecule semiconductors for high-efficiency organic photovoltaics," *Chemical Society Reviews*, vol. 41, no. 11, pp. 4245–4272, 2012.

[178] Y. Li, M. Chander, J. Patrin, J. Weaver, L. Chibante, and R. Smalley, "Adsorption of individual C_{60} molecules on Si (111)," *Physical Review B*, vol. 45, no. 23, p. 13837, 1992.

[179] X.-D. Wang, T. Hashizume, H. Shinohara, Y. Saito, Y. Nishina, and T. Sakurai, "Scanning tunneling microscopy of C_{60} on the Si (111) 7× 7 surface," *Japanese journal of applied physics*, vol. 31, no. 7B, p. L983, 1992.

[180] R. Wilson, G. Meijer, D. S. Bethune, R. Johnson, D. Chambliss, M. Devries, H. Hunziker, and H. Wendt, "Imaging C_{60} clusters on a surface using a scanning tunneling microscope," *Nature*, vol. 348, pp. 621–622, 1990.

[181] D. Chen, J. Chen, and D. Sarid, "Single-monolayer ordered phases of C_{60} molecules on Si(111)-(7×7) surfaces," *Phys. Rev. B*, vol. 50, pp. 10905–10909, 1994.

[182] H. Xu, D. Chen, and W. Creager, "Double domain solid C_{60} on Si (111) 7× 7," *Physical review letters*, vol. 70, no. 12, p. 1850, 1993.

[183] K.-i. Iizumi, K. Saiki, and A. Koma, "Investigation of the interaction between a C_{60} epitaxial film and a Si (111)-7× 7 surface by electron energy loss spectroscopy," *Surface science*, vol. 518, no. 1-2, pp. 126–132, 2002.

[184] K. Sakamoto, D. Kondo, Y. Ushimi, M. Harada, A. Kimura, A. Kakizaki, and S. Suto, "Temperature dependence of the electronic structure of C_{60} films adsorbed on Si (001)-(2× 1) and Si (111)-(7× 7) surfaces," *Physical Review B*, vol. 60, no. 4, p. 2579, 1999.

[185] C. Cepek, P. Schiavuta, M. Sancrotti, and M. Pedio, "Photoemission study of C_{60}/Si(111) adsorption as a function of coverage and annealing temperature," *Phys. Rev. B*, vol. 60, pp. 2068–2073, 1999.

[186] C. Chen, L. Tjeng, P. Rudolf, G. Meigs, J. Rowe, J. Chen, J. McCauley Jr, A. Smith III, A. McGhie, W. Romanow, *et al.*, "Electronic states and phases of K_xC_{60} from photoemission and x-ray absorption spectroscopy," *Nature*, vol. 352, no. 6336, p. 603, 1991.

[187] B. Itchkawitz, J. Long, T. Schedel-Niedrig, M. Kabler, A. Bradshaw, R. Schlögl, and W. Hunter, "Photoemission and C 1s near-edge absorption from photopolymerized C_{60} films," *Chemical Physics Letters*, vol. 243, no. 3, pp. 211 – 216, 1995.

[188] G. B. Adams, J. B. Page, O. F. Sankey, and M. O?Keeffe, "Polymerized C_{60} studied by first-principles molecular dynamics," *Physical Review B*, vol. 50, no. 23, p. 17471, 1994.

[189] S. Gangopadhyay, R. Woolley, R. Danza, M. Phillips, K. Schulte, L. Wang, V. Dhanak, and P. Moriarty, "C_{60} submonolayers on the Si (1 1 1)-(7× 7) surface: Does a mixture of physisorbed and chemisorbed states exist?," *Surface Science*, vol. 603, no. 18, pp. 2896–2901, 2009.

[190] K. Sakamoto, M. Harada, D. Kondo, A. Kimura, A. Kakizaki, and S. Suto, "Bonding state of the C_{60} molecule adsorbed on a Si (111)-(7× 7) surface," *Physical Review B*, vol. 58, no. 20, p. 13951, 1998.

[191] J. Pascual, J. Gómez-Herrero, C. Rogero, A. Baró, D. Sánchez-Portal, E. Artacho, P. Ordejón, and J. Soler, "Seeing molecular orbitals," *Chemical physics letters*, vol. 321, no. 1-2, pp. 78–82, 2000.

[192] D. Sánchez-Portal, E. Artacho, J. I. Pascual, J. Gómez-Herrero, R. M. Martin, and J. M. Soler, "First principles study of the adsorption of C_{60} on Si (1 1 1)," *Surface science*, vol. 482, pp. 39–43, 2001.

[193] R. Rurali, R. Cuadrado, and J. Cerdá, "C_{60} adsorption on the Si (111)-p (7× 7) surface: A theoretical study," *Physical Review B*, vol. 81, no. 7, p. 075419, 2010.

[194] S. Suto, A. Kasuya, O. Ikeno, C.-W. Hu, A. Wawro, R. Nishitani, T. Goto, and Y. Nishina, "Vibrational modes of C_{60} fullerene on Si (111) 7× 7 surface: Estimation of charge transfer from silicon dangling bonds to C_{60} molecules," *Japanese journal of applied physics*, vol. 33, no. 10B, p. L1489, 1994.

[195] S. Suto, K. Sakamoto, T. Wakita, C.-W. Hu, and A. Kasuya, "Vibrational properties and charge transfer of C_{60} adsorbed on Si (111)-(7× 7) and Si (100)-(2× 1) surfaces," *Physical Review B*, vol. 56, no. 12, p. 7439, 1997.

[196] M. Rice and H.-Y. Choi, "Charged-phonon absorption in doped C_{60}," *Physical Review B*, vol. 45, no. 17, p. 10173, 1992.

[197] P. Moriarty, M. Upward, A. Dunn, Y.-R. Ma, P. Beton, and D. Teehan, "C_{60}-terminated Si surfaces: Charge transfer, bonding, and chemical passivation," *Physical Review B*, vol. 57, no. 1, p. 362, 1998.

[198] H. Wang, C. Zeng, Q. Li, B. Wang, J. Yang, J. Hou, and Q. Zhu, "Scanning tunneling spectroscopy of individual C_{60} molecules adsorbed on Si (111)-7× 7 surface," *Surface science*, vol. 442, no. 2, pp. L1024–L1028, 1999.

[199] J. G. Hou, J. Yang, H. Wang, Q. Li, C. Zeng, H. Lin, W. Bing, D. M. Chen, and Q. Zhu, "Identifying molecular orientation of individual C_{60} on a Si(111) - (7×7) surface," *Phys. Rev. Lett.*, vol. 83, pp. 3001–3004, 1999.

[200] K. Takayanagi, Y. Tanishiro, S. Takahashi, and M. Takahashi, "Structure analysis of Si(111)-7 x 7 reconstructed surface by transmission electron diffraction," *Surface Science*, vol. 164, no. 2, pp. 367 – 392, 1985.

[201] R. Tromp, R. Hamers, and J. Demuth, "Quantum states and atomic structure of silicon surfaces," *Science*, vol. 234, no. 4774, pp. 304–309, 1986.

[202] D. R. Jennison, "Auger-electron spectroscopy as a local probe of atomic charge: Si $L_{23}VV$," *Physical Review Letters*, vol. 40, no. 12, p. 807, 1978.

[203] A. Wachs, T. Miller, T. Hsieh, A. Shapiro, and T.-C. Chiang, "Angle-resolved photoemission studies of Ge (111)-c (2× 8), Ge (111)-(1× 1) H, Si (111)-(7× 7), and Si (100)-(2× 1)," *Physical Review B*, vol. 32, no. 4, p. 2326, 1985.

[204] G. Wertheim and D. Buchanan, "Interfacial reaction of C_{60} with silver," *Physical Review B*, vol. 50, no. 15, p. 11070, 1994.

[205] S. J. Chase, W. S. Bacsa, M. G. Mitch, L. J. Pilione, and J. S. Lannin, "Surface-enhanced raman scattering and photoemission of C_{60} on noble-metal surfaces," *Phys. Rev. B*, vol. 46, pp. 7873–7877, 1992.

[206] F. S. Roberts, S. L. Anderson, A. C. Reber, and S. N. Khanna, "Initial and final state effects in the ultraviolet and x-ray photoelectron spectroscopy (UPS and XPS) of size-selected Pd_n clusters supported on TiO_2 (110)," *The Journal of Physical Chemistry C*, vol. 119, no. 11, pp. 6033–6046, 2015.

[207] S. Masuda, H. Ishii, and Y. Harada, "Two-hole states of the outermost surface layer studied by metastable atom electron spectroscopy Si (111)- 7× 7 and Si (100)- 2× 1," *Surface Science*, vol. 242, no. 1-3, pp. 400–403, 1991.

[208] H. D. Hagstrum, "Theory of Auger neutralization of ions at the surface of a diamond-type semiconductor," *Physical Review*, vol. 122, no. 1, p. 83, 1961.

[209] J. Houston, G. Moore, and M. Lagally, "Transition density of states for Si (100) from $L_1L_{23}V$ and $L_{23}VV$ Auger spectra," *Solid State Communications*, vol. 21, no. 9, pp. 879–882, 1977.

[210] H. Xu, D. M. Chen, and W. N. Creager, "Double domain solid C_{60} on Si(111)7×7," *Phys. Rev. Lett.*, vol. 70, pp. 1850–1853, 1993.

[211] J. Weaver, J. L. Martins, T. Komeda, Y. Chen, T. Ohno, G. Kroll, N. Troullier, R. Haufler, and R. Smalley, "Electronic structure of solid C_{60}: experiment and theory," *Physical review letters*, vol. 66, no. 13, p. 1741, 1991.

[212] A. Maxwell, P. Brühwiler, A. Nilsson, N. Mårtensson, and P. Rudolf, "Photoemission, autoionization, and x-ray-absorption spectroscopy of ultrathin-film C_{60} on Au (110)," *Physical Review B*, vol. 49, no. 15, p. 10717, 1994.

[213] H. Freund, "See, for example, h.-j. freund, w. eberhardt, d. heskett, and ew plummer, phys. rev. lett. 50, 768 (1982).," *Phys. Rev. Lett.*, vol. 50, p. 768, 1982.

[214] M. Saunders, H. A. Jiménez-Vázquez, R. J. Cross, S. Mroczkowski, D. I. Freedberg, and F. A. Anet, "Probing the interior of fullerenes by 3 He NMR spectroscopy of endohedral 3 He @ C_{60} and 3 He @ C_{70}," *Nature*, vol. 367, no. 6460, p. 256, 1994.

[215] A. A. Popov, *Endohedral Fullerenes: Electron Transfer and Spin*. Springer, 2017.

[216] G. Jonker and J. V. Santen, "Ferromagnetic compounds of manganese with perovskite structure," *Physica*, vol. 16, no. 3, pp. 337–349, 1950.

[217] D. Sun, L. Yin, C. Sun, H. Guo, Z. Gai, X.-G. Zhang, T. Z. Ward, Z. Cheng, and J. Shen, "Giant magnetoresistance in organic spin valves," *Physical Review Letters*, vol. 104, no. 23, 2010.

[218] V. Dediu, L. E. Hueso, I. Bergenti, A. Riminucci, F. Borgatti, P. Graziosi, C. Newby, F. Casoli, M. P. D. Jong, C. Taliani, and Y. Zhan, "Room-temperature spintronic effects in Alq_3-based hybrid devices," *Physical Review B*, vol. 78, no. 11, 2008.

[219] F. Li, T. Li, F. Chen, and F. Zhang, "Spin injection and transport in organic spin-valves based on fullerene C_{60}," *Organic Electronics*, vol. 15, no. 7, pp. 1657–1663, 2014.

[220] T. D. Nguyen, F. Wang, X.-G. Li, E. Ehrenfreund, and Z. V. Vardeny, "Spin diffusion in fullerene-based devices: Morphology effect," *Physical Review B*, vol. 87, no. 7, 2013.

[221] H. Xie, D. Niu, L. Lyu, H. Zhang, Y. Zhang, P. Liu, P. Wang, D. Wu, and Y. Gao, "Evolution of the electronic structure of $C_{60}/La_{0.67}Sr_{0.33}MnO_3$ interface," *Applied Physics Letters*, vol. 108, no. 1, p. 011603, 2016.

[222] A. Haghiri-Gosnet and J. Renard, "Cmr manganites: physics, thin films and devices," *Journal of Physics D: Applied Physics*, vol. 36, no. 8, p. R127, 2003.

[223] J. Jiang, Q. Chen, and X. Liu, "First-principles study on the electronic structure and optical properties of $La_{0.75}Sr_{0.25}MnO_{3-\sigma}$ materials with oxygen vacancies defects," *Current Applied Physics*, vol. 18, no. 2, pp. 200–208, 2018.

[224] E. Dagotto, T. Hotta, and A. Moreo, "Colossal magnetoresistant materials: the key role of phase separation," *Physics Reports*, vol. 344, no. 1-3, pp. 1–153, 2001.

[225] Y. Tokura, "Critical features of colossal magnetoresistive manganites," *Reports on Progress in Physics*, vol. 69, no. 3, pp. 797–851, 2006.

[226] C. Zener, "Interaction between thed-shells in the transition metals. II. ferromagnetic compounds of manganese with perovskite structure," *Physical Review*, vol. 82, no. 3, pp. 403–405, 1951.

[227] J. Curiale, M. Granada, H. E. Troiani, R. D. Sánchez, A. G. Leyva, P. Levy, and K. Samwer, "Magnetic dead layer in ferromagnetic manganite nanoparticles," *Applied Physics Letters*, vol. 95, no. 4, p. 043106, 2009.

[228] J.-S. Lee, D. A. Arena, P. Yu, C. S. Nelson, R. Fan, C. J. Kinane, S. Langridge, M. D. Rossell, R. Ramesh, and C.-C. Kao, "Hidden magnetic configuration in epitaxial $La_{1-x}Sr_xMnO_3$films," *Physical Review Letters*, vol. 105, no. 25, 2010.

[229] R. Bertacco, A. Tagliaferri, M. Riva, L. Signorini, M. Cantoni, A. Cattoni, F. Ciccacci, B. Davidson, F. Maccherozzi, I. Vobornik, *et al.*, "Surface electronic and magnetic properties of $La_{2/3}$ $Sr_{1/3}$ MnO_3 thin films with extended metallicity above the curie temperature," *Physical Review B*, vol. 78, no. 3, p. 035448, 2008.

[230] T. T. Fister, D. D. Fong, J. A. Eastman, P. M. Baldo, M. J. Highland, P. H. Fuoss, K. R. Balasubramaniam, J. C. Meador, and P. A. Salvador, "In situ characterization of strontium surface segregation in epitaxial $La_{0.7}Sr_{0.3}MnO_3$ thin films as a function of oxygen partial pressure," *Applied Physics Letters*, vol. 93, no. 15, p. 151904, 2008.

[231] Å. Monsen, F. Song, Z. Li, J. Boschker, T. Tybell, E. Wahlström, and J. Wells, "Surface stoichiometry of $La_{0.7}Sr_{0.3}MnO_3$ during in vacuo preparation: A synchrotron photoemission study," *Surface Science*, vol. 606, no. 17-18, pp. 1360–1366, 2012.

[232] L. Poggini, S. Ninova, P. Graziosi, M. Mannini, V. Lanzilotto, B. Cortigiani, L. Malavolti, F. Borgatti, U. Bardi, F. Totti, I. Bergenti, V. A. Dediu, and R. Sessoli, "A combined ion scattering, photoemission, and DFT investigation on the termination layer of a $La_{0.7}Sr_{0.3}MnO_3$ spin injecting electrode," *The Journal of Physical Chemistry C*, vol. 118, no. 25, pp. 13631–13637, 2014.

[233] C. Borca, B. Xu, T. Komesu, H.-K. Jeong, M. Liu, S.-H. Liou, and P. Dowben, "The surface phases of the $La_{0.65}Pb_{0.35}MnO_3$ manganese perovskite surface," *Surface science*, vol. 512, no. 1-2, pp. L346–L352, 2002.

[234] J. Choi, H. Dulli, S.-H. Liou, P. A. Dowben, and M. Langell, "The influence of surface terminal layer and surface defects on the electronic structure of cmr perovskites: $La_{0.65}A_{0.35}MnO_3$ (A= Ca, Sr, Ba)," *physica status solidi (b)*, vol. 214, no. 1, pp. 45–57, 1999.

[235] P. Graziosi, M. Prezioso, A. Gambardella, C. Kitts, R. Rakshit, A. Riminucci, I. Bergenti, F. Borgatti, C. Pernechele, M. Solzi, D. Pullini, D. Busquets-Mataix, and V. Dediu, "Conditions for the growth of smooth $La_{0.7}Sr_{0.3}MnO_3$ thin films by pulsed electron ablation," *Thin Solid Films*, vol. 534, pp. 83–89, 2013.

[236] M. Prezioso, A. Riminucci, P. Graziosi, I. Bergenti, R. Rakshit, R. Cecchini, A. Vianelli, F. Borgatti, N. Haag, M. Willis, A. J. Drew, W. P. Gillin, and V. A. Dediu, "A single-device universal logic gate based on a magnetically enhanced memristor," *Advanced Materials*, vol. 25, no. 4, pp. 534–538, 2012.

[237] M. P. de Jong, I. Bergenti, W. Osikowicz, R. Friedlein, V. A. Dediu, C. Taliani, and W. R. Salaneck, "Valence electronic states related to Mn^{2+} at $La_{0.7}Sr_{0.3}MnO_3$ surfaces characterized by resonant photoemission," *Physical Review B*, vol. 73, no. 5, 2006.